u^b

b
**UNIVERSITÄT
BERN**

In Situ Comet Research – From Rosetta To Comet Interceptor

Inaugural Dissertation
of the Faculty of Science,
University of Bern

presented by

Daniel Robert Müller

from Boswil AG

Supervisor of Doctoral Thesis:
PD Dr. Martin Rubin

Space Research and Planetary Sciences
Physics Institute, University of Bern

In Situ Comet Research – From Rosetta To Comet Interceptor

Inaugural Dissertation
of the Faculty of Science,
University of Bern

presented by

Daniel Robert Müller

from Boswil AG

Supervisor of Doctoral Thesis:

PD Dr. Martin Rubin

Space Research and Planetary Sciences

Physics Institute, University of Bern

Accepted by the Faculty of Science.

Bern, June 11, 2024   The Dean
                              Prof. Dr. Jean-Louis Reymond

I giesse Kafi über d Miuchstrass, Cappuccino usem All.
(Troubas Kater, All Puccino)

Twinkle twinkle little star, how I wonder what you are!
(Jane Taylor)

Abstract

In Situ Comet Research – From Rosetta To Comet Interceptor
by Daniel Robert Müller

Comets, as remnants from the early Solar System, offer valuable insights into its formation and evolution, making them compelling targets for space missions. This thesis examines two recent European Space Agency missions to comets: the Rosetta mission, which extensively studied the short-period comet 67P/Churyumov-Gerasimenko, and the forthcoming Comet Interceptor mission, set to be launched in 2029 and expected to encounter a long-period comet or interstellar object entering the inner Solar System for the first time.

The Rosetta mission, equipped with the ROSINA instrument suite, significantly advanced our understanding of comets. Two publications resulting from ROSINA data analysis are included in this work. The first study, focusing on isotope analysis of water and alkanes, sheds light on the origin and evolution of comets and our Solar System. Notably, it reveals that the deuterium-to-hydrogen (D/H) ratio remained consistent during the comet's perihelion passage, while also determining the D/H and $^{13}C/^{12}C$ ratios of alkanes. The second study investigates outburst trigger mechanisms, distinguishing between different gas composition behaviours observed during outbursts, and providing insights into the comet's nucleus evolution processes.

In parallel, this thesis documents the development and testing of the Mass Analyser for Neutrals in a Coma (MANiaC), a crucial component of the Comet Interceptor instrument suite. Consisting of a neutral density gauge and a time-of-flight mass spectrometer, prototypes of both instruments have been meticulously calibrated and tested to meet mission requirements. Stability measurements and potential improvements for these instruments are presented. The results demonstrate that even in the prototyping phase, the MANiaC instruments already satisfy almost all requirements regarding resolution and stability and that the path to success for MANiaC is laid out.

This thesis underscores the significance of studying comets and highlights the pivotal role of advanced mass spectrometry in unravelling the mysteries of these celestial bodies. Combining data analysis from previous missions and the development of cutting-edge instrumentation for future missions, this work pushes the boundaries of our knowledge about comets and the broader understanding of the Solar System's formation and evolution.

Acknowledgements

Contents

List of Figures

List of Tables

This thesis includes two differently coloured text boxes for background information and requirement specifications. The colours and styles are defined here:

> **Box 0.1: Example of Background Information Box**
>
> This text box provides auxiliary background information.

> This text box shows and explains an instrument requirement.

List of Abbreviations

ADC	Analogue-to-Digital Converter	LEDA	Linear Electron Detector Array
CASYMIR	Calibration System for the Mass spectrometer Instrument ROSINA	LPC	Long-Period Comet
CASYMS	Calibration System for Mass Spectrometers	LV	Low Voltage
CEM	Channel Electron Multiplier	MANiaC	Mass Analyser for Neutrals in a Coma
COPS	Comet Pressure Sensor	MCP	Micro-Channel Plate
D/H	Deuterium-to-Hydrogen ratio	MS	Mass Spectrometer
DFMS	Double Focusing Mass Spectrometer	m/z	Mass-to-charge ratio
DNC	Dynamically New Comet	NDG	Neutral Density Gauge
DPU	Digital Processing Unit	NIST	National Institute of Standards and Technology
EI	Electron Ionisation	OCC	Oort Cloud Comet
ELU	Electronic Unit	OpAmp	Operational Amplifier
ESA	European Space Agency	PA	Potential Array
FC	Faraday Cup	PCB	Printed Circuit Board
FE	Front End	PG	Pixel Gain
FWHM	Full Width at Half Maximum	PRF	Performance requirement
GS	Gain Step	ROSINA	Rosetta Orbiter Spectrometer for Ion and Neutral Analysis
HV	High Voltage	RTOF	Reflectron Time-of-Flight mass spectrometer
IS	Ion Source	SC	Spacecraft
IR1	Instrument Requirement Level 1	SHU	Sensor Head Unit
JAXA	Japan Aerospace Exploration Agency	SPC	Short-Period Comet
JFC	Jupiter-Family Comet	TOF	Time-of-Flight
L2	Lagrange Point 2	VSMOW	Vienna Standard Mean Ocean Water

Introduction

1

1.1 Comets

Comets are among the most remarkable celestial phenomena, captivating both lay people and scientists alike. Throughout history, their sudden appearances and mysterious nature elicited both fascination and fear. Ancient scriptures describe significant glowing stars gliding across the sky, believed to be supernatural effects (Whipple and Green, 1985; Bailey et al., 1990; Brandt and Chapman, 2004). Today, comets are regarded as natural laboratories for the exploration of extreme physical conditions and keys to the understanding of the Solar System history (Gargaud et al., 2023).

A comet is a small icy body formed in the outer regions of the Solar System, typically containing a significant fraction of volatiles. Comets accreted in the protosolar nebula during the formation of the Solar System 4.6 billion years ago and have, for most of their existence, resided in either the Kuiper Belt or the Oort Cloud. Gravitational perturbations due to encounters with giant planets may alter the trajectory of a comet, deflecting it into the inner Solar System and establishing a generally highly eccentric orbit around the Sun. Comets are grouped depending on their orbits and are named according to their group (see Box 1.1).

Comet nuclei are kilometre to tens of kilometre sized, solid icy conglomerates with low density and high porosity. The popular model of the *dirty snowball* was introduced by Fred Whipple (Whipple, 1950, 1951). However, the more recent state of research could rather describe them as *icy dirtballs*, since the structure of cometary nuclei is governed by the non-volatile constituents rather than by ice or snow (Keller, 1989).

Comet nucleus rotation periods range from a few hours to a few days. The density of comet nuclei has been a long-standing question due to the difficulty of estimating the nucleus mass. A precise evaluation can be obtained through the measurement of the trajectory perturbation of a space probe in the small gravity field of the cometary nucleus. Rosetta performed such measurements for comet 67P/Churyumov-Gerasimenko, determining a bulk density of 0.54 g cm^{-3} (Pätzold et al., 2019), confirming that cometary nuclei are indeed porous bodies. Comet nuclei are frequently observed to fragment (see Box 1.2 and Figure 1.1), indicating that they are bodies with weak tensile strength, resembling rubble piles.

Box 1.1: Groups and Naming Convention of Comets

Cometary orbits are divided into two main categories (Thomas, 2020):

- Short-period comets (SPCs): They have a period P < 200 years, and are thought to originate from the Kuiper Belt, located beyond Neptune.
- Long-period comets (LPCs): They have a period P > 200 years, and are believed to originate from the Oort Cloud, a hypothetical spherical reservoir of comets situated beyond the Kuiper Belt. LPCs are alternatively referred to as Oort Cloud comets (OCCs).

The 200-year period threshold is somewhat arbitrary but corresponds to the time since systematic observations with instruments began.
SPCs are further divided into:

- Jupiter-family comets (JFCs): These have P < 20 years, and are concentrated towards the ecliptic plane. Many have aphelia near the heliocentric distance of Jupiter, and their orbital evolution is significantly influenced by Jupiter's gravitational interaction.
- Halley-type comets (HTCs): These have P > 20 years, and have larger aphelia, with a wide range of inclinations. Some, including 1P/Halley, are retrograde with inclinations greater than 90°. They are also known as nearly isotropic comets.

Comets classified as SPCs or those with confirmed observations at more than one perihelion passage are considered periodic. These comets are designated with a number and the prefix "P/" (e.g., comet 33P/Daniel or 120P/Mueller).

Box 1.2: The Collapse of Comet Shoemaker-Levy 9

Comet Shoemaker–Levy 9 (SL9) was discovered in 1993 by astronomers Carolyn and Eugene Shoemaker, along with David Levy. Appearing as a trail of about 20 fragments (Figure 1.1), it was identified as a Jupiter-family comet disrupted by tidal forces during its previous close encounter with Jupiter one year earlier. These fragments collided with Jupiter in July 1994 (Noll et al., 1996). Calculations demonstrated that SL9's breakup could be modelled as the separation of a strengthless rubble pile of smaller cometesimals, with a density of approximately 0.6 g cm^{-3}, a value notably similar to that later found for comet 67P (Asphaug and Benz, 1994).

FIGURE 1.1: Image of comet Shoemaker-Levy 9 as observed using the Hubble Space Telescope in May 1994 before its impact on Jupiter. Credit: NASA, STScI.

The sublimation of ices in comet nuclei drives cometary activity. As a comet approaches the Sun, the ice in its nucleus begins to sublimate, ejecting gas and dust that form an envelope around the nucleus known as the coma. The coma can extend to distances of 10^5 to 10^7 km from the nucleus, depending on the comet's level of outgassing activity. Because the coma is not gravitationally bound, a trail of gas and dust is left behind as the comet moves on its orbit around the Sun, giving rise to its characteristic tail (Figure 1.2). This dust tail curves in the opposite direction of the comet's motion due to the action of gas drag, solar gravity, and solar radiation pressure pushing the dust particles away from the comet. A second tail, the ion tail, is produced by the ionisation of gases in the coma and always points radially away from the Sun as it is swept along with the solar wind.
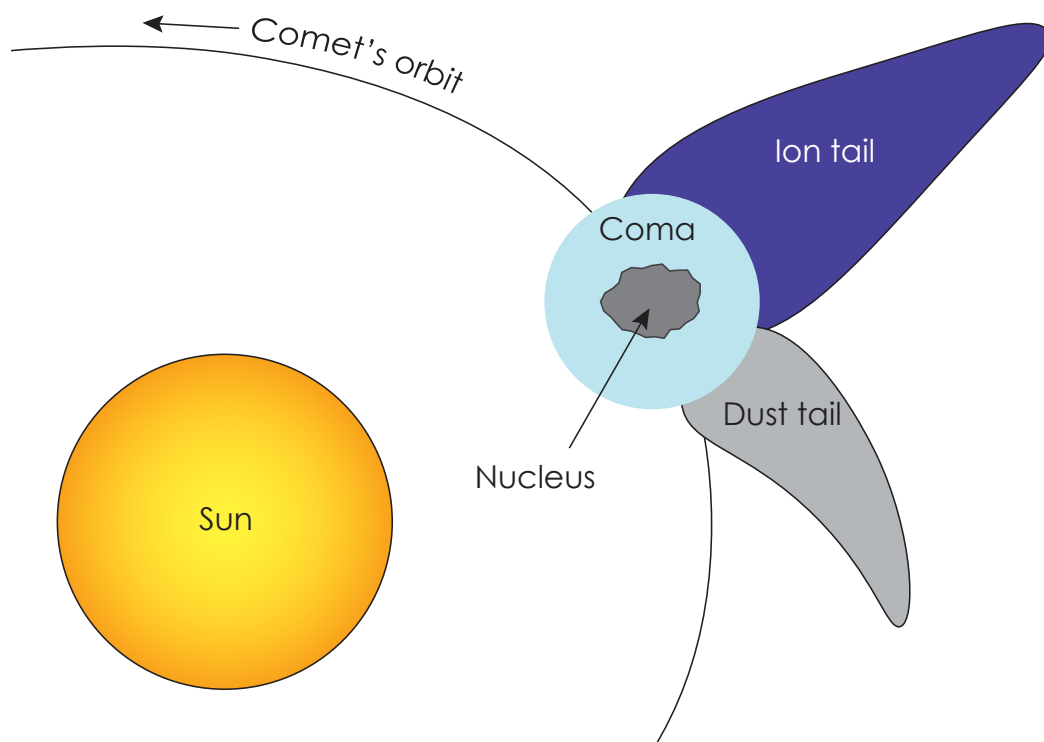
FIGURE 1.2: Morphology of a comet close to the Sun showing its nucleus, coma, and the dust and ion tails (not to scale).

1.2 Comet 67P/Churyumov-Gerasimenko

Comet 67P/Churyumov-Gerasimenko (hereafter 67P), discovered in 1969 by Klim Ivanovich Churyumov and Svetlana Ivanovna Gerasimenko, is a JFC with an orbital period of 6.45 years and a perihelion distance from the Sun of 1.24 au. It has been calculated that before 1840, the comet's perihelion was at about 4 au, and successive dynamical interactions with Jupiter progressively shifted it to its current position. Its latest perihelion passage was in November 2021. Some important properties of 67P are described in Box 1.3.

67P was the target of ESA's Rosetta mission after the original target, comet 46P/ Wirtanen, could not be reached anymore due to delays caused by the failure of the Ariane 5 launcher on the previous launch. The morphology of 67P itself was a major surprise when it was first discovered to be bi-lobate in shape, resembling

a rubber duck (Figure 1.3), during the Rosetta spacecraft's initial approach in July 2014. At this point, the cometary nucleus was finally close enough for the on-board cameras to capture a clear image. This finding was unexpected, as initial predictions based on observations performed with the Hubble Space Telescope suggested a more heterogeneous shape.

Box 1.3: Properties of Comet 67P/Churyumov-Gerasimenko

Nucleus		Orbit	
Small lobe size[a]	$2.6 \times 2.3 \times 1.8$ km	Perihelion dist. from Sun[d]	1.21 au
Large lobe size[a]	$4.1 \times 3.3 \times 1.8$ km	Aphelion dist. from Sun[d]	5.70 au
Mass[b]	1.0×10^{13} kg	Orbital period[d]	6.43 yrs
Mean density[b]	0.54 g/cm^3	Rotation period[e]	12.4 h
Porosity[b]	70 - 80 %		
Albedo[c]	6%		

References: (a) Pajola et al. (2015); (b) Pätzold et al. (2019); (c) Capaccioni et al. (2015); (d) Minor Planet Center (2023); (e) Mottola et al. (2014).
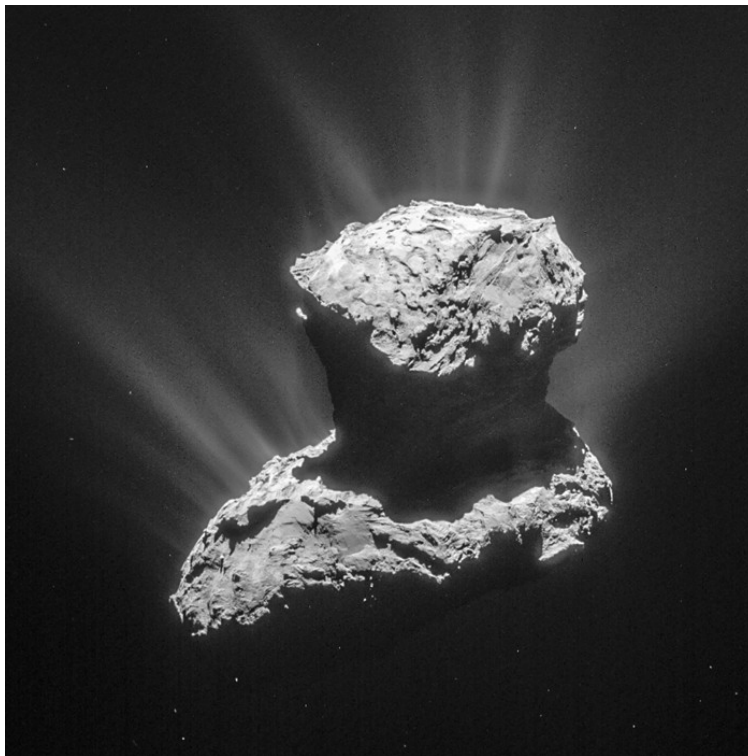
FIGURE 1.3: Full shape image of 67P taken by Rosetta/NavCam. Credit: ESA/Rosetta/ NAVCAM.

Up to date, comet 67P is the most extensively studied comet thanks to the thorough investigation carried out by the Rosetta mission. It is also the first comet where an automated module has landed. Among the many groundbreaking findings (e.g., Fulle et al., 2016; Thomas et al., 2019), some key discoveries of 67P include:

- A high deuterium-to-hydrogen (D/H) ratio of 5.01×10^{-4} has been measured in 67P's water (Altwegg et al., 2015, 2017; Müller et al., 2022). This ratio is more than three times the terrestrial Vienna Standard Mean Ocean Water (VSMOW) value of 1.6×10^{-4} and stands out as the highest value ever observed in a JFC. This finding holds significant implications for the discussion on the origins of terrestrial oceans.

- Comets exhibit complex and individual topography. For centuries, our views of comets were limited to bright streaks in the sky. Rosetta's camera revealed how complex these small icy worlds can be, showcasing cliffs, canyons, boulders, fractures, and regions with different hardness (Thomas, 2020).

- Large fluctuations in composition were discovered in the heterogeneous coma of 67P, demonstrating diurnal and possibly seasonal variations in major outgassing species such as water, carbon monoxide, and carbon dioxide (Hässig et al., 2015).

- Unexpectedly large amounts of O_2 were detected in 67P's coma, indicating that O_2 was a major species of 67P with a coma abundance of (3.80 ± 0.85) % with respect to water (Bieler et al., 2015).

- 67P contains some of the building blocks of life. Rosetta identified organic compounds on the comet supporting this view, including some never seen before on a comet (Altwegg et al., 2016). The amino acid glycine, commonly found in proteins, was spotted in 67P's coma, and phosphorus, a key component of DNA and cell membranes, has been detected in solid particles (Gardner et al., 2020).

1.3   Rosetta Mission

The launch of Rosetta on March 2, 2004, from the Kourou space port in French Guyana marked the beginning of a new era in comet research. While several spacecraft had visited comets by this point, a long-term encounter with a comet had never been performed before. Previous missions focused on short-time encounters, such as single proximity flights through the coma or tail (so-called flybys). During the first comet mission of the European Space Agency (ESA) the spacecraft Giotto successfully flew past comet 1P/Halley and also had a second encounter with comet 26P/Grigg-Skjellerup. In contrast, Rosetta would conduct measurements at various distances and angles between the comet, the Sun, and the spacecraft for more than two years. Additionally, a lander was designed to be the first-ever to land on a comet (see also Box 1.4 describing the mission's name origin). The scientific goals of the Rosetta mission, as outlined by Schwehm and Schulz (1999), included:

- Global characterisation of a cometary nucleus and determination of its dynamic properties, surface morphology, and composition.

- Determination of the chemical, mineralogical, and isotopic compositions of cometary refractories and volatiles.

- Determination of the physical properties and interrelation of volatiles and refractories in a cometary nucleus.

- The study of the development of cometary activity and processes in the surface layer of the nucleus and inner coma, such as interactions of gas and dust.

The long cruise time of more than 10 years until Rosetta's arrival at 67P required a complex series of swing-by manoeuvres to gain the correct acceleration and trajectory. In March 2005, the first of several gravity assist manoeuvres was used to accelerate Rosetta out of Earth's orbit. This was followed by a Martian gravity assist in February 2007 and two more Earth gravity assists in November 2007 and November 2009 to match the comet's orbit. During its journey, Rosetta encountered two asteroids, Steins and Lutetia, in September 2008 and July 2010, respectively. Later on, the increasing heliocentric distance prevented the solar panels of the spacecraft from generating enough energy for a complete system operation. Hence, a planned hibernation of about 2.5 years for all subsystems, including the communication systems onboard Rosetta, was initiated until shortly before the spacecraft arrived at the comet. Rosetta officially arrived on August 6, 2014. This marked the beginning of the Rosetta science phase, during which the spacecraft collected data from comet 67P. Rosetta closely followed the comet, except for a few excursions.

Box 1.4: The Origin of Rosetta's Name

The orbiter probe was named after the Rosetta Stone, an Egyptian stele containing a decree in three scripts (Figure 1.4). The lander, Philae, took its name from the island in the river Nile where an obelisk was found, bearing a bilingual inscription that facilitated the deciphering of the hieroglyphs on the Rosetta Stone. The naming reflects this space mission's ambition to contribute to a deeper understanding of comets and the early Solar System. In addition, the Rosetta spacecraft carried a disc containing thousands of pages of information documenting languages from all over the world.
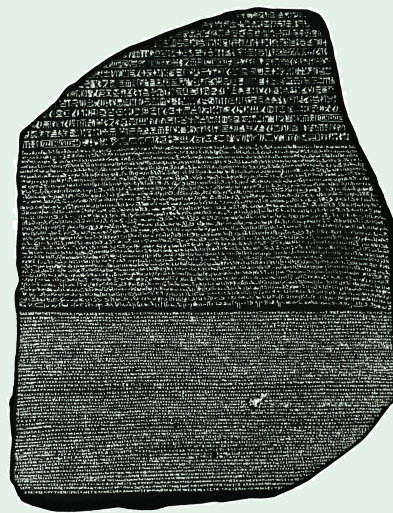
FIGURE 1.4: Rosetta stone. Credit: British Museum, London.

On November 12, 2014, the Rosetta lander unit, Philae, separated from the Rosetta orbiter to perform the first-ever touchdown on a comet. Unfortunately, during Philae's touchdown, the landing devices failed, and the lander could not stabilise on the ground. Instead, it bounced off the surface several times before finally landing in a shadowed area. Although data from the nucleus surface could be collected by Philae, the exact landing spot remained uncertain for almost two years until Philae was finally localised by the OSIRIS camera onboard the orbiter on September 5, 2016. Shortly after, the Rosetta orbiter was intentionally soft-landed onto the nucleus on September 30, 2016, officially closing the mission as the comet was on the outbound leg of its orbit, moving away from the Sun.

The Rosetta spacecraft consisted of an orbiter bearing 11 instrument packages. The lander added 10 more instruments (Schulz, 2010). Table 1.1 gives an overview of the Rosetta instrumentation.

TABLE 1.1: Payload of the Rosetta spacecraft (Schulz, 2010).

Orbiter	
ALICE	Ultraviolet Imaging Spectrometer
CONSERT	Comet Nucleus Sounding Experiment by Radio Wave Transmission
COSIMA	Cometary Secondary Ion Mass Analyser
GIADA	Grain Impact Analyser and Dust Accumulator
MIDAS	Micro-Imaging Dust Analysis System
MIRO	Microwave Instrument for the Rosetta Orbiter
OSIRIS	Optical, Spectroscopic, and Infrared Remote Imaging System
ROSINA	Rosetta Orbiter Spectrometer for Ion and Neutral Analysis
RPC	Rosetta Plasma Consortium
RSI	Radio Science Investigation
VIRTIS	Visible and Infrared Thermal Imaging Spectrometer

Lander	
APXS	Alpha Proton X-ray Spectrometer
CIVA	Comet Nucleus Infrared and Visible Analyser
CONSERT	Comet Nucleus Sounding Experiment by Radio Wave Transmission
COSAC	Cometary Sampling and Composition Experiment
MUPUS	Multi-Purpose Sensor for Surface and Subsurface Science
PTOLEMY	Evolved Gas Analyser for Light Elements
ROLIS	Rosetta Lander Imaging System
ROMAP	Rosetta Lander Magnetometer and Plasma Monitor
SD2	Sample and Distribution Device
SESAME	Surface Electrical Sounding and Acoustic Monitoring Experiment

1.4 ROSINA

One of the instruments onboard the spacecraft, the Rosetta Orbiter Spectrometer for Ion and Neutral Analysis (ROSINA), was designed and developed at the University of Bern to analyse the chemical composition of the volatiles in the coma. The ROSINA instrument was the heaviest payload of Rosetta, weighing 36 kg. It consisted of three different scientific instruments: two mass spectrometers, a Reflectron Time-of-Flight mass spectrometer (RTOF) and a Double Focusing Mass Spectrometer (DFMS), and a pressure sensor, the Comet Pressure Sensor (COPS). Additionally, a Digital Processing Unit (DPU) was attached to the payload.

The RTOF was designed to detect molecules from a mass-to-charge ratio (m/z) of 1 up to 300 in a single spectrum, providing an advantage in terms of time efficiency over a time-consuming mass scan with DFMS. However, this advantage comes along with limitations in mass resolution. To address this, a reflectron was installed in the instrument. The reflectron significantly increased the flight distance of the molecules through the instrument, thereby enhancing the mass resolution. This approach achieved a mass resolution of 500 at 1% peak height. While the RTOF was ideal for providing an overview of the molecular composition of the comet, detailed studies required higher mass resolution. The concept of mass resolution is introduced in more detail in Section 4.2.2.

This could be achieved with the second mass spectrometer, DFMS. It reached a higher mass resolution of 3000 (at 1% peak height) by using an electrostatic and a magnetic field in combination to separate the molecules. Hence, it was ideal for investigating molecular species with similar mass or minor abundance. More quality criteria for mass spectrometers are introduced in Box 1.5. Chapter 2 focuses on the DFMS, as mostly data from this instrument were analysed for this work.

The COPS completed the ROSINA instrument package, which was designed to measure the gas density in the coma. It consisted of two different gauges. In the nude gauge, molecules were first ionised via electron ionisation, and then the current was measured with an electrometer after acceleration. It measured the total neutral particle density in the coma. The second gauge, the ram gauge, thermalised the neutral gas molecules first before ionisation. Consequently, it was capable of measuring ram pressure, which is proportional to the cometary gas flux. Although COPS was not designed to detect cometary dust particles, it was nevertheless able to measure them indirectly via the sublimation products of the volatiles contained therein (Pestoni et al., 2021a,b, 2023).

Each ROSINA instrument was used in combination with the DPU. Its function was the communication between instruments and spacecraft, the storage of data, and commanding of the instruments. The entire ROSINA payload is described in Balsiger et al. (2007). In addition, Scherer et al. (2006) and Gasc et al. (2017) provide detailed descriptions of RTOF.

Box 1.5: Quality Criteria for Mass Spectrometers

Mass spectrometers must meet several criteria to ensure their quality. The performance of mass spectrometers is determined by mass resolution, sensitivity, signal-to-noise ratio, dynamic range, mass range, and scan duration, each playing a crucial role in the instrument's overall effectiveness and reliability. The mass resolution is the instrument's ability to separate two species of close mass. The sensitivity measures how much the signal changes when the analyte quantity increases. It depends on ionisation efficiency, ion extraction from the ionisation source, mass range, and mass analyser transmission. It is expressed as the ratio between ion current and analyte partial pressure [A/Pa]. The sensitivity should not be confused with the detection limit, which is the smallest analyte amount needed to produce a signal distinguishable from background noise. However, the sensitivity is a critical quantity to derive the detection limit.

The signal-to-noise ratio (S/N) describes the uncertainty of an intensity measurement by quantifying the ratio between signal intensity and noise. Noise, being statistical, can be reduced by prolonged data acquisition and averaging spectra. Consequently, an intense peak has a better S/N than a lower intensity peak in the same spectrum. Noise reduction is proportional to the square root of the acquisition time multiplier or the number of averaged spectra.

The dynamic range is the ratio between the minimal and maximal concentrations of compounds that can be detected simultaneously in a sample. The mass range defines the mass-to-charge ratios that the instrument can cover. The scan duration is dependent on the instrument design and ion separation mechanism and can vary between an immediate scan of the full mass range and a step-by-step scan of individual masses within the total mass range.

Double Focusing Mass Spectrometer

2

The ROSINA Double Focusing Mass Spectrometer (DFMS) is a Nier-Johnson type double focusing mass spectrometer with a high mass resolution of m/Δm = 3000 at the 1%-level on the mass-to-charge ratio (*m/z*) 28 (Balsiger et al., 2007). This instrument integrates an electrostatic analyser and a magnetic field sequentially to effectively separate molecules based on their *m/z*. This section explains the working principle of the DFMS and outlines the data analysis procedure.

2.1 DFMS Working Principle

As with any mass spectrometer, the ROSINA/DFMS comprises three main components: the ion source, a mass analyser, and three different detectors:

- The ion source is where the incoming neutral particles undergo electron ionisation.

- The mass analyser includes an electrostatic analyser and a permanent magnet. The ions and charged fragments generated in the ion source are separated based on their *m/z* in the mass analyser.

- The DFMS features three detectors: the MCP/LEDA, consisting of two Micro-Channel Plates (MCPs) combined with a Linear Electron Detector Array (LEDA) as the primary detector, a Channel Electron Multiplier (CEM), and a Faraday Cup (FC).

Figure 2.1 shows a technical drawing of the DFMS, depicting the ion's flight path through the instrument's main optical elements, whereas Figure 2.2 illustrates a cross section of the DFMS.

Molecules entering the DFMS arrive at the ion source, where they undergo electron ionisation, acquiring a positive charge. To achieve this, a filament is heated and electrons are emitted from the filament through a specific voltage setting in the ion source at an emission current of 2, 20, or 200 μA, creating an electron beam. When an electron collides with a neutral molecule, it releases an electron from the valence orbital, resulting in a positively charged molecule due to the loss of a negative charge. The electron ionisation also induces fragmentation of the molecule into smaller pieces, the extent of which depends on the energy of the emitted electrons. A standard emission energy is 70 eV, as commonly used in reference fragmentation databases. However, pre-flight testing of the DFMS has demonstrated improved performance at 45 eV, offering the advantages of reduced fragmentation and increased quantities of
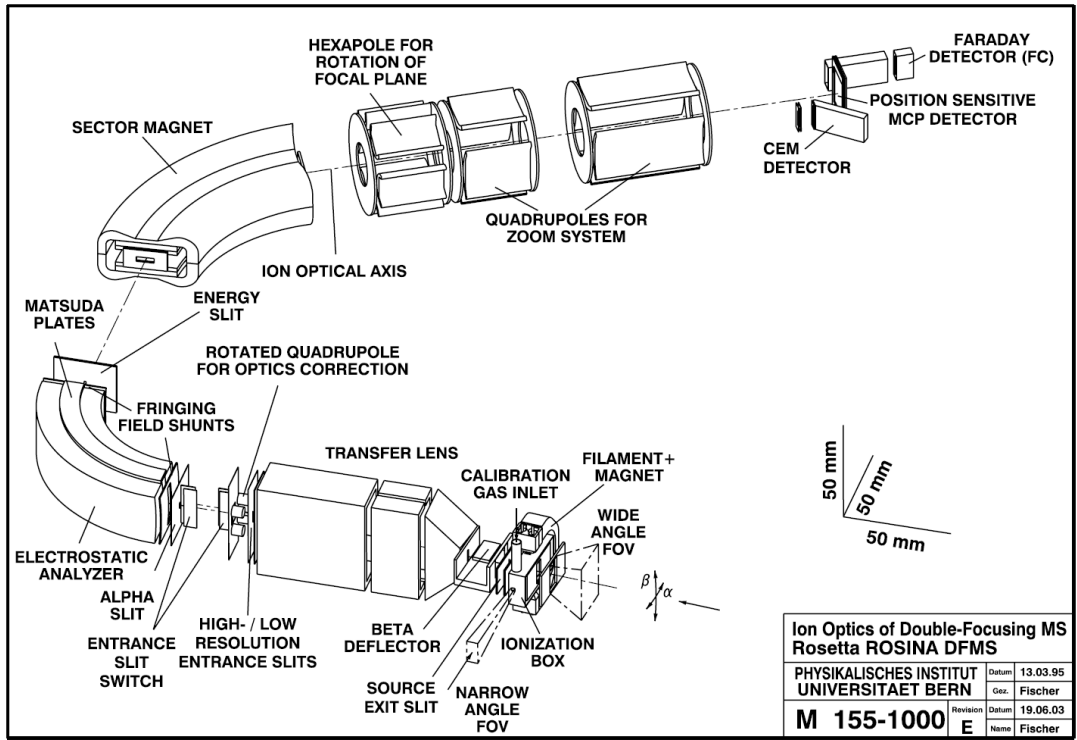
FIGURE 2.1: Drawing of the main ion optical elements of the DFMS including all sections along the ion flight path through the instrument. Source: Balsiger et al. (2007), reproduced with permission from Springer Nature.
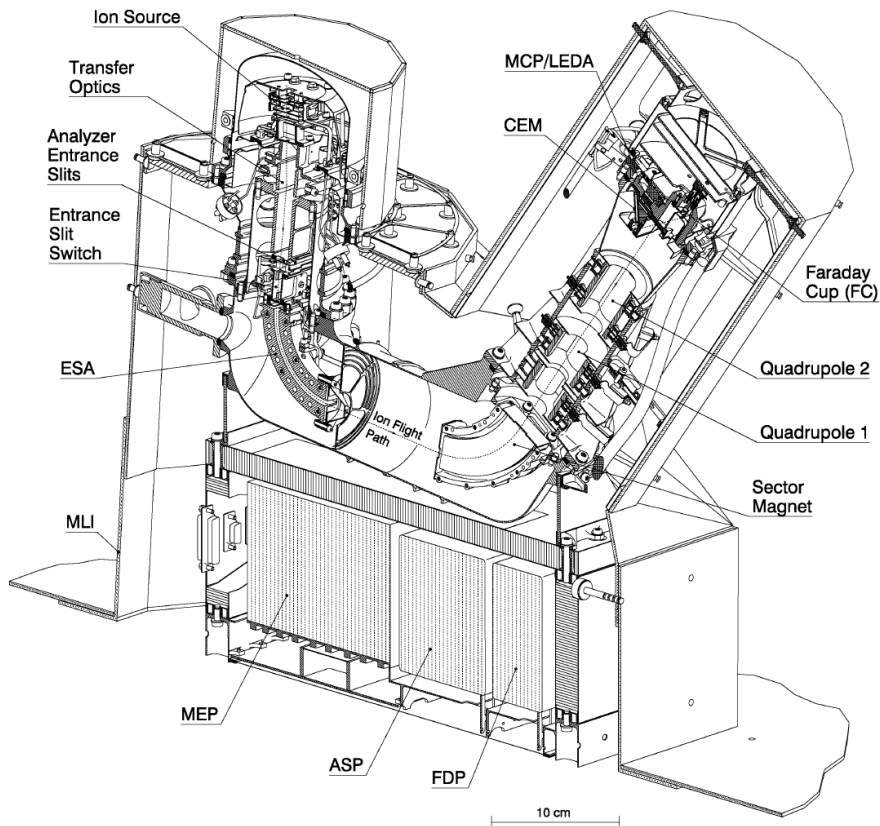
FIGURE 2.2: Cross section of the DFMS showing details of instrument components. Source: Balsiger et al. (2007), reproduced with permission from Springer Nature.

parent molecules after the ionisation process. This difference only introduced minor deviation of DFMS results with those in common databases (Schuhmann, 2020).

To prevent the detection of cometary ions in neutral gas mode, an additional positive potential of 200 V is applied. This prevents primary positively charged cometary ions from entering the instrument in neutral mode. The DFMS can also be operated in ion mode, enabling the collection and analysis of molecules already ionised within the comet's environment.

The newly created ions are then extracted from the ion source through several lenses and are accelerated with the acceleration voltage V_{acc}. This acceleration voltage is mass dependent and approximately follows $1/\sqrt{m}$. Subsequently, the ions pass through a narrow slit of 14 μm for high-resolution mode and 200 μm for low-resolution mode before entering the electrostatic analyser. The electrostatic analyser consists of two toroid-shaped plates with radii of 57.5 mm for the smaller inner plate and 62.5 mm for the larger, outer plate. The analyser directs the ions along a 90° trajectory, correcting for slightly different trajectories and velocities resulting from field gradients in the ion source. Some ions might receive slightly higher kinetic energies depending on their exact starting positions in the ion source. The electrostatic analyser focuses the energy dispersion, allowing molecules of similar energy to converge at the energy slit at the exit of the analyzer. After the electrostatic analyser, the ions enter the 60° sector magnet, which separates the incoming ions according to their momentum per charge and focuses them onto the focal plane behind the magnet.

Upon leaving the sector magnet, the remaining ions enter a hexapole, where the focal plane is aligned relative to the optical axis of the ions. The ions then enter the DFMS zoom optics, which, consisting of two consecutive quadrupoles, can increase the image size at the detector, as the main detector has a limited spatial resolution determined by the pixel size.

Having passed through the zoom optics, the ions reach the detector. Three different types of detectors are implemented in DFMS: a Channel Electron Multiplier, a Faraday Cup, and a Multichannel Plate (MCP, see Box 2.1), aligned along the focal plane. Most measurements have been taken with the MCP, designed as the main detector for DFMS. It is used in combination with a Linear Electron Detector Array (LEDA), consisting of two independent rows (Row A and B) of anodes on the LEDA with 512 pixels each. The output of the MCP/LEDA detector is not the ion current itself but the secondary electron current produced by the impinging ions. This is measured in analogue mode and then converted into a digital signal with an Analogue-to-Digital Converter (ADC). For more information on the detector design and working principle, refer to Balsiger et al. (2007).

DFMS has a very high mass resolution and spectra can be obtained in high or low resolution modes depending on the level of detail needed. This is only possible with a complex instrument design where minimal misalignment of the magnet or analyser would have a significant impact. However, the most significant drawback of the DFMS is the long measurement time. The working principle of how DFMS separates molecules according to their *m/z* only allows mass scans. To do so, voltages are adjusted constantly to allow only molecules around a certain integer mass to pass through the instrument. Such mass scans are time-consuming and measuring from *m/z* 13 to *m/z* 100 (typical measurement mode mass range) takes around 45 minutes. Additionally, the results are complex to analyse as several instrument-related factors need to be considered in the DFMS data treatment. Many of these are energy-dependent, and hence cannot be applied collectively. The following subsection explains the DFMS data treatment.

Box 2.1: Microchannel Plate (MCP)

A microchannel plate (MCP) is a two-dimensional sensor capable of detecting electrons and ions in a vacuum, amplifying the detected signals. MCPs are frequently employed in mass spectrometry detectors. These plates function as continuous electron multipliers, comprising numerous of thin tubes arranged in parallel and slightly tilted towards a plate (Figure 2.3). Within these tubes, an impacting particle triggers the release of secondary electrons on a suitable surface, leading to a multiplication effect. The electron multiplication occurs within the isolated tube (made of glass or ceramic) coated with a resistive film. A voltage gradient is applied along the tube due to the voltage difference of a few hundred volts between the two sides of the MCP, inducing electron acceleration and formation of an electron cascade.

Typically, two MCPs are arranged consecutively to enhance the gain. A common MCP configuration is the Chevron assembly (Figure 2.4) leading to a gain of $\sim 10^6$.
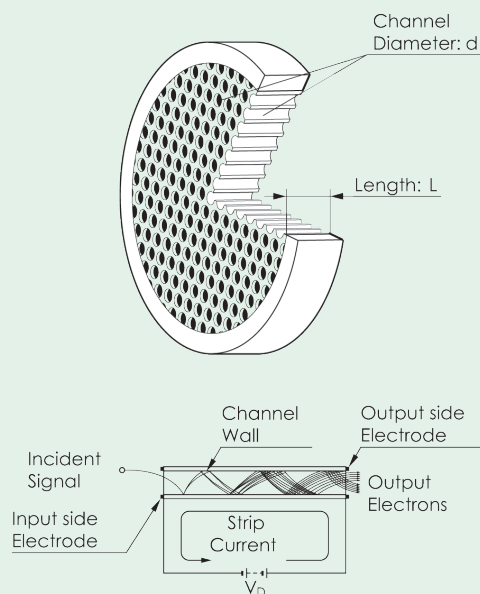
FIGURE 2.3: Schematic structure of MCP. Adapted from Hamamatsu.
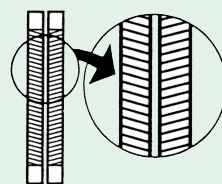
FIGURE 2.4: Schematic of MCP Chevron assembly. Adapted from Hamamatsu.

2.2 DFMS Data Analysis

Various pre-coded measurement modes facilitate the operation of the DFMS. However, the accurate treatment and interpretation of DFMS data remain demanding tasks. Since DFMS performs mass scans, it generates large amounts of raw spectra that necessitate manual application of the mass scale. Given the high mass resolution, small uncertainties can significantly impact data interpretation. Additionally, several instrument-related correction factors must be applied to the spectra to derive accurate ion quantities from the detector signal. Some of these correction factors are mass- and species-dependent, making it impractical to apply them universally to all spectra. Even after the correct application of all conversion and correction factors, interpreting DFMS data remains challenging and requires experience. The necessary steps to process DFMS raw data and obtain the number of incident ions per mass spectrum are as follows:

1. Subtraction of the LEDA offset

2. Correction for overall gain

3. Correction for individual pixel gain

4. Correction for ADC conversion and LEDA anode capacity

5. Application of the mass scale

Figure 2.5 a depicts an example of a DFMS raw spectrum, displaying the signal over the 512 LEDA pixels of one row of the detector for an integration time of 20 s. The result of a full data treatment is then illustrated in Figure 2.5 b, where an accurate mass scale is applied, and the number of detected ions is calculated. Additionally, the individual peaks are fitted with double Gaussian peak profile functions, and the corresponding ionic species are indicated with their sum formula.
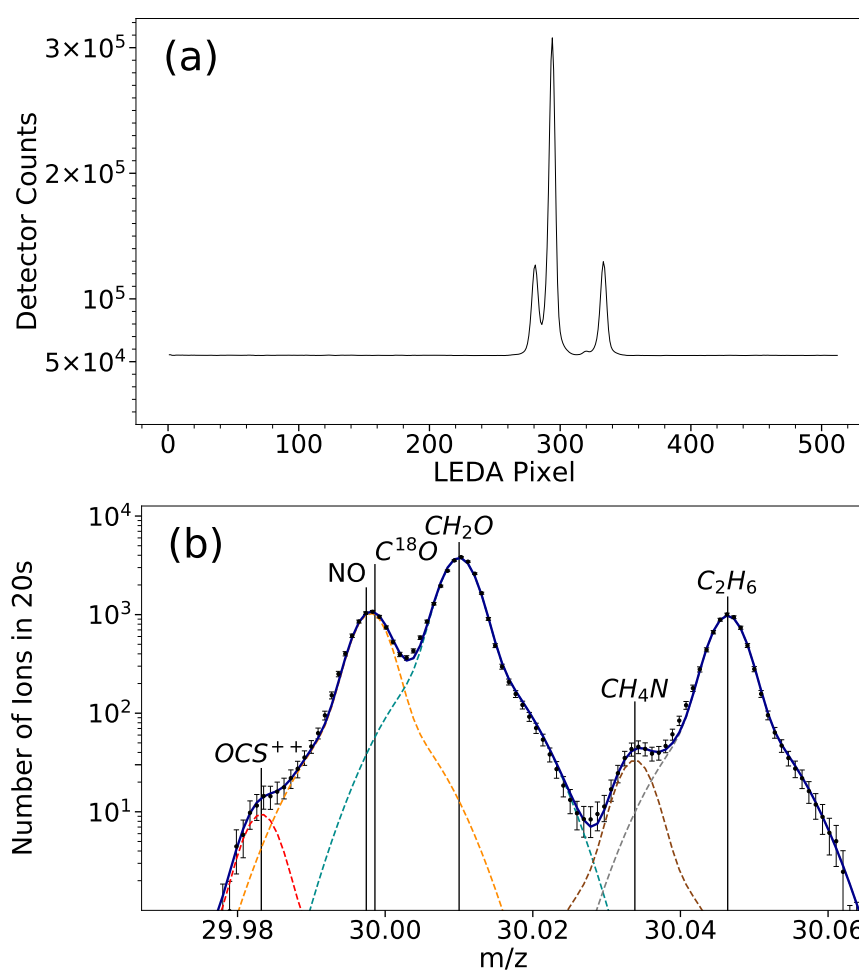
FIGURE 2.5: Example of DFMS spectra for *m/z* 30. Panel a: DFMS raw spectrum from 2014-10-03 19:36 (UTC) displaying the ADC detector counts over the 512 LEDA pixel of the detector for the 20 s integration time. Panel b: High-resolution spectrum of the same data set as in panel a after LEDA offset subtraction, pixel gain and gain correction, and ADC conversion. A suitable mass scale is applied and the x-axis is only shown for the part containing ion signals. Measured data are represented by black dots, including their statistical uncertainties. Individual mass fits and the total sum of the fits are depicted with coloured lines. The peaks of NO and $C^{18}O$ could not be resolved and appear as one peak (orange line). Note the conversion to log scale from panel a to panel b.

2.2.1 LEDA Offset Subtraction

The raw spectrum has an offset of around 53000 counts. This results from the LEDA charging, that has to be applied prior to a measurement. This offset is removed by applying a polynomial fit of either first, second, or third order that follows the baseline of the spectrum and then subtracting the area under the polynomial curve:

$$\text{ADC counts}_{\text{corr}} = \text{ADC counts} - \text{Offset}. \tag{2.1}$$

2.2.2 Gain Correction

Ions impinging on the MCP detector release a cascade of secondary electrons, amplifying the signal. The degree of amplification, referred to as gain, depends on the voltage difference applied to the MCP stack. For DFMS, 16 fixed voltage settings, known as gain steps (GS), have been predefined. The gain can be described as the number of secondary electrons released by each impinging ion:

$$\text{Gain} \propto \frac{\text{Number of secondary electrons}}{\text{Number of ions}}. \tag{2.2}$$

Adjusting the number of counts with the overall gain, Gain(GS), results in a modification of Equation (2.1):

$$\text{ADC counts}_{\text{corr}} = \frac{\text{ADC counts}(\text{p}) - \text{Offset}}{\text{Gain}(\text{GS})}. \tag{2.3}$$

The gain decreased over time due to extensive instrument usage. Details on how to retrieve the gain for each gain step and the most recent gain factors to be used are explained in Schroeder (2020).

2.2.3 Pixel Gain Correction

During DFMS operations, not all 512 anode pixels on each of the LEDA's two rows were equally utilised. The ion beam was typically focused towards the centre of the detector, resulting in more frequent usage and, consequently, more prominent degradation of the pixels in the middle. The correction factors introduced to account for the uneven degradation of the 512 pixels were referred to as the individual pixel gain (PG), to distinguish it from the overall gain of the MCP (Section 2.2.2).

Correcting the individual pixel gain, PG(GS,p), for the background and gain step corrected number of counts leads to an adaptation of Equation (2.3):

$$\text{ADC counts}_{\text{corr}}(\text{p}) = \frac{\text{ADC counts}(\text{p}) - \text{Offset}}{\text{Gain}(\text{GS}) \cdot \text{PG}(\text{GS}, \text{p})}. \tag{2.4}$$

The pixel gain correction factors are dependent on the gain step or detector amplification applied. Consequently, each individual pixel had to be corrected at regular intervals as the degradation of the MCP/LEDA was usage-dependent and increased over time (Schroeder, 2020). Furthermore COPS was used for absolute calibration.

2.2.4 ADC Conversion and LEDA Anode Capacity

Finally, to derive the number of ions, N_{ions}, from the number of counts, or secondary electrons, the electronic conversion needs to be considered. Thus, proportionality constants for both the Analogue-to-Digital Conversion (ADC), $c_{ADC} = 6.105 \times 10^{-4}$ V, and the LEDA anode capacity, $c_{LEDA} = 4.22 \times 10^{-12}$ F are introduced. Additionally, a mass dependent detector yield, Y_s, and the integration time, t, are employed to calculate the number of ions impinging on each pixel, p, per second. This leads to a further modification of Equation (2.4):

$$N_{ions}(p) \, s^{-1} = \frac{ADC \; counts(p) - Offset}{Gain(GS) \cdot PG(GS, p)} \cdot \frac{1}{Y_s} \cdot \frac{c_{ADC} \cdot c_{LEDA}}{e \cdot t}, \tag{2.5}$$

where p is the pixel number ranging from 1 to 512, and $e = 1.602 \times 10^{-19}$ C is the elementary charge. The standard integration time, t, was set to 20 s.

2.2.5 Mass Scale

After calculating the number of ions for each pixel, it is necessary to apply a mass scale to determine which ions represent which molecule. To achieve this, a mass scale assigns a *m/z* value to each of the 512 pixels on each row of the LEDA (Le Roy et al., 2015):

$$m(p) = m_0 \cdot e^{\left(\frac{(p - p_0) \cdot x}{D \cdot z} \right)}, \tag{2.6}$$

where $m(p)$ is the mass-to-charge ratio corresponding to a specific pixel p. m_0 represents the central commanded mass (usually an integer) of the spectrum, and p_0 is the pixel on which m_0 is situated. p_0 is also referred to as pixel zero. x denotes the pixel step width (i.e., 25 μm), D is the dispersion constant, and z is the zoom factor.

It is crucial to apply an accurate mass scale, as even small inaccuracies can lead to misinterpretation of the data. The mass scale application can be challenging, considering that several instrumental factors taken into account are mass-dependent. The zoom factor is typically set to 6.4 for high-resolution measurements. However, for masses lower than *m/z* 21, it is lower, and even for higher masses, a discrepancy of ±0.2 can be observed due to magnet temperature fluctuations. The values of the used zoom factors can be found in Hässig (2013) and Schroeder (2020). A change in the zoom factor results in an accordion effect in the spectra—meaning a widening or narrowing of the spectra along its x-axis and, consequently, a shift of the peak position over the mass scale. The same effect occurs if the dispersion changes, which is typically set to 127'000 for all *m/z* up to 69. For *m/z* 70 and higher, the application of an additional post-acceleration voltage of 1,000 V (compared to 50 V for *m/z* lower than 70) leads to a non-linear drop in the dispersion. However, this has not been used in this thesis, as only *m/z* lower than 70 have been studied. The DFMS mass scale application can be described as an iterative process. In the initial hypothesis, the dominant peak in a spectrum is selected and interpreted, and a preliminary mass scale is applied. In this way, all the remaining peaks in the spectrum can be identified. If the outcome is plausible in terms of settings and chemistry, the final mass scale can be applied. The identification may also be helped by the adjacent spectra, as the values of p_0, D, et cetera should remain relatively consistent.

Finally, to determine the quantity of ions detected per species, a fitting routine has to be applied, and the area under the fitted curve needs to be integrated. The standard fitting routine involves a double-Gaussian distribution (sum of two Gaussian peaks), which is the specific peak shape for the DFMS instrument resulting from its design.

The second Gaussian is dependent on the first one, with its amplitude being roughly 10% of the first Gaussian's signal and its width being about three times broader. All peaks on the same spectrum maintain consistent width and height ratios for the two Gaussian distributions.

Hence, the final amount of detected ions per species is given by the integral of the fitted double-Gaussian distribution:

$$\text{Number of particles} = \int_{-\infty}^{+\infty} \text{counts}(p) \, dp = \sqrt{\pi}(a_1 c_1 + a_2 c_2). \tag{2.7}$$

where a_1 and a_2 are the amplitudes, and c_1 and c_2 are the widths of the first and the second Gaussian, respectively.

A DFMS spectrum consists of two rows on the LEDA for redundancy reasons, referred to as row A and row B. Generally, a discrepancy in the signal and a slight shift of the peaks can be observed between the row A and row B spectra since the ion beam is not perfectly aligned. However, the discrepancy varied over the duration of the mission, depending on the mission phase. One of the two rows is more sensitive due to changing electric field distributions in the ion source. For the derivation of the total count of ions, both signals can be summed up, or one of the two rows can be consistently used.

Publications from ROSINA Data Analysis

<div style="text-align: right; font-size: 3em; color: gray;">3</div>

3.1 High D/H ratios in water and alkanes in comet 67P/Churyumov-Gerasimenko measured with Rosetta/ROSINA DFMS

Studying isotope ratios on comets is crucial because it offers insights into the history and origin of materials in the Solar System. Isotopic abundances, particularly the deuterium-to-hydrogen (D/H) ratio, provide valuable information on the processes that occurred during the formation of comets and the early Solar System. By analysing these ratios, it is possible to reconstruct the conditions and environments that existed billions of years ago, shedding light on fundamental questions about planetary system formation and evolution.

Discrepancies between pre- and post-perihelion measurements of the D/H ratio in water on comet C/2014 Q2 (Lovejoy) (Biver et al., 2016; Paganini et al., 2017), as well as a suggested correlation between the D/H ratio in comets and their active area fraction, pose intriguing questions about the composition and dynamics of comet nuclei (Lis et al., 2019). In this context, the isotope study aims to elucidate the dynamics of the D/H ratio in 67P's water over time, investigating its dependence on factors like heliocentric distance, phase angle, and gas production rate. Additionally, the study delves into the isotopic ratios of alkanes, considering their potential role in understanding the chemical and physical conditions during Solar System formation and the delivery of organic matter to celestial bodies (Lunine and Atreya, 2008; Clark et al., 2009), including Earth. This comprehensive approach shall contribute to the broader understanding of cometary composition and its implications for planetary science.

Key findings of this study include the independence of the D/H ratio in water from various factors such as heliocentric distance and cometary activity level. Additionally, an absolute D/H ratio from HDO/H_2O of $(5.01 \pm 0.40) \times 10^{-4}$ and the $^{16}O/^{17}O$ ratio in water of 2347 ± 191 were obtained.

The D/H ratios in alkanes compared to water are highly elevated. While no correlation between the $^{13}C/^{12}C$ ratio and the D/H ratio for different cometary molecules was found, the observed consistency of the D/H ratio in 67P's water challenges theories of non-steady-state water ice sublimation. However, further confirmation with measurements from other comets and approaches is warranted. The study underscores the need for more data analysis from various Solar System objects to elucidate the origin and history of organic matter.

Credit: D. R. Müller, A&A **662**, A69 (2022), reproduced with permission © ESO.

High D/H ratios in water and alkanes
in comet 67P/Churyumov-Gerasimenko measured
with Rosetta/ROSINA DFMS

D. R. Müller[1] , K. Altwegg[1] , J. J. Berthelier[2] , M. Combi[3] , J. De Keyser[4] , S. A. Fuselier[5,6] , N. Hänni[1] ,
B. Pestoni[1] , M. Rubin[1] , I. R. H. G. Schroeder I[1] , and S. F. Wampfler[7]

[1] Physikalisches Institut, University of Bern, Sidlerstrasse 5, 3012 Bern, Switzerland
   e-mail: `daniel.mueller@unibe.ch`
[2] Laboratoire Atmosphères, Milieux, Observations Spatiales (LATMOS), 4 Avenue de Neptune, 94100 Saint-Maur, France
[3] Department of Climate and Space Sciences and Engineering, University of Michigan, 2455 Hayward, Ann Arbor, MI 48109, USA
[4] Royal Belgian Institute for Space Aeronomy, BIRA-IASB, Ringlaan 3, 1180 Brussels, Belgium
[5] Space Science Directorate, Southwest Research Institute, 6220 Culebra Rd., San Antonio, TX 78228, USA
[6] Department of Physics and Astronomy, The University of Texas at San Antonio, San Antonio, TX 78249, USA
[7] Center for Space and Habitability, University of Bern, Gesellschaftsstrasse 6, 3012 Bern, Switzerland

ABSTRACT

Context. Isotopic abundances in comets are key to understanding and reconstructing the history and origin of material in the Solar System. Data for deuterium-to-hydrogen (D/H) ratios in water are available for several comets. However, no long-term studies of the D/H ratio in water of a comet during its passage around the Sun have been reported thus far. Linear alkanes are important organic molecules that have been found on several Solar System bodies, including comets. To date, the processes of their deuteration are still poorly understood, only the upper limits of isotopic ratios for D/H and $^{13}C/^{12}C$ in linear alkanes are currently available.
Aims. The aim of this work is to carry out a detailed analysis of the D/H ratio in water as a function of cometary activity and spacecraft location above the nucleus. In addition, a first determination of the D/H and $^{13}C/^{12}C$ ratios in the first four linear alkanes, namely, methane (CH_4), ethane (C_2H_6), propane (C_3H_8), and butane (C_4H_{10}) in the coma of 67P/Churyumov-Gerasimenko is provided.
Methods. We analysed in situ measurements from the Rosetta/ROSINA Double Focusing Mass Spectrometer (DFMS).
Results. The D/H ratio from HDO/H_2O and the $^{16}O/^{17}O$ ratio from $H_2^{16}O/H_2^{17}O$ did not change during 67P's passage around the Sun between 2014 and 2016. All D/H ratio measurements were compatible within 1σ, with the mean value of 5.01×10^{-4} and its relative variation of 2.0%. This suggests that the D/H ratio in 67P's coma is independent of heliocentric distance, level of cometary activity, or spacecraft location with respect to the nucleus. Additionally, the $^{16}O/^{17}O$ ratio could be determined with a higher accuracy than previously possible, yielding a value of 2347 with a relative variation of 2.3%. For the alkanes, the D/H ratio is between 4.1 and 4.8 times higher than in H_2O, while the $^{13}C/^{12}C$ ratio is compatible, within the uncertainties, with the available data for other Solar System objects. The relatively high D/H ratio in alkanes is in line with results for other cometary organic molecules and it suggests that these organics may be inherited from the presolar molecular cloud from which the Solar System formed.

Key words. comets: general – comets: individual: 67P/Churyumov-Gerasimenko – instrumentation: detectors – astrochemistry – methods: data analysis

1. Introduction

Comets are considered as reservoirs of material preserved from the early Solar System. By making this material available to in situ exploration, cometary science contributes important information on the history of the Solar System (Drozdovskaya et al. 2019; Mumma & Charnley 2011). Investigating the isotopic abundances of different elements in various molecules in comets is essential, as the isotopic ratios are sensitive to the environmental conditions at the time of the molecules' formation and they provide crucial information for improving our understanding of the origins of cometary material (Biver et al. 2019; Bockelée-Morvan et al. 2015; Hässig et al. 2017).

The best-studied comet to date is comet 67P/Churyumov-Gerasimenko (hereafter, 67P), a Jupiter-family comet (JFC) that was followed by the Rosetta spacecraft during its orbit around the

Sun. In August 2014, Rosetta rendezvoused with 67P at a heliocentric distance of around 3.6 au. It then accompanied the comet through its perihelion at 1.24 au from the Sun and followed the orbit of 67P back out to a distance of almost 4 au, whereupon the spacecraft intentionally soft-landed on the comet's surface at the end of September 2016. The Rosetta spacecraft, as part of a mission launched and operated by the European Space Agency (ESA), helped uncover a great store of new knowledge about 67P, such as its gas and dust composition (e.g. Herny et al. 2021; Longobardo et al. 2020; Pestoni et al. 2021), nucleus surface (e.g. Feller et al. 2019) and temporal evolution (e.g. Combi et al. 2020; Läuter et al. 2020; Rubin et al. 2019). With its lander, Philae, it was even able to acquire gas and volatiles in dust composition data directly on or near the comet's surface by the COSAC (Goesmann et al. 2015) and Ptolemy (Wright et al. 2015) instruments. No prior cometary observation has ever been performed

for as long a duration and with as high a measurement sensitivity as the Rosetta mission.

The Rosetta spacecraft carried several instrument packages on board, one of which was the Rosetta Orbiter Spectrometer for Ion and Neutral Analysis (ROSINA). ROSINA was comprised of two mass spectrometers, the Double Focusing Mass Spectrometer (DFMS) and a Reflectron-type Time-Of-Flight mass spectrometer (RTOF), in addition to the COmet Pressure Sensor (COPS). In particular, DFMS was used for measurements of the molecular and isotopic composition of cometary volatiles (Balsiger et al. 2007). Hässig et al. (2017) showed that the instrument had a sensitivity, dynamic range and mass resolution high enough to detect even trace amounts of rare isotopologues alongside their more abundant counterparts. It has been used by many authors to investigate the isotopic ratios of sulfur (Calmonte et al. 2017; Hässig et al. 2017), carbon (Hässig et al. 2017; Altwegg et al. 2020), the halogens bromine and chlorine (Dhooghe et al. 2017), and oxygen (Altwegg et al. 2020; Hässig et al. 2017; Schroeder et al. 2019b) in 67P. Altwegg et al. (2015, 2017) used it to measure the D/H ratio in water in 67P's coma, using data from the beginning and near the end of the Rosetta mission. Both measurements were consistent within the uncertainties. From HDO/H_2O, a D/H ratio of $(5.3 \pm 0.7) \times 10^{-4}$ was deduced. This is more than three times the terrestrial Vienna Standard Mean Ocean Water (VSMOW) value of 1.5576×10^{-4}, and one of the highest ever measured in a JFC.

Both measurements by Altwegg et al. (2015, 2017) were performed at times when 67P was relatively far from the Sun. The first had relied on data from well before perihelion, in August–September 2014 at a heliocentric distance of 3.4 au, while the second evaluated data from December 2015 at 2 au and the outbound equinox in March 2016 at 2.6 au. Due to the large heliocentric distances of 67P during these measurements, the question arises as to whether the HDO/H_2O ratio would differ at smaller heliocentric distances, when a large increase in sublimation from the surface of the cometary nucleus occurred and fresh layers of the comet's surface were likely exposed. Additionally, different cometary hemispheres were active at different times. At greater heliocentric distances, most of the water outgassed came from the comet's northern latitudes. Conversely, closer to perihelion, the contributions of the southern latitudes were more significant (Keller et al. 2015). Schroeder et al. (2019a) investigated the difference between the comet's two lobes and concluded that no significant difference in the D/H ratio could be observed.

A comparison of different Solar System objects shows a broad variation in D/H ratios, with most objects being enriched in deuterium compared to the protosolar nebula (Altwegg et al. 2015). Different potential mechanisms have been proposed to explain these large variations, for instance solar wind induced water formation and isotopic fractionation. Daly et al. (2021) has stated that isotopically light water reservoirs could have been produced by solar wind implantation into fine-grained silicates. The authors concluded that this may have been a particularly important process in the early Solar System, thus potentially providing a means to recreate Earth's current water isotope ratios. On the other hand, the isotopic fractionation describes the variation in abundances of the isotopes of an element. It arises from both physical and chemical processes and is also temperature-dependent for some molecules. According to Kavelaars et al. (2011), the main reservoir of deuterium in the protosolar nebula was molecular hydrogen with a D/H ratio of 1.5×10^{-5}. Ion–molecule reactions in the interstellar medium or grain surface chemistry can cause fractionation among deuterated species. In the pre-solar cloud, fractionation resulted in

molecules being enriched in deuterium. Isotopic exchange reactions with H_2 in the gas phase of the solar nebula would then lower this enrichment. Various authors suggested that the enrichment in deuterium increases with increasing heliocentric distance (Furuya et al. 2013; Kavelaars et al. 2011; Geiss & Reeves 1981). Comets are assumed to be a source of primordial material from the early Solar System (Wyckoff 1991). Consequently, knowledge of variations in the deuterium enrichment in comets is of high importance, as their compositions are indicative of their regions of origin and the environmental conditions during their formation (Hässig et al. 2017).

Ground-based observations of deuterated water in comet C/2014 Q2 (Lovejoy), appeared to show a change in the D/H ratio in water from pre- to post-perihelion (Paganini et al. 2017). Paganini et al. (2017) measured a post-perihelion D/H ratio of $(3.02 \pm 0.87) \times 10^{-4}$, which was significantly higher than the pre-perihelion value of $(1.4 \pm 0.4) \times 10^{-4}$ measured by Biver et al. (2016). Two explanations for this discrepancy were put forward by Paganini et al. (2017): (1) the ratio of D/H in water changed after perihelion or (2) the D/H ratio in water might have been strongly influenced by a systematic bias in the estimate as different experimental setups were applied. Paganini et al. (2017) used the Near Infrared Spectrograph (NIRSPEC) at the 10-meter W. M. Keck Observatory (Keck II) for their infrared measurements. In contrast, Biver et al. (2016) used radio/sub-mm observations from the IRAM 30 m radio telescope and the Odin 1.1 m submillimeter satellite. The two different approaches and the use of two telescopes with different beam sizes in the measurements by Biver et al. (2016) could provide a possible explanation for the varying D/H results in this comet.

A recent study of the D/H ratio in comets showed that the D/H ratio correlates with the nucleus' active area fraction (Lis et al. 2019). According to the authors' definition, comets with an active fraction larger than 0.5 are called hyperactive comets and typically exhibit D/H ratios in water consistent with the terrestrial value. The authors argue that these hyperactive comets require an additional source of water vapour within their comae, which might be explained by the presence of subliming icy grains ejected from the nucleus. There exist other definitions of hyperactivity in comets, such as in Sunshine & Feaga (2021), and thus the classification of 67P as hyperactive or not is not always clear. Fulle (2021) has hypothesised that the correlation of the D/H ratio with the nucleus' active area fraction might be due to a mixture of water-rich and water-poor pebbles. The author states that the two kinds of pebbles contain different D/H ratio values due to their initial formation conditions. He also suggests that the D/H average in the nuclei may differ from the values measured in cometary comae and can therefore not be obtained by local sample-return missions. According to the author, cryogenic return missions would sample water-rich and water-poor pebbles separately, which would only be representative of their corresponding water-rich or water-poor regions, respectively. A cometary average therefore cannot be measured by local sampling.

This work is the first to assess the scenario of a changing D/H ratio in a comet with numerous data points from in situ measurements spread over a long time period and shall answer the question of whether the D/H ratio in comets is dependent on heliocentric distance, phase angle or gas production rate. To do so, we evaluated the full mission data of ROSINA/DFMS to investigate the D/H ratio in HDO and H_2O over one third of 67P's orbit. The evaluated mission phases are specified in Table 1.

In addition to water, the D/H ratios of different alkanes have been studied. Alkanes are acyclic saturated hydrocarbon

Table 1. D/H in H_2O during different mission phases and compared to previous evaluations.

Mission phase	Dates	D/H in H_2O	Heliocentric distance (au)	# of evaluated spectra
First equinox	May 2015	$(5.03 \pm 0.17) \times 10^{-4}$	1.71–1.52	44
Perihelion	August 2015	$(5.01 \pm 0.20) \times 10^{-4}$	1.24	37
Peak gas production	30 August 2015	$(4.98 \pm 0.25) \times 10^{-4}$	1.26	22
Second equinox	March 2016	$(5.02 \pm 0.17) \times 10^{-4}$	2.45–2.65	47
Relative mean ratio		$(5.01 \pm 0.10) \times 10^{-4}$		150
Absolute mean ratio		$(5.01 \pm 0.41) \times 10^{-4}$		150
Pre-first equinox [a]	Aug./Sep. 2014	$(5.3 \pm 0.7) \times 10^{-4}$	≈ 3.4	26
Pre-second equinox [b]	Dec. 2015/Mar. 2016	$(5.25 \pm 0.7) \times 10^{-4}$	2.0 & 2.6	18

References. [a] Altwegg et al. (2015). [b] Altwegg et al. (2017).

molecules containing only single carbon-carbon bonds. They have been found on several Solar System bodies, including the Earth, and in the atmospheres of the giant planets and Saturn's moon Titan (Clark et al. 2009; Lunine & Atreya 2008). The isotopic ratios in these organic compounds are of special interest as they may provide not only an insight into the chemical and physical conditions before and during the formation of the Solar System, but can also constrain the delivery of organic matter by comets to the early Earth (Doney et al. 2020; Rubin et al. 2019; Schuhmann et al. 2019).

2. Instrumentation and methodology

The ROSINA/DFMS is a Nier-Johnson type double focusing mass spectrometer with a high mass resolution of $m/\Delta m = 3000$ at the 1%-level on the mass-to-charge ratio (m/z) 28 (Balsiger et al. 2007). In the DFMS, incoming neutral gas is ionised by electron impact with an electron energy of 45 eV. Most ions formed are singly charged. For this reason, the charge state will not be indicated in the following, except for the subset of doubly charged ions, such as H_2S^{++}. The newly formed ions are accelerated through a 14 μm slit, deflected by 90 degrees in a toroidal electrostatic analyser and, finally, they undergo a 60 degree deflection in the field of a permanent magnet. With the combination of the different fields, the instrument is tuned to the level that only ions with a specific mass-to-charge ratio make it through the analyser section. The remaining ion beam is amplified by two micro channel plates (MCP) in a Chevron configuration. The electron packet issued from the MCP is finally collected by a position-sensitive Linear Electron Detector Array (LEDA). The LEDA consists of two rows of 512 pixels each (Nevejans et al. 2002).

The MCP potential difference can be varied to adjust its amplification. The amplification is the gain of the MCP. Sixteen different settings or gain steps can be chosen from default voltages. Due to detector ageing, the gains associated with each voltage settings are not constant over time. This has to be accounted for when comparing DFMS data with different gain steps. In addition, the unequal usage of the 512 pixels of the LEDA causes a position-dependent degradation of the detector over time. For this reason, a pixel gain correction needs to be implemented during data evaluation (De Keyser et al. 2019). Gain and pixel gain correction factors are evaluated in Schroeder et al. (2019b).

A single spectrum comprises a range of m/z around a specified integer m/z. For m/z 28, this is ± 0.25. DFMS spectra are fitted on individual mass lines using the sum of two Gaussian peaks (double Gaussian distribution). The second Gaussian depends on the first one as its signal amplitude is approximately 10% of the first Gaussian and its width is about three times broader than the narrow first Gaussian. All peaks on the same spectrum are characterised by the same width and height ratios of the two Gaussian distributions. The interdependence of the two Gaussians is known from thorough calibration measurements by Le Roy et al. (2015) and Hässig et al. (2013, 2015), wherein the combined influence of the molecular ionisation cross-sections, the mass-dependent instrument transfer function, isotope-dependent fractionation patterns due to the electron impact ionisation, and detector yields have been investigated. Their effects are included in the systematic error calculations.

Finally, a mass scale may be applied to the spectrum such that each pixel corresponds to a certain mass. The mass scale is applied as described in detail in Calmonte et al. (2016).

Formally, for each pixel p_i corresponding to a LEDA pixel in the DFMS mass spectrum, the counted number of particles, $\mathrm{counts}(p_i)$, can be described as:

$$\mathrm{counts}(p_i) = a_1 e^{-\left(\frac{p_i - p_0}{c_1}\right)^2} + a_2 e^{-\left(\frac{p_i - p_0}{c_2}\right)^2}, \tag{1}$$

with a_1 and a_2 being the amplitudes of the first and the second Gaussian, respectively, p_0 the pixel zero corresponding to the integer mass (center pixel), and c_1 and c_2 the widths of the two Gaussians. The total number of particles impinging on the detector is represented by the peak area. It is given by the integral of the fitted double-Gaussian distribution:

$$\text{\# of particles} = \int_{-\infty}^{+\infty} \mathrm{counts}(p)\, dp = \sqrt{\pi}(a_1 c_1 + a_2 c_2). \tag{2}$$

Figures 1 and 2 show examples of fitted mass spectra after application of the mass scale. The error bars show the statistical uncertainty on the count number.

Data from different periods during the Rosetta mission have been investigated. The HDO/H_2O ratio in 67P has been examined at the first equinox (May 2015), at perihelion (August 2015), at the time of the peak gas production (end of August and early September 2015), and at the second equinox (March 2016) of 67P. These characteristic time periods have been chosen in order
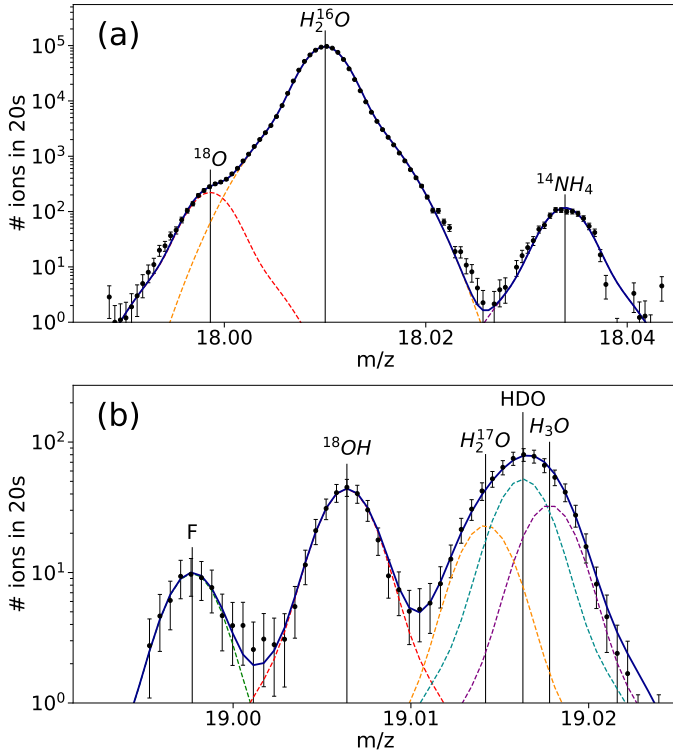
Fig. 1. Sample mass spectra for *m/z* 18 and 19 displaying the signatures of the isotopologues of water. *Panel a*: *m/z* 18 from 2015-05-07 17:38 (UTC). *Panel b*: *m/z* 19 from 2015-05-26 01:35 (UTC). Measured data are represented by black dots including their statistical uncertainties. Individual mass fits and the total sum of the fits are shown with coloured lines.

Fig. 2. Sample mass spectra for *m/z* 30 and 31 showing the signatures of the isotopologues of ethane. *Panel a*: *m/z* 30 from 2014-03-10 19:36 (UTC). The peaks of NO and $C^{18}O$ could not be resolved and appear as one peak (orange line). *Panel b*: *m/z* 31 from 2014-03-10 19:37 (UTC). Measured data are represented by black dots including their statistical uncertainties. The individual mass fits and the total sum of the fits are shown with coloured lines.

Table 2. Relative abundance of alkanes in 67P.

Species	Abundance relative to water [H_2O]	
	May 2015	May 2016
Methane	$(3.43 \pm 0.68) \times 10^{-3}$	$(6.48 \pm 1.30) \times 10^{-2}$
Ethane	$(2.92 \pm 0.58) \times 10^{-3}$	$(5.13 \pm 1.03) \times 10^{-1}$
Propane	$(1.80 \pm 0.36) \times 10^{-4}$	$(2.75 \pm 0.55) \times 10^{-2}$
Butane	not detected	$(5.28 \pm 1.06) \times 10^{-3}$

Notes. Data from Schuhmann et al. (2019).

to determine a potential heliocentric distance dependence on the HDO/H_2O ratio.

In addition, the D/H ratios of the simplest four linear alkanes – methane (CH_4), ethane (C_2H_6), propane (C_3H_8) and butane (C_4H_{10}) – have been studied at times when the alkane signals were clearly visible in the respective spectra. Butane has two structural isomers, *n*-butane and iso-butane, which have the same molecular formula, but with the atoms in a different order. They cannot be distinguished from each other with the DFMS and thus no distinction is made in the following. Methane and ethane have previously been detected in several comets (C/1996 B2 (Hyakutake): Mumma et al. 1996; 153P/Ikeya-Zhang: Kawakita et al. 2003; C/2007 N3 (Lulin): Gibb et al. 2012) and upper limits for their D/H ratios have been reported (Bonev et al. 2009; Doney et al. 2020). Propane and butane were first detected in 67P by Schuhmann et al. (2019). These authors have also published the relative abundances of the simplest four linear alkanes compared to methane and water in 67P's coma for two different time periods. The abundances relative to water are shown in Table 2. The abundance of the simplest four linear alkanes strongly increased from pre- to post-perihelion. No D/H ratios for any of the alkanes considered have been reported to date.

Two sources of uncertainty are relevant for DFMS data analysis: statistical uncertainties in the count rates and systematic uncertainties due to instrumental effects. The statistical uncertainties of the detector counts are proportional to $\sqrt{N}$ for N counts. Additionally, a fitting error has been included in the case of overlapping peaks. This fitting error accounts for a possible ambiguity when peaks cannot be clearly separated and depends on the relative peak intensities and the mass difference between

the peaks. Instrumental effects, arising from pixel-dependent degradation (pixel gain correction) and changes in the detector gain over time, are systematic uncertainties. The uncertainty of the pixel gain is 5% and the uncertainty of the overall gain is 6%. These values were previously derived and applied by Schroeder et al. (2019b). The statistical and fitting uncertainties are considered for each individual measurement point. Uncertainties in the detector and pixel gain, which are of a systematic nature, are only considered for the absolute mean ratios. In the case of HDO/H_2O, the overall gain has a large impact on the evaluation as *m/z* 18 has always been measured on a smaller gain step than *m/z* 19. For the alkanes, the gain uncertainty has to be included for methane and propane. The isotopologues of ethane and butane on the other hand were measured on the same gain step as their main isotopologues and gain corrections are therefore unnecessary. The pixel gain uncertainty, however, applies to all uncertainty calculations.
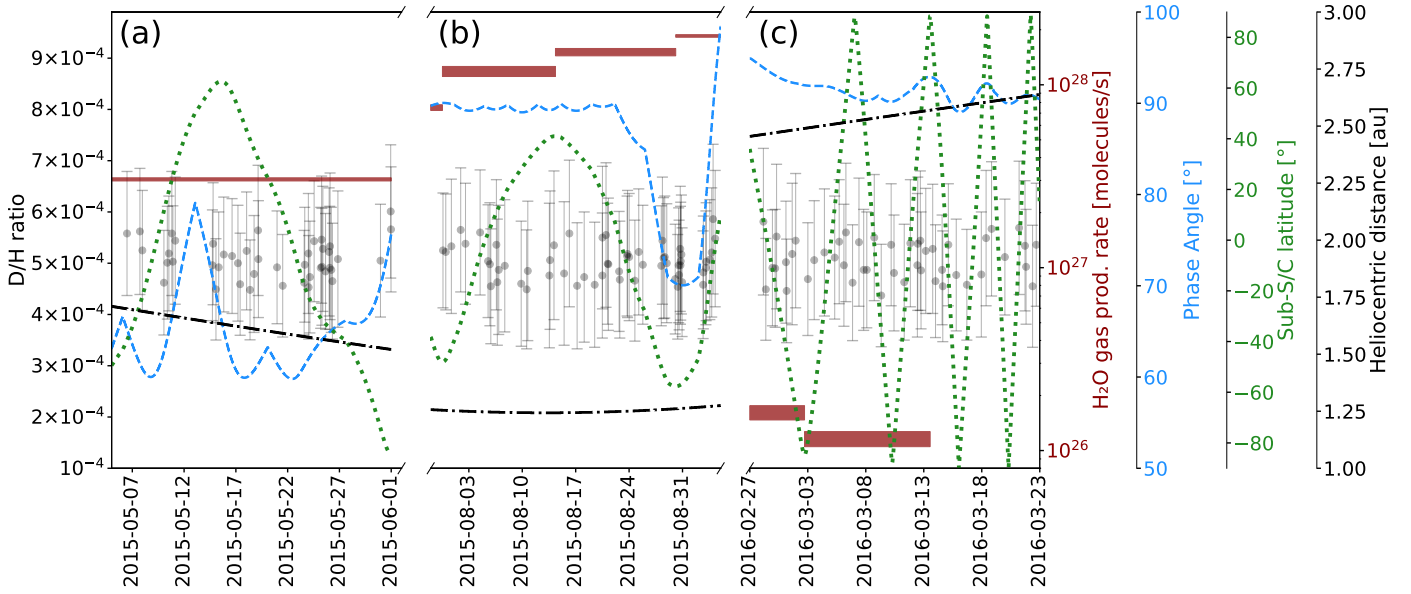
Fig. 3. D/H in H_2O during different mission phases compared to H_2O gas production (Läuter et al. 2020, red), phase angle (blue), sub-S/C latitude (green) and heliocentric distance (black). *Panel a*: first equinox; *Panel b*: perihelion and peak gas production phase; *Panel c*: second equinox. The individual measurement uncertainties represent statistical errors from the count rates and errors from the fit.

3. Results

An extensive analysis of spectra with *m/z* 18 and *m/z* 19 in the coma of 67P showed constant D/H and $^{16}O/^{17}O$ ratios in water during the comet's course around the Sun in 2015 and 2016. Furthermore, the D/H and $^{13}C/^{12}C$ ratios in the simplest four linear alkanes could be resolved. This section summarises the results for each of the aforementioned ratios and explains how the results have been obtained.

3.1. HDO/H_2O

A total of 150 spectra around *m/z* 18 and *m/z* 19 have been investigated. These spectra contain the signatures of $H_2^{16}O$, $H_2^{17}O$ and HDO. Sample spectra for *m/z* 18 and *m/z* 19 are shown in Fig. 1. Using the values from $H_2^{16}O$ and HDO, measured back-to-back within one minute, allows us to derive the D/H ratio from HDO/H_2O as:

$$D/H = \frac{1}{2} \frac{n_{HDO}}{n_{H_2^{16}O}}. \quad (3)$$

The goal of this work was to investigate the D/H ratio in water over the whole mission. Therefore, Rosetta data from the first equinox, perihelion, the time of the peak gas production, and the second equinox have been evaluated as specified in Table 1. These data sets span a wide range of heliocentric distances, observational phase angles, water production rates and sub-spacecraft (sub-S/C) latitudes.

The relative mean D/H ratios for the specified mission phases, considering only statistical and fit uncertainties, are shown in Table 1. The mean values are weighted means with the weight for each individual point being inversely proportional to its statistical uncertainty. This improves the results by giving more weight to more precise measurement points. The relative overall mean value was found to be $(5.01 \pm 0.10) \times 10^{-4}$. All periods are consistent with this mean value within the 1σ uncertainty of 2.0%. There is no observable trend between the periods

in the D/H value. This suggests that the D/H ratio in 67P's coma remains constant throughout the entire Rosetta mission phase, covering one third of 67P's orbit. Additionally, considering the broad diversity of the conditions under which the data have been observed, the D/H ratio in 67P's coma seems to be independent of heliocentric distance, level of cometary activity, and observational phase angle, as well as sub-S/C latitudes. The D/H ratio did not even significantly change during extreme situations such as a maximally active southern hemisphere or a phase angle of almost 70°. Figure 3 shows the individual D/H ratio data points alongside their corresponding H_2O gas production rate (Läuter et al. 2020), phase angle, latitude and cometary distance to the Sun. For the H_2O gas production, Läuter et al. (2020) reported minimum and maximum values according to their uncertainty estimation. No H_2O gas production values were reported by these authors for the time between 13 March 2016 and the end of the measurements during the second equinox. Combi et al. (2020) provided gas production values for individual measurement points acquired with a different approach, with their results for the overall variation of the H_2O gas production rate being in reasonable agreement with Läuter et al. (2020).

For the absolute value, the systematic uncertainty is added. This systematic uncertainty affects all data points equally and leads to an absolute mean D/H ratio of $(5.01 \pm 0.40) \times 10^{-4}$. This is consistent with the previously published values of $(5.3 \pm 0.7) \times 10^{-4}$ found by Altwegg et al. (2015, 2017). These earlier values were determined before a better understanding of the behaviour of the pixel gain and the overall gain of the DFMS over time was available (De Keyser et al. 2019; Schroeder et al. 2019b). By extending the number of spectra from 26 and 18 in Altwegg et al. (2015) and Altwegg et al. (2017), respectively, to 150 spectra in this work, and thanks to the improved characterisation of the DFMS over time, we were able to improve on the uncertainty. For statistical reasons, this uncertainty is inversely proportional to the square root of the number of spectra and thus greatly decreased by the large number of spectra considered here.

Table 3. $^{16}O/^{17}O$ in water during different mission phases.

Mission phase	$^{16}O/^{17}O$
First equinox	2317 ± 91
Perihelion	2318 ± 115
Peak gas production	2398 ± 141
Second equinox	2379 ± 97
Relative mean ratio	2347 ± 53
Absolute mean ratio	2347 ± 191

3.2. $^{16}O/^{17}O$

In addition to the signature of HDO, $H_2^{17}O$ has been measured on m/z 19. Together with the already examined $H_2^{16}O$ on m/z 18, the isotopic ratio of $^{16}O/^{17}O$ could be derived. This has already been done by Schroeder et al. (2019b) in a "note added in proof". However, the authors only investigated data from two distinct dates and only used 35 spectra. With the 150 spectra investigated for the time periods given in Table 1, an updated value can now be presented. Table 3 shows the relative mean $^{16}O/^{17}O$ ratios for the different mission phases, considering only statistical and fit uncertainties. As in Section 3.1, the mean values are weighted means and the uncertainty is inversely proportional to the square root of the number of spectra. The relative overall mean value over all evaluated spectra was found to be 2347 ± 53. All the periods are consistent with this mean value within the 1σ uncertainty of 2.3%. There is no observable trend in the $^{16}O/^{17}O$ ratio among the periods considered. This is in line with the invariability of the $^{16}O/^{18}O$ ratio in Schroeder et al. (2019b). It is, however, in contrast with their average values for the $^{16}O/^{17}O$ ratios, as their $^{16}O/^{17}O$ ratio for the first date is approximately 40% higher than the $^{16}O/^{17}O$ ratio for the second date. An explanation for this might be that Schroeder et al. (2019b) did not include $H_3^{16}O$ in their evaluation of m/z 19 spectra. However, all three molecules, $H_2^{17}O$, HDO and $H_3^{16}O$, need to be included in the analysis as their peaks overlap significantly and the influence of $H_3^{16}O$ should not be ignored. Including the systematic uncertainties of the gains affecting all data points equally, gives an absolute mean $^{16}O/^{17}O$ ratio of 2347 ± 191. This represents an approximately 11% enrichment of ^{17}O compared to the value for terrestrial water of (2632 ± 69) (Meija et al. 2016) and is in line with the enrichment of ^{18}O in 67P's coma (Schroeder et al. 2019b). The $^{16}O/^{17}O$ ratio we derived is compatible within the uncertainties with the value reported in the "note added in proof" in Schroeder et al. (2019b).

3.3. Linear alkanes

The D/H and $^{13}C/^{12}C$ ratios of the first four linear alkanes, namely, methane, ethane, propane and butane, have been evaluated. For all alkanes, C_nH_y, taking into account the statistical correction for the different possible positions of the rare isotopes in the molecule, the D/H and $^{13}C/^{12}C$ ratios are obtained by dividing the measured abundance ratios by $1/y$ and $1/n$, respectively. The alkanes were not always at a detectable level over the entire mission. This required an individual selection of suitable time periods for each of the molecules. For each hydrocarbon, the results will be presented separately in the following subsections.
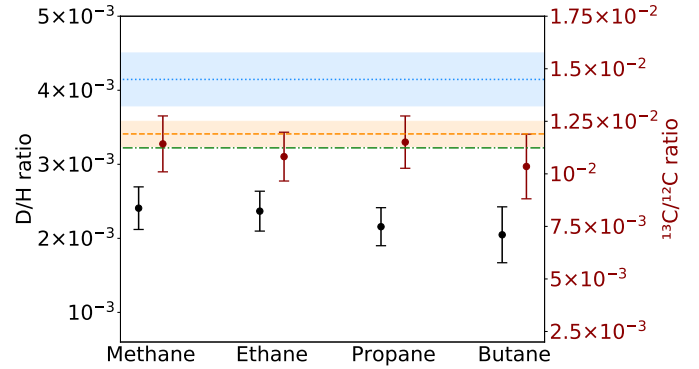
Fig. 4. D/H (black) and $^{13}C/^{12}C$ (red) ratios of the first four linear alkanes compared with $^{13}C/^{12}C$ values in 67P's CO_2 (Hässig et al. 2017, orange), in the Earth (Wilson 1999, green) and in the local ISM (Wilson 1999, blue).

3.3.1. Methane (CH_4)

The methane (CH_4) signature was observed clearly from mid-August 2016 until the beginning of September 2016. Hence, 12 spectra from this time period have been evaluated. Spectra with m/z 16 and m/z 17 have been investigated. Sample spectra are shown in Fig. A.1. The m/z 16 spectra used gain step 15, whereas the m/z 17 spectra used gain step 16. Thus, a gain step correction was needed. The gain step corrections were calibrated with data acquired shortly before this period (Schroeder et al. 2019a). Gain step 16 was used as the baseline by Schroeder et al. (2019a) for the gain step corrections. Consequently, the gain step correction was simple for the ratio calculated from the data considered here. On m/z 17, $^{13}CH_4$ and CH_3D are slightly over-lapping and a clear distinction is not always straightforward. This additional uncertainty has been included in the overall uncertainty.

The $^{13}C/^{12}C$ ratio has already been evaluated several times for 67P by Hässig et al. (2017) and Rubin et al. (2017) for carbon dioxide (CO_2), carbon monoxide (CO), ethylene (C_2H_4) and the ethyl radical C_2H_5 and has been shown to be independent of the parent molecule. Hence, the value of $^{13}C/^{12}C = (1.19 \pm 0.06) \times 10^{-2}$ derived from CO_2 by Hässig et al. (2017) will be used as a comparison for the values derived in this work.

From the measurements of CH_4, $^{13}CH_4$ and CH_3D, the D/H and $^{13}C/^{12}C$ ratios could be derived by taking into account the statistical correction for the four possible positions the D atom can take in the molecule. An average value of $D/H = (2.41 \pm 0.29) \times 10^{-3}$ is found in methane (Fig. 4 and Table 4). This is 4.8 times larger than the D/H ratio from HDO/H_2O but 7.5 times smaller than the D/H ratio from D_2O/HDO (Altwegg et al. 2017). The corresponding ratio of $^{13}C/^{12}C$ is $(1.14 \pm 0.13) \times 10^{-2}$, which is consistent with Hässig et al. (2017). This is additional evidence of the $^{13}C/^{12}C$ ratio being independent of the parent molecule.

3.3.2. Ethane (C_2H_6)

The evaluation of ethane (C_2H_6) was very similar to the one for methane. 20 spectra with m/z 30 and m/z 31 have been evaluated for time periods in the beginning of October 2014 and during the second equinox in March 2016. Here, the gain steps were the same on both m/z spectra and no gain correction was needed. Similar to methane, an overlap between $^{13}C^{12}CH_6$ and C_2H_5D appears on m/z 31. Again, this uncertainty has been included in

Table 4. D/H and $^{13}C/^{12}C$ in linear alkanes.

Alkane	D/H	$^{13}C/^{12}C$
Methane	$(2.41 \pm 0.29) \times 10^{-3}$	$(1.14 \pm 0.13) \times 10^{-2}$
Ethane	$(2.37 \pm 0.27) \times 10^{-3}$	$(1.08 \pm 0.12) \times 10^{-2}$
Propane	$(2.16 \pm 0.26) \times 10^{-3}$	$(1.15 \pm 0.12) \times 10^{-2}$
Butane	$(2.05 \pm 0.38) \times 10^{-3}$	$(1.04 \pm 0.15) \times 10^{-2}$

the overall uncertainty of the corresponding ratios. Sample spectra for m/z 30 and m/z 31 are shown in Fig. 2. It can be seen that NO and $C^{18}O$ strongly overlap and cannot be clearly separated. For this reason, they are fitted together as one peak.

Accounting for the statistical correction for the different possible positions of the rare isotopes in the molecule, an average D/H ratio of $(2.37 \pm 0.27) \times 10^{-3}$ (Fig. 4 and Table 4) and a $^{13}C/^{12}C$ ratio of $(1.08 \pm 0.12) \times 10^{-2}$ have been obtained. This is consistent, within the uncertainties, with Hässig et al. (2017) as well as the result for methane.

3.3.3. Propane (C_3H_8)

There are 14 Spectra with m/z 44 and m/z 45 from the second equinox in March 2016 that have been evaluated for propane (C_3H_8). Sample spectra are shown in Fig. A.2. The spectra with m/z 44 contain a very large amount of CO_2. Consequently, a small gain step was automatically selected by the DFMS while acquiring these spectra. The spectra measured around m/z 45 on the other hand showed consistently lower count rates and were thus measured on a larger gain step. For this reason, a gain correction needed to be applied before the spectra could be compared. The gain steps differed by up to four gain steps as some spectra of m/z 44 were acquired with a very low gain step (i.e. gain step 11). Low gain steps were difficult to calibrate during the calibration measurements and complicate the gain step corrections. However, Hässig et al. (2017) obtained the $^{13}C/^{12}C$ ratio in CO_2 at times when the gain steps of m/z 44 and 45 were much closer. From the $^{13}C/^{12}C$ ratio in CO_2 we thus inferred a gain correction for our measurements.

After applying the gain correction and accounting for the different possible positions of the rare isotopes in the molecule, an average D/H ratio of $(2.16 \pm 0.26) \times 10^{-3}$ was found for propane (C_3H_8, Fig. 4 and Table 4). For $^{13}C/^{12}C$ from $^{13}C^{12}C_2H_8$ and C_3H_8, the value is $(1.15 \pm 0.12) \times 10^{-2}$. Again, this value is compatible with the value from Hässig et al. (2017) and the other linear alkanes.

3.3.4. Butane (C_4H_{10})

For butane (C_4H_{10}), 11 spectra with m/z 58 and m/z 59 have been evaluated from data acquired during the second equinox in March 2016. Here, a gain correction was unnecessary, as both m/z 58 and m/z 59 were measured with the highest gain available. Sample spectra for butane are shown in Fig. A.3.

Taking into account the different possible positions of the D or ^{13}C in the molecule, butane (C_4H_{10}) showed a D/H ratio of $(2.05 \pm 0.38) \times 10^{-3}$ and a $^{13}C/^{12}C$ ratio from $^{13}C^{12}C_3H_{10}$ and C_4H_{10} of $(1.04 \pm 0.15) \times 10^{-2}$ (Fig. 4 and Table 4). As with all of the other linear alkanes considered above, the $^{13}C/^{12}C$ ratio is consistent with Hässig et al. (2017) and the other linear alkanes.

4. Discussion

The ROSINA/DFMS measurements show that the D/H ratio in water does not change during 67P's passage around the Sun between May 2015 and March 2016. It is clear, that the instrument's observations represent an average of the illuminated surface, even though they have been measured at different positions. Hence, we cannot examine any point-to-point variability on the surface itself. However, given the large variability of the phase angles and sub-S/C latitudes during the evaluated measurement phases and their association with different spacecraft distances to the comet, we can conclude that the D/H ratio in water in 67P's coma is independent of heliocentric distance, level of cometary activity, and Rosetta's phase angle as well as sub-S/C latitude (Fig. 3). The relative overall mean value, considering only statistical and fit uncertainties, has a 1σ variation of 2.0% with all investigated periods being consistent. The derived D/H ratio for water is compatible with values previously published in Altwegg et al. (2015, 2017). However, the new values presented in this work are based on a larger number of measurements and hence have smaller error margins. The most accurate absolute value for D/H in HDO/H_2O we obtained from our data is $(5.01 \pm 0.40) \times 10^{-4}$, where the uncertainty includes all statistical and systematic uncertainties.

Paganini et al. (2017) and Biver et al. (2016) reported different values for the D/H ratio in water for comet Lovejoy pre- and post-perihelion. Paganini et al. (2017) favoured the explanation of a systematic difference between the two observations by Biver et al. (2016) as a reason for the changing D/H ratio observed for comet Lovejoy. If the results for comet 67P are valid for other comets, our study indicates a constant D/H ratio, within the uncertainties, and therefore supports the hypothesis of a systematic difference rather than a change in the D/H ratio of comet Lovejoy.

Lis et al. (2019) proposed that the D/H ratio in cometary water correlates with the nucleus' active area fraction. Fulle (2021) modelled this scenario and suggested that the fraction of water-rich and water-poor pebbles influences the D/H ratio in the comet's coma. The data evaluated for this paper show that the D/H ratio is independent of 67P's activity (in the form of H_2O outgassing) and Rosetta's relative position in terms of phase angle and sub-spacecraft latitude; hence, the data do not show any signs of such a scenario for 67P.

Measurements taken of the first four linear alkanes in 67P's coma show that their D/H ratios are all consistent within the uncertainties. The derived values are larger than the aforementioned ratio obtained from HDO/H_2O by a factor of 4.1 to 4.8, but smaller than the D/H ratio obtained from D_2O/HDO (Altwegg et al. 2017). In addition, the D/H ratio in the alkanes is slightly larger than the ratio obtained from HDS (Altwegg et al. 2017) but it is still on the same order of magnitude. The first-time detection of mono- and di-deuterated methanol in a cometary coma was published by Drozdovskaya et al. (2021). The authors evaluated Rosetta/ROSINA data for 67P. With the ROSINA instruments, it is not possible to distinguish between the different chemical compositions of D-methanol (CH_3OD and CH_2DOH) and D_2-methanol (CH_2DOD and CHD_2OH), respectively. Moreover, different approaches for the calculation of the D/H ratio in methanol are possible and it cannot be judged which of the pathways is more reliable. Consequently, although it was not possible to deduce a single D/H ratio in CH_3OH, a range of 0.71–6.6% was given by the authors. This accounts for the different isomers of methanol and includes statistical error propagation in the ROSINA measurements. The authors propose that

methanol and its deuterated isotopologues in comet 67P must have formed in the prestellar core that preceded our Solar System and at a time when it was at a temperature of 10–20 K. Moreover, it is assumed that methanol is a pivotal precursor to complex organic molecules, and hence, could be a source of deuterium for such species (Oba et al. 2016). The presented D/H value in methanol is much larger than the ratios obtained for the first four linear alkanes. However, Drozdovskaya et al. (2021) demonstrate that the upper boundary of 6.6% of their determined D/H range would only apply in the extreme case where all D-methanol was in the form of CH_3OD. In the much more likely case that D-methanol exists in the form of different isomers (Ratajczak et al. 2011), the D/H in methanol would be lower and thus comparable to the D_2O/HDO ratio of $(1.8 \pm 0.9) \times 10^{-2}$ from Altwegg et al. (2017).

Furuya et al. (2016) have described the development of ice structures during the formation of protostellar cores with two layers from molecular clouds. The first layer is the main formation stage of H_2O ice. The second, outer layer is CO/CH_3OH-rich and includes material that underwent enhanced deuteration processes due to low temperatures ($T < 20$ K). Their model shows higher levels of deuterium fractionation of formaldehyde and methanol from the outer layer than in water in the inner layer and gives similar D/H ratios for methanol and D_2O. They suggest that this difference reflects the epochs of the molecules' formation as water ice is formed at an earlier stage of protostellar cloud condensation at elevated temperatures than the ices of formaldehyde and methanol. These conclusions might explain why at 67P the D/H ratios for D_2O/HDO and methanol are similar but much larger compared to D/H in H_2O. The way in which such a scenario would affect the deuteration in hydrocarbons, however, requires further investigation.

Measurements of organics in other comets, for instance, the D/H ratio in HCN in comet C/1995 O1 (Hale-Bopp) (Crovisier et al. 2004) match the values for the first four linear alkanes within the uncertainties.

Paquette et al. (2021) presented the first in situ measurements of the D/H ratios in organic refractory components of cometary dust particles. These cometary dust particles have been captured on metal targets within the coma of comet 67P. The particles were then imaged by a microscope camera and a fraction of them were analysed with the Cometary Secondary Ion Mass Analyzer (COSIMA), a time-of-flight secondary ion mass spectrometer (Kissel et al. 2007). The incident velocities of the particles COSIMA collected were low and they did not suffer a high degree of thermal alteration. Greater thermal alterations occur in flyby missions, where incident velocities experienced by particles are larger by several orders of magnitude (Paquette et al. 2021). The D/H ratio of $(1.57 \pm 0.54) \times 10^{-3}$ in the organic refractory components of 67P's cometary dust is comparable to our D/H ratios in linear alkanes. It is thus also about an order of magnitude higher than the VSMOW for the D/H ratio on Earth. Paquette et al. (2021) have stated, that this relatively high value puts forward the theory that refractory carbonaceous matter in comet 67P is less processed than the most primitive insoluble organic matter (IOM) in meteorites.

Bonev et al. (2009) reported an upper limit of 5×10^{-3} for the D/H ratio in methane in comet C/2004 Q2 (Machholz), while Kawakita et al. (2005) determined an upper limit for the D/H ratio of 1×10^{-2} for comet C/2001 Q4 (NEAT), and Gibb et al. (2012) found an upper limit of 7.5×10^{-3} for comet C/2007 N3 (Lulin). The D/H ratio we determined in methane for 67P is about a factor of two lower than the smallest previously obtained upper limit for this molecule.

An upper limit for the D/H ratio in ethane of 2.6×10^{-3} from modelled emission spectra of comet C/2007 W1 (Boattini) has been determined by Doney et al. (2020). Hence, for ethane, our D/H ratio for 67P is comparable to this upper limit.

This work is the first to present an isotopic ratio for methane, ethane, propane, and butane for comets. No other values are available for comparison.

A comparison of the D/H ratios investigated here with values obtained from different comets and on different organic molecules is shown in Fig. 5. D/H ratios from the Protosolar Nebula, Earth, carbonaceous chondrites (CC), ordinary chondrites (OC), interplanetary dust particles (IDP) and ultracarbonaceous Antarctic micrometeorites (UCCAM) are added for comparison. The D/H ratio from HDO/H_2O is larger for most of the observed comets compared to the terrestrial value, though they show large variations. Variations are also observed within the comet families, the JFCs and the Oort cloud comets (OCC). It also seems that organic compounds in the comets investigated exhibit even larger D/H ratios than water. A comparison of the D/H ratios derived from cometary organics, chondrites, and IDPs to values from the Protosolar Nebula and the VSMOW reveals a pronounced deuterium enrichment in Solar System objects in general. Hoppe et al. (2018) suggested that 67P might be particularly primordial and might have conserved large amounts of presolar matter due to the fact that its D/H ratio corresponds to the highest values proposed for comets to date. Water in chondrites has D/H ratios in between those of the Protosolar Nebula and the highest cometary values. On the other hand, chondritic IOM shows strong D-enrichment as compared to VSMOW. According to Alexander et al. (2010), this deuterium enrichment is not a signature of the primordial H in the presolar cloud, but is caused by different processes. Moreover, Duprat et al. (2010) analysed ultracarbonaceous micrometeorites recovered from central Antarctic snow and found extreme deuterium enrichment in large areas of the organic matter contained therein. In addition, crystalline minerals embedded in the micrometeoritic organic matter have been identified. According to the authors, this suggests that this organic matter reservoir may have formed within the Solar System itself and was not inherited from presolar times. As a summary of their findings, the high D/H ratios, the high organic matter content, and the associated minerals are said to favour an origin from the cold regions of the protoplanetary disc (Duprat et al. 2010).

According to Cleeves et al. (2016), the D/H ratio in both water and organics can become chemically enhanced in cold environments exposed to ionising radiation. The authors proposed the cold interstellar medium, activated by galactic cosmic rays, and the outermost regions of the protoplanetary disc in the presence of stellar or non-stellar ionisation, as two possible environments where this deuterium enrichment could occur. In an earlier study, Cleeves et al. (2014) state that a considerable fraction of the Solar System's water predates the Sun and that a certain amount of such interstellar ice survived the formation of the Solar System and has been incorporated into planetesimals. The authors also identified two factors which might lead to the even higher degree of deuterium enrichment in protoplanetary disc organics as compared to water: (1) the higher volatility and abundance of CO, which is the main carbon reservoir, as compared to O (atomic oxygen), which is the main precursor for water formation, and, (2) a more favourable chemistry for deuterium-fractionation in organics than in water due to a higher exothermicity in the chemical formation reaction (Cleeves et al. 2016).
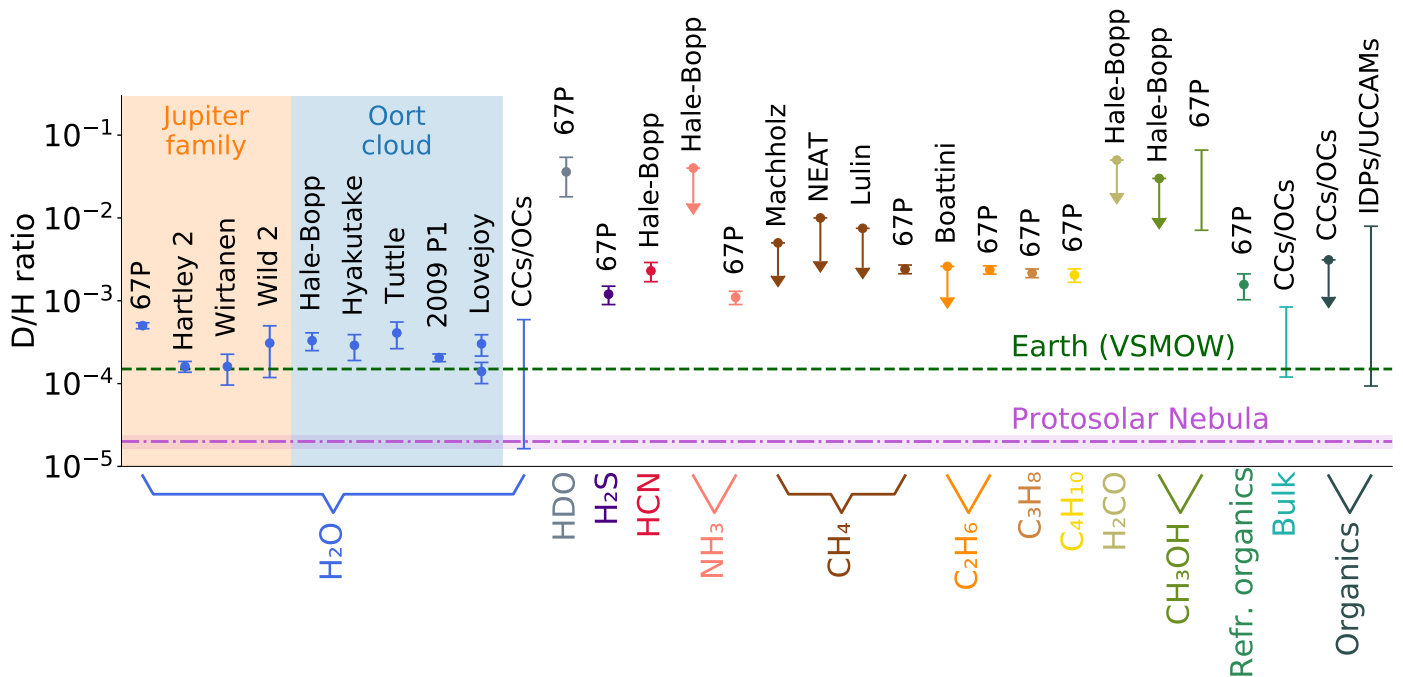
Fig. 5. D/H ratios of water and organic molecules measured in different comets compared to values from the Protosolar Nebula (purple line, Geiss & Gloeckler 2003), the Earth (green line, Wilson 1999), carbonaceous chondrites (CC), ordinary chondrites (OC), interplanetary dust particles (IDP) and ultracarbonaceous Antarctic micrometeorites (UCCAM). D/H in HDO is equal to $2 \cdot D_2O/HDO$. Full references are given in Table B.1.
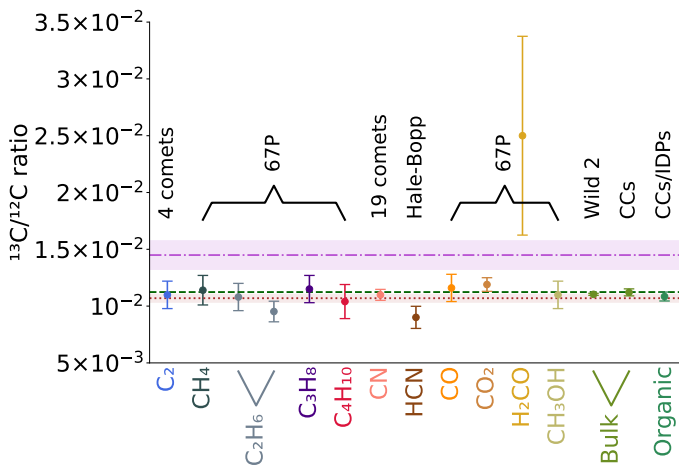
Fig. 6. $^{13}C/^{12}C$ ratios of different organic molecules measured in different comets, carbonaceous chondrites (CC) and interplanetary dust particles (IDP) compared to the terrestrial value (green line, Lyons et al. 2018), the Sun (brown line, Lyons et al. 2018) and the ISM (purple line, Wilson 1999). For C_2 and CN, data from 4 and 19 comets, respectively, have been considered. Full references are given in Table B.2.

Embedded protostars in low-mass star-forming regions exhibit D/H ratios in their water on a level that is similar to the values found for comets (Persson et al. 2014). On the other hand, isolated protostars have D/H ratios of more than double the values observed in embedded protostars (Jensen et al. 2019), and their D/H ratios are thus more similar to those of cometary organics. The high D/H ratios in cometary organic compounds generally suggest that these species may be inherited from the presolar molecular cloud from which the Solar System formed.

The alkanes investigated show $^{13}C/^{12}C$ ratios compatible with published values for CO (Rubin et al. 2017) and CO_2

(Hässig et al. 2017) in 67P and the $^{13}C/^{12}C$ ratio in the Solar System (Wilson 1999). Altwegg et al. (2020) found a $^{13}C/^{12}C$ ratio in ethane of $(0.95 \pm 0.1) \times 10^{-2}$ which matches the results presented in this work within the uncertainties. These authors also revealed that the $^{13}C/^{12}C$ ratio varies for different molecules in 67P's coma, but that, except for H_2CO with its large uncertainty, the $^{13}C/^{12}C$ ratios are in the same range as our values. This picture is supported by data from other comets and even bulk and organic CCs, where the $^{13}C/^{12}C$ ratios for different molecules are similar (Bockelée-Morvan et al. 2015; Hoppe et al. 2018). A comparison of $^{13}C/^{12}C$ ratios for different organic molecules measured in different comets and other Solar System objects is shown in Fig. 6. All these values lie below the local ISM value (Wilson 1999) but are mostly compatible with the terrestrial and the solar value (Lyons et al. 2018). This indicates that isotopic fractionation may have occurred over time and was, at least for most organic molecules, independent of the molecular structure.

In conjunction with the small variations in the $^{13}C/^{12}C$ ratios and the large variations in the D/H ratios, Fig. 7 illustrates that there is no correlation between the $^{13}C/^{12}C$ ratio and the D/H ratio for comets and CCs.

5. Summary and conclusions

In this work, we investigate the isotopic ratios of water and the four simplest alkanes found in the inner coma of comet 67P. The most relevant findings can be summarised as follows:

– The D/H ratio in water in 67P's coma, measured with ROSINA/DFMS, is independent of the heliocentric distance, the level of cometary activity, the spacecraft's phase angle and the sub-spacecraft latitude;
– A 1σ variation of 2.0% is included in the relative overall mean value. All the values derived from the investigated periods are consistent with this value;

Fig. 7. D/H ratios compared to $^{13}C/^{12}C$ ratios of different organic molecules measured in comets 67P and Hale-Bopp and in bulk and organic carbonaceous chondrites (CC). Full references are given in Table B.1 for the D/H ratios and in Table B.2 for the $^{13}C/^{12}C$ ratios.

- From our data, we obtained an absolute D/H ratio from HDO/H_2O of $(5.01 \pm 0.40) \times 10^{-4}$. Many comets exhibit larger D/H ratios in water as compar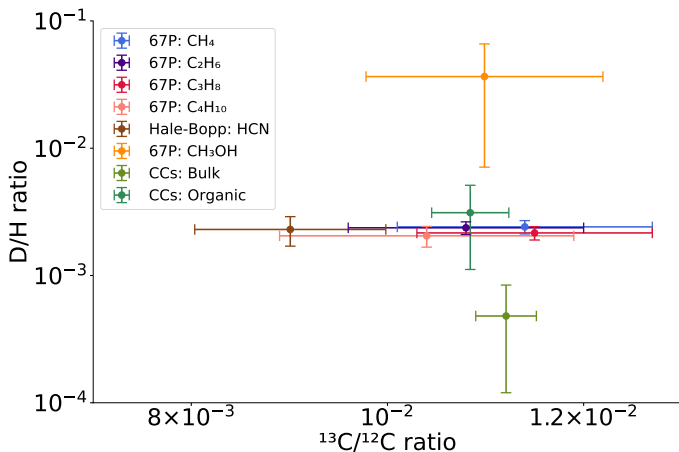ed to the terrestrial value. However, both cometary families, JFCs and OCCs, also include comets with values comparable to the VSMOW value. Hence, the implications for cometary contributions to terrestrial water remain unclear if only cometary water is examined;
- The $^{16}O/^{17}O$ ratio in water in 67P's coma was determined to be constant throughout the mission, with a relative 1σ variation of 2.3%. An absolute $^{16}O/^{17}O$ ratio of 2347 ± 191 has been found;
- The four simplest linear alkanes show larger D/H ratios than 67P's water by a factor of 4.1 to 4.8. Their D/H ratio values are consistent with data from other organic molecules and from different comets;
- A comparison between different sources of cometary matter showed that organic molecules generally exhibit higher D/H ratios than water for all comets reviewed in this work;
- No correlation was found between the $^{13}C/^{12}C$ ratio and the D/H ratio for different cometary molecules.

The observed invariability of the D/H ratio in 67P's coma opposes theories of a non-steady-state regime of water ice sublimation occurring in sporadic time intervals along the comet's orbit. However, this invariability needs to be confirmed for other comets with further measurements and with other measurement approaches. Additionally, 67P's close apparition in November 2021 has been an excellent opportunity to re-measure the D/H ratio using spectroscopic approaches and upcoming results are highly anticipated. On the other hand, to further constrain the history and origin of organic matter in the Solar System, more data from comets and other Solar System objects ought to be analysed and more studies are required to investigate these species' formation pathways.

References

Alexander, C. M. O. D., Fogel, M., Yabuta, H., & Cody, G. D. 2007, Geochim. Cosmochim. Acta, 71, 4380
Alexander, C. M. O. D., Newsome, S. D., Fogel, M. L., et al. 2010, Geochim. Cosmochim. Acta, 74, 4417
Alexander, C. M. O., Bowden, R., Fogel, M. L., et al. 2012, Science, 337, 721
Altwegg, K., Balsiger, H., Bar-Nun, A., et al. 2015, Science, 347, 1261952
Altwegg, K., Balsiger, H., Berthelier, J. J., et al. 2017, Phil. Trans. R. Soc. Lond. A, 375, 20160253
Altwegg, K., Balsiger, H., & Fuselier, S. A. 2019, ARA&A, 57, 113
Altwegg, K., Balsiger, H., Combi, M., et al. 2020, MNRAS, 498, 5855
Balsiger, H., Altwegg, K., Bochsler, P., et al. 2007, Space Sci. Rev., 128, 745
Biver, N., Moreno, R., Bockelée-Morvan, D., et al. 2016, A&A, 589, A78
Biver, N., Bockelée-Morvan, D., Hofstadter, M., et al. 2019, A&A, 630, A19
Bockelée-Morvan, D., Gautier, D., Lis, D. C., et al. 1998, Icarus, 133, 147
Bockelée-Morvan, D., Calmonte, U., Charnley, S., et al. 2015, Space Sci. Rev., 197, 47
Bonev, B. P., Mumma, M. J., Gibb, E. L., et al. 2009, ApJ, 699, 1563
Busemann, H., Young, A. F., O'D. Alexander, C. M., et al. 2006, Science, 312, 727
Calmonte, U., Altwegg, K., Balsiger, H., et al. 2016, MNRAS, 462, S253
Calmonte, U., Altwegg, K., Balsiger, H., et al. 2017, MNRAS, 469, S787
Clark, R. N., Curchin, J. M., Hoefen, T. M., & Swayze, G. A. 2009, J. Geophys. Res. (Planets), 114, E03001
Cleeves, L. I., Bergin, E. A., Alexander, C. M. O. D., et al. 2014, Science, 345, 1590
Cleeves, L. I., Bergin, E. A., O'D. Alexander, C. M., et al. 2016, ApJ, 819, 13
Combi, M., Shou, Y., Fougere, N., et al. 2020, Icarus, 335, 113421
Crovisier, J., Bockelée-Morvan, D., Colom, P., et al. 2004, A&A, 418, 1141
Daly, L., Lee, M. R., Hallis, L. J., et al. 2019, Nat. Astron., 5, 1275
De Keyser, J., Altwegg, K., Gibbons, A., et al. 2019, Int. J. Mass Spectrom., 446, 116232
Dhooghe, F., De Keyser, J., Altwegg, K., et al. 2017, MNRAS, 472, 1336
Doney, K., Kofman, V., Villanueva, G., & Sung, K. 2020, in Amer. Astron. Soc. Meet. Abstr., 235, 226.06
Duprat, J., Dobrică, E., Engrand, C., et al. 2010, Science, 328, 742
Drozdovskaya, M. N., van Dishoeck, E. F., Rubin, M., Jørgensen, J. K., & Altwegg, K. 2019, MNRAS, 490, 50
Drozdovskaya, M. N., Schroeder I, I. R. H. G., Rubin, M., et al. 2021, MNRAS, 500, 4901
Feller, C., Fornasier, S., Ferrari, S., et al. 2019, A&A, 630, A9
Floss, C., & Stadermann, F. J. 2004, in Lunar and Planetary Science Conference, ed. S. Mackwell, & E. Stansbery, 1281
Fulle, M. 2021, MNRAS, 505, 3107
Furuya, K., Aikawa, Y., Nomura, H., Hersant, F., & Wakelam, V. 2013, ApJ, 779, 11
Furuya, K., van Dishoeck, E. F., & Aikawa, Y. 2016, A&A, 586, A127
Geiss, J., & Gloeckler, G. 2003, Space Sci. Rev., 106, 3
Geiss, J., & Reeves, H. 1981, A&A, 93, 189
Gibb, E. L., Bonev, B. P., Villanueva, G., et al. 2012, ApJ, 750, 102
Goesmann, F., Rosenbauer, H., Bredehöft, J. H., et al. 2015, Science, 349, 2.689
Hartogh, P., Lis, D. C., Bockelée-Morvan, D., et al. 2011, Nature, 478, 218
Hässig, M., Altwegg, K., Balsiger, H., et al. 2013, Planet. Space Sci., 84, 148
Hässig, M., Altwegg, K., Berthelier, J. J., et al. 2015, Planet. Space Sci., 105, 175
Hässig, M., Altwegg, K., Balsiger, H., et al. 2017, A&A, 605, A50
Herny, C., Mousis, O., Marschall, R., et al. 2021, Planet. Space Sci., 200, 105194
Hoppe, P., Rubin, M., & Altwegg, K. 2018, Space Sci. Rev., 214, 106
Jensen, S. S., Jørgensen, J. K., Kristensen, L. E., et al. 2019, A&A, 631, A25
Jewitt, D., Matthews, H. E., Owen, T., & Meier, R. 1997, Science, 278, 90
Kavelaars, J. J., Mousis, O., Petit, J.-M., & Weaver, H. A. 2011, ApJ, 734, L30
Kawakita, H., Watanabe, J.-i., Kinoshita, D., Ishiguro, M., & Nakamura, R. 2003, ApJ, 590, 573
Kawakita, H., Watanabe, J.-i., Furusho, R., Fuse, T., & Boice, D. C. 2005, ApJ, 623, L49
Keller, H. U., Mottola, S., Davidsson, B., et al. 2015, A&A, 583, A34
Kerridge, J. F. 1985, Geochim. Cosmochim. Acta, 49, 1707
Kissel, J., Altwegg, K., Clark, B. C., et al. 2007, Space Sci. Rev., 128, 823
Läuter, M., Kramer, T., Rubin, M., & Altwegg, K. 2020, MNRAS, 498, 3995
Le Roy, L., Altwegg, K., Balsiger, H., et al. 2015, A&A, 583, A1
Lis, D. C., Bockelée-Morvan, D., Güsten, R., et al. 2019, A&A, 625, L5

Longobardo, A., Della Corte, V., Rotundi, A., et al. 2020, MNRAS, 496, 125
Lunine, J. I., & Atreya, S. K. 2008, Nat. Geosci., 1, 159
Lyons, J. R., Gharib-Nezhad, E., & Ayres, T. R. 2018, Nat. Commun., 9, 908
Manfroid, J., Jehin, E., Hutsemékers, D., et al. 2009, A&A, 503, 613
McKeegan, K. D., Aléon, J., Bradley, J., et al. 2006, Science, 314, 1724
Meier, R., Owen, T. C., Matthews, H. E., et al. 1998, Science, 279, 842
Meija, J., Coplen, T. B., Berglund, M., et al. 2016, Pure Appl. Chem., 88, 293
Messenger, S. 2000, Nature, 404, 968
Mumma, M. J., & Charnley, S. B. 2011, ARA&A, 49, 471
Mumma, M. J., Disanti, M. A., dello Russo, N., et al. 1996, IAU Circ., 6366, 1
Nevejans, D., Neefs, E., Kavadias, S., Merken, P., & Van Hoof, C. 2002, Int. J. Mass Spectr., 215, 77
Oba, Y., Takano, Y., Watanabe, N., & Kouchi, A. 2016, ApJ, 827, L18
Paganini, L., Mumma, M. J., Gibb, E. L., & Villanueva, G. L. 2017, ApJ, 836, L25
Paquette, J. A., Fray, N., Bardyn, A., et al. 2021, MNRAS, 504, 4940
Pearson, V. K., Sephton, M. A., Gilmour, I., & Franchi, I. A. 2001, in Lunar and Planetary Science Conference, 1861

Persson, M. V., Jørgensen, J. K., van Dishoeck, E. F., & Harsono, D. 2014, A&A, 563, A74
Pestoni, B., Altwegg, K., Balsiger, H., et al. 2021, A&A, 645, A38
Ratajczak, A., Taquet, V., Kahane, C., et al. 2011, A&A, 528, L13
Rubin, M., Altwegg, K., Balsiger, H., et al. 2017, A&A, 601, A123
Rubin, M., Altwegg, K., Balsiger, H., et al. 2019, MNRAS, 489, 594
Schroeder, I. R. H. G., Altwegg, K., Balsiger, H., et al. 2019a, MNRAS, 489, 4734
Schroeder, I. R. H. G., Altwegg, K., Balsiger, H., et al. 2019b, A&A, 630, A29
Schuhmann, M., Altwegg, K., Balsiger, H., et al. 2019, A&A, 630, A31
Stadermann, F. J., Hoppe, P., Floss, C., et al. 2008, Meteor. Planet. Sci., 43, 299
Sunshine, J. M., & Feaga, L. M. 2021, Planet. Sci. J., 2, 92
Wilson, T. L. 1999, Rep. Progr. Phys., 62, 143
Wright, I. P., Sheridan, S., Barber, S. J., et al. 2015, Science, 349, 2.673
Wyckoff, S. 1991, Earth Sci. Rev., 30, 125
Wyckoff, S., Kleine, M., Peterson, B. A., Wehinger, P. A., & Ziurys, L. M. 2000, ApJ, 535, 991
Yang, J., & Epstein, S. 1984, Nature, 311, 544

Appendix A: Mass spectra showing signatures of methane, propane and butane and their isotopologues

Fig. A.1. Sample mass spectra for *m/z* 16 and 17 showing the signatures of the isotopologues of methane. *Panel a*: *m/z* 16 from 2016-03-09 11:13 (UTC). *Panel b*: *m/z* 17 from 2016-03-09 11:14 (UTC). Measured data are represented by black dots including their statistical uncertainties. The individual mass fits and the total sum of the fits are shown with coloured lines.
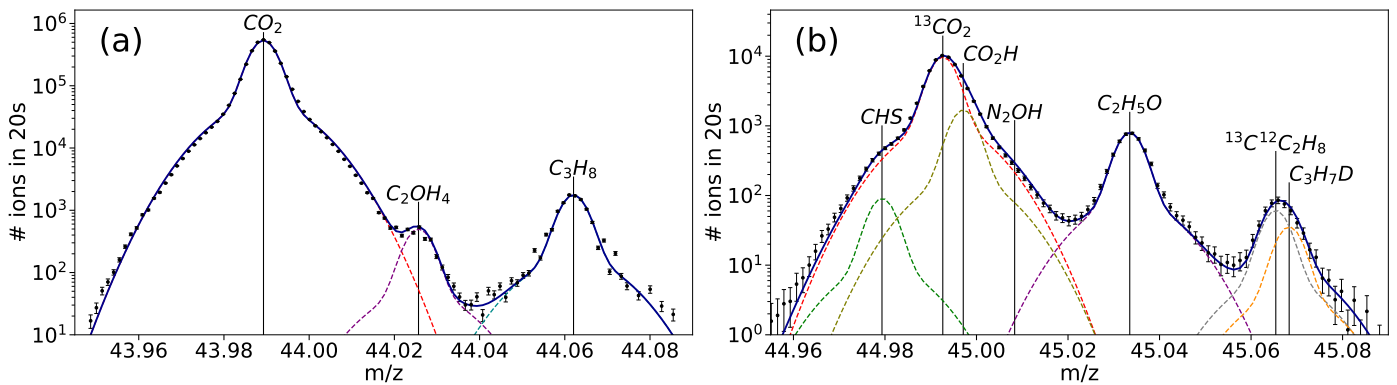
Fig. A.2. Sample mass spectra for *m/z* 44 and 45 showing the signatures of the isotopologues of propane. *Panel a*: *m/z* 44 from 2016-03-20 15:24 (UTC). *Panel b*: *m/z* 45 from 2016-03-20 15:24 (UTC). Measured data are represented by black dots including their statistical uncertainties. The individual mass fits and the total sum of the fits are shown with coloured lines.

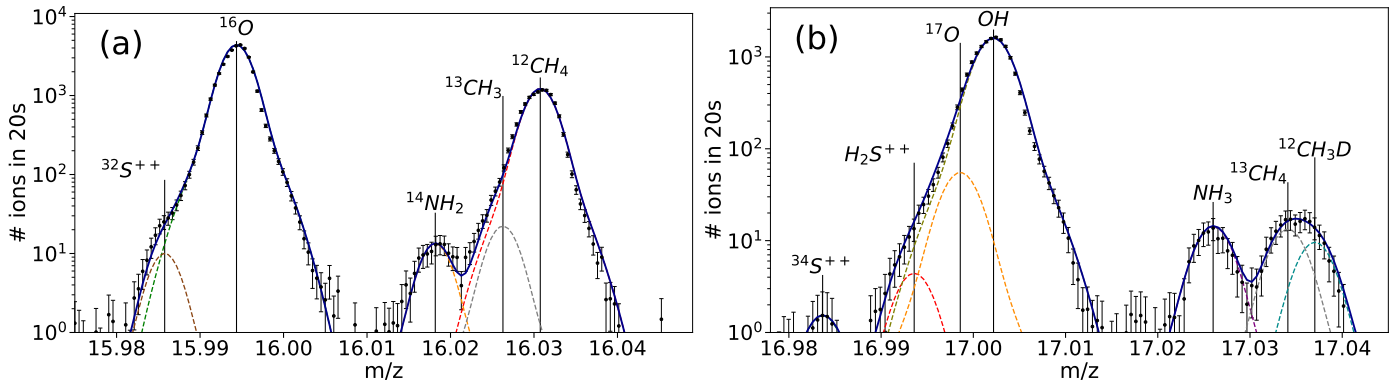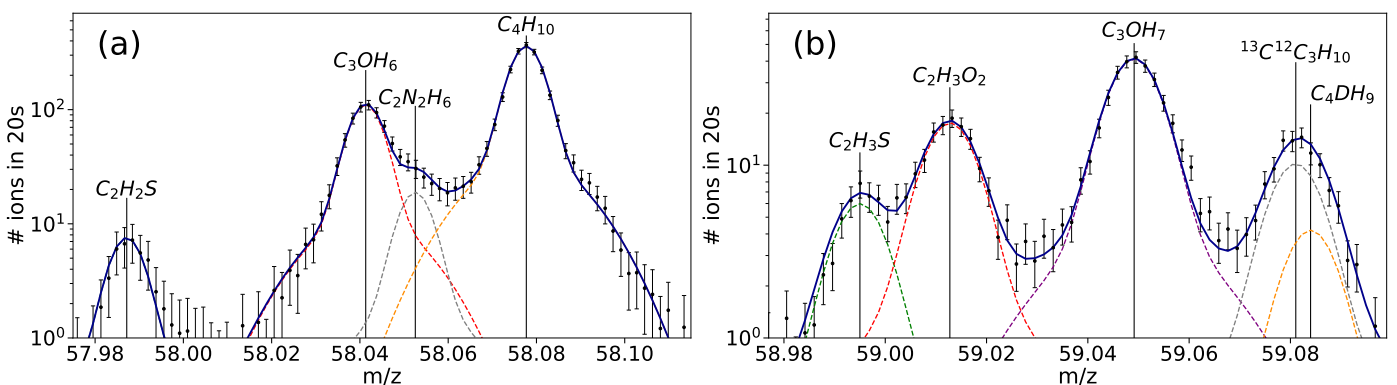**Fig. A.3.** Sample mass spectra for *m/z* 58 and 59 showing the signatures of the isotopologues of butane. *Panel a*: *m/z* 58 from 2016-03-19 22:45 (UTC). *Panel b*: *m/z* 59 from 2016-03-19 22:45 (UTC). Measured data are represented by black dots including their statistical uncertainties. The individual mass fits and the total sum of the fits are shown with coloured lines.

Appendix B: Reference tables for literature values used in figures

Table B.1. Literature values for D/H in comets, CCs and IDPs.

Molecule	Source	D/H	Reference
H_2O	67P	$(5.01 \pm 0.41) \cdot 10^{-4}$	This work
H_2O	103P/Hartley 2	$(1.61 \pm 0.24) \cdot 10^{-4}$	Hartogh et al. (2011)
H_2O	46P/Wirtanen	$(1.61 \pm 0.65) \cdot 10^{-4}$	Lis et al. (2019)
H_2O	81P/Wild 2	$(1.18 - 4.98) \cdot 10^{-4}$	McKeegan et al. (2006)
H_2O	C/1995 O1 (Hale-Bopp)	$(3.3 \pm 0.8) \cdot 10^{-4}$	Meier et al. (1998)
H_2O	C/1996 B2 (Hyakutake)	$(2.9 \pm 1) \cdot 10^{-4}$	Bockelée-Morvan et al. (1998)
H_2O	8P/Tuttle	$(4.09 \pm 1.45) \cdot 10^{-4}$	Bockelée-Morvan et al. (2015)
H_2O	C/2009 P1 (Garradd)	$(2.06 \pm 0.22) \cdot 10^{-4}$	Bockelée-Morvan et al. (2015)
H_2O	C/2014 Q2 (Lovejoy)	$(1.4 \pm 0.4) \cdot 10^{-4}$	Biver et al. (2016)
H_2O	C/2014 Q2 (Lovejoy)	$(3.02 \pm 0.87) \cdot 10^{-4}$	Paganini et al. (2017)
H_2O	CCs/OCs	$(0.16 - 5.9) \cdot 10^{-4}$	Alexander et al. (2010, 2012)
$HDO^{[a]}$	67P	$(3.6 \pm 1.8) \cdot 10^{-2}$	Altwegg et al. (2017)
H_2S	67P	$(1.2 \pm 0.3) \cdot 10^{-3}$	Altwegg et al. (2017)
HCN	C/1995 O1 (Hale-Bopp)	$(2.3 \pm 0.6) \cdot 10^{-3}$	Crovisier et al. (2004)
NH_3	C/1995 O1 (Hale-Bopp)	$< 4 \cdot 10^{-2}$	Crovisier et al. (2004)
NH_3	67P	$(1.1 \pm 0.2) \cdot 10^{-3}$	Altwegg et al. (2019)
CH_4	C/2004 Q2 (Machholz)	$< 5 \cdot 10^{-3}$	Bonev et al. (2009)
CH_4	C/2001 Q4 (NEAT)	$< 1 \cdot 10^{-2}$	Kawakita et al. (2005)
CH_4	C/2007 N3 (Lulin)	$< 7.5 \cdot 10^{-3}$	Gibb et al. (2012)
CH_4	67P	$(2.41 \pm 0.29) \cdot 10^{-3}$	This work
C_2H_6	C/2007 W1 (Boattini)	$< 2.6 \cdot 10^{-3}$	Doney et al. (2020)
C_2H_6	67P	$(2.37 \pm 0.27) \cdot 10^{-3}$	This work
C_3H_8	67P	$(2.16 \pm 0.26) \cdot 10^{-3}$	This work
C_4H_{10}	67P	$(2.05 \pm 0.38) \cdot 10^{-3}$	This work
H_2CO	C/1995 O1 (Hale-Bopp)	$< 5 \cdot 10^{-2}$	Crovisier et al. (2004)
CH_3OH	C/1995 O1 (Hale-Bopp)	$< 3 \cdot 10^{-2}$	Crovisier et al. (2004)
CH_3OH	67P	$(0.71 - 6.63) \cdot 10^{-2}$	Drozdovskaya et al. (2021)
Refr. Organics	67P	$(1.57 \pm 0.54) \cdot 10^{-3}$	Paquette et al. (2021)
Bulk	CCs/OCs	$(1.2 - 8.4) \cdot 10^{-3}$	Alexander et al. (2010, 2012); Kerridge (1985); Pearson et al. (2001); Yang & Epstein (1984)
Organics	CCs/OCs	$< 3.1 \cdot 10^{-3}$	Alexander et al. (2007, 2010); Busemann et al. (2006)
Organics	IDPs/UCCAMs	$9 \cdot 10^{-5} - 8 \cdot 10^{-3}$	Duprat et al. (2010); Messenger (2000)

References. (a) D/H in HDO is equal to $2 \cdot D_2O/HDO$

Table B.2. Literature values for $^{13}C/^{12}C$ in comets, CCs and IDPs.

Molecule	Source	$^{13}C/^{12}C$	Reference
C_2	4 comets	$(1.10 \pm 0.12) \cdot 10^{-2}$	Wyckoff et al. (2000)
CH_4	67P	$(1.14 \pm 0.13) \cdot 10^{-2}$	This work
C_2H_6	67P	$(1.08 \pm 0.12) \cdot 10^{-2}$	This work
C_2H_6	67P	$(9.5 \pm 0.9) \cdot 10^{-3}$	Altwegg et al. (2020)
C_3H_8	67P	$(1.15 \pm 0.12) \cdot 10^{-2}$	This work
C_4H_{10}	67P	$(1.04 \pm 0.15) \cdot 10^{-2}$	This work
CN	19 comets	$(1.10 \pm 0.05) \cdot 10^{-2}$	Manfroid et al. (2009)
HCN	C/1995 O1 (Hale-Bopp)	$(9.0 \pm 1.0) \cdot 10^{-3}$	Jewitt et al. (1997)
CO	67P	$(1.16 \pm 0.12) \cdot 10^{-2}$	Rubin et al. (2017)
CO_2	67P	$(1.19 \pm 0.06) \cdot 10^{-2}$	Hässig et al. (2017)
H_2CO	67P	$(2.5 \pm 0.9) \cdot 10^{-2}$	Altwegg et al. (2020)
CH_3OH	67P	$(1.10 \pm 0.12) \cdot 10^{-2}$	Altwegg et al. (2020)
Bulk	81P/Wild 2	$(1.1 \pm 0.01) \cdot 10^{-2}$	Stadermann et al. (2008)
Bulk	CCs	$(1.09 - 1.15) \cdot 10^{-2}$	Alexander et al. (2010, 2012); Pearson et al. (2001)
Organics	CCs/IDPs	$(1.05 - 1.12) \cdot 10^{-2}$	Alexander et al. (2007); Floss & Stadermann (2004)

3.2 Deciphering cometary outbursts: Linking gas composition changes to trigger mechanisms

Cometary outbursts are fascinating phenomena that significantly influence the structure of the coma (Hughes, 1975, 1991). These events, characterised by dust and gas emissions, play a key role in understanding cometary activity. Despite various proposed trigger mechanisms, such as cliff collapses (e.g., Vincent et al., 2016, Pajola et al., 2017), pressure pockets (e.g., Belton et al., 2013, Agarwal et al., 2017, Bockelée-Morvan et al., 2022), and the amorphous-to-crystalline phase transition of water ice (e.g., Agarwal et al., 2017), the underlying processes remain poorly understood (e.g., Shinnaka et al., 2018, Wierzchos and Womack, 2020, Bockelée-Morvan et al., 2022). In this study, the coma gas composition from multiple outbursts on comet 67P/Churyumov-Gerasimenko is analysed using data from the Rosetta/ROSINA instruments. The analysis focuses on the evolution of gas composition within the comet's coma during these outburst events, with the aim of shedding light on the mechanisms driving cometary activity.

This work compared two distinct mechanisms behind cometary outbursts, which are differentiated by the location of the source and the surface topography. Outbursts triggered by landslides or cliff collapses are likely to be water-driven, as fresh water ice is more exposed near the surface. Conversely, perihelion eruptions are associated with increased highly volatile species, especially CO_2, from subsurface pockets. Gas may seep from these pockets prior to dust ejection, indicating a gradual release of volatile species. The depletion of volatile species near the surface may provide an explanation for the distinction between the H_2O-dominated events over CO_2-dominated events. The Rosetta mission's extensive coverage of 67P's outgassing has allowed detailed analysis of more than 40 outburst events, revealing different compositions associated with different triggering mechanisms. However, unanswered questions, such as the correlation between dust and gas components and the heliocentric distance dependence of outburst triggers, require further studies combining laboratory work, simulations, observations and missions to fully understand cometary outbursts and activity.

Credit: Daniel R. Müller, MNRAS **529**, 2763-2776 (2024), reproduced with permission from Oxford University Press.

Deciphering cometary outbursts: linking gas composition changes to trigger mechanisms

Daniel R. Müller [ORCID],[1]* Kathrin Altwegg [ORCID],[1] Jean-Jacques Berthelier [ORCID],[2] Michael R. Combi [ORCID],[3] Johan De Keyser [ORCID],[4] Stephen A. Fuselier [ORCID],[5,6] Philippe Garnier,[7] Nora Hänni [ORCID],[1] Urs Mall [ORCID],[8] Martin Rubin [ORCID],[1] Susanne F. Wampfler [ORCID][9] and Peter Wurz [ORCID][1,9]

[1]*Space Research and Planetary Sciences, Physics Institute, University of Bern, Sidlerstrasse 5, CH-3012 Bern, Switzerland*
[2]*Laboratoire Atmosphères, Milieux, Observations Spatiales (LATMOS), 4 Avenue de Neptune, F-94100 Saint-Maur, France*
[3]*Department of Climate and Space Sciences and Engineering, University of Michigan, 2455 Hayward, Ann Arbor, MI 48109, USA*
[4]*Royal Belgian Institute for Space Aeronomy, BIRA-IASB, Ringlaan 3, B-1180 Brussels, Belgium*
[5]*Space Science Directorate, Southwest Research Institute, 6220 Culebra Rd., San Antonio, TX 78228, USA*
[6]*Department of Physics and Astronomy, The University of Texas at San Antonio, San Antonio, TX 78249, USA*
[7]*IRAP, Université de Toulouse, CNRS, CNES, UPS, 9 Avenue du Colonel Roche, F-31028 Toulouse, France*
[8]*Max-Planck Institute for Solar System Research, Justus-von-Liebig-Weg 3, D-37077 Göttingen, Germany*
[9]*Center for Space and Habitability, University of Bern, Gesellschaftsstrasse 6, CH-3012 Bern, Switzerland*

ABSTRACT

Dust and gas outbursts are recurrent cometary phenomena, playing a crucial role in shaping the coma. Proposed outburst trigger mechanisms include cliff collapse, pressure pockets, and amorphous-to-crystalline phase transition of water ice; however, the underlying processes remain inadequately understood. In this study, we analyse *Rosetta*/ROSINA data from multiple outbursts on comet 67P/Churyumov-Gerasimenko and present the evolution of the gas composition in the comet's coma during outburst events. We distinguish two distinct categories of cometary outbursts on the comet: water-driven events characterized by rapid (minutes to hours) changes in coma composition, and CO_2-driven events displaying a slow, prolonged (hours to days) increase in highly volatile species. We tentatively associate these different gas composition patterns with different trigger mechanisms. Exposure of fresh ice due to cliff collapse leads to a notable water enhancement, while most perihelion outbursts coincide with substantial density increases of CO_2. We propose that these CO_2-driven events originate from subsurface gas-filled cavities, whose walls are suggested to have been sealed by earlier refreezing of CO_2 migrating from warmer spots, hence increasing the cavity pressure required to burst.

Key words: instrumentation: detectors – methods: data analysis – comets: general – comets: individual: 67P/Churyumov-Gerasimenko.

1 INTRODUCTION

Comet outbursts are universal and recurring phenomena. Hughes (1975, 1991) demonstrated that outbursts are common events and occur episodically on all comets. These transient phenomena, marked by sudden mass ejections, play a crucial role in understanding the evolutionary processes shaping the surface of comets, while offering valuable insights into the physical properties of their nuclei (Hughes 1991). Despite extensive research (e.g. Lin et al. 2009; Ishiguro et al. 2014, 2016; Shinnaka et al. 2018; Wierzchos & Womack 2020; Bockelée-Morvan et al. 2022) questions persist about their underlying nature and triggering mechanisms.

Prialnik, A'Hearn & Meech (2008) proposed a mechanism to explain short-lived outbursts observed during the Deep Impact mission on 9P/Tempel 1. They suggested that solar radiation generates a heat wave, causing ice sublimation beneath the dust layer. This

vapour migrates towards the surface, but refreezes before it gets there because, due to the slow process, by the time the heatwave reaches the ice, the area has moved out of the sunlight, causing the temperature to drop. The subsequent sunrise leads to the evaporation of the newly formed ice within the dust layer. Belton et al. (2008) proposed a similar mechanism for outbursts on the same comet, but independent of direct solar illumination. In addition to the transport of H_2O vapour described by Prialnik, A'Hearn & Meech (2008), they propose thermal stresses and subsurface effects to control the initiation of outbursts.

In contrast to the relatively small outbursts on 9P/Tempel 1, a massive outburst occurred on 17P/Holmes in 2007. The substantial gas production rate during this event is suggested to be the result of either the explosive sublimation of a highly volatile region in the comet's surface layer or a transient outgassing event involving the entire nucleus (Lin et al. 2009). Moreover, Bockelée-Morvan et al. (2022) identified a correlation between coma brightness and CO gas production during outbursts on comet 29P/Schwassmann-Wachmann 1 (29P) in 2007 and 2010. Following these events, the

* E-mail: daniel.mueller@unibe.ch

CO gas production rate remained elevated for several days. Their findings, coupled with the slow rotation of 29P, led to the suggestion that fractures or pits on the nucleus surface may act as efficient heat traps, enhancing outgassing compared to a uniformly illuminated surface. Similarly, for outburst events observed on 29P between 2018 and 2021, the driving activity was suggested to come mostly from CO outgassing (Lin 2023). Conversely, Wierzchos & Womack (2020) observed dust outbursts on the same comet not correlated to CO outgassing. They state that this may hint at CO being intimately mixed with the dust component in the nucleus, or if CO is primarily released through a porous material.

Hughes (1975) summarized potential outburst triggering mechanisms, including pressure release from gas pockets, explosive radicals, amorphous-to-crystalline ice transition, impact cratering by boulders, break-up of nucleus, and nuclear crushing. They also suggested that there is not just one single mechanism triggering cometary outbursts.

The *Rosetta* mission provided unique insights into comet 67P/Churyumov-Gerasimenko (hereafter 67P), rendering it the best-studied comet to date, and significantly advanced our understanding of these objects (e.g. Altwegg et al. 2015; Sierks et al. 2015; Fulle et al. 2016; Altwegg, Balsiger & Fuselier 2019; Thomas et al. 2019; Hänni et al. 2022). 67P displayed numerous localized dust and gas jet features (e.g. Agarwal et al. 2017; Bockelée-Morvan et al. 2017; Lin et al. 2017; Schmitt et al. 2017), offering a unique opportunity to investigate these outburst phenomena across extended time frames and in exceptional detail.

Skorov et al. (2016) formulated a physical model to explain outbursts observed within fractured terrains on comet 67P near perihelion. They postulated that as the stresses on the nucleus increased during the perihelion approach, pre-existing cracks or fractures would deepen, reaching into underlying material rich in highly volatile ices in equilibrium with the surrounding environment. The sudden propagation of these fractures would trigger a violent sublimation of the highly volatile ices. Their proposed mechanism is independent of the solar illumination history of specific regions or the presence of large, sealed cavities within the nucleus. A parallel explanation was offered by Pajola et al. (2017), where images of an outburst source region on comet 67P were compared, leading to the conclusion that this specific event has been caused by a cliff collapse. Further numerical simulations of dusty material demonstrated that avalanches could generate a transient, tightly focused outburst plume closely resembling the observed morphology of outbursts emanating from the surface of 67P (Steckloff & Melosh 2016). However, this mechanism predicts that such outbursts should not be directly associated with any increase in gas production (Steckloff & Melosh 2016).

A comprehensive study of outbursts on 67P was carried out by Vincent et al. (2016a). They analysed optical images recorded by the *Rosetta* cameras for a 3-month period around 67P's perihelion passage in 2015 August and identified 34 different dust outbursts. These outbursts were characterized by sudden brightness increases in the coma, lasting only a few minutes, which are distinct from the typically less bright dust jets continuously observed on the rotating comet nucleus (Vincent et al. 2016b). The source locations of the dust outbursts were primarily in the Southern hemisphere, the summer hemisphere at that time, in line with previous observations that show that active sources generally migrate to subsolar regions (Ip et al. 2016; Läuter et al. 2019). They are often found near steep scarps, cliffs, and pits (Rinaldi et al. 2018). Furthermore, Vincent et al. (2016a) observed that outburst events could be classified into two groups, depending on whether they occur at local sunrise or at local noon. Bockelée-Morvan et al. (2017) investigated two outbursts on

67P using infrared data from *Rosetta*/VIRTIS and found evidence of small grains and agglomerates. However, the column densities of H_2O and CO_2 did not change during these events. The authors concluded that these outbursts were likely caused by a cliff collapse similar to the one studied by Pajola et al. (2017).

In this paper, we investigate 45 outbursts on comet 67P observed during various phases of ESA's *Rosetta* mission, with the goal to enhance our understanding of cometary outburst mechanisms. The changes in the gas composition of the comet's coma, as measured with the *Rosetta* Orbiter Spectrometer for Ion and Neutral Analysis (*Rosetta*/ROSINA; Balsiger et al. 2007), are associated with two distinct outburst trigger mechanisms. This nuanced exploration is made possible by the exceptional, continuous monitoring of comet 67P by the *Rosetta*/ROSINA instruments. Section 2 provides details of the ROSINA instruments and data processing procedures, while Section 3 presents the measurements acquired by *Rosetta*. The ensuing discussion in Section 4 brings together our findings and concludes this study.

2 METHODS

2.1 ROSINA/DFMS instrumentation and data treatment

The ROSINA Double Focusing Mass Spectrometer (ROSINA/DFMS) is a double focusing mass spectrometer in Nier–Johnson configuration with a field of view of $20° \times 20°$. Instrument details are given by Balsiger et al. (2007). ROSINA/DFMS contains a toroidally shaped electrostatic analyser, filtering ions for their kinetic energy, and a curved permanent magnet, where the momentum of the ions is filtered. This combination separates different mass-to-charge ratios (m/z) of the incoming ions. The ions are produced by electron impact ionization using a hot filament. The DFMS is a scanning mass spectrometer, where each mass range around an integer m/z is measured sequentially. To do so, a suitable set of voltages is applied to the ion optical system to select a given m/z ratio. In addition, the voltage across the multichannel plate (MCP) detector is adjusted to achieve an appropriately amplified electron current proportional to the incident ion flux. This adjustment creates a gain variation for each measurement and increases the dynamic range of the instrument. The mass resolution is 3000 at the 1 per cent level of the peak for m/z 28 (Balsiger et al. 2007).

After identifying the species in the mass spectrum, a mass scale is applied and the species' signal is integrated (De Keyser et al. 2019). Further, after applying species-dependent sensitivities and fragmentation patterns, the partial densities are obtained after normalization to the total density measured by the ROSINA COmet Pressure Sensor (ROSINA/COPS). More details on DFMS data analysis are given by Le Roy et al. (2015) and Calmonte et al. (2016).

Including the voltage settling time (roughly 10 s per spectrum) and the integration time of the measurement (20 s), a full scan in the typical mass range from m/z 13 to m/z 100 takes about 45 min. In addition, each scan includes two additional m/z 18 measurements, one at the beginning and one at the end of the measurement cycle. This doubling is used to monitor the water activity changes of the comet over the duration of the scan.

2.2 ROSINA/RTOF instrumentation and data treatment

The ROSINA Reflectron-type Time-Of-Flight (ROSINA/RTOF) is the second mass spectrometer of the ROSINA experiment (Scherer et al. 2006). It is designed to measure cometary neutral gas and ions

with a wide and instantaneous mass range (from 1 m/z to > 300 m/z) and high temporal resolution.

Charged particles are extracted from the ionization chamber towards the drift tube by an extraction grid, applying a pull pulse at a frequency of 2, 5, or 10 kHz. The ions pass through the drift tube, are reflected in the reflectron, pass again through the drift tube and finally reach the detector. The time of flight of each molecule is proportional to the square root of the mass-per-charge of the species.

The first step of the data analysis is to apply the corresponding mass scale to all spectra (Gasc et al. 2017). The second step is integrating the peaks corresponding to the species of interest. The integration yields the numerical area below the curve, which represents the number of ions per 200 or 400 s integration time depending on the operating mode. Having obtained the number of ions per species, corrections due to sensitivity and fragmentation pattern of each molecule were applied as detailed in Gasc et al. (2017). Finally, after normalization to the measured total densities by ROSINA/COPS, the corresponding partial densities of the observed molecules are retrieved. More details of the data analysis applied to ROSINA/RTOF are given in Gasc et al. (2017).

2.3 ROSINA/COPS instrumentation and data treatment

The Comet Pressure Sensor (COPS) completed the ROSINA instrument package (Balsiger et al. 2007). It was designed to measure the gas density in the coma and consisted of two different gauges. In the nude gauge, molecules were first ionized via electron impact, and then the current was measured with an electrometer after acceleration. This gauge measured the total neutral particle density in the coma. The ion current relative to the electron current is related to the density of the neutral gas inside the NG after application of the laboratory-derived calibration factors (Graf et al. 2004; Tzou 2017). The simplicity of the sensor makes it a reliable and stable monitor for the gas density of the comet in the vicinity of the spacecraft. The second gauge, the ram gauge, thermalized the neutral gas molecules first before ionization. Hence, it measured the ram pressure, which is equivalent to the cometary gas flux.

2.4 Data selection and analysis

The outbursts identified by Vincent et al. (2016a) were described as transient jets that were present in a given image, but not in the preceding and following images. Images were taken with a 5 to 30 min cadence, setting a limited timing precision. The lifetime of the dust outburst is minutes up to a few tens of minutes. Knowing the source locations of the dust outbursts, the gas composition in the coma around such events has been studied temporally and spatially. We analysed ROSINA/DFMS data, acquired during the 2015 July–September time period described by Vincent et al. (2016a) and the periods around the outbursts listed in Table 1. In addition, we investigated ROSINA/RTOF data for the 2016 February 19 event, reported by Grün et al. (2016).

To examine the outburst events using ROSINA data, it was necessary to determine the specific instances when the *Rosetta* spacecraft was positioned above a source location corresponding to any of the outbursts. To do so, an angular window of $\pm$ 25° in subspacecraft longitude and latitude with respect to the source location was selected. This angular window takes into account the lateral expansion of the gas (e.g. Combi et al. 2012) and the initial, non-radial outflow direction, the duration of a measurement cycle of DFMS, as well as the instrument's spatial resolution for determining the surface distribution of the emission (Marschall et al.

Table 1. Summary of all published outburst events on 67P not included in the summer fireworks (Vincent et al. 2016a). For events detected with ROSINA/DFMS the maximum density enhancements for CO_2 and CO relative to H_2O are given. Most of these events were H_2O dominated and thus, density enhancements <1 mean that H_2O was the most dominant driver for the considered event and the enhancement of H_2O would be the inverse of the given value. Uncertainties on the enhancements are ±18 per cent, mostly due to instrument calibration uncertainties (Le Roy et al. 2015; Calmonte et al. 2016).

Event Date	Region	ROSINA Detection	Enhancement CO_2	CO
2014 Apr[1]	Not given[d]	Too far	–	–
2015 Mar 12[2]	Imhotep[c]	Inst. off	–	–
2015 May 23[3]	Not given[d]	Yes	0.2	0.2
2015 July 10[4]	Aswan[a]	Inst. off	–	–
2015 Aug 10[5]	Khonsu[d]	Inst. off	–	–
2015 Sept 03[6]	Not given[d]	No loc.	–	–
2015 Sept 13[5,7]	Imhotep[d]	Yes	0.9	0.5
2015 Sept 14[5,7]	Atum[d]	Yes	0.9	0.4
2015 Sept 23–30[6]	Not given[d]	No loc.	–	–
2015 Nov 07[8]	Southern neck[b]	Yes	8.4	1.2
2016 Jan 06[9]	Imhotep[a]	Yes	0.6	0.3
2016 Feb 19[10]	Atum[a]	Yes	0.5	0.2
2016 July 03[9]	Imhotep[a]	Yes	0.5	0.7

Notes. References: (1) Tubiana et al. (2015); (2) Knollenberg et al. (2016); (3) Feldman et al. (2016); (4) Pajola et al. (2017); (5) Rinaldi et al. (2018); (6) Lin et al. (2017); (7) Bockelée-Morvan et al. (2017); (8) Noonan et al. (2021) (Event B); (9) Agarwal et al. (2017); (10) Grün et al. (2016). Local time of event: (a) sunrise; (b) midday; (c) night; (d) unknown.

2020b). However, it does not take into account the highly non-spherical morphology of the nucleus. Mitigating this limitation, and accounting for varying spacecraft-nucleus distances, the data set was subjected to normalization. This process, underpinned by the individual spacecraft-event source distance for each measurement instance, effectively rectified the diverse viewing geometries. Given the spatial proximity of several outbursts, a careful evaluation of each data set and its associated measurement configuration was indispensable to be able to link the ROSINA data to distinct events in the images.

It is important to consider the temporal offset between remote sensing (e.g. *Rosetta* cameras) and *in situ* observations (e.g. ROSINA instrument) of the same event. *In situ* measurements require gas to flow into the instrument, while cameras are most sensitive to illuminated dust outbursts from a phase angle of 90°. Additionally, the outflowing gas from the outbursts is much faster ($\approx$ 0.5–0.9 km s^{-1}; Biver et al. 2019) than the dust grains ($\approx$ 22–65 m s^{-1}; Rinaldi et al. 2018). We took these various effects into consideration in the analysis of the ROSINA data. Additionally, it is clear that the gas flow smears out inhomogeneities in surface production from small-scale source regions (a few metres to a few tens of metres) when the gas is measured at a distance. During 2015 July to September, the spacecraft was far away from the comet's surface (>180 km). Hence, it is not possible to exactly localize the source of the gas density enhancements recursively observed over several nucleus rotations with the ROSINA instruments. Nevertheless, the measured gas density enhancements are an indicator for the general outgassing behaviour of the source regions and their surrounding areas.

For this analysis, the densities of different volatiles are compared to H_2O. Fig. A3 shows how to retrieve the data used. To calculate the enhancement each time *Rosetta* was above the source location, the peak density of both CO_2 and H_2O has been selected and corrected
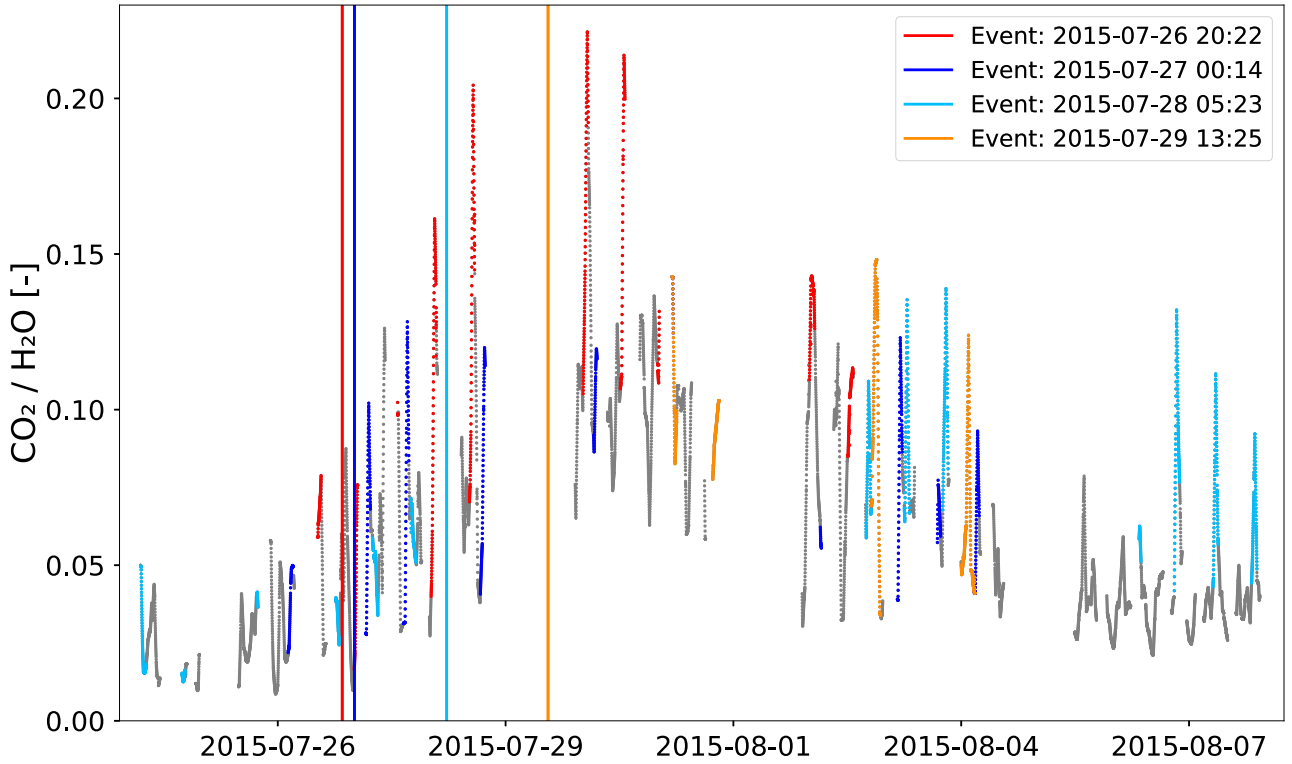
Figure 1. Ion count ratio from ROSINA/DFMS for CO_2 relative to H_2O from 2015 July 24 until August 8. The coloured data points show measurements taken when the *Rosetta* spacecraft was flying over the identified source location of the respective event observed by the *Rosetta* cameras at the time marked by the corresponding vertical line. For a better representation, only a part of the summer fireworks' period (Vincent et al. 2016a) and only four distinct events are shown. The first three events were morning outburst whereas the last event (orange) was a midday outburst.

considering the quiescent coma. It is possible that the peak values are slightly shifted in time due to the mass scanning nature of the instrument. These time shifts, on the order of a few minutes, do not affect the enhancement calculations as the time-scales associated to *Rosetta* passing above the active region is substantially longer. Finally, the relative density enhancement for the volatile species *x* is then calculated by:

$$e_x = \frac{(n_x/n_{H_2O})_{peak}}{(n_x/n_{H_2O})_{qs}} = \frac{(c_x/c_{H_2O})_{peak}}{(c_x/c_{H_2O})_{qs}} \quad (1)$$

with *n* the density and *c* the DFMS detector signal where fragment contributions have been removed (Rubin et al. 2019).

The density enhancement, e_x, shows how much the ratio at the peak, within the aforementioned subspacecraft longitude and latitude window (denoted as *peak*), is increased at that time compared to the quiescent coma ratio (denoted by *qs*). Consequently, it shows the increased release of a volatile species during an outburst event as compared to the nominal comet outgassing. The quiescent coma is retrieved from measurements at the same activity levels of the comet and similar *Rosetta* positions as the source location of the dust outburst (see Extended Data Fig. A3). A caveat to using this definition of the relative enhancement calculation exploiting two ratios is that an enhancement increase might also occur if there was a decrease in just the H_2O density. However, as background corrections are applied to equation (1), a decrease of H_2O would imply a negative ratio, which has not been observed for any of the events analysed. All of the events showed behaviours similar to what is depicted in Figs 2 and A3.

3 RESULTS

3.1 Summer fireworks

The 34 so-called summer fireworks outbursts during the summer of 2015 (from 2015 July 10 to September 26), studied by Vincent et al. (2016a), represent the largest sample of examined outbursts to date. While the dust features associated with these outbursts have been thoroughly analysed (Vincent et al. 2016a), little is known about their gas component. Thus, we investigated gas abundance ratios for the most abundant highly volatile species detected in comet 67P's coma (Rubin et al. 2019) relative to H_2O using data from *Rosetta*/ROSINA.

Fig. 1 depicts the CO_2 signal compared to H_2O measured with ROSINA/DFMS from 2015 July 24 to August 8 to show how the changes in this ratio are attributable to fly-overs of the *Rosetta* spacecraft over the corresponding outburst event source regions. For a better representation, only this part of the complete summer fireworks period is shown together with a selection of three distinct events. For the full time period, we refer to Extended Data Figs A1 and A2. CO_2 is the second most abundant gas after H_2O (Hoang et al. 2019; Läuter et al. 2019; Rubin et al. 2019). In the following, gas ratios relative to H_2O will be discussed and thus only the gas in the numerator will be mentioned to simplify the nomenclature.

The typical signature of the outbursts during the summer fireworks period, when the spacecraft was positioned above one of the source regions (Vincent et al. 2016a), was an increase in the relative abundance of highly volatile species (i.e. species with sublimation temperatures below that of water), especially CO_2, which later returned to pre-outburst levels. In contrast, H_2O showed only marginal increases (Fig. 2). As a result, the activity of highly volatile species

Figure 2. Gas densities of H_2O and CO_2 normalized to their quiescent coma levels during the CO_2 enhanced outburst from 2015 July 26 measured with ROSINA/DFMS. The quiescent values have been retrieved a few hours before the dust event. Uncertainties are only shown on every 10th data point for H_2O and on every 5th data point for the other volatiles to improve visibility. The vertical line represents the time when the event has been detected by the *Rosetta* cameras and the green areas represent the time when the spacecraft was above the considered out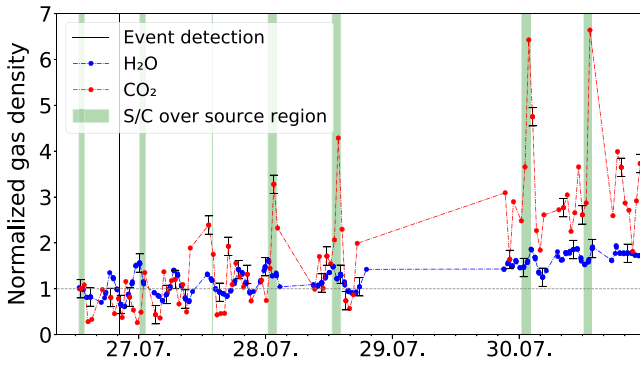burst source region. The grey horizontal line shows the quiescent level of the normalized data. The continuous increase of both H_2O and CO_2 is due to the spacecraft's movement across the generally more active Southern hemisphere of 67P during that time.

gradually increased and typically ceased a few days after the visible outburst.

The enhancement in relative abundance in 67P's coma for each flyover was calculated following the methodology described in Section 2.4 and detailed results are given in Table A1. While the enhancement patterns exhibit similarities across all events, characterized by an increase around the time of the event being detected by the cameras and followed by a decrease a few days later, they differ in terms of the starting time, duration, and magnitude of enhancement. Analysis of the weighted mean enhancement in relative abundance as a function of time with respect to the optical detection of the dust feature of the events reveals that the average enhancement of volatiles already starts up to three days (∼6 rotations) prior to the observed expulsion of dust indicating that the dust component of the outbursts may be preceded by an increase in outgassing of highly volatiles (Fig. 3). Subsequently, the mean density enhancement gradually

decays, with a notably slow decrease over a period of up to 8 d (∼16 rotations) compared to the short-lived nature of the ejected dust during the event observed by the cameras. Hence, only the combined analysis of dust and gas can give a comprehensive view of the nature of the outbursts and their trigger mechanisms. The average enhancement is weighted with the weight for each individual point being inversely proportional to its statistical uncertainty, so that events where *Rosetta* was closer to the source region and the data are less smeared out are given a higher weight than events measured from a larger distance with less signal and more measurement uncertainties. The considered data set has been thoroughly analysed and most of the individual outbursts were well separable. None the less, it is possible that different events may overlap, increasing the mean density enhancement, especially at times long before and long after the observed dust outbursts. In addition, events not observed by the *Rosetta* cameras might also contribute to the mean density enhancement over time.

Fig. 4 illustrates the average density enhancement relative to water for the most abundant species detected in comet 67P's coma (Rubin et al. 2019) during the summer 2015 events. The mean enhancement for the sunrise and midday events, as well as the mean enhancement over all summer 2015 events, are presented separately. When considering all events combined, CO_2, ethane (C_2H_6), and propane (C_3H_8) exhibit higher enhancements (approximately ×13) compared to carbon monoxide (CO), hydrogen sulphide (H_2S), ammonia (NH_3), methane (CH_4), formaldehyde (H_2CO), methanol (CH_3OH), and hydrogen cyanide (HCN) (×3 to ×6). These findings align with Rubin et al. (2023), where C_2H_6 and C_3H_8 are primarily associated with CO_2, while CO, H_2S, NH_3, CH_4, H_2CO, CH_3OH, and HCN are distributed in roughly equal proportions between water and CO_2. Consequently, the enhancement of the latter molecules is reduced to the fraction associated to CO_2. This results in their enhancement being smaller than that of CO_2 and its associated molecules, but larger than that of water and its associated molecules. Additionally, it appears plausible that part of the signal from molecules, such as to NH_3, originates from semivolatile salts on dust grains (Altwegg et al. 2020, 2022), ejected during the outburst. The correlation between O_2 and H_2O is consistent with previous observations (Bieler et al. 2015; Rubin et al. 2023). Consequently, these results suggest that CO_2, as the most abundant highly volatile species, plays a pivotal role in driving outburst events and carries a suite of associated species along.

Figure 3. Weighted mean density enhancement for CO_2 during the summer fireworks outburst events as a function of time. The enhancement is the maximum of the ratio CO_2/H_2O during each fly-over divided by the same ratio in the quiescent coma. Time zero represents the time when the dust event has been observed with the *Rosetta* cameras (timing precision is 5 to 10 min). The horizontal line shows the unchanged ratio (enhancement factor of 1). Only events exhibiting a CO_2 enhancement are considered.

Figure 4. Weighted mean values of maximum density enhancement separated for sunrise and midday events and all events combined for the summer fireworks 2015 period reported by Vincent et al. (2016a). The uncertainties show the standard deviation of the mean including uncertainties of the individual measurements as explained in Section 2 as well as the variation of H_2O for each considered event. The black horizontal line shows the unchanged ratio (enhancement factor of 1). The volatiles are sorted by their relative bulk abundance compared to H_2O (Rubin et al. 2019).

In agreement with Vincent et al. (2016a), our analysis supports the categorization of summer firework events into two groups: sunrise and midday events, determined by the local time of the outburst source regions. On average, with the exception of NH_3, sunrise events exhibit slightly higher density enhancements compared to midday events (Fig. 4). However, the error bars overlap and uncertainties persist due to the limited temporal coverage of the outburst events. Thus, clear differentiation between these groups is not possible as also no correlation exists between the outburst type and its local time (Vincent et al. 2016a). None the less, Vincent et al. (2016a) suggested that the two groups might be associated with different mechanisms. Noon outbursts may be linked to buried pockets of volatiles, which require time to get heated enough to trigger an outburst. Shortly after noon is when the local (sub)-surface reaches its maximum temperature. On the other hand, early morning outbursts occur almost immediately as the Sun rises. Despite the temperature possibly not being very high, the very low thermal inertia ensures that these local times exhibit the steepest temperature gradient. The surface heats up rapidly, with the gradient being large enough to trigger thermal cracking, potentially leading to surface breakage. This rapid heating might explain the slightly higher volatile enhancements for the sunrise events, as the immediate surface breakage might release gas more intensively. For slowly heated pockets, the confined gas might already start to seep out more gradually before the abrupt ejection of dust occurs. However, this is only a suggestion and the data are not sufficiently different to make a definitive statement. An explanation on why NH_3 exhibits a converse enhancement for the two groups might be that NH_3 comes from ammonium salts that might take some time and need high temperature to sublimate or build up which is possible for the midday events.
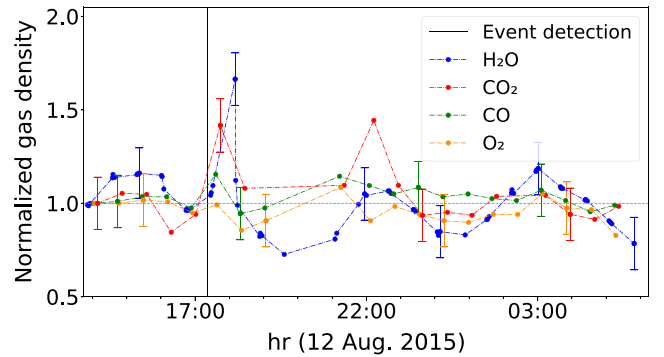
Figure 5. Gas densities of H_2O, CO_2, CO, and O_2 normalized to their quiescent coma levels during the water enhanced outburst 2015 August 12 measured with ROSINA/DFMS. The quiescent values have been retrieved a few hours before the dust event. Uncertainties are only shown on every 10th data point for H_2O and on every 5th data point for the other volatiles to improve visibility. The vertical line represents the time when the event has been detected by the *Rosetta* cameras. The grey horizontal line shows the quiescent level of the normalized data.

As anticipated, not all summer firework events exhibited an enhancement of highly volatile species. Some events displayed no volatile enhancement or even an increase in the water signal. For instance, the event on 2015 August 12 (#14 in Vincent et al. 2016a), resulted in a twofold increase of H_2O compared to CO_2 and an increase of a factor 5 of water compared to CO (Fig. 5). This event has a source region with a morphology expected from the modelling of cliff collapses. Hence, considering the water enhancement, this event might have been triggered by a cliff collapse. Another event hinting
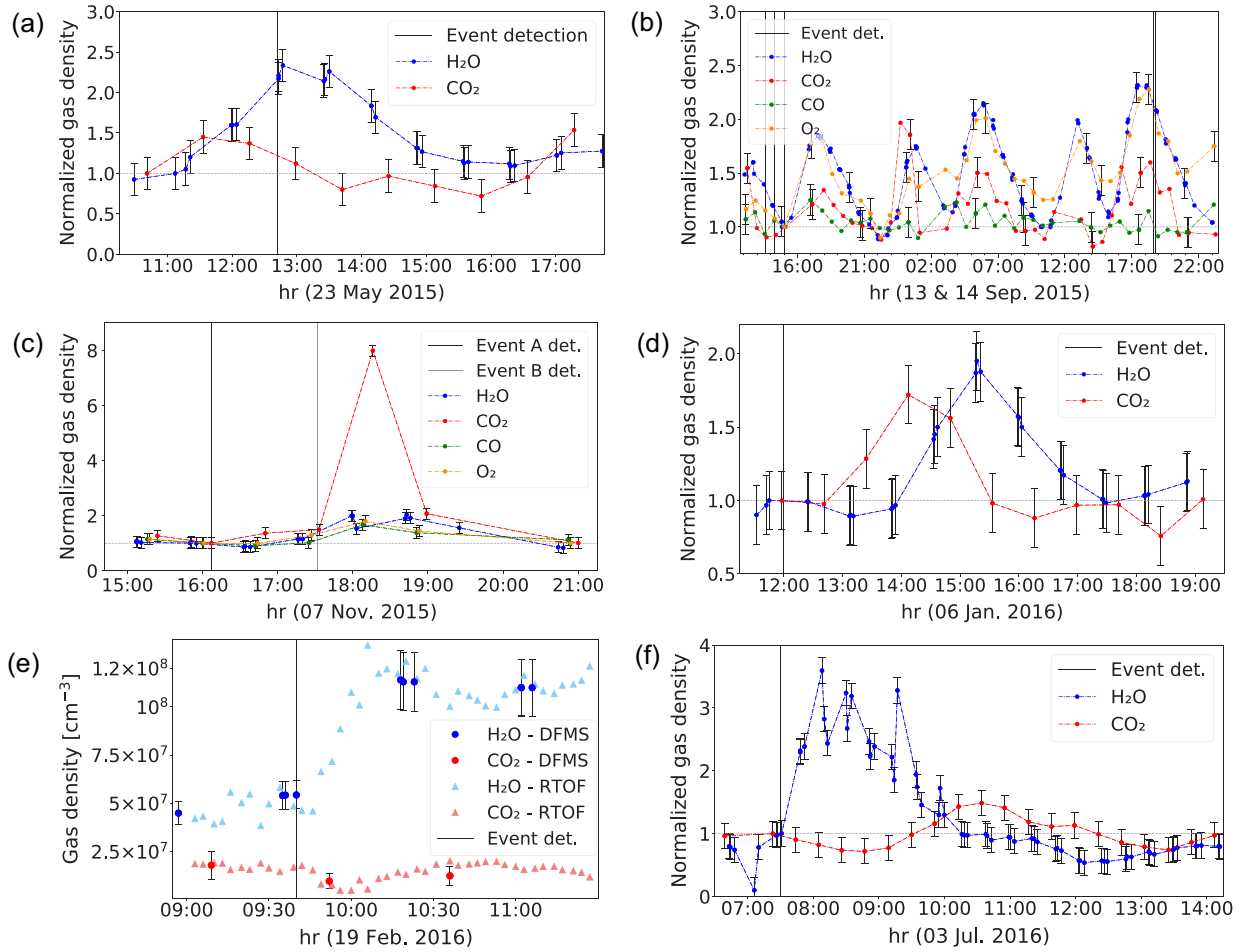
Figure 6. Gas densities of H_2O and CO_2 normalized to their quiescent coma levels during the outbursts of (a) 2015 May 23, (b) 2015 September 13 and 14, (c) 2015 November 7, (d) 2016 January 6, and (f) 2016 July 3 measured with ROSINA/DFMS. Panel (e) represents the absolute gas densities of H_2O and CO_2 for the outburst observed on 2016 February 19 measured with both the ROSINA/DFMS and the ROSINA/RTOF. The absolute densities are displayed in panel (e) to underline that both instruments acquired the same absolute results and no normalization or instrument effect occurred. Error bars show uncertainties of the DFMS measurements. In panel (b), uncertainties are only displayed on every 15th data point for H_2O and on every 5th data point for the other volatiles to improve readability. RTOF uncertainties are not shown because they are of the order of the symbols. The vertical lines represent the times when the dust events have initially been detected by the *Rosetta* cameras (the dust events could have started up to 5 to 30 min before). The grey horizontal lines show the quiescent level of the normalized data.

at a cliff collapse was on 2015 September 14 (#33 in Vincent et al. 2016a), showing a 15 per cent increase in water density compared to CO_2 and a twofold increase compared to CO (Fig. 6b). This event has already been investigated with the *Rosetta* Visible InfraRed Thermal Imaging Spectrometer (VIRTIS) (Bockelée-Morvan et al. 2017) where the authors stated that no large increase of H_2O and CO_2 has been measured but very small grains or agglomerates should be present. They suggested an excess signal of organic species and hydrocarbons where our results show an increase of CH_3OH by about 50 per cent, aligning with their results. Unfortunately, ROSINA measurements are unavailable for the event on 2015 July 10 (#1 in Vincent et al. 2016a), described as an additional cliff collapse event by Pajola et al. (2017). Thus, while most summer fireworks events showed enhancements in highly volatile species, particularly CO_2, cliff collapse events also occurred during this period, marked by slight increases in the water signal.

The spacecraft trajectory determined when the ROSINA instruments were able to measure above an outburst source region. Hence, illumination or local time during the observation are purely defined by the spacecraft trajectory and no conclusion can be drawn from

whether or not the measurements were taken above an illuminated surface. However, ROSINA measures the gas cloud ejected during the event after its travel and dispersion, so that the conditions at the time of the observations only depend on the conditions at the time of the dust event and on the dynamics of the gas cloud, not on the instantaneous conditions at the time of the observation. The spacecraft was mostly on a terminator orbit with a phase angle of $90°$. Consequently, although the spacecraft's position and viewing geometry do not permit a measurement of the immediate outburst gas and a smear-out of inhomogeneities due to the large distance of the spacecraft to the comet's surface is expected, ROSINA is still able to investigate the composition of the outgassing of the source regions and their surrounding areas both before, during, and after the dust event.

3.2 Other outbursts

Besides the outbursts described in Vincent et al. (2016a), a few other outburst events have been detected on 67P during the *Rosetta* mission. Table 1 provides a list of these events, including their

estimated source location on the nucleus, and whether or not they were detected by the ROSINA instruments. The first reported event (Tubiana et al. 2015) occurred when the *Rosetta* spacecraft was too far from the comet for ROSINA to detect volatile signals above the spacecraft background (Schläppi et al. 2010), and during the second event (Knollenberg et al. 2016), the ROSINA instruments were not operating.

Feldman et al. (2016) examined outbursts occurring between 2015 May and July using the Alice far-UV spectrograph. These events were unrelated to the summer fireworks and were not detected in the visible wavelength range captured by the other *Rosetta* cameras. Unfortunately, *Rosetta* was mostly above the less active Northern hemisphere and the outburst source locations for these events remain unknown. Nevertheless, the event on 2015 May 23 showed peaks in the relative abundance of different volatiles detected by DFMS (Fig. 6a), with a rapid increase in H_2O observed just 8 min after detection by Alice (Feldman et al. 2016). The enhancement of H_2O relative to CO_2 and CO was $\times 10$ and $\times 4.5$, respectively. The O_2 levels also increased together with H_2O. Considerable amounts of H_2O and notably high densities of O_2 compared to the quiescent level were also reported by Feldman et al. (2016), indicating that the event on 2015 May 23 was driven by H_2O sublimation.

The events on 2015 July 10 and 2015 August 10, as described in Pajola et al. (2017) and Rinaldi et al. (2018), respectively, were not observed because DFMS was not operated during that period. Outbursts on 2015 September 13 and 14 were observed by VIRTIS (Bockelée-Morvan et al. 2017; Rinaldi et al. 2018). The researchers concluded that the outburst measurements could be attributed to the presence of very small ice particles. While the CO signal measured with DFMS remained relatively constant, the signatures of H_2O, CO_2, and O_2 increased slightly. There was no significant enhancement of H_2O relative to CO_2, with only a twofold increase in H_2O relative to CO (Fig. 6b). O_2 closely followed the H_2O signal, as explained by the association of these two molecules (Rubin et al. 2023).

Lin et al. (2017) studied additional outbursts during the summer fireworks phase, alongside those in Vincent et al. (2016a). Unfortunately, the source locations of these outbursts remain unknown and the mass spectrometers of ROSINA were inactive from 2015 September 23 to 30 due to large cometary distances, missing a substantial portion of these events.

Noonan et al. (2021) investigated two outbursts (A and B) occurring on 2015 November 7 (A: 16:07 UTC, B: 17:32 UTC), and determined their source locations. The gas composition during the events was captured by DFMS measurements (Fig. 6c). Outburst A did not show significant signal changes. However, outburst B exhibited a notable increase in CO_2 with only a marginal increase in H_2O. No DFMS data were available after 19:30 UTC. The gas enhancement ratio of approximately $\times 8$ for CO_2 to H_2O aligns with the findings of the summer 2015 outbursts and supports the highly volatile-dominated nature of outburst B as proposed by Noonan et al. (2021).

A well-documented outburst took place on 2016 February 19, and was extensively observed by multiple *Rosetta* instruments (Grün et al. 2016). The source of the outburst was identified in the Atum region, near a steep cliff, where thermal stress, fracture mechanics, and gravity possibly triggered a landslide, exposing fresh ice to direct sunlight and triggering the release of gas and dust. Both ROSINA/RTOF and ROSINA/DFMS instruments were operated during that time and observed a notable increase in H_2O accompanied by a more or less stable CO_2 signal (Fig. 6e), indicating

a water-driven outburst with a density enhancement of $\times 2$ for water compared to CO_2. The H_2O signal rapidly increased and remained high during the analysed time period, which aligns with observations by the MIRO instrument of the gas surrounding *Rosetta* (Grün et al. 2016).

On 2016 July 3, a distinct outburst took place in the Imhotep region's circular Basin F, which was observed by multiple *Rosetta* instruments (Agarwal et al. 2017). The outburst occurred during local sunrise and resulted in the formation of a 10-metre-sized dust-free icy patch on the surface. Data from ROSINA/DFMS revealed a significant increase in H_2O following the event, with short spikes reaching up to 3.5 times the quiescent level (Fig. 6f). Including a time shift due to different velocities of the gas and the dust, this is consistent with the GIADA data (Agarwal et al. 2017). The density enhancements of water relative to CO_2 and CO were $\times 2.2$ and $\times 1.5$, respectively.

Additionally, a smaller but similar dust plume was observed by Agarwal et al. (2017) on 2016 January 6, near the source region of the 2016 July event, shortly after the local sunrise, suggesting the south-western walls of the circular depressions in the Imhotep Basin F as preferred location for morning outbursts. The DFMS data showed that the H_2O density increased more than the CO_2 by a factor of 1.6 with a shift in time of about one hour, suggesting a water-driven event (Fig. 6d). The analysis of both outbursts was limited to a short-term analysis due to limited coverage.

The analysis of published outburst events reveals a clear distinction between water-dominated and CO_2-dominated events. Most of the events, excluding the summer 2015 period, were primarily driven by water (Table 1). Notably, the event B (Noonan et al. 2021) on 2015 November 7 stands out as a CO_2-dominated outburst occurring outside the summer 2015 period. The distinct driving mechanisms may be associated with different conditions at the source regions. Water-dominated events mostly occurred outside the most active surface areas in terms of surface emission rates (Läuter et al. 2019) or below cliffs, while the CO_2-dominated event on 2015 November 7 occurred in a source region with multiple documented events (Vincent et al. 2016a). These findings highlight the diversity and complexity of outburst dynamics.

4 DISCUSSION

The ROSINA study of 45 outbursts on 67P shows two distinct groups of events: water-driven and CO_2-driven outbursts. These groups also exhibit a different temporal evolution. The water-driven events showed rapid changes in the coma composition, enhancing the density of H_2O more than that of other coma constituents for only a few hours. In contrast, the CO_2-driven group of events (summer fireworks and event B of 2015 November 7) displayed a slow increase even before the event was observed by the *Rosetta* cameras in the form of a bright dust jet lasting only a few minutes, and an even slower subsequent decrease of CO_2 compared to H_2O in the coma above the source region, lasting for several days. Thus, the coma composition at the distance of *Rosetta* changes much more slowly than the observed dust ejection for the same events.

We find that several highly volatile species such as CO_2, CO, and alkanes have been largely enhanced during the CO_2-driven gas outbursts. CO_2 being the most abundant molecule after H_2O (Rubin et al. 2019), its enhancement during these events is most significant. The clear distinction in coma composition during the outbursts as well as their different temporal behaviour leads to the conclusion that these groups of events are triggered by two different mechanisms.
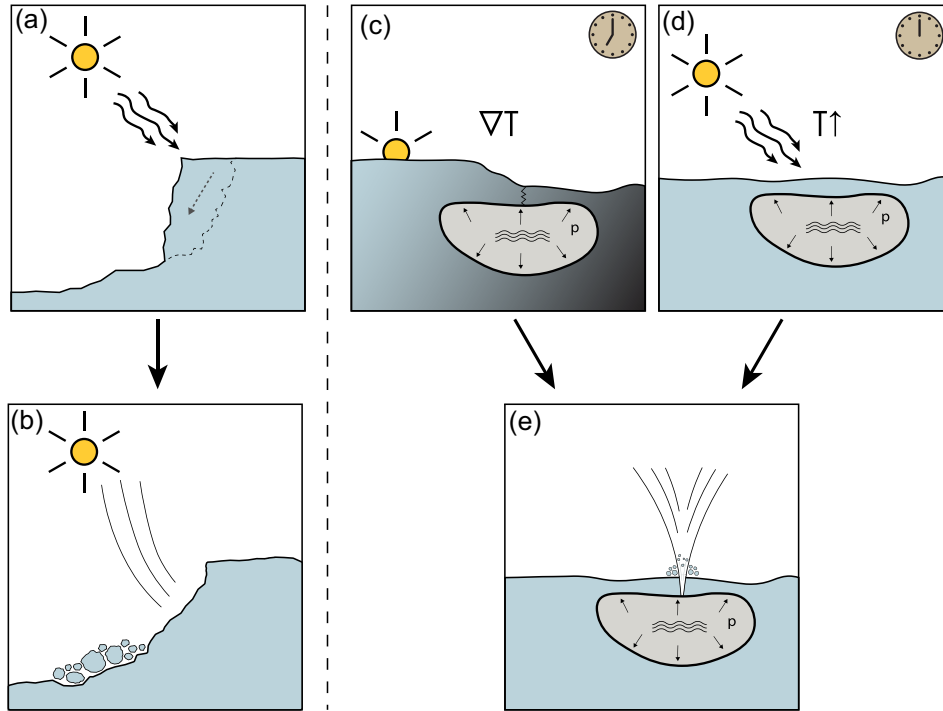
Figure 7. Schematics of outburst trigger mechanisms: (1) Cliff collapse: (a) Solar illumination heats up a cliff that collapses due to thermal formation of small cracks. The collapse releases dust from the surface seen as an outburst in the visible range of the cameras. (b) After the collapse, freshly exposed water ice sublimates and the released gas can be measured by the *Rosetta* instruments. (2) Gas pockets: (c) A large temperature gradient due to the local sunrise induces cracks where subsurface pressure pockets containing volatiles can release their pressurized gas leading to an outburst. (d) The high temperature at local noon heats up the surface and subsurface. This increases the pressure in the gas pockets until the pressure is high enough to overcome the tensile strength of the surface inducing an outburst. (e) When the surface cracks are large enough or the pressure has been increased enough as shown in (c) and (d), the pressurized gas pockets violently release dust and gas. Panels (c)–(e) only show the triggering mechanism of the event and do not display the continuous outgassing before and after the CO_2-driven outbursts.

Earlier studies proposed three main outburst trigger mechanisms:

(i) High-pressure pockets of highly volatile species below the surface layers (e.g. Belton et al. 2013; Agarwal et al. 2017; Bockelée-Morvan et al. 2022).

(ii) Collapse of cliffs (e.g. Vincent et al. 2016a; Pajola et al. 2017).

(iii) Amorphous-to-crystalline phase transition of water (e.g. Agarwal et al. 2017).

Agarwal et al. (2017) proposed that the transition of water from amorphous to crystalline ice might induce a sublimation rate similar to the measured dust production rate. This would only be true for pure water ice. However, pure water ice is neither observed in interstellar clouds, nor on the ice mantles on interstellar dust grains, which are believed to be the source of the ices in cometary nuclei. Interstellar water ices contain substantial amounts of impurities including CO_2, CO, and CH_4 (e.g. Crovisier 1999; Boogert, Gerakines & Whittet 2015). In a non-pure water ice mixture with more than 2 per cent impurities, as expected for a comet, the transition from amorphous to crystalline ice has been demonstrated to be endothermic (Kouchi & Sirono 2001). These authors also state that an endothermic crystallization suppresses outbursts.

Contrarily, Prialnik & Jewitt (2022) propose that a burst of crystallization could be initiated by a heat wave propagating from the insolated comet surface to the crystalline–amorphous ice boundary, provided it carries sufficient energy to raise the local temperature to the crystallization point. Once this occurs and the boundary has moved deeper into the nucleus, later heat waves from the surface are too weak to rekindle crystallization when reaching the boundary, leading to a quiescent period. Sublimation then causes the surface to recede from the crystalline–amorphous ice boundary until a new burst of crystallization occurs. This, in turn, affects the time span to the next spurt of crystallization. Hence, this process is particularly relevant for new comets with amorphous ice close to the surface, active beyond the distance where ice sublimation controls cometary activity, as observed in comets C/2003 A2 (Gleason) by Meech et al. (2009) or C/2017 K2 (PANSTARRS) by Jewitt et al. (2017) at 11.5 and 23 au, respectively. Another possible scenario is that crystallization and gas confinement occur together, leading to an outburst (Samarasinha 2001). Despite several observations, simulations, and laboratory studies of cometary outbursts, Prialnik & Jewitt (2022) note that direct evidence for the role of amorphous ice in comets remains elusive due to its nature and burial below the surface in evolved comets like 67P. Consequently more laboratory work to determine the thermophysical properties of amorphous and crystalline ices, especially when loaded with other volatiles, is needed to confirm if the transition from amorphous to crystalline water ice remains a plausible outburst trigger mechanism.

Alternatively, pockets of volatiles below the devolatilized surface layer might build up pressure until they overcome the tensile strength of the surface above and cracks start to appear in the surface layer. The cracks might be formed by a large temperature gradient due to the local sunrise combined with the small thermal inertia of the comet's surface (Fig. 7c). Another possibility is that the cracks slowly progress until the pressure in the gas pockets is high enough (due to the high noon temperature; Fig. 7d) for a bursting to occur. All the gas is released and drags along some of the surrounding

non-volatile material (Fig. 7e). Notably, both of these processes are not on/off processes, i.e. gas may be seeping out from smaller cracks already before the big outburst, which is consistent with the findings of our analysis, as a slow increase in highly volatile species has been measured already before the dust ejection occurred. This combined process can be understood similarly to a pressure cooker where some steam gets released through the safety valve before the pressure increases too much. At a certain pressure, the small seeping cracks cannot release enough gas to maintain the pressure below the pocket's tensile strength and an explosive event occurs, which is what *Rosetta*'s cameras registered as the dust feature of the outburst. If the thermophysical properties of amorphous and crystalline ices support the theory that their transition might trigger outburst events, it would also be plausible that this effect could be responsible for the cracks initiating the bursting of gas pockets. It is prudent to note, that the CO_2-dominated events occurred around generally more active areas on the comet nucleus. Hence, the increase long before the outburst has been observed by the cameras, and long after it ceased (Fig. 3), might also be supported by a generally more active source region. Additionally, the bursting of a pressure pocket not only releases the confined gas but also exposes areas of fresh ice that sublimates and hence increases the densities of H_2O as well as of the volatiles associated with the water ice (Rubin et al. 2023) for a longer time than the dust outburst observed with the cameras, leading to a prolonged enhancement of CO_2 and other highly volatile species.

To have gas pockets, where a significant gas pressure builds up, the porous structure of the comet interior has to be sealed. A possible mechanism could be refreezing of CO_2. It is known that for 67P, CO_2 sublimates long after water stops sublimating on the outbound leg of the comet's orbit (Läuter et al. 2019) from areas, which by then are no longer exposed to sunlight. Such an extended orbital frost cycle of CO_2 has been proposed by Rubin et al. (2023). Due to low gravity, the sublimating gas will be dispersed in all directions, not only upwards, but sideways and downwards. In the interior, it will eventually encounter colder temperatures, where it can refreeze, creating a volatile enriched ice layer (Prialnik & Jewitt 2022). This mechanism may not only explain the extended orbital frost cycle but also presents a potential diurnal day-to-night refreezing process, leading to the creation of gas pockets in regions dominated by highly volatile species over short time-scales.

Laboratory experiments for Martian conditions show that CO_2 is deposited in the form of ice slabs or crystals depending on temperature and pressure (Portyankina et al. 2019). In the experiments, the ice layer conformally coats all the surfaces of the cooling plate, draping even protruding elements. Although the conditions in the comet are different from the laboratory experiments (pressure, temperature, porosity, composition, size), a similar process could happen, where CO_2 covers the porous material with an impermeable layer, which has a considerable tensile strength, enough to confine a gas pocket at elevated pressure (Prialnik & Jewitt 2022). Laboratory experiments show that an ultimate CO_2 ice tensile strength of ∼2–6 MPa is reached (Kaufmann et al. 2020). This strength is in agreement with the suggested ∼2 MPa tensile strength of water ice under Martian conditions used in earlier studies (Mellon 1997). On 67P, once the surface areas come into summer again, a similar effect could take place even though the cometary surface is mostly covered by dust and not transparent as seen on Mars. None the less, CO_2 starts to sublimate from the top building up pressure in the pocket. Eventually the surface layer will crack due to the buildup of the inside pressure and/or due to erosion of the surface layer.

The possibility of gas pockets has already been discussed for comet 9P/Tempel (Belton et al. 2008). The authors concluded that this mechanism will lead to the formation of a small pit or depression and potentially exposes fresh and highly volatile material that will continue to sublime (Belton et al. 2013). A similar result has been discussed for comet 67P in the case of the Imhotep outburst observed in 2015 February (Knollenberg et al. 2016).

The source regions of the summer fireworks are situated near morphological boundaries, clustered into three primary regions displaying irregularities in contrast to the generally flat morphology of the Southern hemisphere. This seems to indicate a link between morphology and outbursts (Vincent et al. 2016a). These source regions are notably rich in CO_2. Nine activity areas, encompassing the most active surface elements contributing to 50 per cent of the total emission, were identified by Läuter et al. (2019), with most summer fireworks sources located in these high-activity areas. The same authors also demonstrated that these areas remain CO_2-rich throughout the mission. This raises the question whether the here described enhancement of highly volatile species might be a result of the overall CO_2-rich outgassing behaviour of the comet's Southern hemisphere.

Läuter et al. (2019) utilized the same ROSINA data set as presented here. However, their results are based on data averaged over specific periods and their results are presented for three intervals with data averaged over 50 d for the data before and after perihelion and even 100 d for data around perihelion. This methodology averages over short-lived events like outbursts, potentially impacting the identification of Southern active sources by Läuter et al. (2019). None the less, the presence of the same CO_2-rich areas long before and after perihelion, where outbursts occurred, suggests that this weighting of the outburst signal did not distort the overall picture of high-activity areas presented by Läuter et al. (2019). This is supported by the steady increase in the overall CO_2/H_2O ratio seen in our data when the spacecraft was in Southern latitudes (see quiescent coma behaviour of the signal in Figs A1 and A2).

The source locations of H_2O and O_2 follow the subsolar latitude and correlate with each other. Notably, H_2O displayed high activity in these regions during summer 2015, while only a few summer fireworks events showed an increase in H_2O compared to highly volatile species. The high and confined activity of H_2O in the same areas as CO_2 around perihelion would decrease the CO_2/H_2O ratio if it was merely an artefact of the generally CO_2-rich outgassing of the outburst source regions.

A typical event is the one on 2015 July 28 (#5 in Vincent et al. 2016a). It is located in high-activity area 3 in Läuter et al. (2019), which was not among the most CO_2-rich areas during perihelion. Nevertheless, the CO_2/H_2O ratio exhibited a pattern for this event as for events in more CO_2-active areas, and comparable enhancements in 67P's coma were determined (Fig. 1 and Table A1).

When comparing the CO emission of the nine high-activity areas presented in Läuter et al. (2019) to the emission of H_2O, CO_2, and O_2, the CO signal is much more distributed and diluted during perihelion compared to the very localized outgassing of the other species. Thus, one would expect that the ratio of CO to H_2O should not increase much when measured in one of the high-activity areas. Nevertheless, our results show an enhancement of CO. In summary, most summer fireworks outburst events originate from generally CO_2-rich sources, however, they are clearly contributing an additional amount of highly volatile species to the overall outgassing behaviour.

The events described in Noonan et al. (2021) have been located close to the summer fireworks' source regions. The ROSINA/DFMS data also show gas density enhancements for CO_2 and CO. The

volatile enhancement in the outburst gas supports the scenario of pockets of gas in those areas and shows that the related activity is independent of the subsolar latitude (Läuter et al. 2019).

Unlike the events described by Noonan et al. (2021) and most of the events in Vincent et al. (2016a), the events reported by Grün et al. (2016), Agarwal et al. (2017), and the first event investigated by Feldman et al. (2016) show a large increase in H_2O with no CO_2 or CO enhancement. These outbursts showed short-lived H_2O enhancements, suggesting that they have been triggered by a different mechanism than the CO_2 outbursts – most likely by a cliff collapse as could be shown by Pajola et al. (2017). This conclusion is supported by the suggestion by Grün et al. (2016) that thermal stress in the surface material may have triggered a landslide (Fig. 7a) that exposed fresh H_2O ice to direct solar illumination (Fig. 7b).

It is prudent to note that the available set of outburst events is relatively small and confined to one individual comet. Furthermore, the measurement conditions, while corrected to the best of our abilities, varied for each event. The significant disparities observed in the distribution and temporal evolution of activity on cometary nuclei suggest that the heliocentric evolution of activity can be highly individual for each comet (Marschall et al. 2020a), and generalizations patterns might be misleading. Moreover, given the large temporal differences between the outburst behaviour of the dust and the gas components, only their combined analysis provides a comprehensive view of the nature of the outbursts and their trigger mechanisms.

5 CONCLUSION

We conclude that outbursts appear due to two different mechanisms depending on their source location and associated surface topography. These mechanisms can be differentiated by their respective and distinct outgassing behaviour. Landslides or cliff collapses may cause an outburst event which would most probably be a water-driven event as fresh water ice would be found closer to the surface than, e.g. CO_2, and hence would be more exposed to solar illumination. However, most reported outburst events during the perihelion passage correlate with an increased composition of highly volatile species, especially CO_2, and generally higher activity source regions (Läuter et al. 2019). These events are most likely triggered by break-up of subsurface pockets of volatiles when the pressure inside overcomes the tensile strength of the cavity boundary layers. From these pockets, gas may seep out from smaller cracks already before the dust outburst as a slow increase in highly volatile species has been measured already before the dust ejection occurred. The surface and near-surface layers of the comet exhibit a general depletion in more volatile species, such as CO_2. This depletion may provide an explanation for the distinction between events dominated by H_2O and CO_2. H_2O events typically arise from occurrences in the surface or near-surface layers, while CO_2 events are likely to originate from greater depths where CO_2 did not yet find a way to evaporate freely. This distinction may highlight the influence of depth on the compositional characteristics of cometary outburst events. Nevertheless, in both cases, the exposure of fresh material implies extended enhanced outgassing after the dust outburst already ceased.

The unique temporal coverage of 67P's outgassing throughout the *Rosetta* mission has allowed a thorough analysis of the evolution and composition of the outgassing for more than 40 outburst events. The results indicate that the composition is linked to different trigger mechanisms, one related to cliff collapse, where water dominates the outgassing pattern, and pressure cooker-like ruptures of subsurface pockets, which are characterized by a strong enhancement of highly volatile species such as CO_2. These results are relevant for understanding changes in the outgassing patterns of comets from ground-based and *in situ* observations. However, open questions remain, such as the direct correlation between the different temporal behaviour of the dust and gas components of outbursts and the heliocentric distance dependence of the different triggering mechanisms for outbursts. Answering these questions requires further laboratory studies, sophisticated numerical simulations, observations, and missions monitoring a comet with high-resolution instruments over a prolonged time to gain a full understanding of cometary outbursts.

DATA AVAILABILITY

All *Rosetta*/ROSINA data are available through the NASA Planetary Data System (PDS) and ESA's Planetary Science Archive (PSA).

REFERENCES

Agarwal J. et al., 2017, MNRAS, 469, s606
Altwegg K. et al., 2015, Science, 347, 1261952
Altwegg K., Balsiger H., Fuselier S. A., 2019, ARA&A, 57, 113
Altwegg K. et al., 2020, Nat. Astron., 4, 533
Altwegg K. et al., 2022, MNRAS, 516, 3900
Balsiger H. et al., 2007, Space Sci. Rev., 128, 745
Belton M. J. S., Feldman P. D., A'Hearn M. F., Carcich B., 2008, Icarus, 198, 189
Belton M. J. S. et al., 2013, Icarus, 222, 477
Bieler A. et al., 2015, Nature, 526, 678
Biver N. et al., 2019, A&A, 630, A19
Bockelée-Morvan D. et al., 2017, MNRAS, 469, S443
Bockelée-Morvan D. et al., 2022, A&A, 664, A95
Boogert A. C. A., Gerakines P. A., Whittet D. C. B., 2015, ARA&A, 53, 541
Calmonte U. et al., 2016, MNRAS, 462, S253
Combi M. R., Tenishev V. M., Rubin M., Fougere N., Gombosi T. I., 2012, ApJ, 749, 29
Crovisier J., 1999, in Greenberg J. M., Li A., eds, NATO Advanced Study Institute (ASI) Series C Vol. 523, Formation and Evolution of Solids in Space. Springer, Dordrecht, p. 389
De Keyser J. et al., 2019, Int. J. Mass Spect., 446, 116232
Feldman P. D. et al., 2016, ApJ, 825, L8
Fulle M., Altobelli N., Buratti B., Choukroun M., Fulchignoni M., Grün E., Taylor M. G. G. T., Weissman P., 2016, MNRAS, 462, S2
Gasc S. et al., 2017, Planet. Space Sci., 135, 64
Graf S. et al., 2004, J. Geophys. Res. (Planets), 109, E07S08
Grün E. et al., 2016, MNRAS, 462, S220
Hänni N., Altwegg K., Combi M., Fuselier S. A., De Keyser J., Rubin M., Wampfler S. F., 2022, Nat. Commun., 13, 3639
Hoang M. et al., 2019, A&A, 630, A33

Hughes D. W., 1975, Q. J. R. Astron. Soc., 16, 410

Hughes D. W., 1991, in Newburn R. L., Jr., Neugebauer M., Rahe J., eds, Astrophysics and Space Science Library Vol. 167, IAU Colloq. 116: Comets in the post-Halley era. Springer, Dordrecht, p. 825

Ip W.-H. et al., 2016, EGU General Assembly Conference Abstracts, EGU General Assembly Conference Abstracts, EPSC2016

Ishiguro M. et al., 2014, ApJ, 787, 55

Ishiguro M. et al., 2016, AJ, 152, 169

Jewitt D., Hui M.-T., Mutchler M., Weaver H., Li J., Agarwal J., 2017, ApJ, 847, L19

Kaufmann E., Attree N., Bradwell T., Hagermann A., 2020, J. Geophys. Res. (Planets), 125, e06217

Knollenberg J. et al., 2016, A&A, 596, A89

Kouchi A., Sirono S.-i., 2001, Geophys. Res. Let., 28, 827

Läuter M., Kramer T., Rubin M., Altwegg K., 2019, MNRAS, 483, 852

Le Roy L. et al., 2015, A&A, 583, A1

Lin Z.-Y., 2023, PASJ, 75, 462

Lin Z.-Y., Lin C.-S., Ip W.-H., Lara L. M., 2009, AJ, 138, 625

Lin Z.-Y. et al., 2017, MNRAS, 469, S731

Marschall R. et al., 2020a, Space Sci. Rev., 216, 130

Marschall R., Liao Y., Thomas N., Wu J.-S., 2020b, Icarus, 346, 113742

Meech K. J. et al., 2009, Icarus, 201, 719

Mellon M. T., 1997, J. Geophys. Res., 102, 25617

Noonan J. W. et al., 2021, AJ, 162, 4

Pajola M. et al., 2017, Nat. Astron., 1, 0092

Portyankina G., Merrison J., Iversen J. J., Yoldi Z., Hansen C. J., Aye K. M., Pommerol A., Thomas N., 2019, Icarus, 322, 210

Prialnik D., Jewitt D., 2022, preprint (arXiv:2209.05907)

Prialnik D., A'Hearn M. F., Meech K. J., 2008, MNRAS, 388, L20

Rinaldi G. et al., 2018, MNRAS, 481, 1235

Rubin M. et al., 2019, MNRAS, 489, 594

Rubin M. et al., 2023, MNRAS, 526, 4209

Samarasinha N. H., 2001, Icarus, 154, 540

Scherer S. et al., 2006, Int. J. Mass Spect., 251, 73

Schläppi B. et al., 2010, J. Geophys. Res. (Space Physics), 115, A12313

Schmitt M. I. et al., 2017, MNRAS, 469, S380

Shinnaka Y., Ootsubo T., Kawakita H., Yamaguchi M., Honda M., Watanabe J.-i., 2018, AJ, 156, 242

Sierks H. et al., 2015, Science, 347, aaa1044

Skorov Y. V., Rezac L., Hartogh P., Bazilevsky A. T., Keller H. U., 2016, A&A, 593, A76

Steckloff J., Melosh H. J., 2016, AAS/Division for Planetary Sciences Meeting Abstracts #48, 206.06

Thomas N. et al., 2019, Space Sci. Rev., 215, 47

Tubiana C. et al., 2015, A&A, 573, A62

Tzou C.-Y., 2017, PhD thesis. University of Bern, Switzerland

Vincent J. B. et al., 2016a, MNRAS, 462, S184

Vincent J. B. et al., 2016b, A&A, 587, A14

Wierzchos K., Womack M., 2020, AJ, 159, 136

APPENDIX A: EXTENDED DATA
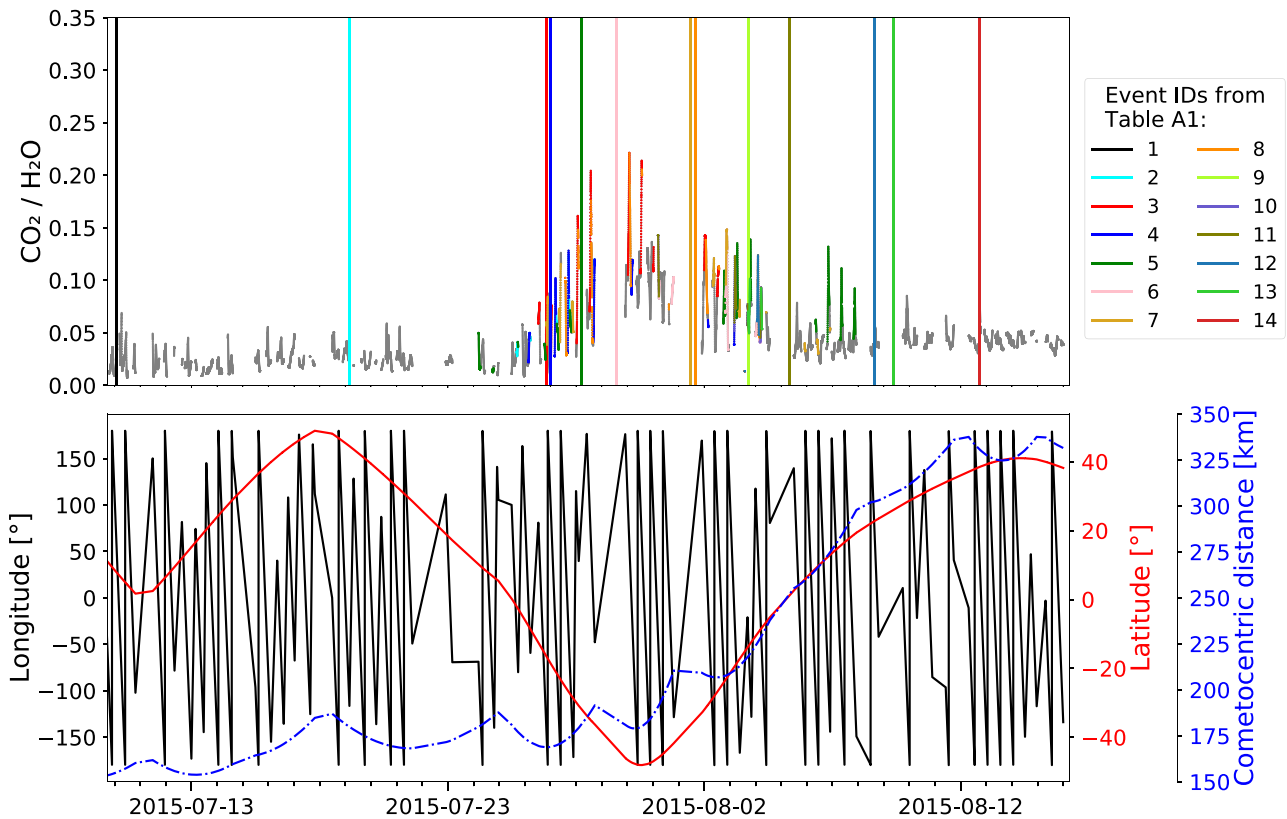
Figure A1. Top panel: Ion count ratio for CO_2 relative to H_2O for the first part of the summer fireworks from 2015 July 10 to August 17. The coloured data points show measurements taken when the *Rosetta* sub-spacecraft longitude and latitude was within $25°$ from the identified source location of the respective event. The vertical lines show the times when the events were detected by one of *Rosetta*'s cameras (Event IDs according to Vincent et al. 2016a, see Table A1). Bottom panel: Spacecraft longitude, latitude, and distance to the comet for the same time frame.
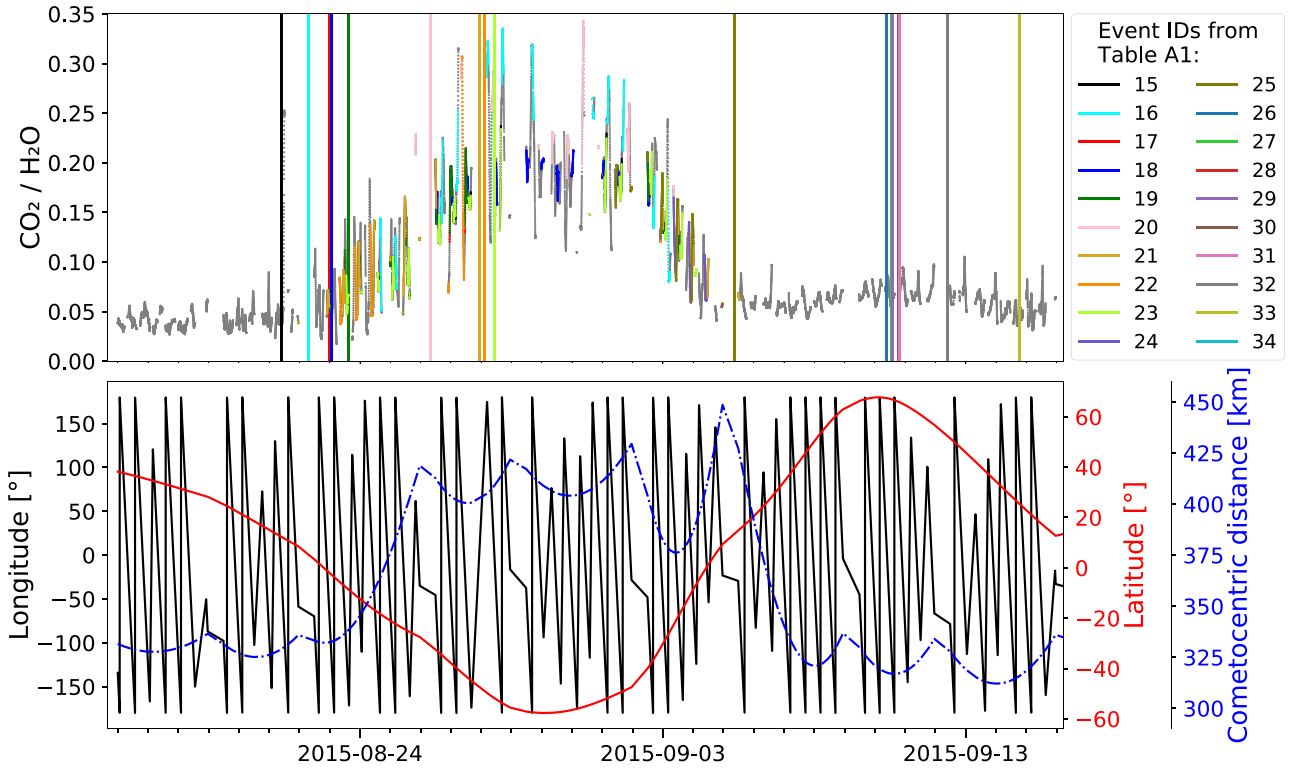
Figure A2. The same as in Fig. A1 but for the second part of the summer fireworks from 2015 August 16 to 2015 September 16.
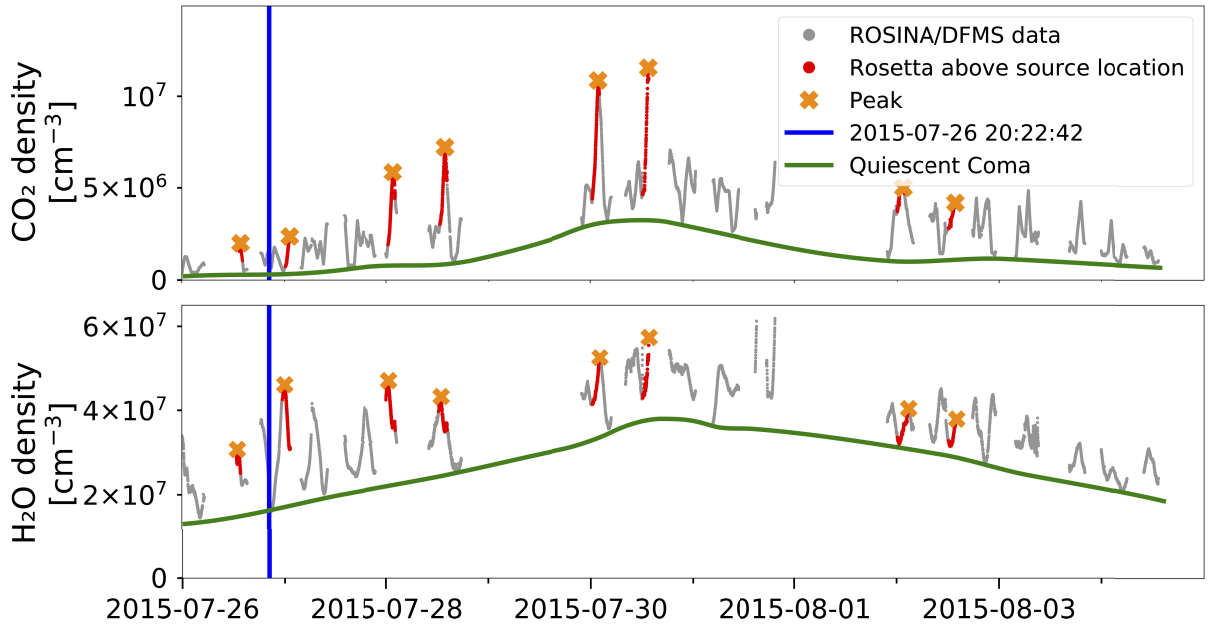
Figure A3. Typical ROSINA/DFMS densities of CO_2 and H_2O from 2015 July 26 until 2015 August 4 to show the analysis approach for the event on 2015 July 26, 20:22 UTC. To calculate the enhancement each time *Rosetta* was above the source location (i.e. for all phases with red measurement points), the peak value (orange cross) of CO_2 has been selected and corrected to the quiescent coma (green line). The same has been done for H_2O for the time when CO_2 showed its maximum. The peak values are slightly shifted in time due to the mass scanning nature of the instrument. These time shifts, on the order of a few minutes, do not affect the enhancement calculations as the time-scales associated to passing above the active region is substantially longer. The enhancement is then calculated based on equation (1).

Table A1. Gas density enhancements in the coma of 67P of the summer fireworks events (Vincent et al. 2016a). Most of these events were CO_2 dominated, density enhancements <1 mean that H_2O was the most dominant driver for the considered event and the enhancement of H_2O would be the inverse of the given value. Uncertainties on the enhancements are ± 18 per cent, mostly due to instrument calibration uncertainties (Le Roy et al. 2015; Calmonte et al. 2016).

ID	Event Date (UTC)	cdist (km)	Lat (deg)	Lon (deg)	Time since sunrise (h)	CO_2	CO	O_2	H_2S	NH_3	CH_4	H_2CO	C_2H_6	CH_3OH	HCN	C_3H_8
1	2015-07-10T02:10:18	155	74	200	3.62	No observation										
2	2015-07-19T03:38:09	180	−24	296	3.09	8.3	1.8	0.7	3.1	2.3	3.3	3.4	9.8	3.7	4.0	13.5
3	2015-07-26T20:22:42	168	−36	75	11.16	19.7	7.1	0.7	4.0	2.7	9.7	6.1	26.9	12.2	8.8	18.5
4	2015-07-27T00:14:29	168	−31	333	10.24	21.8	12.1	1.6	4.3	6.6	8.2	3.5	26.2	9.6	7.8	22.6
5	2015-07-28T05:23:43	181	−4	264	10.73	6.9	2.2	0.9	2.7	2.6	3.1	3.4	7.3	3.5	3.3	13.5
6	2015-07-29T13:25:28	186	−37	300	3.69	18.8	5.3	0.8	3.8	4.2	3.5	2.9	21.2	9.6	3.6	20.6
7	2015-08-01T10:53:15	214	−12	196	10.51	13.8	5.7	0.8	2.1	3.2	3.5	2.9	17.7	7.7	6.4	12.4
8	2015-08-01T15:44:50	211	−28	34	10.68	16.1	4.9	2.2	4.1	2.5	4.5	3.5	13.6	6.1	4.5	12.9
9	2015-08-03T17:27:03	218	−75	303	9.97	2.2	0.4	1.1	1.4	0.9	0.7	0.3	2.3	1.1	1.2	N/A
10	2015-08-05T07:25:05	253	−25	320	10.32	23.9	6.7	2.3	4.3	4.8	3.6	3.4	16.6	6.2	6.3	16.7
11	2015-08-05T08:05:15	253	−23	318	10.47	Indistinguishable from #10										
12	2015-08-08T15:21:48	303	−30	51	3.41	14.0	4.9	2.2	2.8	2.5	4.5	3.5	13.6	6.1	4.5	12.9
13	2015-08-09T09:15:14	304	−30	298	9.94	6.9	6.2	2.3	1.9	2.2	3.3	3.3	15.5	5.9	5.7	16.4
14	2015-08-12T17:21:20	332	−30	58	3.32	0.6	0.2	0.2	0.6	0.7	2.5	0.4	1.6	0.7	0.3	N/A
15	2015-08-21T09:44:53	330	−32	227	10.61	4.1	1.7	1.1	1.2	2.1	1.3	1.8	4.9	2.1	2.4	5.4
16	2015-08-22T06:47:04	336	−40	168	3.15	24.3	14.0	1.8	4.2	5.4	7.8	6.2	20.5	7.9	5.1	23.3
17	2015-08-22T23:46:21	334	−25	316	11.60	18.7	6.8	2.1	1.7	2.3	4.8	1.2	19.1	4.4	4.8	13.6
18	2015-08-23T01:39:38	334	−53	292	3.33	4.3	3.3	2.1	1.6	6.9	4.8	3.5	6.6	2.1	3.8	4.2
19	2015-08-23T15:12:48	340	−23	314	3.28	Indistinguishable from #17										
20	2015-08-26T07:51:04	417	−41	42	10.43	15.1	11.1	1.9	2.3	1.7	6.7	2.5	9.8	4.7	4.4	10.6
21	2015-08-27T22:58:04	404	−8	321	10.76	18.7	4.5	0.7	1.8	2.5	1.6	1.5	16.8	2.0	5.9	13.6
22	2015-08-28T02:29:21	404	−21	24	3.07	5.1	1.7	1.0	1.3	1.4	1.6	1.8	4.2	2.1	1.6	5.0
23	2015-08-28T10:10:57	410	−31	229	3.63	4.1	1.0	2.6	2.9	2.5	1.3	4.5	2.5	1.8	5.7	5.4
24	2015-09-05T08:50:02	436	−15	26	11.63	No observation										
25	2015-09-05T09:00:02	435	−31	330	3.14	No observation										
26	2015-09-10T08:59:49	318	−25	67	3.33	No enhancements detected										
27	2015-09-10T13:06:14	317	−23	292	3.22	No enhancements detected										
28	2015-09-10T13:36:14	317	−21	307	3.46	No enhancements detected										
29	2015-09-10T14:11:15	317	−15	10	11.07	No enhancements detected										
30	2015-09-10T18:57:41	318	−15	10	9.93	No enhancements detected										
31	2015-09-10T19:27:41	318	−30	286	10.82	No enhancements detected										
32	2015-09-12T09:41:00	330	−12	318	11.44	1.0	1.1	0.8	1.2	1.7	1.7	2.0	1.1	0.5	0.7	N/A
33	2015-09-14T18:47:00	316	−25	198	3.36	0.9	0.4	1.0	1.5	0.8	0.6	0.8	1.1	1.5	0.4	N/A
34	2015-09-26T12:03:32	818	−40	307	10.47	DFMS Turned off										

This paper has been typeset from a TeX/LaTeX file prepared by the author.

Comet Interceptor

<div style="text-align: right; font-size: 3em;">4</div>

One of the unexpected findings from the Rosetta mission was the significant modification of the nucleus surface, either through erosion or fall back of material, due to the repeated close perihelion passages of 67P (Thomas, 2020). This underscores the importance of investigating more pristine comets that have not experienced multiple cycles of activity. This is the goal of ESA's F-class mission Comet Interceptor, which will be the first mission to visit a Dynamically New Comet (DNC, see Box 4.1). F-class missions must take under a decade from selection to launch and weigh less than 1000 kg.

> **Box 4.1: Dynamically New Comet (DNC)**
>
> Dynamically New Comets (DNCs) represent a subset of long-period comets originating from the Oort cloud, situated at the farthest reaches of our Solar System (refer to Box 1.1). Historically, comet exploration missions have predominantly targeted short-period comets, such as 67P, which originate from the nearer Kuiper Belt region and have experienced multiple perihelion passages resulting in significant thermal processing. In contrast, Oort cloud objects were ejected into the remote Oort cloud during the early phases of Solar System formation and have remained largely unaltered since. These comets serve as remarkably pristine remnants from the epoch of planetary formation. Upon their re-entry into the inner Solar System, they become some of the most brightest comets due to solar heating (Snodgrass and Jones, 2019).
>
> Although these comets are interesting to observe with telescopes due to their brightness, exploring them with a spacecraft is challenging. The main difficulty is that they are usually discovered only a few months to a few years before they reach their closest point to the Sun. After that, they quickly travel back to the outer Solar System and do not return for tens of thousands of years. This short time window makes it hard to plan, build, and launch a space mission to study them *in situ* (Jones et al., 2024).

4.1 Mission Background

The significant achievements of missions like Giotto and Rosetta in exploring comets are undeniable. However, these pioneering efforts have primarily focused on SPCs that have undergone repeated close approaches to the Sun. Consequently, these

comets have experienced surface compositional changes, morphological alterations, and the accumulation of thick dust layers on their nuclei. Over 800 SPCs, with more than 470 being numbered and observed at multiple perihelion passages, are known. In contrast, there are over three thousand long-period comets (LPCs) observed in history, with many being dynamically new, having traversed the inner Solar System only once and retaining their original characteristics. Unfortunately, no LPC or DNC has been explored by a space mission or studied in detail with modern instrumentation due to the unpredictability of their apparition, which makes intensive coordinated observing campaigns difficult to organise. Yet, critical questions about the formation and evolution of the early Solar System remain unanswered. Understanding the extent to which cometary bombardment contributed to delivering water to Earth's oceans and how early organic material from comets influenced the emergence of life are paramount. To address these questions, we need insights into the chemical inventory of the early Solar System, which can only be obtained by studying pristine or nearly pristine material in LPCs and, particularly, DNCs. Key information, including isotope abundances and the D/H ratio, is essential. Comet Interceptor aims to contribute to this understanding by providing an inventory of organic molecules and other species relevant to prebiotic chemistry, shedding light on the role comets played in the rapid emergence of life on Earth after its formation (Jones et al., 2024).
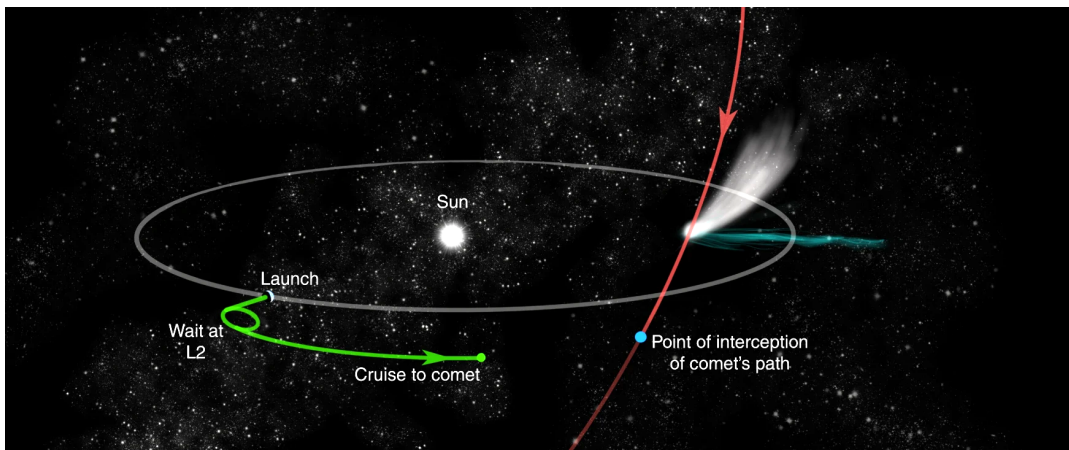
FIGURE 4.1: Sketch of the mission phases of Comet Interceptor (not to scale). The spacecraft is launched from Earth and remains at L2 until a suitable comet is discovered. It then departs on an interplanetary cruise to reach the comet at the optimal time and location. The smaller probes are released just before reaching the comet. The trajectory of the spacecraft is shown in green and the comet's orbit is drawn in red. Credit: Snodgrass and Jones (2019).

The relatively brief interval between the discovery of LPCs and their perihelion passage renders the prospect of launching a space mission to intercept them unfeasible. To overcome this issue, Comet Interceptor proposes a unique approach: instead of a direct launch to a predetermined target, it introduces a flexible spacecraft designed to encounter an unknown target at an unspecified future time. Taking advantage of the Sun-Earth Lagrange Point 2 (L2, see Box 4.2), the spacecraft awaits the discovery of a suitable comet (Figure 4.1). Additionally, advances in ground-based astronomy, facilitated by major new survey telescope facilities, enhance the feasibility of this approach. Routine monitoring of objects beyond the orbit of Uranus are expected to yield numerous comet discoveries with several years of lead time before perihelion. Upon the discovery of a new comet, the orbit of the body will be analysed to determine whether it is a potential candidate for a future encounter for

Comet Interceptor. Once a suitable target is identified, a detailed trajectory analysis will ascertain the precise departure and encounter circumstances. The waiting phase at L2 will be succeeded by a cruise phase and the comet fly-by, with a maximum total mission duration of six years. Comet Interceptor will share the launcher with the ARIEL mission, which is scheduled for 2029 and will also target the L2 point (Jones et al., 2024).

Box 4.2: Sun-Earth Lagrange Points

Lagrange Points are strategic locations in space where gravitational forces between two celestial bodies (e.g., Sun and Earth), create regions of enhanced attraction and repulsion. These points serve as advantageous parking spots for spacecraft, allowing them to maintain a fixed position with minimal fuel consumption. The five Lagrange Points represent locations where a smaller mass can orbit between two larger masses, striking a delicate balance of gravitational pull and centripetal force, as addressed by Joseph-Louis Lagrange (Lagrange, 1892).

Among the Lagrange Points, three (L1, L2, and L3) are unstable, aligning with the line connecting the two large masses. The stable Lagrange Points (L4 and L5) form the apex of equilateral triangles with the large masses at their vertices. Earth's L1 point, offering an uninterrupted view of the Sun, currently hosts the Solar and Heliospheric Observatory Satellite (SOHO). The L2 point, home to the James Webb Space Telescope (JWST), is ideal for astronomy due to its proximity to Earth, favourable communication conditions, solar power accessibility, and an unobstructed view of deep space. Despite their benefits, L1 and L2 exhibit instability in under a month, necessitating regular satellite course and attitude corrections. Figure 4.2 illustrates the Lagrange points for the Sun-Earth system, highlighting the required satellite course corrections with an orange ellipse.
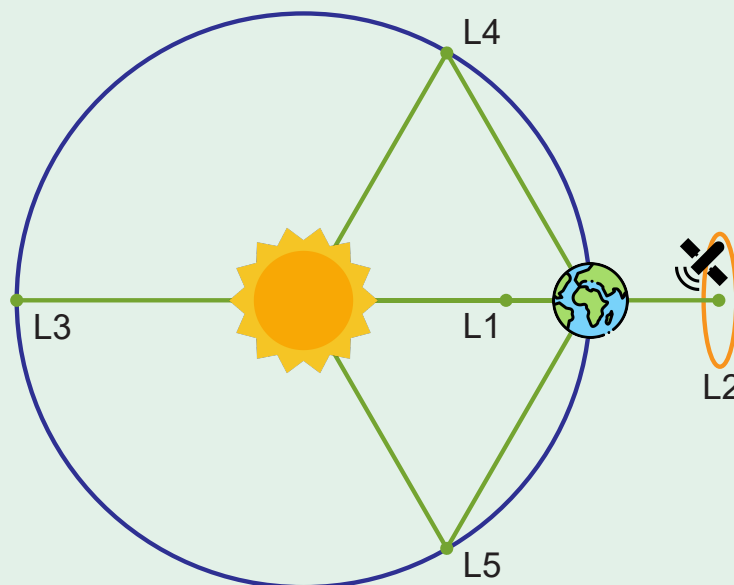

FIGURE 4.2: Lagrange points in the Sun–Earth system (not to scale).

Comet Interceptor, besides offering a unique encounter with near-pristine material from the Solar System's formation at a nominal closest approach distance of 1000 km, introduces an unprecedented capability. It will deploy two sub-probes, B1 and B2, following distinct trajectories at approximately 850 km and 400 km from the comet (Figure 4.3). This innovative approach ensures simultaneous, spatially resolved information on the 3-dimensional properties of the target comet (Jones et al., 2024).
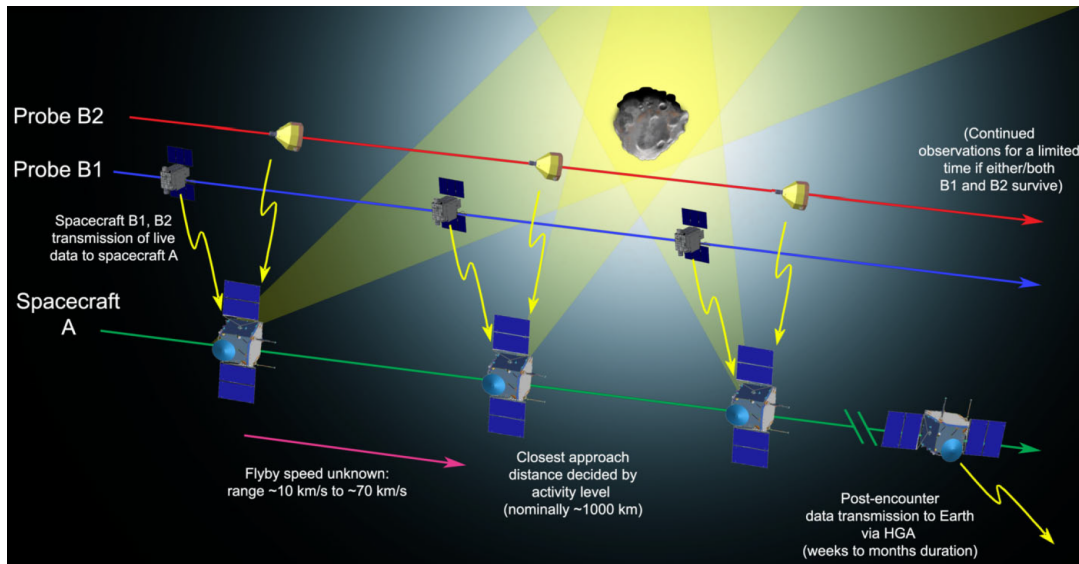
FIGURE 4.3: Illustration of the proposed encounter sequence for Comet Interceptor (not to scale). The green, blue, and red lines represent the trajectories of the three spacecraft (SC): A, B1 and B2, respectively. SC A follows the furthest trajectory from the nucleus, performing remote sensing and in situ observations and receiving data from SC B1 and B2, which follow closer trajectories. After the encounter, SC A transmits stored data from all three platforms to Earth. Credit: Jones et al. (2024).

4.1.1 Science Objectives

The primary goal of the Comet Interceptor mission is to enhance the comprehension of comet diversity. By studying a relatively unprocessed comet that has been active for only a few years, the mission provides a unique view of comet evolution, differing from comets that have frequently approached the Sun. Simultaneous multi-point measurements during a multi-spacecraft flyby will offer significant insights into the 3D structure of the coma, including its composition, chemical reactions, and interactions with the nucleus and solar wind. This will help explore the complex, dynamic structure of interacting plasma and fields across various spatial scales (Snodgrass and Jones, 2019).

The mission definition study report breaks down the mission goals into two themes and respective questions (Jones et al., 2022, 2024):

- Comet Nucleus Science - What are the surface composition, shape, morphology, and structure of the target object?
- Comet Environment Science - What is the composition of the gas and dust in the coma, its connection to the nucleus activity, and the nature of its interaction with the solar wind?

This brings up the science objectives described in Table 4.1.

TABLE 4.1: Science objectives of Comet Interceptor (Jones et al., 2022, 2024).

Science Theme	Science Objective
Comet Nucleus Science	Characterise the target shape, size, and rotation state.
	Characterise the target morphology.
	Assess the bulk composition of the target surface.
Comet Environment Science	Characterise and map the bulk neutral composition of the coma and determine any local structure and connection to the nucleus.
	Determine the isotopic composition of the coma.
	Characterise the structure of the dust environment of the coma and determine any connection to the nucleus.
	Characterise the coma dust properties, including reflectance and polarimetric properties, and determine dust fluxes.
	Determine motion and evolution of ion rays and other coma and tail features including dust and gas.
	Characterise the plasma environment around the target, determine any resulting boundaries, and assess energy, mass and momentum transfer.

4.1.2 Payload

To achieve the scientific objectives, several payloads were selected for Comet Interceptor. In the Nucleus Theme, Spacecraft A's Comet Camera (CoCa) will analyse the nucleus's physical properties with high-resolution images. The Modular InfraRed Molecules and Ices Sensor (MIRMIS) will contribute infrared spectra for compositional and thermal insights. Support comes from the Narrow Angle Camera (NAC) on Probe B1 and the Optical Periscope Imager for Comet (OPIC) on Probe B2, providing different perspectives, stereo views, and increased surface coverage during the flyby.

For the Comet Environment Theme, the Mass Analyser for Neutrals in a Coma (MANiaC) will measure coma composition and isotopic ratios *in situ*. MIRMIS will perform gas composition measurements remotely. Additionally, the Hydrogen Imager (HI) on Probe B1 monitors cometary water production over months. The dust spatial distribution is explored from various viewpoints by CoCa on Spacecraft A, the Wide Angle Camera (WAC) on Probe B1, OPIC, and the all-sky imager Entire Visible Sky (EnVisS) on Probe B1. EnVisS, with polarimetric measurements, and the Dust Impact Sensor and Counter (DISC), part of the Dust, Fields, and Plasma (DFP) instrument, contribute to understanding dust properties and mass distribution. Investigating cometary plasma and its interaction with the solar wind involves simultaneous magnetic field measurements by magnetometers on all three spacecraft and plasma properties determination through three spectrometers in the DFP and an ion mass spectrometer in the Plasma Suite (PS) onboard Probe B1. A summary of the payloads is given in Table 4.2 and a graphic representation of the three spacecraft including their respective instruments is given in Figure 4.4. The European Space Agency (ESA) will provide spacecrafts A and B2, while spacecraft B1 will be delivered by the Japan Aerospace Exploration Agency (JAXA) (Jones et al., 2024).

TABLE 4.2: Comet Interceptor spacecraft and instruments.

Spacecraft	Instrument	Description
A (ESA)	CoCa	Visible/NIR Imager
	MIRMIS	NIR/Thermal IR Spectral Imager
	MANiaC	Mass Spectrometer
	DFP-A	Dust, Fields & Plasma
B1 (JAXA)	HI	Lyman-Alpha Hydrogen Imager
	PS	Plasma Suite
	NAC/WAC	Telescopic & Wide Angle Camera
B2 (ESA)	EnVisS	All-Sky Multispectral Visible Imager
	OPIC	Visible/NIR Imager
	DFP-B2	Dust, Fields & Plasma
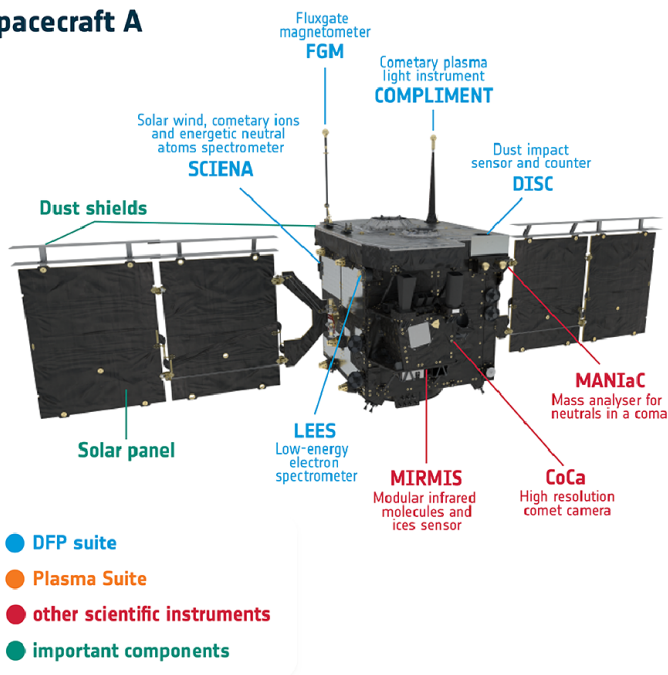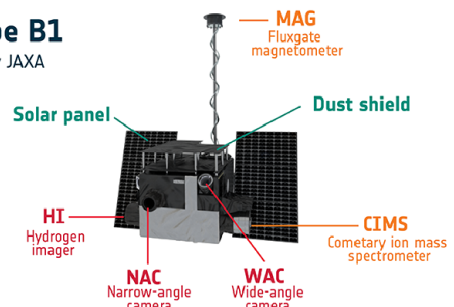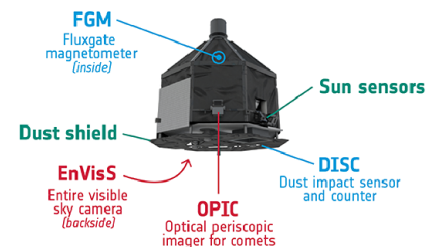
FIGURE 4.4: Overview of the three Comet Interceptor spacecraft and their respective instrument suites. Credit: ESA / ATG.

4.2 Mass Analyser for Neutrals in a Coma (MANiaC)

The payload Mass Analyser for Neutrals in a Coma (MANiaC), situated on spacecraft A, is dedicated to the *in situ* measurement of the neutral gas coma and is built in a consortium lead by the University of Bern. MANiaC comprises two instruments, a time-of-flight mass spectrometer (Sensor Head Unit, SHU) and a Bayard-Alpert style neutral density gauge (NDG), and the Electronic Unit (ELU) (Figure 4.5). The mass spectrometer determines the relative abundances of cometary volatiles, while the neutral density gauge measures the total gas density. These combined measurements allow the determination of absolute densities of volatile species during the fly-by, enabling the derivation of elemental, molecular, and isotope abundances of the

gases. The ELU includes all the electronics to drive the SHU and NDG and serves as interface to the spacecraft. The primary scientific objectives of MANiaC, as outlined in Section 4.1.1, address the following science questions (Jones et al., 2022, 2024):

- Measure the abundance of the major volatiles H_2O, CO, and CO_2 in the coma to study the target's activity and associated gas mass loss rate. These results may also be combined and compared with Earth-based remote sensing observations.

- Derive the D/H ratio in H_2O to study the origin of water ice in the comet and investigate potential sources of water on Earth.

- Evaluate the amounts of other key volatiles, such as O_2 and other highly volatile species, and compare them to the respective abundances found in SPCs studied earlier.

- Obtain an inventory of (complex) organic molecules and other species possibly relevant in prebiotic chemistry.

- Measure the composition and abundance of icy grains if some are collected in the instrument.
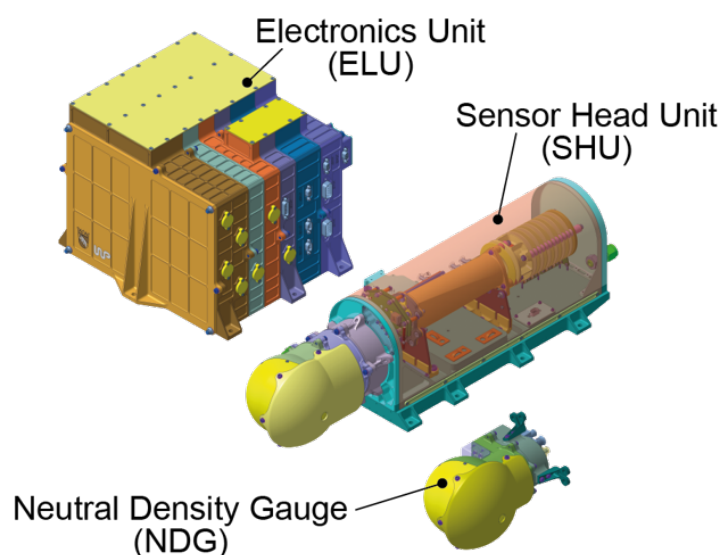
FIGURE 4.5: 3D overview of MANiaC consisting of a time-of-flight mass spectrometer (SHU), the Neutral Density Gauge (NDG), and the Electronic Unit (ELU). The long axis of the SHU corresponds to 470 mm as a reference. Only the antechamber spheres of both the NDG and the SHU (yellow caps) are exposed to the gas and dust flow of the coma and are covered by dedicated dust shields. The rest is enclosed and protected inside the spacecraft.

The spacecraft's relative fly-by velocity is estimated to be in the range of 10 to 70 km/s, significantly exceeding the neutral gas speed of the comet's outgassing ($\sim$1 km/s). Therefore, MANiaC will be positioned on the spacecraft with the aperture always directed along the relative motion of the spacecraft. To accommodate the broad range of potential fly-by velocities, both the SHU and the NDG are equipped with antechambers for the thermalisation of the incoming gas. Afterwards, the neutral gas entering the ion source undergoes ionisation upon impact with 70 eV electrons emitted by a hot filament. In the NDG, the resulting ions are measured as a current by a sensitive electrometer, proportional to the gas density inside the antechamber and, consequently, the surrounding coma. In the SHU, the newly formed ions experience

acceleration through a sharp extraction voltage pulse into the drift section. After passing the reflectron (an opposing electric field), the ions traverse the drift section again before reaching the MCP detector. The uniform energy provided by the voltage pulse enables conversion of their arrival time on the detector into a mass-to-charge ratio.

After the extraction pulse, a rapid Analogue-to-Digital Converter (ADC) records 65'536 channels of 0.5 ns each, corresponding to a time-of-flight range from 0 to 32.768 μs and a mass-to-charge range from m/z 1 up to m/z 1000. Extractions occur every 100 μs (i.e., 10 kHz extraction), and the channels are summed to a variable number of extractions, resulting in a single mass-per-charge spectrum. The SHU is designed for a mass resolution of m/Δm > 800 for a mass-to-charge greater than 40 and a density range of 10^{-6} to 10^{-14} mbar. Both the SHU and the NDG, with a density range of 10^{-5} to 10^{-11} mbar, will operate continuously during the fly-by, using measurements far from the comet to assess spacecraft background. An adjustable measurement integration time between 0.05 and 100 s per spectrum is implemented for the SHU to accommodate the wide range of potential fly-by velocities. The NDG's read-out interval is fixed to 0.05 s (20 Hz). After the fly-by, locally stored mass spectra will be compressed for later transmission to Earth.

The following subsections discuss the working principles of the SHU and the NDG in more detail.

4.2.1 SHU Working Principle

As already mentioned in Section 2.1, a MS is an instrument that is able to analyse a gas stream of ions, sorting them according to their m/z and producing a mass spectrum from which the relative abundances of the components present can be determined. It always consists of an inlet system for inserting the probe, an ion source component, one or several analysers to separate the ions based on their m/z, a detector to measure the quantity of ions exiting the analyser, and a processor to process the data to create the mass spectrum. A technical drawing of the SHU is shown in Appendix A in Figure A.2. The entrance hole of the antechamber works as inlet system of the SHU. As explained in Section 4.2, due to the high fly-by velocity, a thermalisation process needs to take place inside the antechamber to be able to measure the incoming gas stream. Details about the antechamber and its enhancement calculations including laboratory measurements are described in Sections 5.1.3 and 5.1.4. After thermalisation the neutral gas enters the ion source and undergoes ionisation.

Electron Ionisation

The initial step in analysing a compound within a MS involves generating gas-phase ions from the neutral molecules in the mixture. Ions can be positively or negatively charged atoms or molecules. This ion generation process, known as ionisation, allows a MS to measure both cations (positive ions) and anions (negative ions). Ionising a molecule requires a specific ionisation energy, with the first ionisation energy being the minimum energy needed to remove an electron from a neutral molecule in its ground state, resulting in an ion also in its ground state. Subsequent ionisation energies, for further electron removal from higher orbitals, are known as second ionisation energy and so forth. The unit of energy for ionisation is typically measured in electronvolts (eV), where 1 eV corresponds to the energy gained by an electron passing through a potential difference of 1 V. Ionisation energies for the majority of elements typically fall within the range of 7 to 15 eV (Gross, 2017).

Several techniques are available for ionising molecules. For gas-phase samples, electron ionisation (EI) is a highly effective method. In this technique, an electron beam is directed perpendicular to the stream of molecules using a hot filament. Electrons emitted from the cathodic filament travel towards the anode, acting as the electron collector. The electrons hitting the molecules need at least the minimum ionisation energy for ionising the molecules, but the likelihood of a full transfer of this energy during the collision is low, resulting in a small ionisation efficiency. However, increasing the electron energy quickly boosts the ionisation efficiency. Fortunately, the highest ionisation efficiency for most molecules occurs at around 70 eV. Consequently, many instruments, including MANiaC, use a potential difference of 70 eV. This provides electrons with a kinetic energy, generally sufficient for ionising most molecules, albeit causing extensive fragmentation. While fragmentation complicates spectrum analysis, it also yields valuable structural information for interpreting unknown analytes. At an ionisation energy of 70 eV, the majority of ions are singly charged, with m/z corresponding to the molecule's mass. Therefore, in this work, the charge state will only be mentioned if it differs from $z = 1$.

Figure 4.6 provides a simplified depiction of an ion source region.
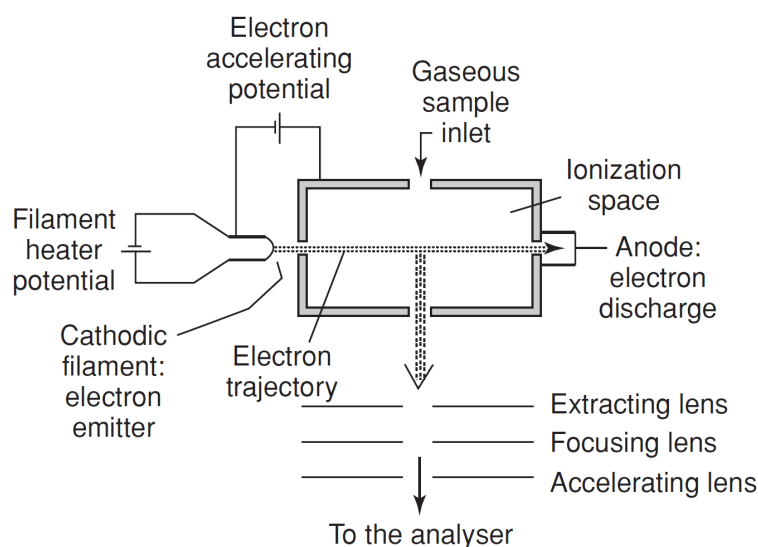
FIGURE 4.6: Schematic of electron ionisation source: The cathodic filament emits electrons, which are accelerated by the electron acceleration potential. These electrons interact with the gaseous sample, causing ionisation. The ionised sample is then extracted from the ion source by the extracting lens and guided through corresponding lenses, where it is further focused and accelerated until reaching the analyser. Source: de Hoffmann and Stroobant (2007), reproduced with permission from Wiley.

Time-of-Flight Analyser

In a Time-of-Flight mass spectrometer (TOF-MS) ions are ejected from the ion source region in bundles. This is typically achieved by transiently applying the necessary potentials on the source focusing lenses, creating a pulsed extraction voltage. Subsequently, the ions are then accelerated towards the flight tube by a potential difference applied between an electrode and the extraction grid, ensuring they acquire the same kinetic energy before entering the field-free region, also known as the drift region. Due to their varying masses, the ions undergo separation based on their velocities,

eventually reaching the detector located at the opposite end of the flight tube. Mass-to-charge ratios are determined by measuring the flight time required for ions to traverse the field-free region between the source and the detector. Specifically, as an ion with mass m and total charge z is accelerated by a potential V_s before leaving the source, its electric potential energy E_{el} is transformed into kinetic energy E_k:

$$E_k = \frac{mv^2}{2} = zV_s = E_{el} \quad \Rightarrow v = \sqrt{\frac{2zV_s}{m}}. \tag{4.1}$$

After initial acceleration, the ion travels in a straight line at a constant velocity towards the detector. Therefore, the time t required to traverse the distance L before reaching the detector is expressed as:

$$t = L\sqrt{\frac{m}{2zV_s}} = \frac{L}{\sqrt{2V_s}} \cdot \sqrt{\frac{m}{z}}. \tag{4.2}$$

Equation (4.2) illustrates that m/z can be determined from a measurement of t, with L and V_s being constants. It also indicates that, under equal conditions, the lower the mass of an ion, the faster it will reach the detector.

In principle, the upper mass range of a TOF instrument has no limit, except for the speed of data transfer and the data storage capacity of the computer. However, it interferes with the subsequent extraction, hence a larger mass range is traded with lower sensitivity. Another advantage of these instruments is their high transmission efficiency, leading to very high sensitivity. All ions are generated in a short time span, and temporal separation enables directing all of them towards the detector. Therefore, all formed ions are, in principle, analysed. The analysis speed of TOF analysers is very fast, and a spectrum over a broad mass range can be obtained in microseconds. Hence, it is theoretically possible to produce several thousand TOF mass spectra in one second over a very wide mass range. However, in practice, for most applications, the small number of ions detected in each individual spectrum is insufficient to provide the required precision of mass or abundance measurement, and thus individual mass spectra need to be summed up.

Another interesting characteristic of the TOF analyser lies in its relatively simple mass calibration with only two reference points needed. As in all mass spectrometers, the TOF-MS requires a calibration equation to relate and convert the physical property (i.e., the flight time) that is measured to a mass-to-charge value. As already mentioned, the flight time of an ion is directly related to its mass and hence, $m/z = At^2$, with A a constant to be defined. However, this is the ideal equation, and in practice, there are delays from the time the control electronics send a start pulse to the time that high voltage is present on the pulser grid and a delay from the time an ion reaches the front surface of the ion detector until the signal generated by that ion is digitised by the acquisition electronics. Hence, the true flight time cannot be measured and it is necessary to correct the measured time, t_m, by subtracting the sum of delays, referred to as t_0. Correcting for this, one can write the mass-to-charge ratio as:

$$m/z = A(t_m - t_0)^2, \tag{4.3}$$

where A and t_0 are constants and t_m is the measured time of the peak used for calibration. The two constants can be obtained by identifying at least two known species in the spectrum and solving the problem for the two unknown variables. As long as the two identified species are not too close together, a simple two-point calibration is usually accurate enough.

Reflectron Time-of-Flight Analyser

Due to random motion, the assumption that all produced ions have the same kinetic energy is not entirely accurate. Consequently, ions with slightly greater energy will possess a higher speed, arriving at the detector earlier than ions with lower kinetic energy, despite having the same mass. This phenomenon leads to peak broadening and a reduction in the instrument's mass resolution. To mitigate the impact of the random energy distribution in the TOF instrument and enhance resolution, an electrostatic reflector, also known as a reflectron, has been introduced. The reflectron functions as an ion mirror by deflecting ions and directing them back through the flight tube. The basic reflectron type, the single-stage reflectron, typically consists of a series of equally spaced grid electrodes or ring electrodes connected via a resistive network of equal-value resistors (de Hoffmann and Stroobant, 2007).

The reflectron is positioned behind the drift region, opposite to the ion source, with the detector placed on the source side of the ion mirror to capture ions after reflection. In the most common instrument geometry, the detector is off-axis concerning the initial direction of the ion beam. By adjusting the reflectron at a slight angle relative to the ions leaving the source, the detector can be positioned adjacent to the ion source, effectively doubling the flight path of the reflectron TOF (RTOF) compared to a linear TOF, thereby increasing the resolution.

More importantly, the reflectron corrects the initial kinetic energy dispersion of ions with the same m/z leaving the source. Ions with greater kinetic energy, and thus higher velocity, penetrate the reflectron more deeply than ions with lower kinetic energy. Consequently, faster ions spend more time in the reflectron and reach the detector at the same time as slower ions with the same m/z. Figure 4.7 shows a schematic representation of a TOF instrument equipped with a reflectron.
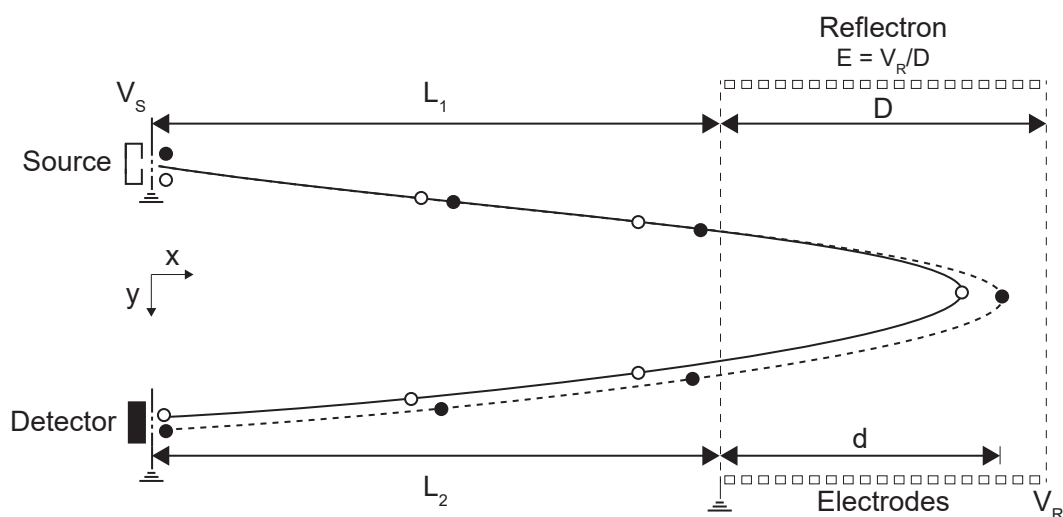
FIGURE 4.7: Schematic representation of a TOF instrument equipped with a reflectron. ● represent ions of a given mass with the correct kinetic energy, while ○ denotes ions of the same mass but with a kinetic energy that is too low. The latter reach the reflectron later but exit earlier with the same kinetic energy as before. Hence, with appropriately chosen voltages, path lengths and fields, both types of ions reach the detector simultaneously and an energy focusing can be achieved. The variables are defined in the main body of the text in this section. Source: de Hoffmann and Stroobant (2007), reproduced with permission from Wiley.

If the potential of the reflectron V_R with length D results in an electric field in the reflectron of $E = V_R/D$, an ion of charge z with kinetic energy E_k (from Equation (4.1)) will enter with a velocity v_{ix} and penetrate the reflectron to a depth d such that:

$$d = \frac{E_k}{zE} = \frac{zV_s}{zV_R/D} = \frac{V_sD}{V_R}. \tag{4.4}$$

The ions' speed along the x axis, v_x, will be zero at d, and its mean velocity into the reflectron will be equal to $v_{ix}/2$. The time needed to penetrate to a distance d will thus be:

$$t_d = \frac{d}{v_{ix}/2}. \tag{4.5}$$

The ion will be symmetrically repelled outside of the reflectron, so that its kinetic energy will be restored to the same absolute value as before, with the velocity in the opposite direction. The total flight length in the reflectron is thus $2d$, and the total time t_r in the reflectron is:

$$t_r = 2t_d = \frac{4d}{v_{ix}}. \tag{4.6}$$

The total flight length in the drift region is $L_1 + L_2$, with L_1 and L_2 the distances covered before and after the reflectron, respectively. Hence, the total time t in the drift region is:

$$t = \frac{L_1 + L_2}{v_{ix}}. \tag{4.7}$$

Finally, the total flight time is the sum of the flight time in the drift region and the reflectron:

$$t_{tot} = t + t_r = \frac{L_1 + L_2 + 4d}{v_{ix}} \stackrel{Eq. \ 4.1}{=} \sqrt{\frac{m}{z}} \frac{1}{\sqrt{2eV_s}} (L_1 + L_2 + 4d). \tag{4.8}$$

Assuming two ions of equal mass, one coming from the source with the correct kinetic energy E_k and the other with a kinetic energy E'_k, their ratio is defined as:

$$\frac{E'_k}{E_k} = a^2. \tag{4.9}$$

As a result, their velocities along the x-axis in the field-free area will differ,

$$v_x = \sqrt{\frac{2E_k}{m}} \quad \text{and} \quad v'_x = \sqrt{\frac{2E'_k}{m}} = \sqrt{\frac{2E_k a^2}{m}} = av_x, \tag{4.10}$$

leading to varying traversal times in the drift region for the total path $L = L_1 + L_2$

$$t = L/v_x \quad \text{and} \quad t' = L/v'_x = t/a. \tag{4.11}$$

Subsequently, the ions will penetrate into the reflectron to a depth d or d':

$$d = E_k/(zE) \quad \text{and} \quad d' = E'_k/(zE) = a^2 d, \tag{4.12}$$

with E the electric field in the reflectron region. The time spent by the ions in the reflectron is:

$$t_r = 4d/v_x \quad \text{and} \quad t'_r = 4d'/v'_x = 4ad/v_x = at_r. \tag{4.13}$$

Finally, the total flight time of both ions with the same *m/z* but having different kinetic energies will be the sum of the flight time in the drift region and the reflectron:

$$t_{tot} = t + t_r$$
$$t'_{tot} = t/a + at_r.$$

(4.14)

This means that if $a > 1$, the ion with an excess kinetic energy will have a shorter flight time out of the reflectron (t/a), but a longer one in the reflectron (at_r). The opposite holds for $a < 1$. The variations of the flight times thus compensate each other. A correct compensation, yielding the same total flight time for all ions sharing the same mass but having different kinetic energies, requires choosing the proper values for E, V_s, L_1 and L_2. A complete treatment would take into account the displacement along the y axis. However, in practice, the reflection angle is typically less than 2°, and its influence will be small.

4.2.2 Spectrum Analysis

Section 4.2.1 explains the process of applying a mass scale to the raw data, transforming the acquired time spectrum into a mass spectrum. The nature and structure of the analyte can then be deduced from the spectrum and the abundance of its ions. However, as few analytes exclusively generate one type of ion, most aggregates yield a non-trivial mass spectrum. Additionally, when multiple substances coexist in the analyte mixture, the analysis becomes considerably more intricate and necessitates a more in-depth investigation. Analysing such spectra is a skill that demands specific attention, particularly in the field of organic chemistry (e.g., Hänni et al., 2022). Some concepts used while analysing these more complex spectra, including fragmentation patterns, instrument sensitivity, isotope ratios, and mass resolution, are explained in this section.

Fragmentation Patterns

Fragmentation patterns constitute an integral aspect of mass spectrometry, referring to the generation of neutral or ionised single atoms or molecules (fragments) from the original neutral analyte (parent). The extent and nature of fragmentation depend on various factors, most importantly on the ionisation method of the instrument and the applied ionisation energy. The MANiaC SHU utilises electron ionisation to ionise its analyte (see Section 4.2.1). This method is known to induce extensive fragmentation, leading to complex fragmentation patterns. In contrast, softer ionisation methods often exhibit simpler patterns, characterised by a smaller number of fragments with lower abundances. However, each ionisation method has its limitations, making the electron ionisation method well-suited for space applications. An illustration of the fragmentation of methane is described in Figure 4.8.

The ionisation energy is another critical factor influencing fragmentation. It is expected that fragmentation will increase with electron energy. Nevertheless, a 70 eV ionisation, as used for the MANiaC SHU, is standard due to the broad efficiency maximum around this value for most organic compounds (see Section 4.2.1).

Fragmentation patterns can both positively and negatively impact evaluation. On one hand, additional peaks may obscure signals from other compounds that would otherwise be visible at the mass-to-charge ratio where the fragments emerge. This introduces uncertainty in overall abundance estimations, as not all fragments can be considered, and some may produce weak signals. Moreover, each supplementary

peak adds to the uncertainty associated with that peak. On the other hand, having literature references or calibration measurements with a pure compound enables the retrieval of the distinctive fragmentation pattern for a specific molecule, facilitating its identification. This is particularly valuable in organic chemistry, where molecules with the same atomic weight but distinct structures (i.e., structural isomers) often exhibit unique fragmentation patterns. This may serve as a molecular fingerprint, aiding the identification of compounds in a crowded spectrum and significantly enhancing the analysis. Box 4.3 describes the fragmentation pattern of methane and compares the results from SHU measurements with data from the database of the National Institute of Standards and Technology (NIST). This database provides access to mass spectral data, including fragmentation patterns for the electron ionisation method.

Box 4.3: Fragmentation Pattern of Methane (CH$_4$)

As an illustration of the fragmentation phenomena, we examine the fragmentation pattern of methane (CH$_4$). Methane (m/z 16) can undergo fragmentation into CH$_3$ (m/z 15), CH$_2$ (m/z 14), CH (m/z 13), C (m/z 12), and H (m/z 1) ions (as most ions formed are singly positive charged, the charge state will not be indicated in the following). Furthermore, both methane and its fragments may contain heavy isotopes of hydrogen and carbon, reflecting their natural abundances on Earth. Consequently, methane also exhibits a signal on m/z 17, attributable to the presence of ^{13}C, which constitutes approximately 1% of ^{12}C. The influence of deuterium (heavy hydrogen) can be neglected at this scale due to its negligible abundance.

Figure 4.8 compares the measured fragmentation pattern obtained with the SHU against the expected values sourced from the NIST database. It becomes evident that the SHU exhibits fewer fragmentation events than anticipated from the database. This deviation could possibly be an inherent instrumental effect. Typically, each mass spectrometer possesses unique characteristics determined by its geometry and ionisation methods, thereby necessitating derivation of sensitivity and fragmentation patterns through empirical measurements. Ideally, such assessments should be conducted using the flight model prior to launch (Le Roy et al., 2015) or the flight spare thereafter.
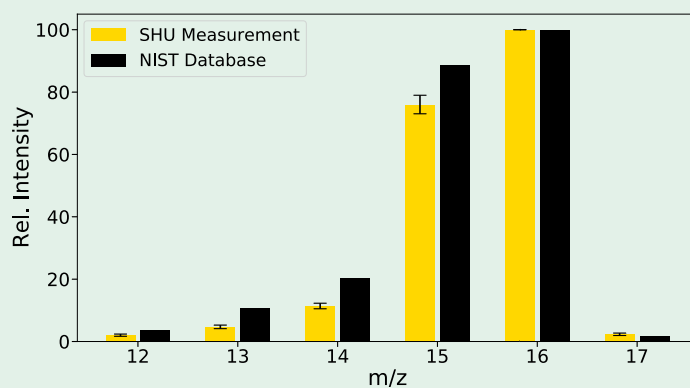

FIGURE 4.8: Fragmentation pattern of the SHU for methane (CH$_4$) compared to the NIST database (NIST Mass Spectrometry Data Center, 2023).

Instrument Sensitivity

Having determined the fragmentation pattern of a compound, the instrument's sensitivity to said compound can be determined. The fragmentation patterns are needed here for calculating the total ion yield detected by the instrument which is a necessity across different pressure levels. The sensitivity, denoted as S_{total}, is formulated as per Schuhmann (2020):

$$S_{total} = \frac{I_{ion}}{p \cdot I_{emission}}, \tag{4.15}$$

with S_{total} the sensitivity (cm^3/molecules), $I_{emission}$ the emission current (A), p the molecular density (cm^{-3}) and I_{ion} the detected ion current (A).

The molecular density p is approximated by dividing the pressure by the product of temperature and the Boltzmann constant. A pressure correction factor is applied due to the original pressure recordings being relative to nitrogen (refer to Appendix B). The total ion current, defined as the sum of ions detected during the calibration measurement of a compound, C_{ion}, multiplied by its elementary charge, q, yields the subsequent equation:

$$S_{total} = \frac{C_{ion} \cdot q}{p \cdot I_{emission}}. \tag{4.16}$$

In essence, the sensitivity is the total ion current detected by the MCP detector divided by the gas density. It thus quantifies the proportion of the sample detected relative to the total sample in the instrument. The so-called sensitivity factor is derived by comparing sensitivities at different pressure levels and is equal to the slope of the fit between these pressure levels.

Isotope Ratios

Many elements exist in nature as mixtures of isotopes. For instance, natural carbon on Earth is composed of 98.90% ^{12}C and 1.10% ^{13}C isotopes (de Hoffmann and Stroobant, 2007). In high-resolution mass spectrometry, the separation of masses by *m/z* results in the distinct peaks representing the natural isotopes, thus yielding multiple peaks for a chemically pure substance. Statistical methods are commonly employed to calculate the expected isotopic pattern, taking into account the abundance of each isotope.

To illustrate this, consider the example of molecular chlorine, which exhibits a more intricate isotope pattern than carbon due to the distribution of its isotopes. Terrestrial chlorine has two stable isotopes, ^{35}Cl (75.5%) and ^{37}Cl (24.5%). The isotope pattern for the Cl_2^+ ion can be calculated using the results shown in Table 4.3.

Generally, to determine the intensity distribution pattern of a molecule with n atoms of an element X with the isotopes A_X, B_X, ... and the corresponding isotope abundances I_{AX}, I_{BX}, ... one can use the following:

$$(I_{AX} + I_{BX} + ...)^n. \tag{4.17}$$

For a compound consisting of n atoms of element X with two isotopes A_X and B_X, Equation (4.17) leads to:

$$(I_{AX}^n + n \cdot I_{AX}^{n-1} I_{BX} + \frac{n(n-1)}{2} \cdot I_{AX}^{n-2} I_{BX}^2 + ...). \tag{4.18}$$

TABLE 4.3: Exemplary calculation of the isotope pattern of Cl_2. Intensities usually get normalised to the most abundant isotope ion, which in this case would be $^{35}Cl_2^+$. Isotope probabilities from NIST Mass Spectrometry Data Center (2023).

m/z	Isotope Combination	Probabilities			Normalised Probabilities
70	$^{35}Cl_2$	$0.755^2 = 0.570$		0.570	100.0%
72	$^{35}Cl^{37}Cl$ $^{37}Cl^{35}Cl$	$0.755 \cdot 0.245 = 0.185$ $0.245 \cdot 0.755 = 0.185$	intensities add up	0.370	64.9%
74	$^{37}Cl_2$	$0.245^2 = 0.060$		0.060	10.5%

The intensity distribution for a molecule consisting of several types of atoms X, Y, Z, ..., can then be calculated as:

$$(I_{AX} + I_{BX} + ...)^{n_X} \cdot (I_{AY} + I_{BY} + ...)^{n_Y} \cdot (I_{Az} + I_{BZ} + ...)^{n_Z} \cdot ... \quad (4.19)$$

Exemplary isotope patterns for chlorine and bromine are described in Box 4.4.

> **Box 4.4: Isotope Patterns of Molecules with High Abundance Isotopes**
>
> Several elements exhibit substantial abundance of isotopes, such as silicon, sulphur, chlorine, and bromine. ^{37}Cl comprises approximately one-third of the abundance of ^{35}Cl, and ^{81}Br has roughly the same abundance as ^{79}Br. Consequently, the relative intensities of both the molecular ion peak and its associated isotope peaks provide a direct indication of the number of chlorine and bromine atoms present in the given molecular formula. For instance, a molecule with one bromine will exhibit a peak at m/z = M and a peak of similar intensity at m/z = M+2. A molecule with two bromine atoms will display peaks at m/z = M, M+2, and M+4 with an approximate intensity ratio of 1:2:1. The presence of various numbers of chlorine and bromine atoms in a molecular formula is indicated by the intensity patterns depicted in Figure 4.9.
>
>
>
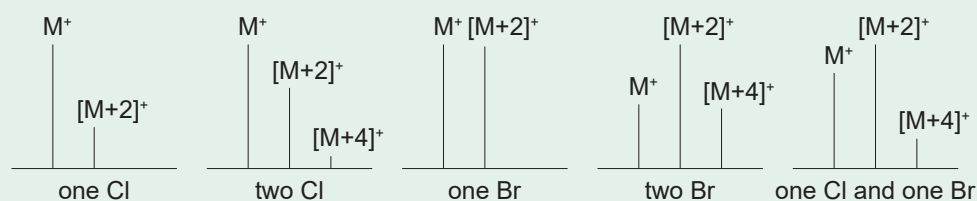> FIGURE 4.9: Isotope pattern of a molecule of chlorine and bromine. Terrestrial isotope abundance and idea for graphical description from Gross (2017).

Mass Resolution

Until now, it has been assumed that nominal masses would be adequately spaced for accurate detection. However, this is not always the case and is contingent on the mass spectrometer's resolving power. The separation observed in a mass spectrum is

denoted as mass resolution R. Mass resolution is defined as the smallest difference in m/z that can be distinguished at a specific signal, i.e., at a specific m/z value:

$$R = \frac{M}{\Delta M} = \text{resolution}$$
$$\Delta M = \text{peak width at a given height}$$
$$M = \text{center mass of the corresponding peak}$$

(4.20)

Thus, the resolution is dimensionless. The capability of a device to resolve adjacent peaks is called (mass) resolving power. This value is derived from the peak width at a certain percentage of the peak height, expressed as a function of mass. Higher resolution leads to greater peak separation, ensuring more precise mass determinations. Different peak width definitions exist. In particular, the width of the peak is measured at a specific fraction of its height, whether that is 0.5%, 5%, 10%, or 50%. This work will employ the full peak width at 50% height, also known as the Full-Width-Half-Maximum (FWHM).

Spectra illustrating peaks with higher resolution compared to lower ones are shown in in Figure 4.10.
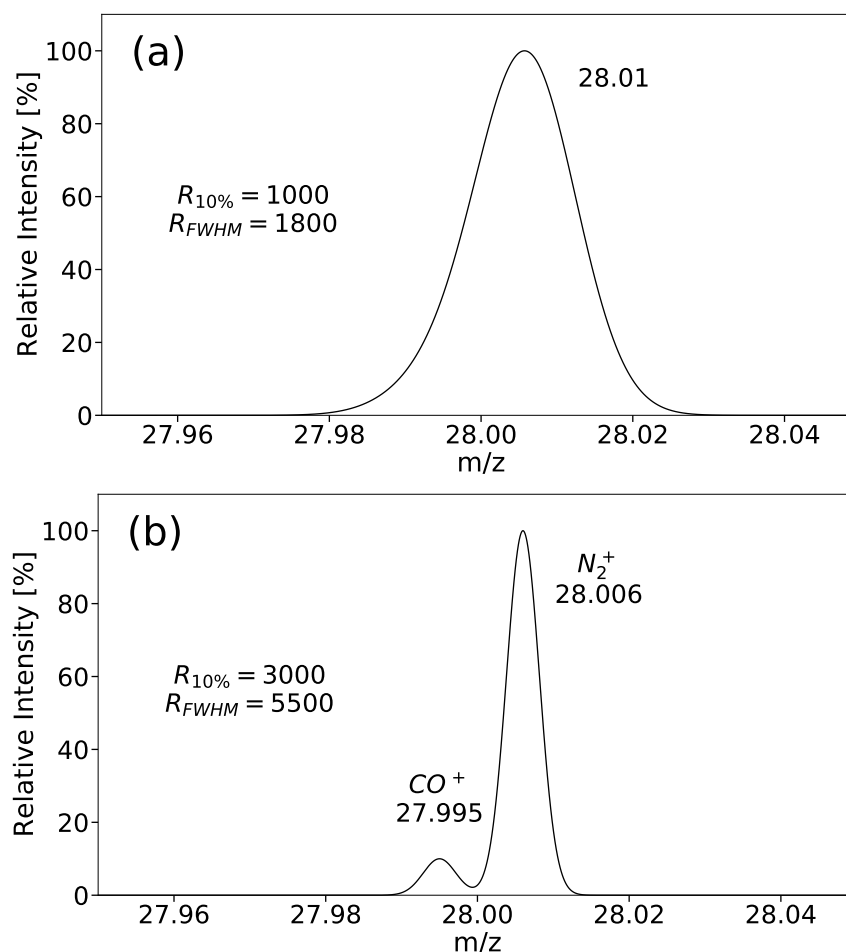
FIGURE 4.10: Example illustrating different mass resolutions for m/z 28, containing the molecules CO and N_2 in simulated spectra. Panel a: In the low-resolution spectrum, CO and N_2 are indistinguishable, as only one peak at m/z 28.01 is observed. Panel b: In the high-resolution spectrum, CO and N_2 are clearly distinguishable. The figure also emphasises the impact of the resolution definition; the resolution values at the 10%-level and at FWHM differ by a factor of 1.8 in the case of Gaussian peak shapes.

4.2.3 NDG Working Principle

The Neutral Density Gauge (NDG) is built upon the Rosetta/ROSINA COPS ram gauge. This Bayard-Alpert style ionisation gauge measures the total gas density and serves as an additional reference for the abundances obtained with the mass spectrometer. The gauge measures the ram pressure while consistently pointing in the direction of motion (Rubin, 2021). Ram pressure results from the pressure exerted on a body moving through a fluid medium. It is caused by the relative bulk motion of the fluid rather than random thermal motion. The NDG features a spherical equilibrium cavity (antechamber) designed to isotropise and thermalise incoming neutral gas to the wall temperature before reaching the ionisation region. The antechamber (Figure 4.11 a) has an 80 mm diameter and a 5 mm aperture facing the comet.

Free electrons are emitted from the hot filament emitter at +30 V (Figure 4.11 b) and accelerated towards the ionisation region set at +180 V (Figure 4.11 c). There, thermalised molecules undergo electron ionisation (Section 4.2.1). The resulting ions are trapped and guided towards the collector by a three-element lens-like configuration comprising the anode grid (-12 V, Figure 4.11 d), the base plate (Figure 4.11 e) with a 3 mm diameter aperture at its centre (0 V), and the reflector (+110 V, Figure 4.11 f). The reflector is a hemisphere with a 15 mm diameter and an apex aperture, through which the collector is mounted. Finally, the ions are collected by the cathode and detected by a sensitive electrometer (Figure 4.11 g). The measured ion current is directly proportional to the particle density inside the antechamber. A technical drawing is depicted in Appendix A in Figure A.1.
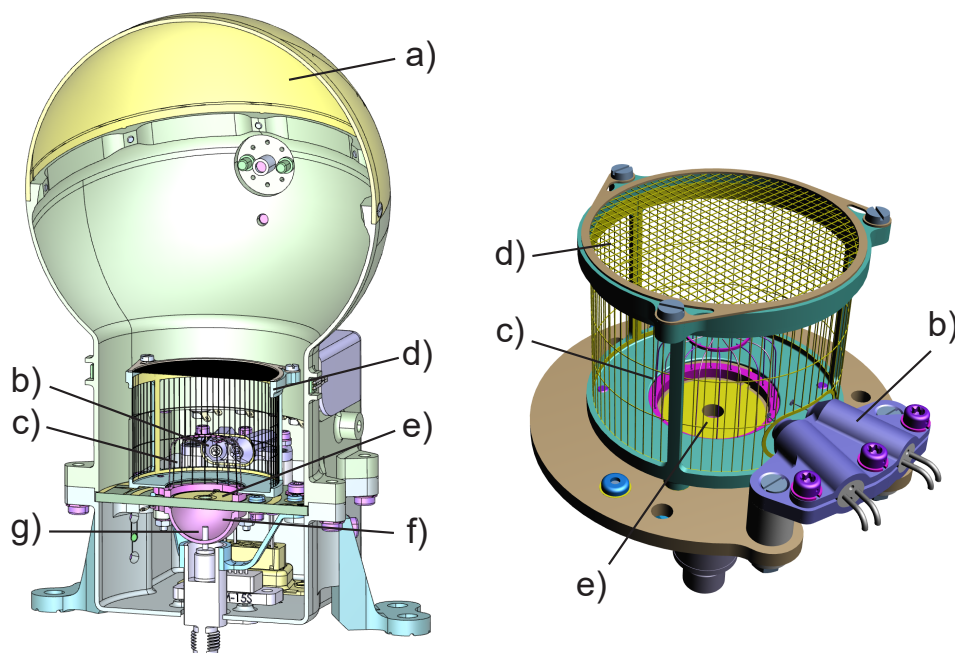

FIGURE 4.11: 3D drawing of the NDG. Left: full NDG including antechamber (a), hemispherical reflector (f), and cathode (g). Right: close-up of the ionisation region including filament emitter (b), anode grid (c), electron repeller (d), and base plate (e).

4.2.4 Instrument Requirement Specifications

Both sub-instruments of the MANiaC instrument suite need to be tested and calibrated according to their instrument requirements defined as follows (Mehta, 2023a):

– IR1-PRF-1:   Dynamic range
MANiaC shall achieve $\geq 10^6$ dynamic range.
Detection of all major and major minor species to the ‰-level with respect to the dominant water peak.

– IR1-PRF-2:   Mass resolution
MANiaC shall achieve a mass resolution of m/Δm = 800.
Target is a mass resolution of m/Δm = 1000.

– IR1-PRF-3:   Mass range
MANiaC shall achieve a mass range 1 – 1000 *m/z*.

– IR1-PRF-4:   Temporal resolution
MANiaC (SHU and NDG) shall achieve a temporal resolution of 0.05 s.

– IR1-PRF-5:   Stability
Relative abundances from MANiaC and total densities from NDG shall be stable (within 10%) for 1 hour of operation.

– IR1-PRF-6:   Detection limit SHU
Species with an ambient density of 1000 cm^{-3} shall be detectable.

– IR1-PRF-7:   Detection range NDG
The NDG shall detect pressures in the range between 10^{-5} – 10^{-11} mbar.

– IR1-PRF-8:   NDG density measurement accuracy
The NDG shall have an accuracy of 10% from 10^{-5} – 10^{-11} mbar within 1 – 10 s integration time.

To check whether the instrument prototype already fulfils these requirements is vital for the future development and commissioning of the flight instrument. The final evaluation of these requirements will be presented in Chapter 7.

Results from NDG Measurements

<div style="text-align: right">5</div>

This section gathers the results from testing the MANiaC NDG pressure gauge sub-instrument prototype and shows the results from ion optical simulations of the NDG model. Measurements are an important part of the instrument development and commissioning phases whereas the computer simulations serve as a tool to rapidly replicate several instrument configurations in order to find a suitable setting.

5.1 NDG Calibrations

Numerous NDG calibration experiments were carried out in the laboratory facilities at the University of Bern. This section explains the particulars of each experimental setup and presents the calibration outcomes, all with the aim of meeting the instrument requirement specifications outlined in Section 4.2.4. Section 5.1.1 provides insights into the experiments and their results conducted in a static vacuum environment, while Sections 5.1.3 and 5.1.4 present the results of dynamic tests conducted at low and high gas velocities, respectively.

5.1.1 Static Measurements

Static measurements were done when the instrument was placed in a constant density environment. This means that no velocities and time dependencies have been applied except for the pressure changes. Additionally, a settling time has been used after the pressure changes to enable the environment to be considered stable. The subsequent sections delve into various constant density measurements, explaining their distinct characteristics and presenting the obtained results.

Sensor Current as Function of Pressure

The anode measures the ion current produced by ionisation of the gas in the NDG. A direct correlation exists between the pressure in the NDG and the recorded ion current. This correlation requires calibration and the experiment detailed here aims to define the pertinent parameters. The pressure within the vacuum chamber, and consequently in the NDG, underwent sequential changes from low to high pressure by introducing N_2 into the chamber. Throughout this experiment, the emission current remained constant.

Starting at minimal pressure and incrementally raising it in accordance with predetermined pressure steps, the ion current at each pressure stage was measured. Figure 5.1 illustrates a representative measurement, displaying a staircase-like pattern in the experimental data points, as anticipated when incrementing the pressure

step wise. Each step's average was calculated, as depicted by the coloured lines corresponding to their respective pressure values. The stars denote the start and end points of the averaging measurements, representing a stable phase of pressure and signal.
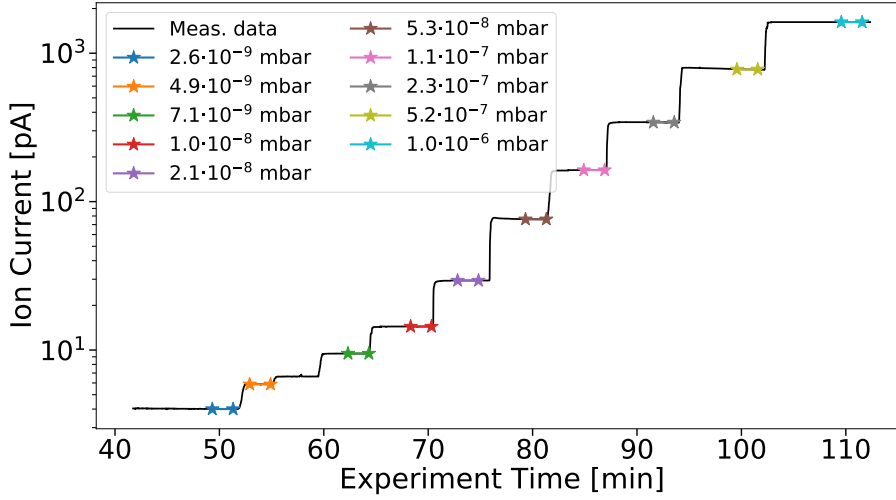

FIGURE 5.1: Exemplary measurement data of a static NDG test. Colours show the averaged ion current measured at their corresponding pressure.

Multiple sets of measurements have been conducted. The background of each measurement changed according to the background pressure in the vacuum chamber. Upon subtracting the individual background measurement for each data set, Figure 5.2 emerges. Background removal is performed as follows:

$$I_{ion, \, corrected}(p) = I_{ion, \, measured}(p) - I_{ion, \, measured}(p_{background}). \tag{5.1}$$

The background-corrected signals across different measurement sets closely align at each pressure. By linear approximation of the dataset, one obtains the gradient of each measurement set. The average gradient of the ion current with respect to pressure variation is found to be $(1.58 \pm 0.08) \cdot 10^9$ pA mbar^{-1}. This variation of 4.8% demonstrates good accuracy, satisfying the requirements outlined in Section 4.2.4.

The sensitivity is calculated as:

$$s = \frac{I_{ion, \, corrected} - I_{offset}}{I_{emission}} \frac{1}{p(N_2)}, \tag{5.2}$$

where I_{offset} is the current measured with the anode for no emission and $p(N_2)$ is the static chamber pressure during the measurement. The former is the individual measurement error of the anode. It has been measured in the sub-emission mode, where the filament heater current is fixed just below the emission limit. The measured offset current ranges between -17 fA and -26 fA, constituting less than 1% of the lowest measured ion currents at the background pressure and even less for higher pressures. Consequently, it is disregarded in the subsequent calculation. The pressure gauge's measurement precision, at a constant error of 15%, is not illustrated in the graphs for visibility reasons.

By dividing the average gradient of the measurements by the emission current of 100 μA, the sensitivity is determined to be 15.8 mbar^{-1}. For comparison, the sensitivity of the nude gauge in COPS, a pressure gauge comparable to the NDG, has been experimentally defined as 27.75 mbar^{-1} (Graf et al., 2004). However, their measurements

used argon as the calibration gas, which ionises more readily, resulting in a higher ion current and sensitivity than when using N_2. Applying a correction factor (see Appendix B) to the COPS's Ar-sensitivity, a corrected sensitivity of 21.5 mbar^{-1} is obtained. This is in the same order of magnitude as the experimental sensitivity for the NDG prototype model obtained in this section, confirming the similarity of the COPS ram gauge and the NDG prototype.
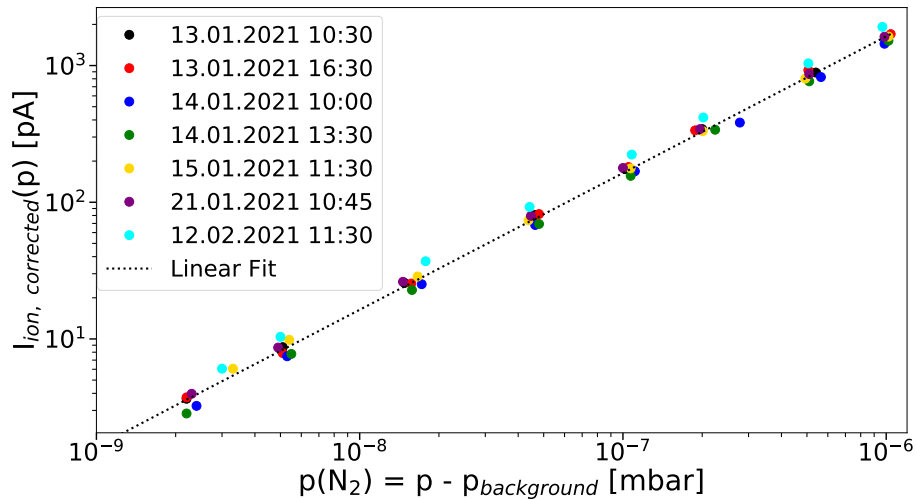

FIGURE 5.2: Background corrected ion current as function of background corrected vacuum chamber pressure. The linear fit has been done considering all data points.

Sensor Current as Function of Emission Current

It is important to verify the accuracy of the signal even for very small collector ion currents. Since the vacuum chamber's minimum pressure is constrained by pumping limitations, reducing the emission current becomes a viable approach to attain lower ion currents at the same pressure. Equally crucial is confirming the linearity between emission current and ion current at identical pressures, an adaptation that might not only conserve power but also increases the instrument's dynamic range.

In this specific experiment, the emission current underwent incremental reduction from 100 μA to 10 μA, with simultaneous measurement of the ion current. The results depicted in Figure 5.3 show the measured ion currents as the emission current varies across different pressures. The observed linear correlation between ion current, emission current, and pressure is noteworthy. Furthermore, exemplary repeatability is evident in the data, as illustrated by two nearly overlapping curves recorded at a pressure of $1.2 \cdot 10^{-9}$ mbar. This consistency underscores the reliability of the experiment, bolstering confidence in the accuracy of the ion current measurements under varying emission conditions.

Investigation of AC-Filament Controller Efficiency

Efficient energy utilisation is paramount in space missions. While DC-controllers typically regulate filaments, employing an AC-controller could minimise conversion losses, especially when utilising transformers to maintain required emission currents. This study explores the efficacy of an in-house developed AC-filament controller, serving as a potential backup option should issues arise with the conventional DC-controller during future instrument development campaigns.
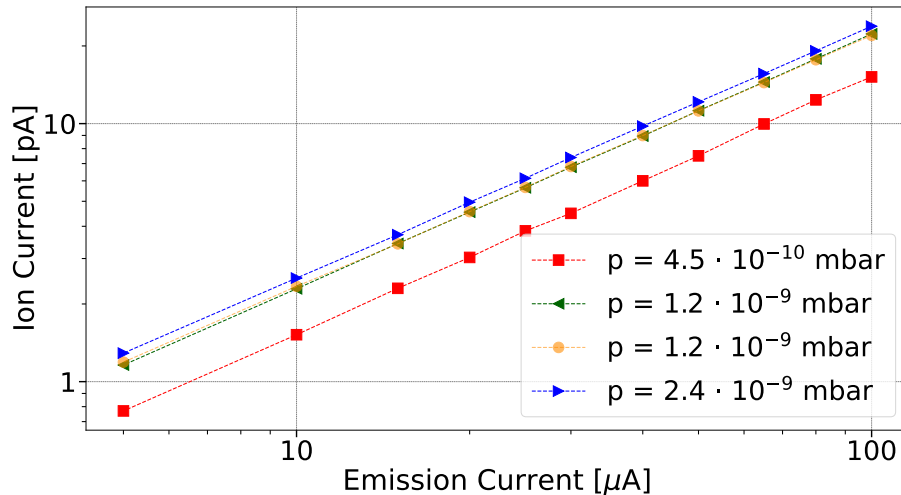
FIGURE 5.3: Measured ion current during emission current variations at different chamber pressures.

Multiple experimental runs were conducted with the AC-filament controller, preserving constant emission current while varying pressure. Figure 5.4 illustrates a comparison between AC- and DC-filament controller results, indicating that the former yields higher ion currents under identical conditions. Interestingly, the fitted curve gradient for AC-filaments is approximately double (32.3 mbar^{-1}) that of DC-filaments (15.8 mbar^{-1}), despite similar heating currents and power during experiments. This disparity, however, remains unexplained. The sensitivity of AC-filaments reaches 32.3 mbar^{-1}, surpassing the corrected sensitivity of 21.5 mbar^{-1} for the COPS nude gauge (Section 5.1.1 and Graf et al., 2004). These promising results suggest that the AC-filament controller exhibits robust performance, potentially serving as a reliable backup for the DC-filament controller in future test campaigns.
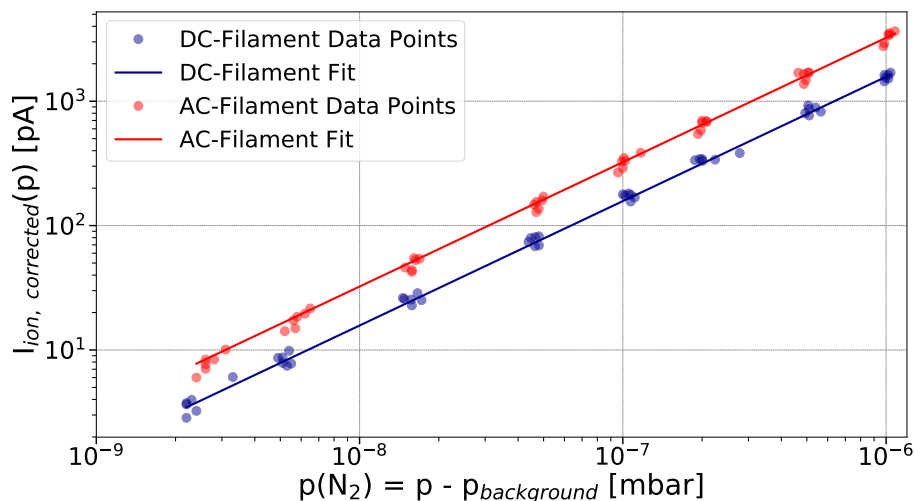

FIGURE 5.4: Background corrected ion current as function of background corrected vacuum chamber pressure for measurements with both the DC- and AC-Filament. The linear fits have been done considering all data points.

Sensitivity Variation Across Different Gases

As previously stated, a conversion factor is necessary when dealing with gases other than nitrogen, given that the pressure gauges are often normalised to nitrogen (refer to Appendix B). This section delves into the methodology employed for calculating this factor for key gases pertinent to the Comet Interceptor mission, providing subsequent results. The concept of instrument sensitivity, demonstrated in Section 5.1.1, is pivotal to this analysis. The relative conversion factor f_i for gas i is computed as follows:

$$f_i = \frac{s_i}{s_{N_2}},$$ (5.3)

where s_i represents the sensitivity of gas i, while s_{N_2} stands for the sensitivity of nitrogen, the standard gas. This conversion factor quantifies the likelihood of ionisation for a molecule of gas i compared to molecular nitrogen. A similar outcome can be obtained by comparing the ionisation cross sections of the respective gases.

The sensitivity analysis encompasses noble gases such as helium (He), neon (Ne), krypton (Kr), and xenon (Xe), as well as water (H_2O), carbon dioxide (CO_2), carbon monoxide (CO), and oxygen (O_2) – the prevalent gases on comet 67P (Rubin et al., 2019). Hydrogen (H_2), the most common gas in space, was also included. These gases were introduced into the vacuum chamber at varying pressures, as illustrated in Section 5.1.1, and the resulting signals were measured by the NDG. A linear regression was then fitted to the collected data, with the gradient of the regression being directly proportional to the sensitivity of the gas. The conversion factors were subsequently calculated based on these sensitivities.

The *Pfeiffer PBR 260* gauge (Compact FullRange BA Gauge) served as the pressure gauge for this experiment, featuring a 15% error in absolute measurement accuracy and a 5% error in measurement repeatability (Pfeiffer Vacuum GmbH, 2005). As the offset measurement is eliminated during background correction with Equation (5.2), the absolute error cancels out. However, the measurement repeatability needs to be factored into the error propagation.

Table 5.1 presents the conversion factors and instrument sensitivities measured and derived for the NDG. All conversion factors for the gases align with literature values within the specified uncertainties. Furthermore, the instrument sensitivity for each gas correlates with the sensitivity of nitrogen, affirming the NDG's consistent sensitivity to various gases in accordance with established literature.

TABLE 5.1: Conversion factors and sensitivities of the NDG with respect to important cometary gases. Literature values are taken from Pfeiffer Vacuum GmbH (2005).

Gas	Conversion Factor (NDG)	Conversion Factor (Literature)	Deviation [%]	Instrument Sensitivity [mbar^{-1}]
H_2	2.30 ± 0.26	2.4	4.2	12.04 ± 0.81
He	6.05 ± 0.44	5.9	2.5	12.84 ± 0.79
Ne	4.60 ± 0.53	4.1	12.2	14.07 ± 1.09
H_2O	0.95 ± 0.26	1.0	5.0	11.86 ± 1.07
CO	0.93 ± 0.08	1.0	7.0	11.60 ± 0.62
N_2	1.00 (definition)	1.0	-	12.53 ± 0.75
O_2	0.95 ± 0.09	1.0	5.0	11.91 ± 0.66
Kr	0.53 ± 0.06	0.5	6.0	13.17 ± 0.71
CO_2	0.90 ± 0.12	1.0	10.0	11.31 ± 0.68
Xe	0.40 ± 0.16	0.4	0.0	12.51 ± 1.07

5.1.2 NDG-e Front End

The NDG Front End (FE) is one of the most complex sub-circuits within the NDG electronics. Historically, the OPA128 trans-impedance operational amplifier (OpAmp) has been used to detect small currents in the range of a few 100 fA. However, due to obsolescence concerns for the Comet Interceptor mission, a replacement, LMP7704, has been identified. This potential substitute underwent thorough verification of its capabilities and accuracy through various measurement experiments. The latest prototype, NDG-e FE 0V1, has been subjected to testing, and the results are shown in this section.

The trans-impedance OpAmp inverts the measurement signal to facilitate accurate readout through analogue-to-digital conversion. It employs a dual-gain solution with two switchable resistance values (see Figure 5.5). This configuration allows for dynamic adjustment of the OpAmp's total gain between a high gain of 10^{10} and a low gain of 10^7. The high gain is applied for small pressures and correspondingly low ion currents, while the low gain suits high pressures and elevated ion currents.
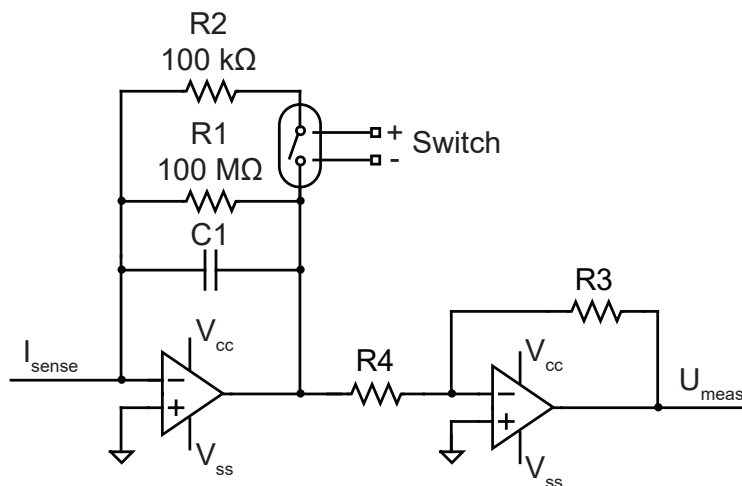

FIGURE 5.5: Principle schematic of the NDG-e FE trans-impedance OpAmp. Adapted from Gerber and Müller (2021).

The testing objectives for the NDG-e FE included:

- Measurement of the incoming signal generated by a precise signal generator across the entire detection range, with measurements taken at magnitude steps.

- Demonstration of measurement accuracy in accordance with instrument requirement specifications (Section 4.2.4).

- Determination of integration times for distinguishing small signal changes. Integration time was necessary for obtaining an average value capable of discerning subtle signal changes at low currents.

- Measurement of time constants for rising and falling flanks during input signal changes.

The measurement setup is depicted in Figure 5.6. Unlike the direct current measurement described in previous sections, the NDG-e FE 0V1 converts the incoming current to a voltage via a resistor. The voltage is then stored by a digital multimeter (DMM). The incoming current, generated by a reference source, was adjusted by $\pm$ 1%, 5%, 10%, 50%, and 100% at each magnitude across the detection range.
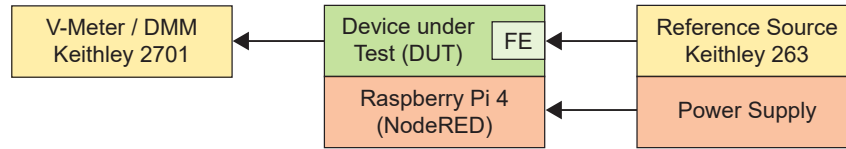
FIGURE 5.6: Schematics of measurement setup for NDG-e FE.

The acquired signal was averaged over two minutes to achieve a stable measurement average. Figure 5.7 illustrates these measurement averages for both high and low gains of the NDG-e FE 0V1. The figure reveals signal saturation at the lower end of the measurement range of both gains, necessitating calibration for accuracy. Additionally, an overflow effect was observed at the higher end of the measurement range of both gains, restricting the NDG-e FE's measurement range. Consequently, adjustments were made to the NDG-e FE board by increasing the resistance for high gain to 1 GΩ and for low gain to 1MΩ, effectively increasing both gains by a factor of ten. Following this calibration and background signal removal, the measured current could be corrected to match expected values within 5%. Only at the 100 fA level, the corrected signal was 27% lower than the input current, indicating the substantial influence of background at this level.

Figure 5.7 demonstrates that the updated high gain is accurate from around 100 fA up to 5 nA, while the low gain is accurate from around 10 pA up to 5 μA. Consequently, with the updated resistors, the gain change is intended to be implemented between 100 pA and 1 nA.

After evaluating the response time of the NDG-e FE with the updated gain (see Section 5.1.2), a solution was sought to decrease the response time. Thus, the capacitance of the NDG-e FE board needed reduction. In the prototype, this was achieved by using a fly-wiring, i.e., a direct connection between the input signal and the OpAmp with a wire instead of a printed connection on the printed circuit board (PCB). While this approach may not be feasible for the flight model, the adaptation significantly decreased the response time (Section 5.1.2), indicating that the capacitance on the PCB needs to be decreased by using different materials and shorter paths. The current calibration results were similar with and without the fly-wire connection, validating this change as an effective solution (Figure 5.8). Hence, a lower capacitance board is to be designed for the flight model.
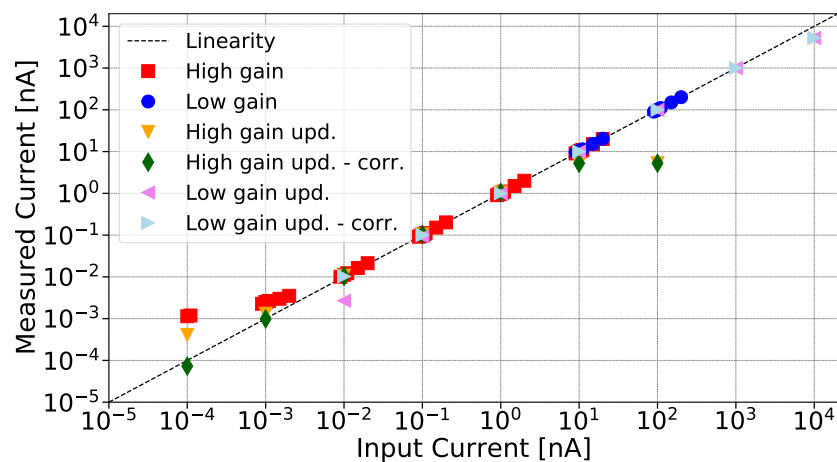

FIGURE 5.7: Current measured with NDG-e FE compared to corresponding input current, with and without offset correction.
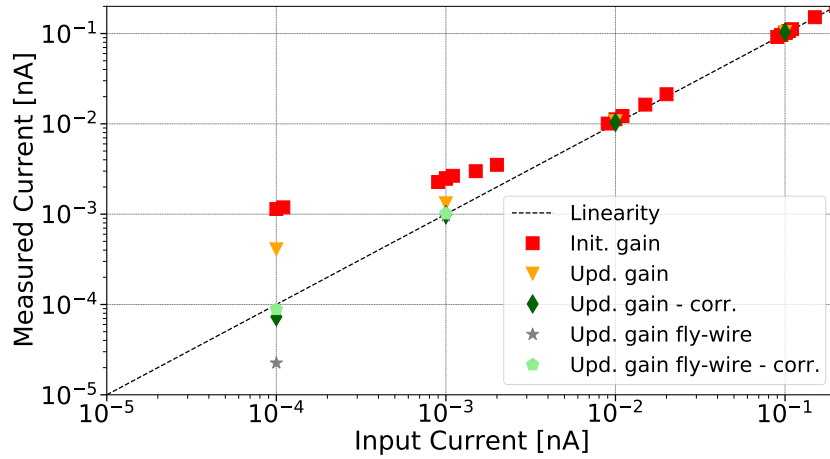
FIGURE 5.8: Current measured with NDG-e FE compared to corresponding input current at the low end of the detection range for the initial gain, the updated gain, and the fly-wire gain, with and without offset correction.

Response Time

To assess the response time of the NDG-e FE, a baseline current was changed by $\pm$ 1%, 5%, 10%, 50%, and 100% for each current magnitude in the NDG's detection range. The change was executed via a step function, allowing the determination of the settling time after a signal change. The response time of the NDG-e FE 0V1 was evaluated by fitting an exponential rise or decay function to the step-wise increase or decrease, respectively:

$$I(t) = I_{start} + (I_{end} - I_{start}) \cdot (1 - e^{-\frac{t}{\tau}}), \tag{5.4}$$

where $I_{start}(t)$ and $I_{end}(t)$ represent the input current before and after the step-wise change, respectively, $I_{end} - I_{start}$ describes the signal change, ΔI, and τ is the time constant. With this function, at time $t = \tau$, $I(t = \tau)$ has increased by $0.63 \cdot \Delta I$ for the rising signal, meaning the time constant is the duration after 63% of the final value is reached. For the falling signal, at time $t = \tau$, $I(t = \tau)$ has decreased to $0.37 \cdot \Delta I$, indicating the time constant is the period after it has fallen to 37% of the initial signal.

The initial gain exhibited response times of approximately 3 s for the high gain and less than 1 s for the low gain. After updating and increasing the gain for both stages, the response time of the high gain considerably increased to about 25 s, while the low gain showed no significant change. Consequently, the fly-wire configuration was introduced to decrease wiring capacitance, resulting in a substantial decrease in response time below 0.1 s (see example for a 10% step change from 1.0 nA to 1.1 nA in Figure 5.9). Therefore, for the flight model, the capacitance of the PCB needs considerable reduction, necessitating the use of different PCB board material and different current paths.

Small Input Change Detection

For each current magnitude in the NDG's detection range, the input current was altered by $\pm$ 1%, 5%, 10%, 50%, and 100% compared to the baseline magnitude. The incoming signal was measured over a two-minute period with an acquisition at every 0.02 s. The objective was to determine the integration time required to clearly distinguish various input currents. The measurements have been taken with the
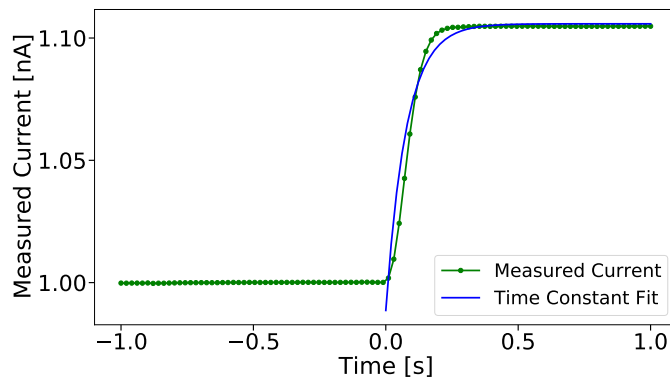
FIGURE 5.9: Fitting of response time with Equation (5.4) for the step change from 1.0 nA to 1.1 nA. Measurements taken with the updated high gain and fly-wire configuration.

updated high gain and the fly-wire configuration, as it proved to be accurate and considerably decreased the response time of the measurements. Figure 5.10 shows a comparison between the fly-wire and the PCB configurations with the updated high gain at a 1 pA input signal, where the fly-wire exhibits less offset and a more stable signal.
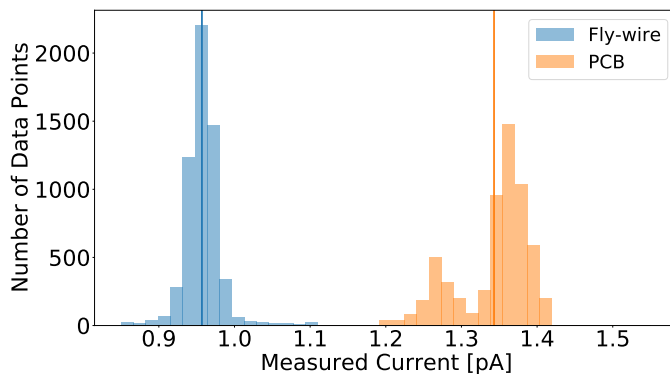

FIGURE 5.10: Measurement histogram at 1 pA for the fly-wire and PCB configurations. The fly-wire configuration has less offset and is more stable compared to the PCB configuration.

Currents above 10 pA could be directly distinguished without the need for integration time. Small changes around a current of 1 pA and lower required an integration time to distinguish them. Figure 5.11 shows that at the 1 pA level, a 10% signal change could be directly detected. However, for a 5% change, an integration time of 0.8 s was needed. For even smaller changes, more data points needed integration (i.e., 7 s integration time for a 1% change at the 1 pA level). Although the NDG should be capable of measuring down to 100 fA, obtaining these values proved challenging due to the noise of the prototype front end, which is substantial compared to the measured signal. At the 100 fA level, the integration time for a change in 10% was approximately 200 s, where no integrated data point from the baseline current of 100 fA overlapped with the 10% higher current of 110 fA. This result should be approached cautiously, as the measurements are very close to the front end's own measurement noise, and a different setup might yield different results. Thus, with the current measurement setup, too much noise was apparent, making it challenging to distinctly distinguish small input current changes at the 100 fA level.
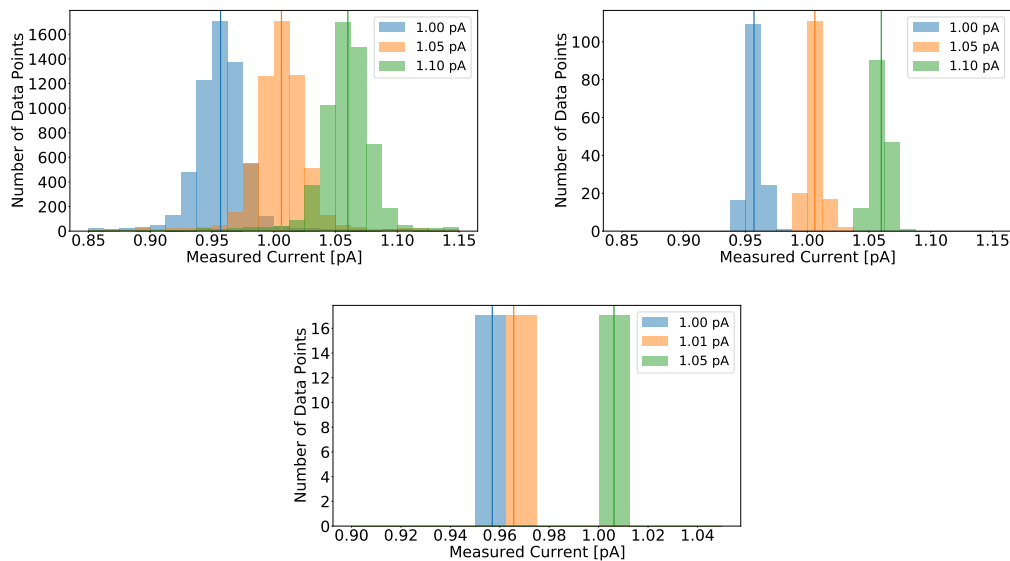
FIGURE 5.11: Histogram of measurements at the 1 pA level with +1%, +5%, and +10% value changes with the fly-wire configuration of the NDG-e FE. Top left: Actual measurement points show small overlap between 1.00 pA, 1.05 pA, and 1.10 pA. The mean of all data points (vertical lines) show, that a slight negative offset is present. Top right: Histogram of values integrated over 0.8 s showing no overlap between the different input currents. Bottom: Histogram of values integrated over 7 s showing no overlap between the different input currents of 1.00 pA, 1.01 pA, and 1.05 pA.

OpAmp Temperature Dependence

Determining the temperature dependence of the OpAmp in the NDG-e FE is essential for understanding its performance under varying thermal conditions. In this investigation, the circuit board was subjected to different temperatures, and measurements of the background signal (no input applied to the board) were conducted. The results, presented in Figure 5.12, illustrate the influence of temperature on the background signal of the OpAmp. Each data point represents an average of measurements taken over a 20-second interval, while the error bars indicate the standard deviation.

The uncertainty associated with temperature measurements is estimated to 10%, considering potential imperfections in the experimental setup. The OpAmp circuit exhibited a temperature dependence on the order of a few tens of mV, as depicted in Figure 5.12. It is noteworthy that the full instrument's temperature dependence will be comprehensively determined during the calibration of the flight model. This broader assessment is crucial for accurately characterising the instrument's behaviour under the thermal conditions it will encounter in space.

This preliminary analysis of the OpAmp temperature dependence underscores the importance of accounting for thermal effects in the NDG-e FE. The observed variations in background signals emphasise the need for a thorough understanding of temperature-related performance changes, ensuring the reliability and accuracy of the instrument's measurements during the Comet Interceptor mission.

Summary of the Measurements with the NDG-e FE

The experiments detailed above yield diverse insights into signal offset, stability, and the ability to discern signal changes with the NDG-e FE. Key findings are summarised as follows:
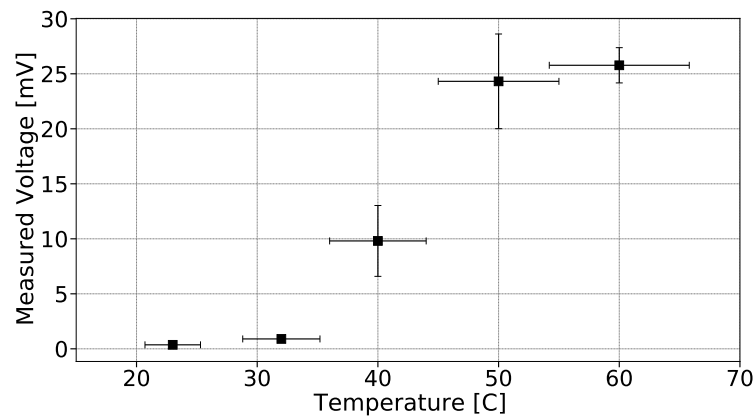
FIGURE 5.12: Background voltage of the OpAmp as a function of temperature.

- The impact of noise introduces discrepancies at the lower end of both gain steps, deviating from theoretical values. This discrepancy complicates the calibration process for the NDG, urging further refinement in the development of the NDG-e FE. Exploring alternatives such as selecting a different PCB material and enhancing noise isolation in the measurement path may offer potential solutions. The extent of improvement in signal offset remains challenging to estimate.

- Individual data points are directly distinguishable for higher signals. However, for signals at 1 pA and below, an integration time becomes necessary to differentiate small signal changes. Streamlining the measurement setup complexity holds promise for enhancing integration times, especially by mitigating influences from leakage currents and relay effects.

- Increasing the high gain enhances measurement results, particularly at the 1 pA level. This augmentation allows better signal separation and reduced integration times. However, a trade-off exists, as the time constant increases by a factor of 10. The updated low gain exhibits similar time constants, underscoring the predominant influence of capacitance on the measurement response. Consequently, a concerted effort to decrease capacitance in the measurement circuit is imperative for further reducing response times.

- Employing the fly-wiring method proves instrumental in enhancing signal stability and, notably, reducing response times. This shows the significance of PCB capacitance in determining the measured response time. Consequently, future development initiatives should prioritise a substantial reduction in PCB capacitance.

- The time constants for various rising and falling step signals are approximated. The fly-wire configuration, coupled with increased gain, demonstrates time constants of less than 0.1 s. This insight into transient responses is crucial for understanding the instrument's dynamic behaviour.

In conclusion, these findings provide valuable guidance for optimising the NDG-e FE, ensuring its robust performance and reliability in the intricate measurement scenarios anticipated during the Comet Interceptor mission.

5.1.3 Dynamic Measurements in CASYMIR

The fly-by velocity of Comet Interceptor, ranging from 10 to 70 km/s, induces a density enhancement within the NDG and SHU antechambers. This requires careful calibration in laboratory conditions, and the University of Bern possesses dedicated facilities for this purpose. This section details the dynamic measurements conducted in the CASYMIR vacuum chamber where neutral gas beams with velocities of $1 - 6$ km/s can be formed. These velocities are below the required range but are used as an initial verification of the working principle of the density enhancement in the NDG's antechamber. Higher velocities are later reached with ion beams in a different facility and will be discussed in Section 5.1.4.

CASYMIR Calibration System

To simulate the neutral gaseous atmosphere of comets for mass spectrometer calibration, the University of Bern designed the CAlibration SYstem for the Mass spectrometer Instrument ROSINA (CASYMIR). This fully automated ultra-high vacuum system features a gas mixing unit, allowing the creation of molecular beams and static environments with diverse gas compositions. Originally developed for calibrating the Rosetta/ROSINA instruments (Westermann, 2000; Westermann et al., 2001), CASYMIR now serves the purpose of calibrating the NDG and SHU for the Comet Interceptor mission.

The dynamic calibration mode involves using a neutral molecular beam, generated by expanding gas through a heated 80 μm diameter nozzle. The resulting beam passes through a skimmer to extract the central portion of the beam and an iris diaphragm acting as an adjustable slit before reaching the MANiaC instrument (see Figure 5.13 for an overview of the CASYMIR facility). The NDG is mounted on a 5-degree-of-freedom alignment table, allowing precise alignment with the incoming beam and testing of different beam incidence angles (Figure 5.14).

Beam Detection

The chamber containing the NDG can be moved with a 5-axis table, enabling a stepwise beam search procedure to find the correct horizontal and lateral positions to centre the beam to the NDG's entrance hole. Figure 5.15 illustrates the measurement results obtained during this procedure, determining the optimal positions at X = -17 mm and Z = -62 mm, which were subsequently fixed for the following experiments.

Sensor Current as Function of Beam Incidence Angle

The NDG's ability to rotate around the axis of the antechamber's entrance aperture allows for the simulation of a non-parallel flight direction, introducing an offset angle to the gas beam (Figure 5.16). Various measurements were conducted using different gas mixtures (H_2 with N_2, Ar, and Kr) to observe the NDG's behaviour at different angles and velocities (see Table 5.2).

A cosine function, defined in Equation (5.5), was employed to model the gas flow into the antechamber, where the amplitude (A) and frequency (B) depend on the gas velocity.

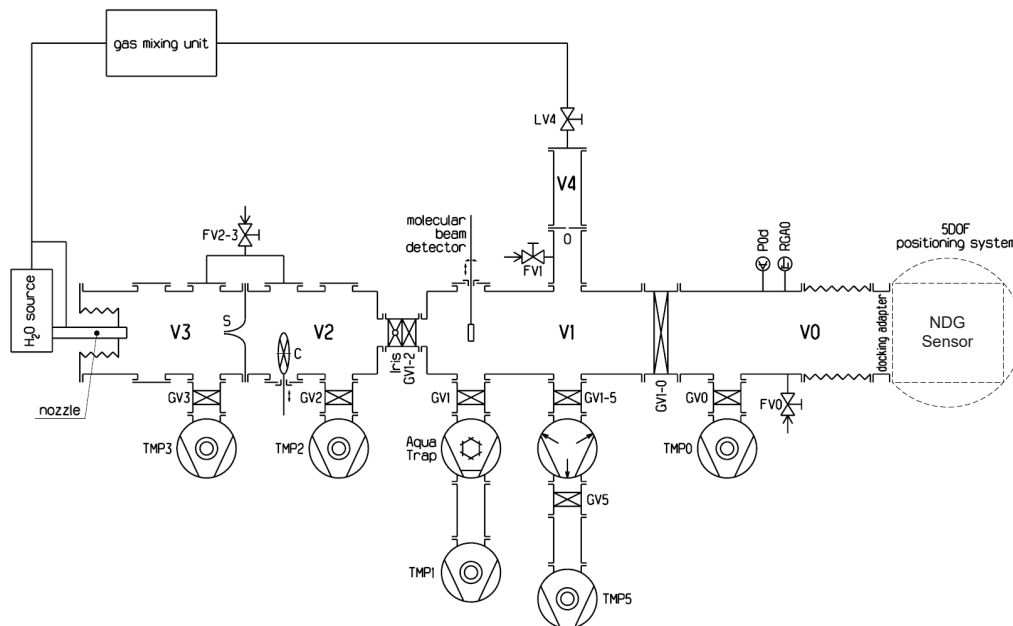$$I_{ion}(\alpha) = A \cdot cos(B\alpha). \tag{5.5}$$

FIGURE 5.13: Schematic diagram of the CASYMIR facility. The main components are the chamber with docking adapter V0, the main vacuum chamber V1, the collimator chamber V2, the expansion chamber V3, and the reference chamber V4. Chambers V0 to V3 are pumped by individual turbo-molecular pumps (TMP 0 – 5). Additional components include the skimmer S to extract the central part of the beam, the chopper disk C to measure beam velocity, the iris diaphragm as an adjustable slit, and the molecular beam detector. Source: Graf et al. (2004), reproduced with permission from Wiley.
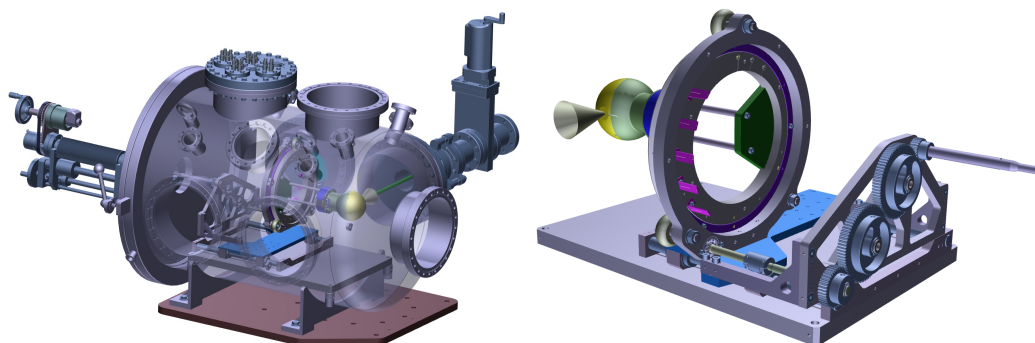

FIGURE 5.14: Left: CASYMIR vacuum chamber setup with NDG. Parts of the chamber are displayed transparent to show the position of the NDG in the chamber. The NDG is depicted with the antechamber mounted (yellow). The neutral gas beam is indicated in green. Right: The NDG is mounted to a rotating table to precisely align the setup with the neutral gas beam. The field of view (FOV) of the NDG is given by the yellow funnel, which is not a real component of the instrument but is only shown for understanding the FOV.
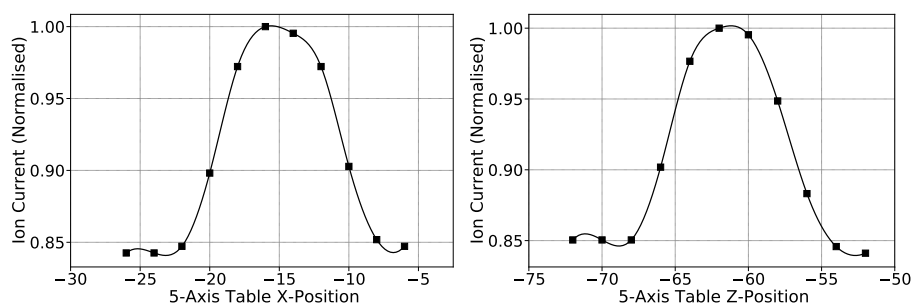

FIGURE 5.15: Normalised ion current during beam search.

TABLE 5.2: Beam flow mixtures for incidence angle experiments in CASYMIR with: $T_{Nozzle} = 605°$ C, iris diaphragm opening = 10%, and NDG emission current $I_{emission} = 20 \mu$A.

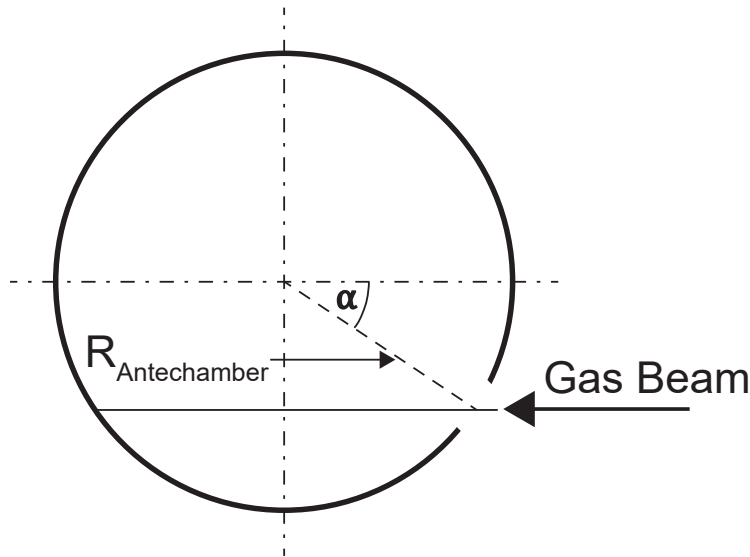| Flow Mixture	Measured Velocity
10 sscm H_2 & 10 sscm N_2	1200 km/s
10 sscm H_2 & 10 sscm Ar	910 km/s
2 sscm H_2 & 10 sscm Kr	600 km/s

FIGURE 5.16: Geometrical definitions for angle dependence.

Figure 5.17 presents measurement results and cosine function fits, showing a consistent frequency across all measurements, with amplitude variations reflecting gas velocity differences not seen due to the normalisation of the data for better comparison. A slight shift towards negative angles in all measurements suggests a nuanced behaviour, which might be attributed to factors such as chamber geometry or background effects.

It is to note that the different gases in the mixtures have distinct ionisation cross-sections, requiring correction factors (see Appendix B). Although the correction is necessary, its complexity, especially with mixed gas flows, is beyond the scope of this chapter focused on demonstrating the incidence angle's influence on measured ion current rather than comparing different gas flows.

Similar measurements conducted with the NDG-e FE, using gas beams of 15 sccm Ar and a mixture of 10 sscm H_2 and 10 sccm Ar, revealed the same angular dependence, confirming no discernible influence from the read-out electronics (Figure 5.17).

Sensor Current as Function of Beam Velocity

The expected correlation between the measured ion current signal and the beam velocity, and consequently the CASYMIR beam nozzle temperature, prompted a series of experiments. The beam nozzle temperature was varied from room temperature to nearly 1000 K, employing different gas beams (refer to Table 5.3 for gas species and corresponding flows). Throughout these steps, the beam velocity, ion current, and corresponding chamber pressure were measured, maintaining a constant emission
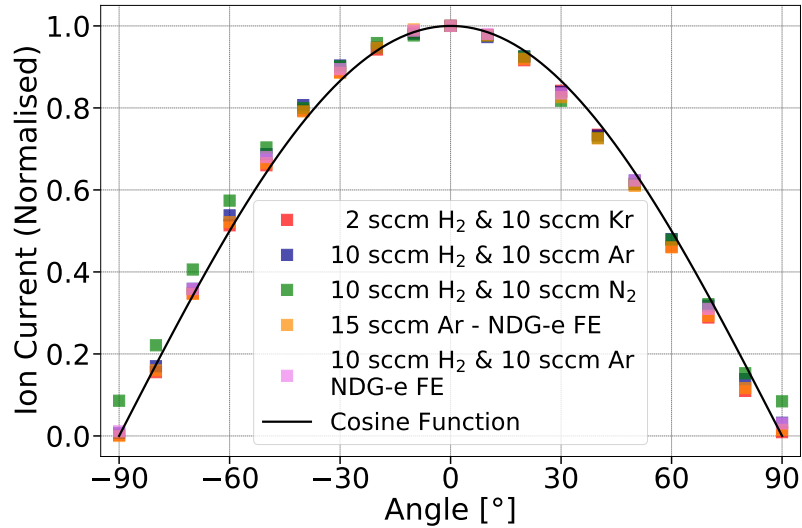
FIGURE 5.17: Angular dependence of measured ion current normalised to maximum signal for different gas mixtures with the cosine function fit.

current of 100 μA. Due to thermal considerations, the nozzle required re-calibration for each temperature step, introducing some measurement uncertainty. Despite the uniform heating power applied, slight variations in nozzle temperatures among different gases occurred due to cooling effects induced by the gas flow.

TABLE 5.3: Used gases and corresponding beam flows as well as heating power and the approximate resulting nozzle temperature for CASYMIR beam velocity calibrations.

Gas	Flow [sccm]	Power [W]	Approx. Temp. [°C]
H_2	15	0	15
N_2	10	22	205
Ar	15	50	350
Kr	5	80	500
		112	600
		160	715
		310	950

Given the anticipated high fly-by velocity range of $10 - 70$ km/s, the NDG uses an antechamber to thermalise the cometary neutral gas. Inside this antechamber, the density is expected to increase compared to the ambient density in the comet's coma, a phenomenon known as the ram effect (Section 4.2.3). The ram effect can be calculated using the formula (Rubin, 2021):

$$\frac{n_{NDG}}{n_{coma}} = 4 \frac{v_{in}}{v_{therm}} \approx 4 \frac{v_{flyby} \, cos(\alpha)}{v_{therm}}, \tag{5.6}$$

where n_{NDG} is the density inside the NDG gauge, n_{coma} is the density in the coma of the comet, v_{in} is the inflow velocity, v_{flyby} is the fly-by velocity of the spacecraft, v_{therm} is the thermal velocity in the antechamber, and α is the angle of the fly-by corresponding to the coma of the comet.

For the experiments, an incidence angle of $\alpha = 0°$ was chosen. In addition, the fly-by velocity is the beam velocity and the density in the coma is the density in the beam. The thermal velocity is defined as:

$$v_{therm}(m,\ T_{ante}) = \sqrt{\frac{8\ k\ T_{ante}}{\pi\ m}},$$ (5.7)

where k is the Boltzmann constant, T_{ante} is the temperature in the antechamber, and m is the mass of the gas. Three temperature sensors placed at different locations of the NDG provided measurements from which an antechamber temperature of approximately 350 K was derived.

Inserting experimental values into the equation gives:

$$\frac{n_{NDG}}{n_{Beam}} = 4\frac{v_{beam}}{v_{therm}}.$$ (5.8)

Measuring and calculating the right-hand side of this equation was straightforward. For the left-hand side, the measured pressures in the NDG and in the beam were resolved as follows:

$$p_i = \frac{I_{ion}\ -\ I_{bg}}{I_{em}\ s_{gas}},$$ (5.9)

where s_{gas} represents the NDG's sensitivity adapted to the corresponding gas, considering gas correction factors from Appendix B, and I_{em} is the emission current of the filament. Initial tests in CASYMIR demonstrated the working principle of the instrument when placed in a neutral gas beam. However, the inability to directly measure the unenhanced pressure in the beam introduced a disparity in the theoretical enhancement calculation. The experiment detailed here aimed to directly measure the beam pressure to verify the expected enhancement from theory. Two NDGs were placed into the chamber (Figure 5.18). The primary NDG had the standard configuration with the antechamber (closed NDG), while the second NDG lacked an antechamber (open NDG) and thus did not enhance the pressure inside the instrument. The enhanced pressure in the NDG p_{NDG} was measured with the closed NDG, whereas the pressure in the beam p_{Beam} was measured with the open NDG. For both, the density is calculated as:

$$n_i = \frac{p_i}{kT_{ante}}.$$ (5.10)

Introducing n_{NDG} and n_{Beam} from Equation (5.10) into Equation (5.8), the density enhancement could be calculated.

The setup could be moved on a horizontal axis, directing the incoming gas beam to either the open or the enclosed NDG. This allowed the open NDG to be positioned in the gas beam for measuring the beam's absolute density. Subsequently, the closed NDG was moved into place, and its enhanced density was measured. With these two measurements, the density enhancement could be determined.

Figure 5.19 illustrates the velocity dependence of the density enhancement for the measured neutral gas beams. The curves of both sides of Equation (5.8) (black and red curves in Figure 5.19) were expected to overlap based on theory. However, none of the measured gases exhibited this overlap, necessitating an additional correction for laboratory measurements. The neutral gas beam expands on its trajectory, causing the pressure measured with the NDG to be smaller than the full pressure the beam should have at a certain velocity. According to Westermann (2000), the width of the
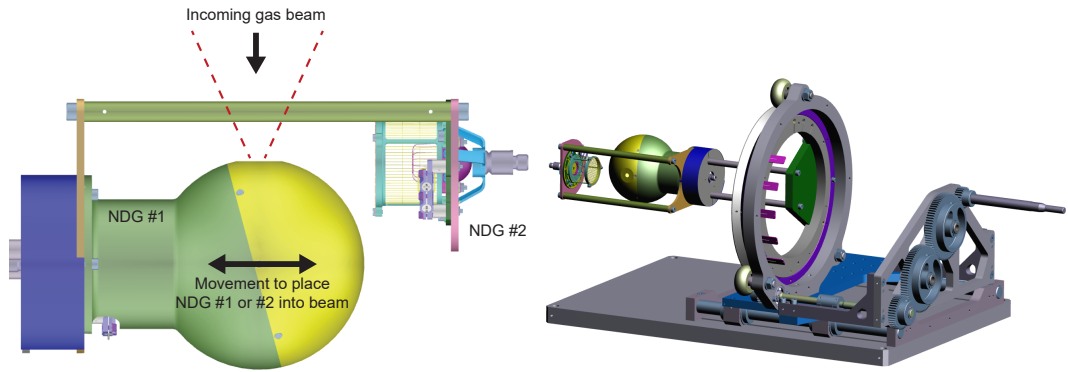
FIGURE 5.18: Schematics of double NDG configuration. Left: both NDGs installed on the turntable in CASYMIR vacuum chamber. Right: Top view onto the two NDGs showing the incoming beam and the possibility to move the instruments on a horizontal axis.
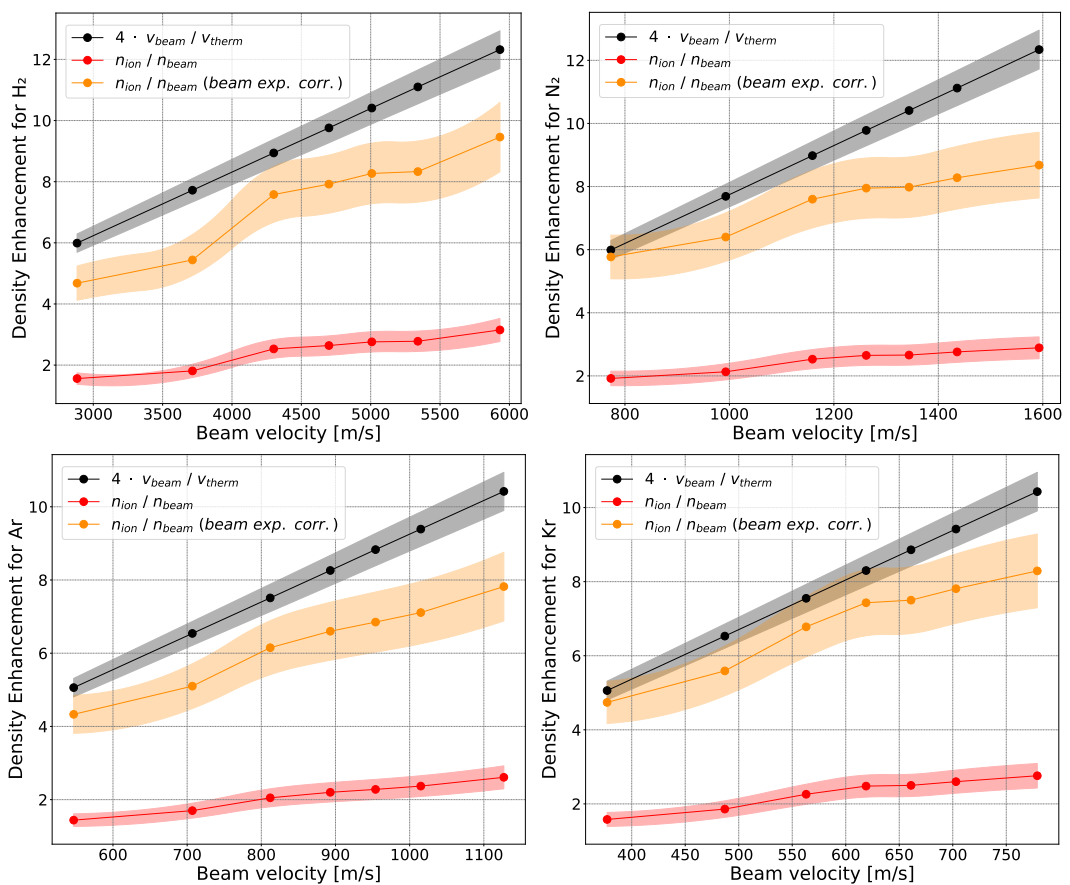

FIGURE 5.19: Velocity dependence of density enhancement for H_2, N_2, Ar, and Kr (left to right, top to bottom). The black curves represent the theoretical enhancement, the red curves represent the density enhancement measured with the two NDG's whereas the orange curve shows the measured values corrected for the beam expansion. The shaded areas represent the respective uncertainty regions of the different enhancements.

beam at the instrument interface is approximately two times wider than at the beam detector, due to the beam expanding along its path of 863 mm. If the beam expands, the number of molecules per cross-sectional area along its flight path decreases and thus the measured pressure in the NDG decreases. To correct for this, beam width measurements have been taken with the beam detector as well as with the NDG.

The discrepancy between the beam profile measured with the NDG and the beam detector is demonstrated in Figure 5.20. The beam width measured with the NDG, 1130 mm behind the beam detector, is approximately three times wider than the one measured with the beam detector. This expansion coefficient of three explains the measured expansion of the gas, considering geometrical changes along the flight path (Figure 5.13).
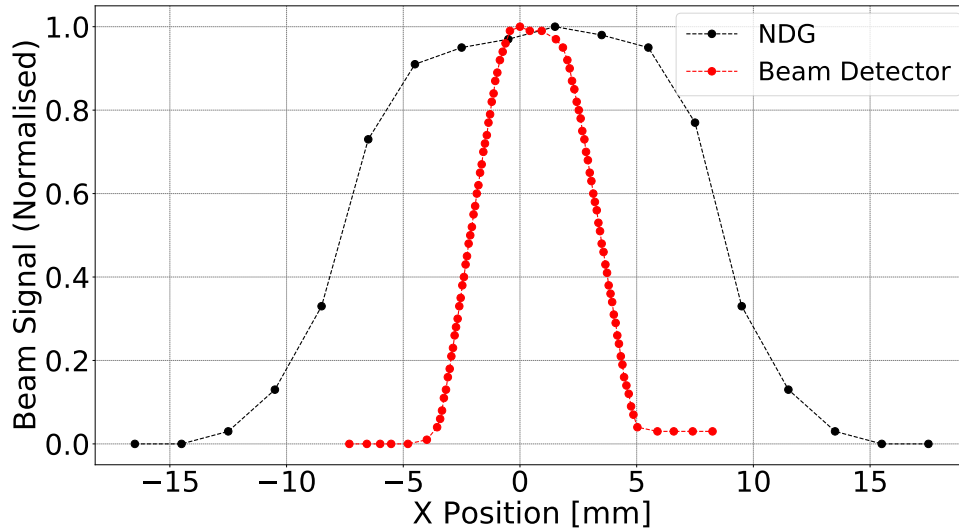

FIGURE 5.20: Comparison of beam widths measured with the NDG (black) and the beam detector (red) of CASYMIR. The two detectors are 1130 mm apart.

Correcting the measured values for beam expansion, the pressure enhancement measurements closely align with the velocity enhancement (orange lines in Figure 5.19), with overlapping uncertainty regions observed for most gases. Remaining differences may be attributed to the finite chamber size or potential underestimation of measurement uncertainties. The finite chamber size causes gas molecules to hit the back walls and return to the sensor. While this is less of an issue for the enclosed NDG, where the antechamber entrance hole is directed toward the gas beam, the open NDG might have also measured particles rebounding from the walls. This enhances the measured density in the beam, resulting in a slight shift between the orange and black curves in Figure 5.19.

Compensating for the measurement offset to the theoretical density enhancement requires a deviation factor for the laboratory experiments. The deviation factors are calculated for each gas as follows:

$$F_{deviation} \quad = \quad 4 \frac{v_{beam}}{v_{therm}} \bigg/ \frac{n_{NDG}}{n_{Beam}}. \tag{5.11}$$

The resulting deviations are given in Table 5.4. They are independent of the gases' mass due to the beam expansion correction introduced above. The mean deviation factor is 1.24 ± 0.09, indicating that, on average, the measured density enhancements are 24% below the theoretical enhancements. However, the measurement uncertainties are $\pm 20\%$, and the influence of gas returning from the walls introduces additional, unquantified uncertainty. Figure 5.21 presents the measured density enhancements corrected with their respective deviation factor for H_2. The values are well-distributed along the estimated density enhancement curve.

TABLE 5.4: Deviations in the evaluated enhancement compared to the theoretical enhancement for gases measured in CASYMIR.

Gas	Deviation Factor
H_2	1.29
N_2	1.24
Ar	1.27
Kr	1.16
Mean	1.24 ± 0.09

To conclude, accounting for beam expansion and additional measurement uncertainties related to over-pressure due to gas molecules rebounding from chamber walls, the theoretical and measured density enhancements are comparable and the offset between them remained relatively stable as a function of mass. Nevertheless, since the velocity range used in these experiments is much lower than the estimated fly-by velocity and uncertainties are relatively large, extrapolation from this data should be considered with caution. A potential solution is to measure with a higher velocity beam, which is feasible in the test facility CASYMS (Section 5.1.4), albeit with an already ionised gas beam.
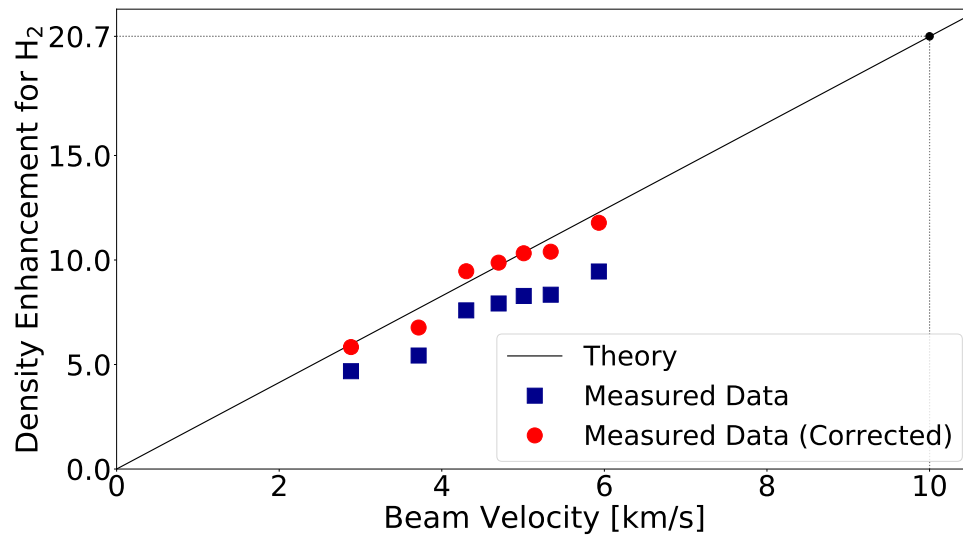
FIGURE 5.21: Measured density enhancement compared to beam velocity for H_2. The experimental data has been corrected for the beam expansion with a factor 3 (blue squares) and, additionally, with the deviation factor from Table 5.4 (red circles). The value of 10 km/s for the fly-by-velocity is the lower limit to what is expected during the mission.

5.1.4 Dynamic Measurements in CASYMS

The CAlibration SYstem for Mass Spectrometers (CASYMS) was used for dynamic gas measurements to simulate fly-by velocities higher than in CASYMIR (Section 5.1.3). In the CASYMS facility, ion beams with velocities in the range of $10 - 70$ km/s can be produced and directed towards the NDG.

CASYMS Calibration System

CASYMS, developed at the University of Bern, is indispensable for calibrating ion mass spectrometers. It provides a large-area (up to 250 cm^2), highly parallel ($\pm 0.5°$), and spatially uniform ($\pm 5\%$) ion beam across an extensive energy-per-charge spectrum spanning from 5 eV/charge to 10 keV/charge. Notably, it can produce ions with multiple charge states, such as He^{2+} or Xe^{9+}. Its core elements encompass an electron cyclotron resonance (ECR) ion source (Bodendorfer, 2008), yielding an ion current up to approximately 1 µA, a 90° crossed electric and magnetic field mass spectrometer for mixed or mass-selected beam generation, and a unique beam expansion system ensuring uniform coverage of a large area (Ghielmetti et al., 1983). Refer to Figure 5.22 for an illustration of the CASYMS facility and its core components.

In essence, the process entails the generation of ions using an ECR source, followed by pre-acceleration to an energy of 5 keV/charge (Bodendorfer, 2008). Subsequently, a mass/charge analysis is performed to eliminate undesired species, after which the ions are either accelerated or decelerated to reach their final energy-per-charge before entering the drift tube. The ion beam undergoes high-frequency rastering and expansion to ensure uniformity at the sensor opening of the instrument. Diagnostic probes stationed along the beam path monitor crucial parameters, including ion species, intensity profile, and absolute current. Operated within an ultra-high vacuum (UHV) chamber with pressures typically around 10^{-8} mbar, the entire UHV system is housed within a laminar clean room. The CASYMS calibration system has proven its efficacy by successfully calibrating numerous ion mass spectrometers that have been launched into space (Balsiger et al., 2007; Ghielmetti et al., 1983).
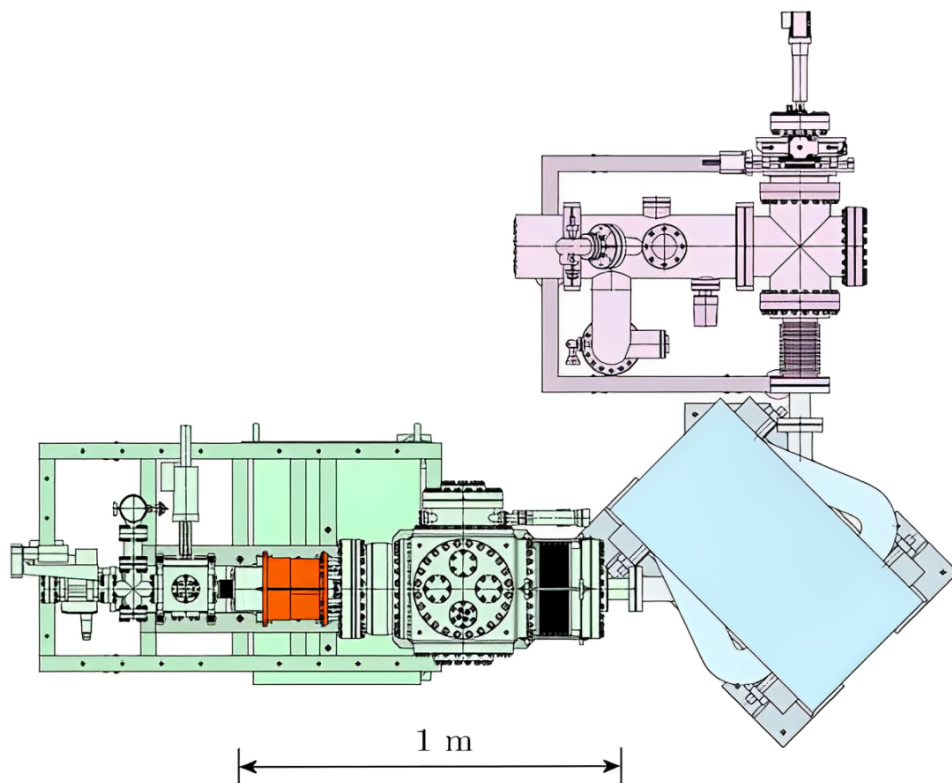

1 m

FIGURE 5.22: Top view of the CASYMS calibration facility including the ion source in orange and its surrounding compartment in green, the 90° mass separation magnet in blue and the beam expansion and measurement system in violet. Source: Bodendorfer (2008).

Sensor Current as Function of Beam Velocity

When fast moving molecules enter the NDG, the measured density gets enhanced due to the thermalisation of the incoming gas molecules in the antechamber. The theoretical considerations are the same as in Section 5.1.3 and the enhancement gets calculated recalling Equation (5.8). In CASYMS, the density in the beam (n_{Beam}) is measured using a Faraday cup, which measures the current generated by the impinging ions (see Box 5.1). In this experiment, only singly charged ions have been selected, and thus the density of the beam can be calculated as:

$$n_{Beam} = \frac{I_{Faraday}}{e \cdot A \cdot v_{beam}},\tag{5.12}$$

with $I_{Faraday}$ the current measured with the Faraday cup, e the elementary charge, A the measurement area of the Faraday cup, and v_{beam} the beam velocity.

Box 5.1: Faraday Cup

A Faraday cup is a metal cup or hollow cylinder designed to capture charged particles in a vacuum (Brown and Tautfest, 1956). Connected to ground via a resistor, it neutralises ions by accepting or donating electrons upon impact, generating a current. This current, amplified and measured, quantifies the charge of the ions or electrons striking the cup. An illustration of a Faraday Cup is shown in Figure 5.23.

Secondary electrons emitted upon ion impact can introduce errors if they are not suppressed. To enhance the accuracy of this detector, measures are taken to suppress secondary electron emission and reflected ions. Strategies include coating cups with low-secondary-ion-producing carbon, modifying the cup shape, introducing weak magnetic fields, or incorporating voltage-driven suppressor baffles (de Hoffmann and Stroobant, 2007).

For a continuous beam of singly charged ions ($z = 1$), the rate of ions hitting the cup per unit time (N/t) equals the measured current (I) divided by the elementary charge (e): $N/t = I/e$.
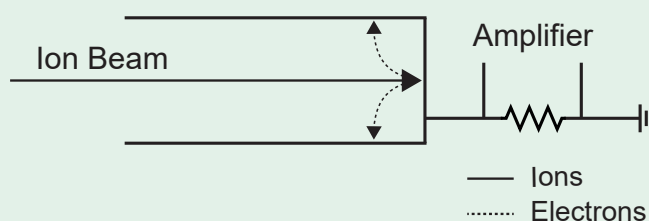

FIGURE 5.23: Schematic diagram of a Faraday cup. Source: de Hoffmann and Stroobant (2007), reproduced with permission from Wiley.

To test this theory for velocities in the expected fly-by range of the Comet Interceptor mission, measurements with N^+, O^+, Ar^+, and Kr^+ were conducted in CASYMS. Figure 5.24 shows the results, with measured density enhancements in red and theoretical enhancements in black. The beam velocities achieved during the experiments start at 30 km/s for the heaviest molecule tested (i.e., Kr^+), exceeding the lower bound of the predicted fly-by velocity, and reach over 100 km/s with the lighter molecules N^+ and O^+, surpassing the upper bound. The lower velocity bound of the
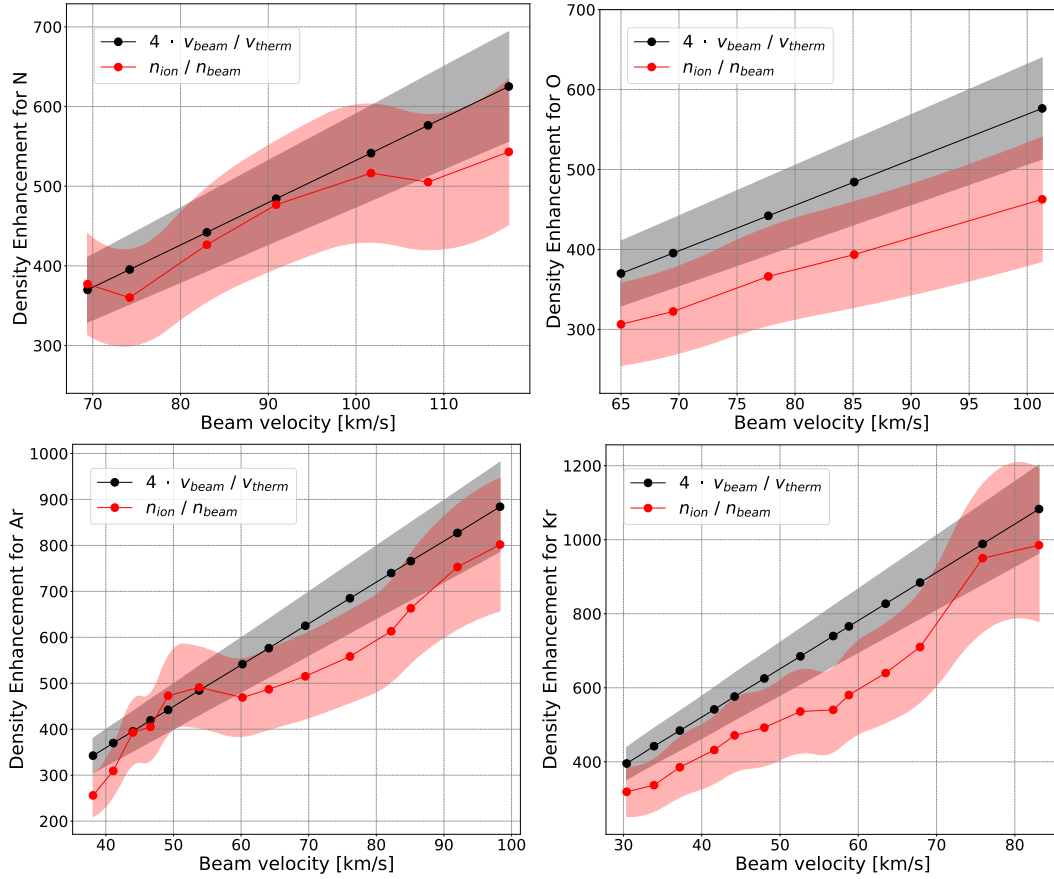
FIGURE 5.24: Velocity dependence of density enhancement for N, O, Ar, and Kr (left to right, top to bottom). The black curves represent the theoretical enhancement, and the red curves represent the density enhancement measured with the NDG compared to the beam density measured with the Faraday cup. The shaded areas represent the respective uncertainty regions of the different enhancements.

experiments was determined by the NDG's detection limit for the ion beam signal (≈ 10 pA) under the influence of chamber background and beam signal strength, and depends on molecule mass. The density enhancement measurements for N^+ and Ar^+ match almost perfectly with theoretical predictions, while the results for O^+ and Kr^+ are slightly below. Since the ions in the CASYMS beam are confined and controlled by high voltages throughout their passage through the calibration facility, velocity changes due to beam expansion are negligible compared to the overall measurement uncertainties. Similar to Section 5.1.3 and Equation (5.11), deviation factors have been calculated and are shown in Table 5.5.

TABLE 5.5: Deviations in the evaluated enhancement compared to the theoretical enhancement for gases measured in CASYMS.

Gas	Deviation Factor
N^+	1.07
O^+	1.23
Ar^+	1.13
Kr^+	1.25
Mean	1.17 ± 0.11

On average, the deviation factors for the CASYMS measurements are slightly smaller compared to the CASYMIR measurements (Table 5.4). The mean deviation factor is 1.17 ± 0.11, with measurement uncertainties in the range of $\pm 20\%$. This demonstrates that the enhancement theory holds well even for large velocities, including velocities in the mission fly-by range of $10 - 70$ km/s.

5.1.5 Combination of Dynamic Measurements

Combining the findings from Section 5.1.3 and Section 5.1.4 provides a comprehensive understanding of the dynamic measurements conducted with the NDG. Figure 5.25, illustrates the density enhancement measured with the NDG in both the CASYMIR and CASYMS facilities, compared to the beam velocity for argon and krypton. Additionally, the anticipated fly-by velocity range for the Comet Interceptor mission is shown (light green in Figure 5.25). All measured enhancements overlap with the theoretical enhancement within uncertainties for both gases. The data are consistent over a wide range of velocities, including much of the upper bound of the target fly-by velocity range and velocities well below the target range. The inability to fully encompass the target fly-by velocity range is due to facility limitations for higher velocities in CASYMIR and detection limit considerations for lower velocities in CASYMS.

Considering all data acquired in the CASYMIR and CASYMS facilities, a mean deviation factor of 1.18 ± 0.10 is found, demonstrating that the measurements are compatible with the theory within uncertainties. The small variation in the mean deviation factor also indicates that the experiments exhibit high precision and repeatability. In conclusion, the strong agreement between theoretical and experimental density enhancements, despite facility constraints, demonstrates the robustness of the enhancement theory. The results confirm that the density enhancement can be reliably computed using the theoretical framework.
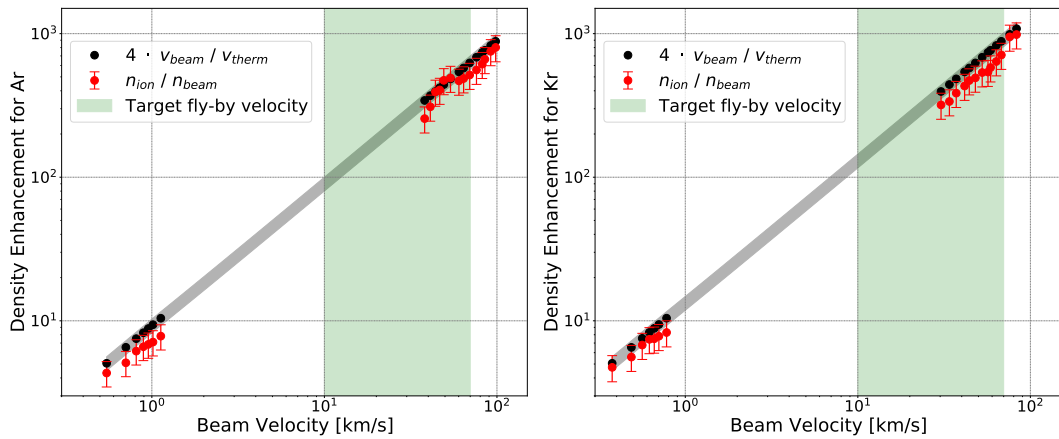
FIGURE 5.25: Velocity dependence of density enhancement for Ar (left) and Kr (right) for combined measurements in CASYMIR (low velocities) and CASYMS (high velocities). The black curves represent the theoretical enhancement and the red data points represent the density enhancement measured with the NDG in the CASYMIR and CASYMS facilities including uncertainties. The green shaded areas represent the target fly-by velocity range for the Comet Interceptor mission.

5.2 Computational Simulation and Optimisation of the NDG

Computational simulations and optimisations are imperative for predicting the behaviour of the instrument. This section delves into particle trajectory simulations of ionised particles within the NDG and presents optimisations of the available voltages.

5.2.1 SIMION

The computational software *SIMION* serves as a tool to calculate electric fields and trajectories of charged particles within those fields. It facilitates the assessment of an instrument's performance by considering different electric potentials in the model and the initial conditions of charged particles. Widely used for simulating instruments like mass spectrometers (Dahl, 2000), SIMION is integral to understanding the NDG's behaviour.

To construct a computational model, the instrument's geometry is translated into individual potential arrays (PAs) in SIMION. These PAs, mesh points representing different parts of the instrument, also incorporate the potentials of various electrodes. Instead of being designed as a single PA, multiple PAs are combined into a SIMION workbench. The voltages of individual PAs can be set directly in SIMION or programmatically with a *.lua file. Automation is preferred, enabling a straightforward change in the *.lua file for voltage optimisation. This automatic adaptation streamlines the process by adjusting the voltages of each PA according to the specified values in the file.

Critical to the simulation are the initial conditions of particles. The number of particles, their mass and charge, starting position, velocity, and kinetic energy must be defined. Three ion initial conditions have been programmed and simulated and are described subsequently in the following section.

5.2.2 Particle Initial Conditions

In the actual device, an electron beam is produced by the hot filament emitter, with free electrons accelerated and guided towards the ionisation zone (Section 4.2.3). Simulating electron ionisation with SIMION presents challenges, leading to the development of various strategies.

Variant 1: Electrons Mutate into Ions During Flight

This variant involves a sophisticated electron-ion interaction simulation. Electrons are accelerated from the hot filament emitter towards the ionisation zone and based on thermodynamic and gas laws, a function determines whether an electron hits an atom or a molecule (see Figure 5.26, top). The probability of such a hit, influenced by the mean free path in the gas, transforms the electron into an ion simulating the ion generation and conserving the particle's energy. The mean free path, λ_{mean} is the average distance an electron can travel in a gas composed of neutral molecules until it hits another molecule in the gas. It can be estimated from kinetic theory and is approximated under the assumptions of the ideal gas law as (Nave, 2017):

$$\lambda_{mean} \approx \frac{1}{n \cdot \sigma} \approx \frac{R \cdot T}{\sqrt{2} \cdot \pi \cdot r_{molecule}^2 \cdot N_A \cdot p},$$

(5.13)

with n the density of neutral molecules, σ the ionisation cross section, R the ideal gas constant, T the absolute temperature, $r_{molecule}$ the molecule radius, N_A the Avogadro number, and p the pressure.
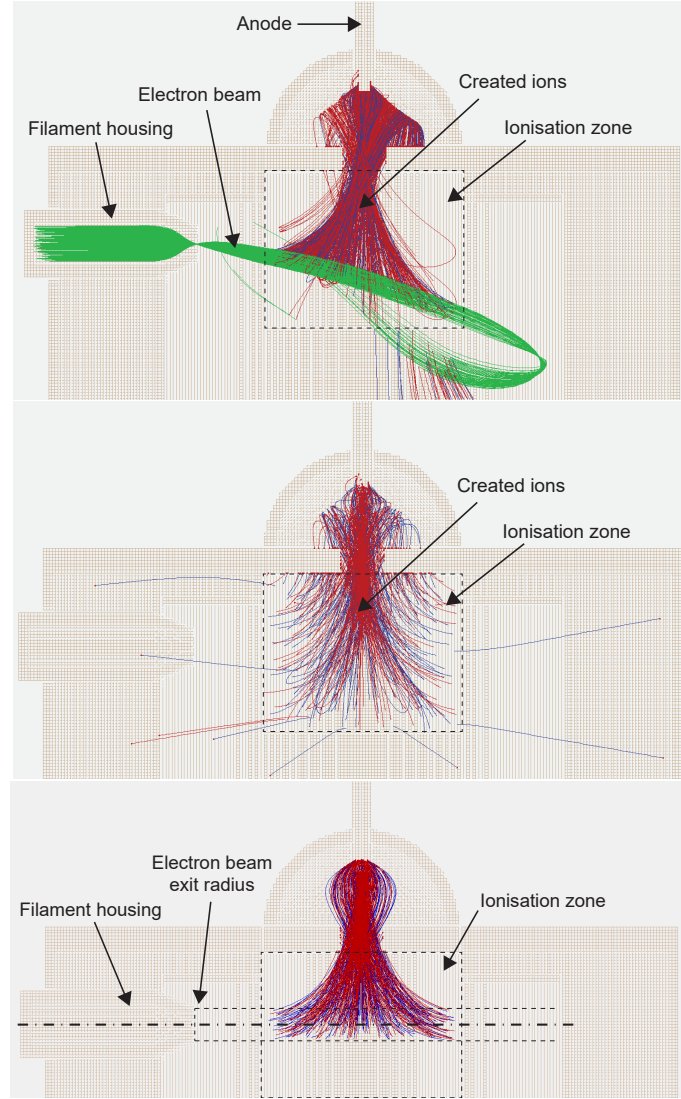
FIGURE 5.26: H_2O ion (blue), CO_2 ion (red), and electron (green) definition for NDG simulations for variants 1, 2, and 3 (from top to bottom). In all variants, ions are formed exclusively within the ionisation zone (i.e., within the anode grid). Ions formed outside this zone are repelled by the anode grid's positive potential and are therefore not detected by the anode. Consequently, to simplify the simulation, these ions are not considered.

When the mean free path is known, the collision probability P can be estimated as follows:

$$P(collision) = 1 - e^{-v_{electron} \cdot \frac{\Delta t_{electron}}{\lambda_{mean}}}, \qquad (5.14)$$

with $v_{electron}$ the electron's speed at time t, and $\Delta t_{electron}$ the electron time step. The next step is to define the initial conditions of the newly formed ion, i.e. the velocity of the ion. To do so, the root mean square velocity (v_{rms}) is calculated after Graham's Law (Laidler and Meiser, 1999):

$$v_{rms} = \sqrt{\frac{3 \cdot R \cdot T}{m_{ion}}}, \qquad (5.15)$$

with m_{ion} the ion's molar mass.

This root mean square velocity defines the average velocity an ion with mass m_{ion} has, corresponding to the kinetic theory of gases. However, it does not say anything about the direction of the moving ion. In this simulation, v_{rms} has been randomly distributed into space. Hence, each ion gets a random direction with a total velocity v_{rms}. Having defined the position and velocity vector of the new-born ion, it will move under the applied voltages according to its charge.

Variant 2: Ions Placed & Distributed in the Whole Ionisation Zone

This simpler variant involves creating and randomly distributing particles throughout the entire ionisation zone (see Figure 5.26, middle). With no electrons created, electron ionisation is not simulated. The particles are only affected by the applied voltages in the model. To have a more realistic model, a Gaussian velocity distribution with a standard deviation based on the Maxwell-Boltzmann distribution of a kinetic gas is applied to the particles (Laidler and Meiser, 1999). This theory assumes gas particles move with random velocities. No direction is preferred, and the components of the velocity vectors are independently and normally distributed with parameters:

$$\mu = v_{mean} = 0 \quad \text{and} \quad \sigma = \sqrt{\frac{k_B \cdot T}{m_{ion}}}, \tag{5.16}$$

where the parameter μ is the mean or expectation of the distribution, while the parameter σ is its standard deviation.

Variant 3: Ions Placed & Distributed Locally

Recognising issues with ion impingement on the anode and ion loss in variant 2, this variant places ions cylindrically distributed in the ionisation zone along the axis of the filament housing, with the same length as the filament housing exit radius (see Figure 5.26, bottom). The same velocity distribution as in variant 2 is applied.

5.2.3 Voltage Optimisation

The voltage set applied to the electrodes has been optimised to have the largest possible incidence rate (E), the ratio of ions hitting the anode to the total number generated. The optimisation function is formulated as:

$$\begin{aligned}
\min_{x \in \Re} \quad & -E = \left(-\frac{n_{hit\ anode}(x)}{n_{generated}} \right) \\
\text{s.t.} \quad & x_{l,i} - x_i \le 0 \qquad i = 1, ..., n \\
& x_i - x_{u,i} \le 0 \qquad i = 1, ..., n,
\end{aligned} \tag{5.17}$$

$n_{hit\ anode}$ being the number of ions splatting on the anode, $n_{generated}$ the number of generated ions, x the vector of changeable voltages, $x_{l,i}$ the lower and $x_{u,i}$ the upper bound of the electrode i as described in Figure 4.11.

The optimisation process involves fixed parameters such as temperature and pressure during all variants, set to $T = 273\ K$ and $p = 10^{-8}\ mbar$. The MIDACO algorithm (Mixed Integer Distributed Ant Colony Optimisation), a derivative-free, evolutionary hybrid algorithm, is used for optimisation (Schlueter, 2019). The voltages of the hemispherical reflector, reflector base plate, anode grid, and electron repeller are optimised, while the filament housing voltage remains constant, simulated only in the first approach and connected to the electron repeller in the actual hardware. The algorithm runs until iteration or computation time criteria are met, with a maximum of 1000 iterations and 3 hours for all variants.

TABLE 5.6: Results from NDG voltage optimisation.

x	Name	Optimal Voltage [V]		Variant 3		Initial Conditions [V]
		Variant 1	Variant 2	Run 1	Run 2	
1	Hemisph. Reflector	200.6	88.2	55.1	25.9	110.0
2	Base Plate	6.9	204.3	229.8	156.4	0.0
3	Anode Grid	129.3	204.4	230.0	156.8	180.0
4	Electron Repeller	-95.9	-35.7	-44.6	-66.4	-12.0
	Incidence Rate	0.902	0.969	1.000	1.000	

Table 5.6 summaries the optimisation results for the three different particle initial distribution conditions. For variant 3, a secondary optimisation run explores reduced voltage bounds, demonstrating potential energy savings without sacrificing information. Incidence rates for all variants exceed 90%, with variant 2 achieving almost 97% and variant 3 attracting 100% of created ions. The lower value of variant 1 might be explained with the asymmetric distribution of the created ions due to the skew-shaped electron beam. The skewness induces ion flight paths which cross the ion focusing lens at a high angle and the ions can therefore not be redirected towards the electron collector.

Comparing optimal voltage values reveals significant differences between variants and initial conditions. Notably, variant 1 yields distinct optimal voltage values, possibly attributed to asymmetric ion flight paths, inducing a larger reflector voltage and a low ion lens voltage. Variants 2 and 3 consistently show closely aligned optimal voltages for the ion focusing lens and the ionisation zone. These findings suggest potential simplifications in the electrical supply system design if validated in real measurements.

The study underscores the sensitivity of results to different model and optimisation conditions. Although the simulations present various variable combinations leading to favourable outcomes, experimental research on the flight model and spare instrument is essential for defining optimal voltages for the real NDG in Comet Interceptor. An exploration of voltage changes for the NDG is detailed in Section 2.2.1.

5.2.4 Experimental Optimisation and Simulation Model Adaptation

To validate and enhance the computational models discussed in Section 5.2, a comprehensive parameter study of the NDG's voltages has been executed in the laboratory. The experimental results and the ensuing adjustments made to the computational model based on the experimental study are described in this section.

The SIMION model from Section 5.2 underwent modifications by merging variants two and three. This combined model used a cylindrical ion distribution centred on the filament housing, with a radius of 62 mm and a length of 47 mm. The ions' initial conditions retained a Gaussian velocity distribution with a standard deviation according to the Maxwell-Boltzmann distribution of a kinetic gas. The simulation considered an even distribution of H_2O, CO_2, and N_2.

Anode Grid

The anode grid voltage was systematically varied from 150 V to 230 V on the NDG prototype, and the resulting ion current was measured at each voltage step. The objective was to establish the relative relationship between the anode grid voltage and the measured ion current. The observed signal changes were normalised to the baseline voltage settings (Mehta, 2023b), and the percentage change concerning the baseline is presented in Figure 5.27. The graph indicates a peak in the measured ion current at 200 V, slightly higher than the baseline voltage of 180 V. The computational simulation did not represent the anode grid dependencies from the experimental measurements, possibly since the model excluded the filament and ejected electrons, creating ions at a fixed place. However, the improvements with the physical instrument and the computational model are both marginal, less than 5%, indicating that the anode grid does not need to be largely optimised from its baseline voltage.

Hemispherical Reflector

The voltage of the hemispherical reflector was varied between 50 V and 200 V. The resulting ion current shows an increasing signal with the rising voltage, reaching an increase of up to 25% compared to the baseline settings (Figure 5.27). A plateau is observed around 180 V, beyond which further voltage increase leads to a decrease in the measured signal. This suggests that the maximum is at 180 V, likely influenced by the anode grid voltage. The computational model successfully replicated the influence of the hemispherical reflector voltage, aligning well with the experimental trends. This indicates the model's capability to reproduce the hemispherical reflector voltage trends for further optimisation.

Reflector Base Plate

The reflector base voltage was adjusted from -30 V to +30 V. Applying a negative voltage increased the acquired signal by up to 10%, while a positive voltage decreased the signal by a similar magnitude (Figure 5.27). Similar to the hemispherical reflector, the voltage of the reflector base was well reproduced in the computational model. The model reproduced the signal trends, although the slope of the signal decrease with increasing voltage was slightly smaller compared to the experiments. It is, however, unfortunate that these changes will not influence the final hardware, as the reflector base plate will be connected to the ground in the flight model.

Electron Repeller

The electron repeller voltage was altered between -18 V and -2 V. An increase in the measured signal of approximately 5.5% was achieved by increasing the electron repeller voltage (Figure 5.27). A plateau was observed between -6 V and -4 V, beyond which further voltage increase led to a decrease in the signal. The electron repeller has not been simulated in this version of the computational model as no electrons are simulated and ions have only been placed inside the anode grid.

Filament Offset

The filament offset voltage was adjusted between 0 V and 40 V. The results indicate that the baseline achieved the peak value of the acquired signal, suggesting that no voltage changes are required for the filament offset (Figure 5.27). The filament offset is not simulated in the model for the same reasons as for the electron repeller.
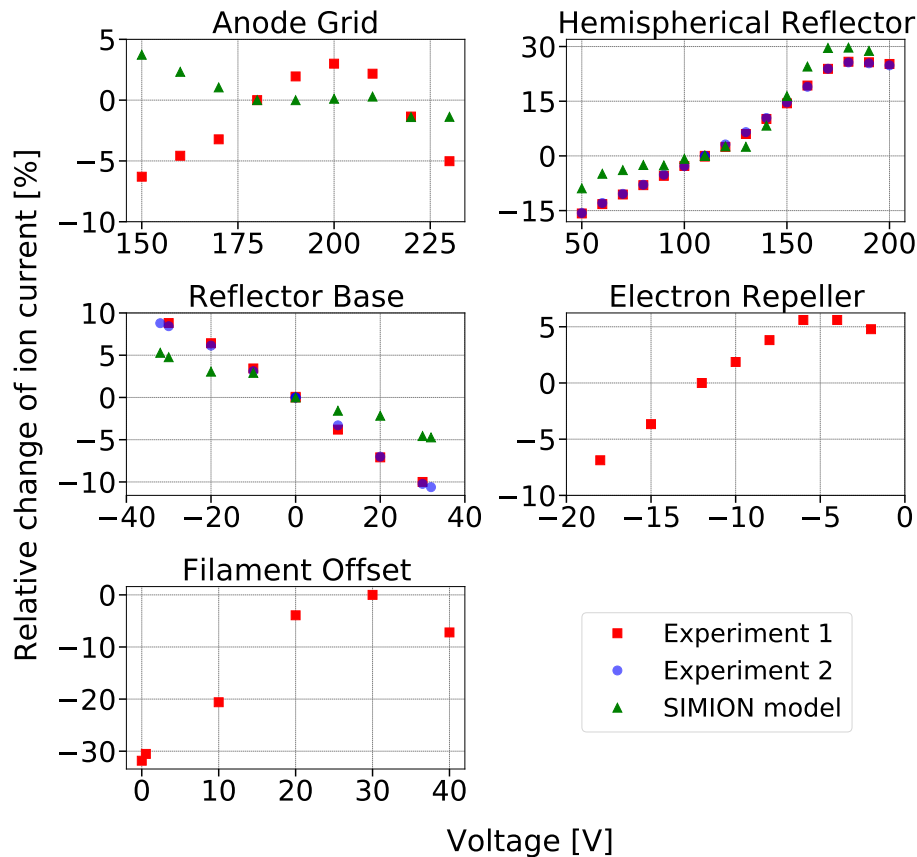
FIGURE 5.27: Experiment and simulation results for parameter study of NDG voltages.

Combined Voltage Changes According to Parameter Study Results

The combined effect of voltage changes, based on the individual findings, was explored. The relative change in acquired signal compared to the baseline voltages was measured. Figure 5.28 presents the results in a 5-D plot, with axes representing the anode grid, hemispherical reflector, and reflector base voltages. The size of the data points conveys information about the electron repeller voltage, while the colours indicate the relative current change in percentage. The results indicate that a maximum is reached with 200 V on the anode grid, consistent with the individual voltage changes (Figure 5.27). The reflector base voltage exhibits a similar influence to that observed in individual changes. Additionally, the voltage of the hemispherical reflector can be increased to 200 V when the anode grid is also set to 200 V. This supports the assumption made in Section 5.2.4 that the maximum of the hemispherical reflector voltage aligns with the anode grid voltage, both accelerating ions toward the collector. While the influence of the electron repeller voltage is not immediately apparent in Figure 5.28, the limited data points suggest a shift of its individual maximum being between -4 V and -6 V to -10 V. Additionally, the electron repeller is also needed to keep external electrons (e.g., from dust impact plumes, see Section 5.2.5) outside.

An improvement of up to 42% was achieved through combined voltage changes, clearly surpassing the improvement obtained through individual changes.
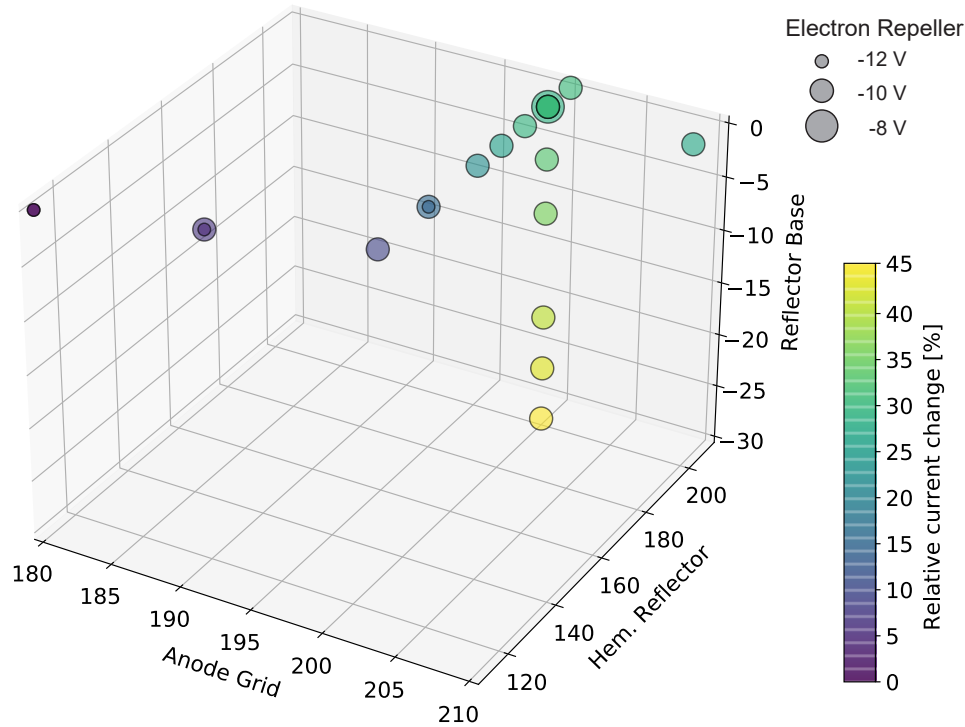
FIGURE 5.28: Relative change in ion current compared to baseline voltage settings (Mehta, 2023b) by changing anode grid, hemispherical reflector, reflector base, and electron repeller voltages with the NDG prototype in the laboratory.

Computational Optimisation of Hemispherical Reflector and Reflector Base

Computational optimisation of the hemispherical reflector and reflector base voltages was performed as in Section 5.2.3 by using the improved model from Section 5.2.4. Two optimisation runs were executed with different starting points, demonstrating convergence after about 700 iterations. The results indicated that the optimal hemispherical reflector voltage ranged between 190.8 V and 192.9 V, with a reflector base plate voltage between 23.0 V and 25.7 V. The signal improvement ranged from 45.2% to 51.7%. The minor dispersion between the two results suggests global convergence, with differences falling within model uncertainties. In conclusion, increasing the hemispherical reflector voltage to approximately 190 V and the reflector base voltage to about 24 V could improve the acquired signal by approximately 50%. This result is in line with the experimental results from Section 5.2.4, showing only minor differences of a few per cent, and demonstrates the working principle of the SIMION simulation model.

TABLE 5.7: Results of computational optimisation with variable hemispherical reflector and reflector base voltages.

Opt. #		Hemisph. Reflector	Reflector Base	Signal Improvement
1	Init. Conditions	110.0	0.0	
	Best Result	190.8	25.7	+51.7%
2	Init. Conditions	150.0	15.0	
	Best Result	192.9	23.0	+45.2%

5.2.5 Hypervelocity Impact and Plasma Phenomenon

The Comet Interceptor spacecraft is anticipated to perform a cometary fly-by with a relative velocity between 10 and 70 km/s. At this speed range, data from previous missions suggest the likelihood of hypervelocity impacts, where dust particles smaller than one milligram could enter the antechamber and collide with its material. Hypervelocity impacts are defined in literature in two ways (Fletcher et al., 2015): (a) an impactor traveling at a velocity exceeding the target material's speed of sound (generally 5–10 km/s), resulting in the generatoin of a shockwave; or (b) an impact where isotropic pressure initially dominates over deviatoric stresses within the solid. Impacts from meteoroids, space debris, and cometary dust grains with a high relative velocity larger than 10 km/s typically align with one of these definitions. Such impacts can lead to mechanical damage to the spacecraft or its instruments, but they also result in the generation of a plasma (Figure 5.29).
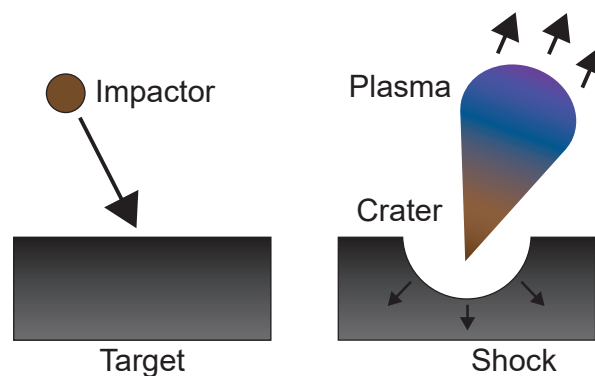

FIGURE 5.29: Hypervelocity impact creating a plasma. Reprinted from Fletcher et al. (2015), with the permission of AIP Publishing.

The stages of this phenomenon can be described as follows (see Figure 5.30 for an illustration): Following a hypervelocity impact by an object with a mass between 10^{-15} and 10^{-9} g, the resulting shockwave propagates both through the target and back through the impactor. At velocities exceeding ≈ 8 km/s, the entire impactor vaporises, with the residual energy being transferred to the target. The material behind the shockwave vaporises and ionises, forming a plasma with a density comparable to that of solid matter ($\approx 10^{28}$ m^{-3}). This dense plasma, with relatively low temperatures (down to 1 eV), is strongly non-ideal, influencing the equation of state, the energy transfer rate between ions and electrons, and critically, the charge state. As the shockwave expands, the energy density decreases, vaporisation halts, and a crater forms. Within the crater, various phases including plasma, gas, liquid, and two-phase flow coexist. Throughout this process, a significant pressure gradient exerts force on the plasma, driving its rapid expansion into the surrounding vacuum. During this expansion, the plasma transitions from non-ideal to ideal, from Maxwellian to non-Maxwellian distributions, and from highly collisional to collisionless. The latter transition effectively freezes the charge state within the plasma (Fletcher et al., 2015).

Fletcher et al. (2015) performed impact experiments, identifying impact speed as the critical parameter since many plasma properties exhibit minimal variation with impactor mass. While variations in mass influence the crater size and the total generated charge, their measurements and simulations indicate negligible effects on temperature or charge state. Measurements were taken along the central axis of the plume at the point where the plasma first transitions to a collisionless state. This transition point is estimated where $\omega_p / v_{ei} = 1$, with v_{ei} representing the Coulomb
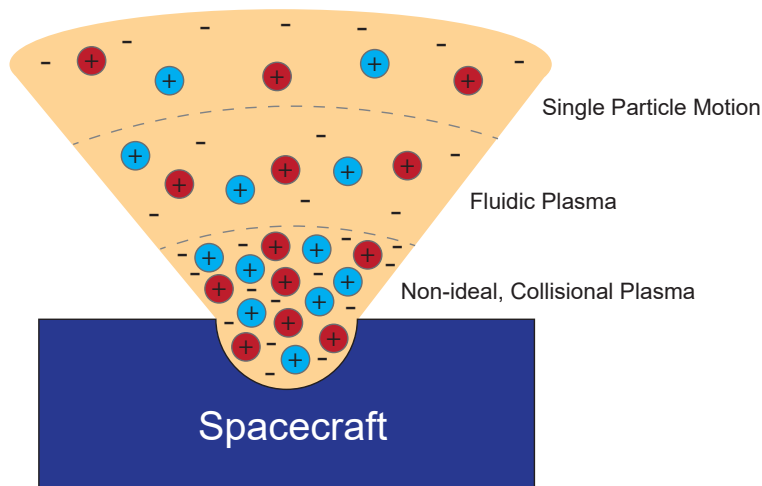
FIGURE 5.30: Cross-section of distinct expansion phases of a plasma – a non-ideal, collisional phase, a fluid-like plasma phase, and a single particle motion expansion phase. Electrons are represented by dashed markings while different ion species are indicated by coloured positively charged particles. The figure is not drawn to scale and for illustrative purposes only. Reprinted from Tarantino et al. (2018), with the permission of AIP Publishing.

collision frequency and ω_p the plasma frequency. The impact speed larger than ≈ 30 km/s resulted in a plume temperature plateau at ≈ 2.5 eV, while the expansion speed, influenced by the impactor mass, was of the same order as the impact speed itself (Fletcher et al., 2015).

Using information from Fletcher et al. (2015), a SIMION model was developed to simulate the influence of plasma-induced electrons on the NDG. Assumptions made to facilitate the model include:

- Only the last stage of the plasma, the single-particle motion, is modelled.
- Electrons from the plasma plume initially spread in all directions away from the inner antechamber surface in a cone with a half-angle of 45°.
- An electron kinetic energy of 2.5 eV is considered.

The antechamber's entrance hole, with a diameter of 5 mm, allows micro-particles ranging from a few ng to 1 μg and a diameter of approximately 5 μm to pass through at large entrance angles. Larger particles might only enter at smaller entrance angles. Additionally, the larger the grain the less frequent they are found in the coma. According to Rubin, 2021, grains with a radius of 10 μm have an impact probability of about 60%.

In simulations, the plasma plume was positioned at the antechamber's interior surface at different positions with respective entrance angles α between -15° and 45°. During the comet fly-by, the entrance angle of the gas flow will only be within a few degrees. The simulations indicate that, under the mentioned assumptions, a stable grounding of the antechamber at 0 V and a stable electron push-back due to the -12 V electron repeller prevent electrons from entering the electron repeller and the ionisation zone (Figure 5.31 a).

To identify the boundaries when electrons might pass through the electron repeller, different setting variations were explored. By increasing the electron repeller voltage to -2 V, some electrons pass through and ionise the neutral gas inside the anode grid, irrespective of the incidence angle (Figure 5.31 b). If the antechamber grounding were unstable, varying its voltage revealed that only at -10 V could some electrons
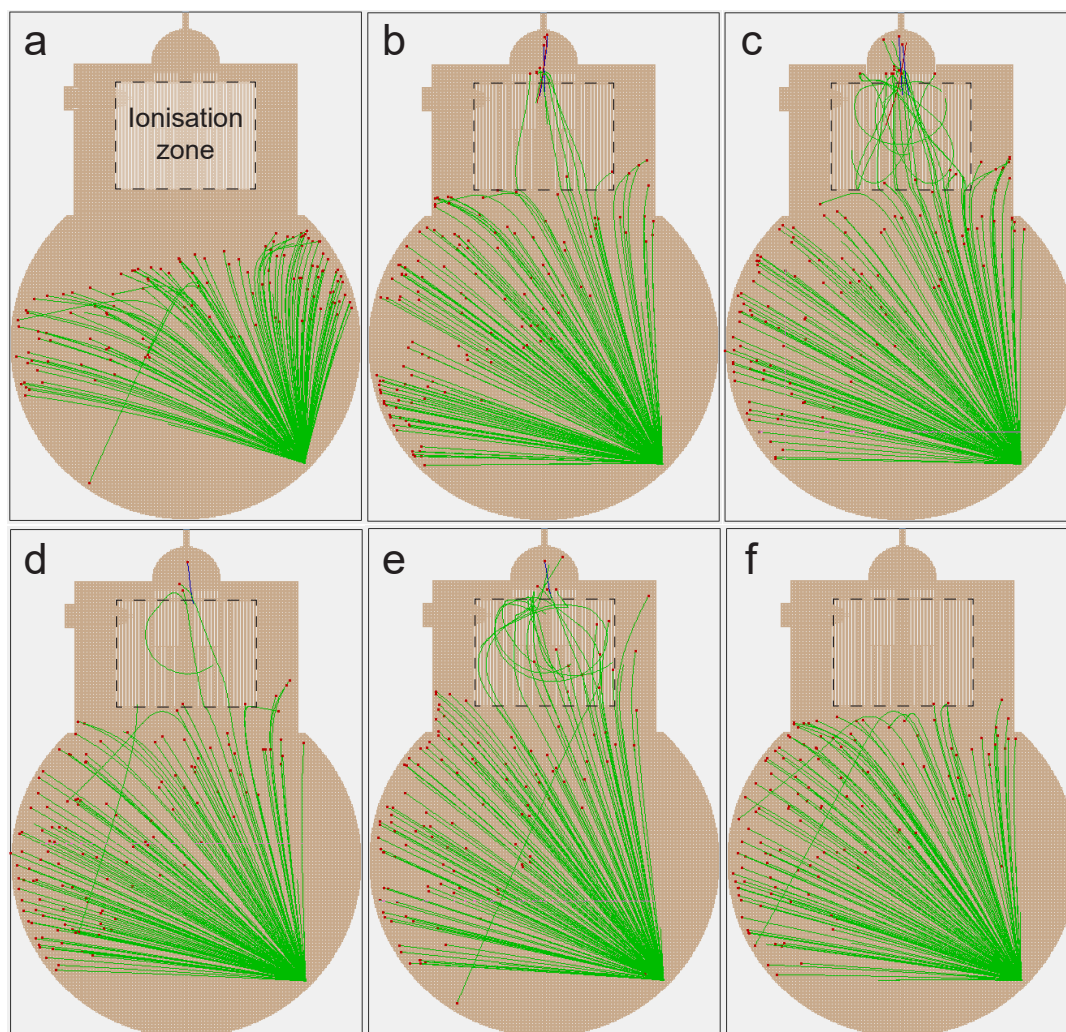
FIGURE 5.31: Hypervelocity impact simulations for different voltage configurations and plasma temperatures. The impact plasma plume at an impact angle of 22.5° and a plasma temperature of 2.5 eV creates electrons which are then deviated by the instrument's potential. The electron flight paths are marked with green lines, while their splat positions are marked with red dots. If electrons enter the ionisation region they ionise molecules which are then measured by the ion collector (red and blue lines represent ion flight paths for CO_2 and H_2O, respectively, which are only appearing in panels b – e). Different scenarios are considered: Panel a: Baseline NDG voltages. Panel b: Electron repeller voltage changed from -12 V to -2 V. Panel c: Antechamber charges itself up to -10 V. Panel d: Plasma temperature of 13 eV with baseline voltage settings. Panel e: Plasma temperature of 40 eV with baseline voltage settings. Panel f: Plasma temperature of 40 eV with electron repeller voltage of -40 V.

from the plasma overcome the electron repeller barrier and ionise the neutral gas, independently of the incidence angle of the dust particle (Figure 5.31 c).

An important uncertainty factor is the plasma temperature. In Fletcher et al. (2015), the plasma temperature was measured on the central axis at the collisionless border of the expanding plasma. This is not possible to simulate in SIMION and it is thus highly likely that the plasma temperature needs to be implemented with a higher value. With standard voltage settings, some electrons can pass through the electron repeller at 13 eV (Figure 5.31 d) and higher, which is a factor of 5 higher than the value measured in Fletcher et al. (2015). However, these authors mention different sources measuring

up to 40 eV, which would significantly increase the number of electrons overcoming the electron repeller barrier (Figure 5.31 e). For a possible plasma temperature of 40 eV, the electron repeller voltage would need to be decreased to approximately -40 V to prevent any electrons from entering the ionisation zone (Figure 5.31 f). However, the exact voltage would need to be determined experimentally, as the plasma temperature has a large spread of values in the literature.

In conclusion, the study investigates hypervelocity impacts and resulting plasma effects on the MANiaC NDG. Using insights from Fletcher et al. (2015), a SIMION model is developed, highlighting the importance of stable grounding and electron repeller settings to prevent electron intrusion. The model shows that an electron entering the ionisation zone from the created plasma is unlikely under the current voltage and grounding settings. However, uncertainties in plasma temperature underscore the need for a careful parameter refinement. The results provide valuable considerations for spacecraft survivability during the cometary fly-by.

Results from SHU Measurements

<div style="text-align: right; font-size: 3em;">6</div>

This section gathers the results from testing the prototype of the MANiaC mass spectrometer SHU. Calibration measurements were performed to ensure the instrument meets its requirements. First, a voltage parameter study is presented, examining various voltage sets and their influence on signal strength. Subsequently, signal stability measurements conducted during calibration, a noise analysis, long-term detector behaviour, and the influence of the pulser performance on the mass resolution are discussed. For additional calibration results, please refer to Stanic (2024).

6.1   Voltage Parameter Study

The SHU is driven by 17 different voltages, creating a complex system when trying to find an optimal voltage set for the best ion-optical performance. Thus, voltage optimisation is one of the most intricate tasks of the instrument, requiring precise knowledge of both system design and subsystem interactions. Key knowledge areas include the temporal behaviour of the ion source (IS) and electronics, voltage sensitivities and ramping mechanisms, resolution dependence on *m/z*, spectrum evaluation, resource consumption for calculations, and the optimisation algorithm itself. This section introduces the optimiser used for the SHU and discusses voltage constraints identified during various optimisation iterations.

Modifying voltages on the electrodes of the ion optical system alters the electric fields in the sensor, thereby changing ion trajectories. This adaptation can affect the time of flight of individual species and modify the resulting peak shapes.

The optimiser comprises three main elements: a domain, an objective function, and an algorithm for evaluating the objective function within its domain. For the SHU, the domain is defined by the allowable voltage sets derived from the default voltage limits (Mehta, 2023b), which restrict the optimisation range. The operator can further constrain this range. The voltages act as independent variables for the objective function, which converts each acquired mass spectrum (for a given voltage set) into a real number. The algorithm then attempts to minimise this number by changing the voltage set until it converges to a minimum (Fausch, 2020).

An Adaptive Particle Swarm Algorithm (APSA) (Zhan et al., 2009; Bieler et al., 2011; Hofer, 2015), similar to the algorithm in Section 5.2.3, is used. This algorithm evaluates particles (voltage sets) over several generations (iterations). A particle is a vector where the voltages to be optimised represent its elements. This multi-objective optimisation algorithm is advantageous as the domain is highly parameter-dependent. Furthermore, it has proven itself for previous space instruments (e.g., Fausch, 2020; Föhn, 2021).

The objective function rates the mass spectrum or a selected peak of that spectrum. The algorithm directly rates the raw spectrum in units of samples as a time spectrum, requiring no post-processing. Various methods exist to rate spectrum quality, including peak height analysis, signal-to-noise ratio analysis, Gaussian peak fitting, and moment analysis.

A commonly used objective function in mass spectrometry and gas chromatography is based on robust statistical moment analysis of a time signal (Morton and Young, 1995). It uses the zeroth moment (area), the second moment (peak width), and the third standardised moment (skewness). For the SHU prototyping phase, a simplified statistical moment analysis was used as the objective function ($f(x)$), comparing the ratio of the squared amplitude (A^2) of a single peak with its FWHM:

$$\min_{x \in \mathcal{D}} f(x) = -\frac{A^2}{FWHM},$$ (6.1)

with x the vector of voltages and $\mathcal{D}$ the domain of feasible voltage sets. The *m/z* 40 peak of the noble gas argon was chosen as a model peak for three key reasons: its *m/z* is sufficiently high to ensure that the influence of the high-voltage pulser on peak resolution is acceptable, no fragmentation occurs for noble gases, making the peak heights independent of fragmentation effects from different IS settings, and argon is readily available for laboratory measurements.

During the SHU prototyping phase, 13 voltages were optimised automatically. Optimisation runs were separated into IS voltages (LVs) and separation region voltages (HVs) to simplify individual optimisation complexity, reduce measurement time, and ensure proper filament operation especially while changing IS voltages (see Figure A.2 for the composition of the IS and the separation region voltages consisting of the drift region and the reflectron). Due to the use of laboratory electronics, long cables, and vacuum chamber feedthroughs during prototyping, no voltage set has been established that could be directly used as an optimal voltage set in a flight model. However, trends and possible voltage constraints emerged during the more than 30 optimisation runs completed in this study.

Figure 6.1 and Figure 6.2 present the data acquired during numerous optimisation runs for the IS and separation region voltages, respectively. In both figures, the subplots in the lower left triangle show correlation plots between the different voltages and the score (S), which is the optimisation function ($f(x)$) normalised to its initial function value at the start of the optimisation for each run. The higher the score, the better the evaluation of the objective function. Low scores are plotted in black, with higher scores in progressively lighter brown. The diagonal subplots display histograms of the voltage and score distribution across all evaluations. The upper right triangle subplots show the Pearson correlation coefficient for each pair of voltages. An absolute Pearson correlation coefficient of 1 indicates a perfect linear correlation, while 0 indicates no linear correlation. In the lower left triangle subplots, linear correlation approximations are drawn in violet for (absolute) Pearson correlation coefficients larger than 0.5. The 95% confidence intervals for achieving at least half of the best score during optimisations are shown in grey in the last row of the figures. By constraining the voltages within these grey areas, there is a 95% confidence of achieving at least half of the best scores, significantly reducing the feasible domain and improving optimisation time. For the IS voltages, the ranges can be considerably decreased, while the high voltages in the separation region should remain relatively loose. Table 6.1 shows the 95% confidence intervals for all optimised voltages to reach at least 0.5 and 0.25 times the maximum score from the optimisations. The intervals

do not differ significantly between the two score thresholds, ensuring that the exact choice of the score threshold does not largely alter the result.

Some voltages show strong correlations that should be considered. The strongest correlations in the IS are between the IS entrance, IS repeller 1, and filament housing (Figure 6.1). Thus, increasing IS repeller 1 implies increasing the IS entrance while decreasing the filament housing, and vice versa. In the separation region, strong negative correlations exist between acceleration 3 and both the reflectron retarder and reflectron backplane (Figure 6.2). This is likely because, as acceleration 3 (a negative voltage) increases, ions receive less acceleration and are slower, requiring less deceleration, hence lower retarder and backplane voltages. The same reasoning applies to the reflectron repeller voltage, though the correlation is weaker. Additionally, a decrease in the reflectron retarder and repeller voltages strongly correlates with a decrease in the repeller backplane voltage. Slower ions penetrate less deeply into the reflectron, allowing for lower retarder, repeller, and backplane voltages.
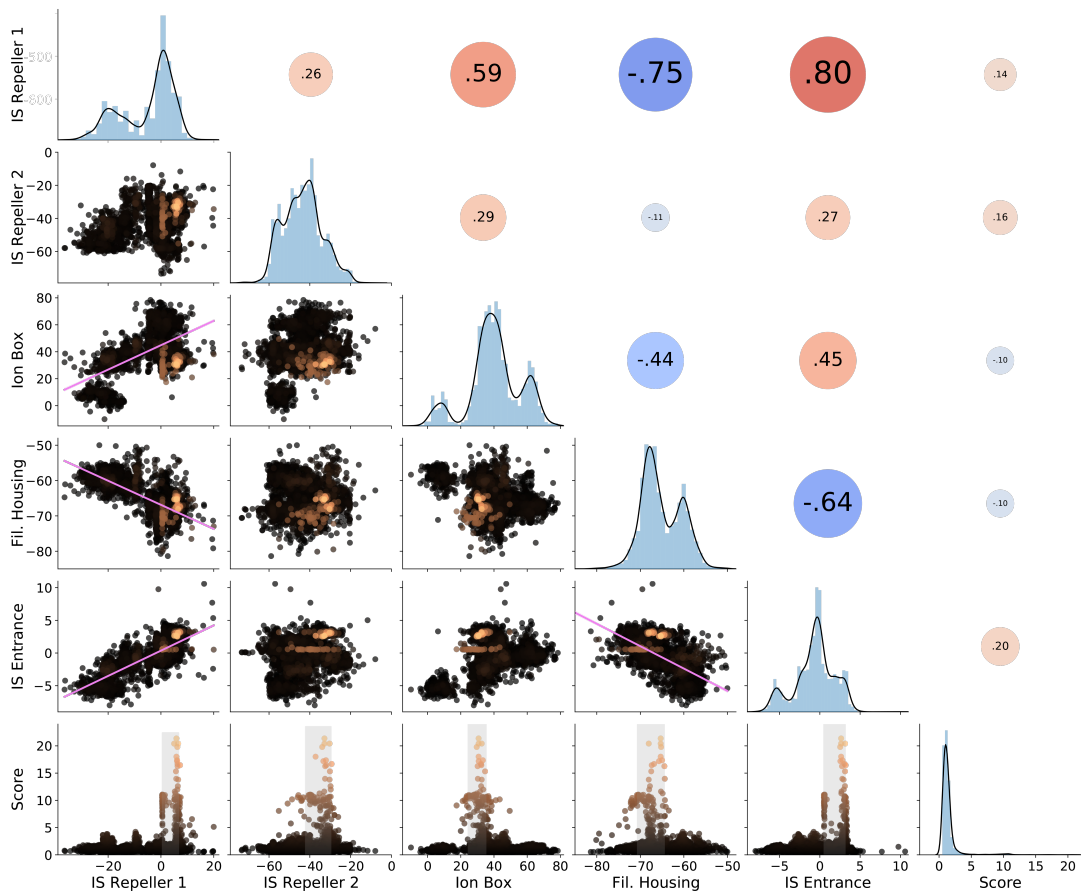

FIGURE 6.1: Voltage parameter correlation plot for IS voltages. Subplots in the lower left triangle show correlation plots between the different voltages and the score. Low scores are plotted in black, while higher scores transition to lighter brown. For Pearson correlation coefficients with an absolute value greater than 0.5, a linear correlation approximation is depicted in violet. The bottom row also displays the 95% confidence intervals (in grey) for reaching at least half of the best score achieved during optimisations. Diagonal subplots represent histograms of the voltage and score distribution across all evaluations. Upper right triangle subplots show the colour-coded Pearson correlation coefficient for each pair of voltages, with blue indicating negative correlations and red indicating positive correlations.
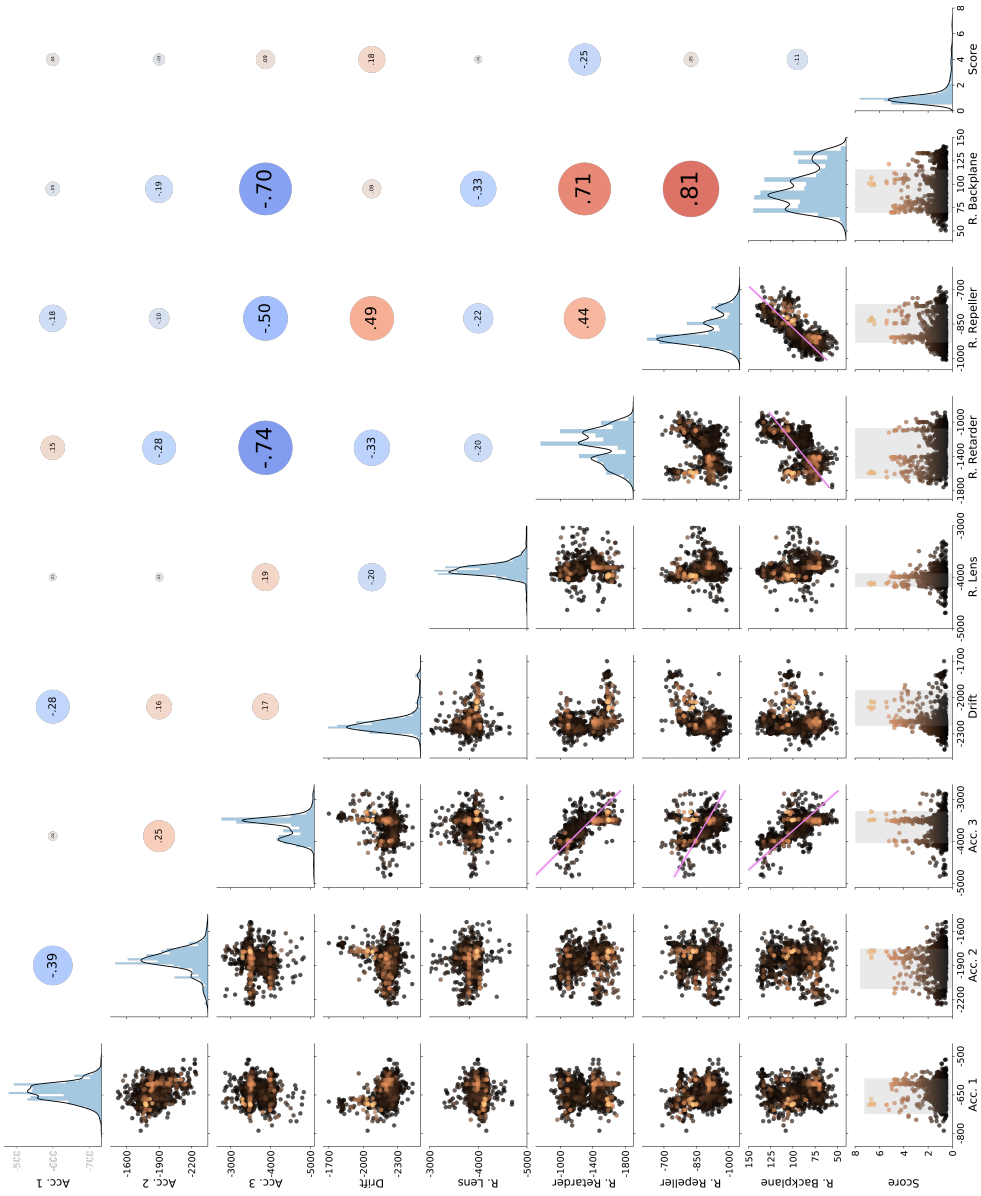
FIGURE 6.2: Same as Figure 6.1, but for the high voltages in the SHU's separation region instead of the IS voltages.

TABLE 6.1: Default limits for optimised voltages (Mehta, 2023b) and 95% confidence intervals for the score (S) to reach at least 0.5 and 0.25 times the maximum score (S_{max}) from the optimisations.

Voltage	Default Limits	95% Confidence Interval for $S > 0.5 \cdot S_{max}$	95% Confidence Interval for $S > 0.25 \cdot S_{max}$
IS Repeller 1	[-150, 150]	[0.5, 6.7]	[0.5, 7.5]
IS Repeller 2	[-150, 150]	[-42.2, -29.7]	[-49.1, -28.1]
Ion Box	[-150, 150]	[24.5, 35.2]	[21.5, 40.2]
Fil. Housing	[-150, 150]	[-70.7, -64.5]	[-73.0, -64.2]
IS Entrance	[-50, 50]	[0.5 , 3.2]	[0.5, 3.3]
Acc. 1	[-2000, 0]	[-721.9, -587.4]	[-731.1, -571.3]
Acc. 2	[-2000, 0]	[-2100.0, -1755.9]	[-2126.9, -1739.9]
Acc. 3	[-6000, 0]	[-4034.4, -3296.0]	[-4098.6 , -3274.7]
Drift	[-3000, 0]	[-2230.2, -1939.7]	[-2285.4, -1936.5]
R. Lens	[-6000, 0]	[-4181.3, -3932.6]	[-4182.0, -3768.0]
R. Retarder	[-2000, 0]	[-1654.1, -1078.1]	[-1691.0, -1000.2]
R. Repeller	[-2000, 0]	[-929.1, -765.3]	[-940.6, -759.9]
R. Backplane	[-150, 150]	[70.0, 115.3]	[70.0, 133.3]

6.2 Signal Stability

The instrument requirements mandate a signal stability of within 10% for at least one hour of operation (Section 4.2.4). Initial tests revealed inadequate signal stability. Consequently, various components were systematically replaced and tests were repeated until a satisfactory stability was achieved. This section provides an overview of the different configuration changes made.

Ion Source Investigation

The observed steady decrease in detector signal was initially attributed to unexpected charging in the ion source (IS). Subsequently, the IS was disassembled and examined under a microscope. Significant sputtering of the filament resulted in burning marks on several parts of the IS. Although the burning marks were predominantly minor and unlikely to alter the IS's functionality, the aluminium heater plate exhibited clear signs of charging, as evidenced by the burning marks indicating electrical field presence on the plate. To eliminate burning marks and IS charging as potential causes of signal instability, the IS was replaced with a pristine one and the heater plate was removed. Figure 6.3 illustrates the burning marks on different parts of the IS.

Unfortunately, the evolution of the main peak of the test gas over the experimental time, following the installation of the SHU with the pristine IS, indicated that approximately 70% of the initial signal was lost within the first 5 hours. Subsequent optimisation efforts only marginally increased the signal. Consequently, exchanging the IS did not improve the signal stability.
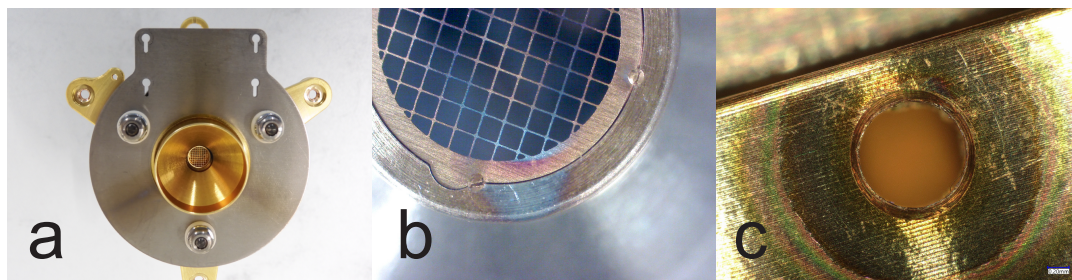
FIGURE 6.3: Burning marks on the SHU ion source. Panel a: Aluminium heating plate. Panel b: Backplane assembly. Panel c: Ion box holes where the emitted electrons from the filament should pass through to enter the ionisation zone.

Vacuum Chamber and Setup Exchange

Following the unsuccessful attempt to improve signal stability by changing the IS, the next course of action was to transition to a different vacuum chamber. This transition allowed for simultaneous testing of various setup changes, as all these factors differed in the new chamber:

- Stability of high and low voltage (HV and LV) power supplies

- Integrity of detector signal and power supply feedthroughs

- Chamber grounding scheme

- Data acquisition system

A 5-day measurement campaign revealed a signal loss of approximately 75% over 100 hours, despite numerous setup optimisations. Within the initial five hours, the signal loss approached nearly 40%. Thus, neither the chamber itself nor the power supplies or the data acquisition system were identified as the cause of the signal loss.

Detector and MCP Exchange

To determine whether the used detector or the MCPs degraded quickly over time, new MCPs were installed into the detector of a different TOF-MS, which was then mounted onto the SHU.

The results indicated an initial increase in signal upon instrument start-up, followed by a rapid decrease of about 60% within 18 hours. Despite voltage optimisations, the initial signal could not be restored, signifying insufficient signal stability.

Connect Detector Directly to IS

Following the successful preparation and testing of the CI detector (Section 6.4), it was connected to the instrument and the entire setup was returned to the initial vacuum chamber. To isolate whether signal instability stemmed from the drift tube or the reflectron, the detector was directly connected to the IS (Figure 6.4). Although this precluded the measurement of a real spectrum, the signal from the injected gas could still be discerned (Figure 6.5). Results indicated that after two days of testing, a signal loss of approximately half was still present. Thus, the measured signal remained insufficiently stable. Furthermore, the full configuration exhibited a significantly higher signal, approximately 25 times greater. Consequently, no evident cause of signal loss could be attributed to the drift tube or the reflectron.

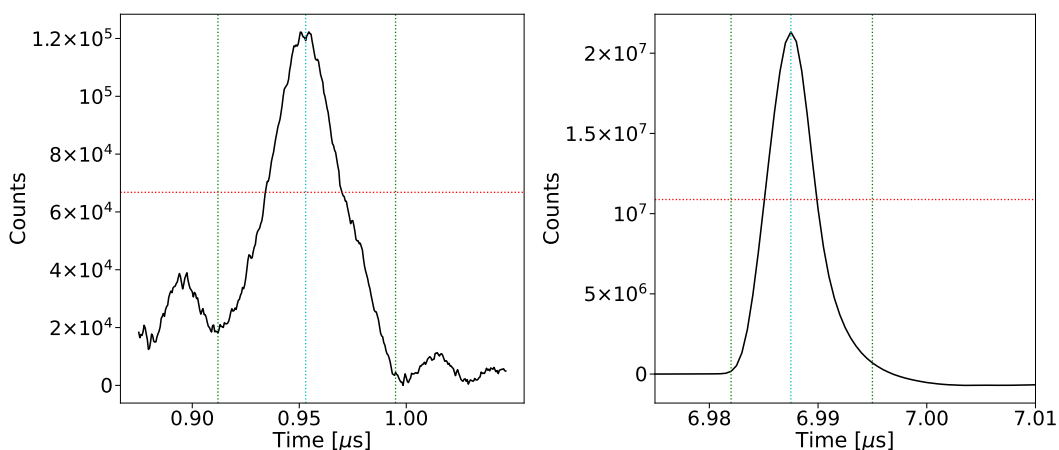FIGURE 6.4: Ion source connected directly to the detector.

FIGURE 6.5: Argon peak measured with SHU. Left: IS directly connected to detector. Right: full instrument configuration. The total number of ions measured was approximately 25 times higher with the full configuration compared to the direct configuration, indicating a significant loss in the latter that may be attributed to a non-collimated ion stream resulting from the absence of acceleration and focusing voltages.

Connect Detector Directly to Different IS

After the aforementioned tests, suspicion turned toward the IS as the potential cause of signal instability. Subsequently, the IS was replaced with one from a different TOF-MS, featuring a distinct design and using a different voltage set. Similar to the preceding section, the detector was directly connected to the IS. However, due to the inability to measure a real spectrum, a different gas (e.g., Xenon) had to be employed, as the original test gas was indiscernible amidst the noise. Regrettably, the measurements yielded minimal success, with the signal barely distinguishable from the noise. Although no clear signal loss was evident within the initial hours, over time, the signal became indiscernible, suggesting a gradual decrease until reaching noise levels. Consequently, replacing the IS failed to enhance signal stability.

Switch Filament

To ascertain whether the existing filament contributed to the signal instability, it was replaced with a new, pristine filament. The resulting behaviour mirrored that observed previously, with a signal loss of approximately 70% within 15 hours. Thus, the filament itself was not attributed to signal loss.

Improved Shielding and Filtering of Input Voltages

Shielding of the LV and HV supply cables with aluminium tape and filtering with ferrites aimed to mitigate potential large or fluctuating noise floors, which could lead to signal loss. Unfortunately, despite these adapted measures, signal stability remained poor, with considerable signal loss persisting.

Increased Pulser Input Voltages

Following the exhaustive tests mentioned above, focus shifted to the pulser. Consequently, the pulser input voltages (SET and RELEASE) were raised from 3.3 V to 5 V to assess the stability of the pulser's controller with increased input. Subsequently, after the startup phase and optimisation, signal loss over 20 hours reduced to approximately 30%. Although this improvement was noted, it failed to meet requirements and was observed at a relatively low signal level, where less signal loss was anticipated. Nevertheless, this outcome underscored the significant influence of the pulser on overall signal stability.

Pulser Tapering and Improved Detector Grounding

To evaluate the stability of the pulser output, an additional cable was introduced at the extraction grid to measure the extraction grid response outside the vacuum chamber during experiments. This increased the pulser response time due to added capacitance, particularly doubling the fall time of the pulse. Notably, signal stability was consistently observed over numerous hours when the pulser fall time was extended (Figure 6.6 , top), indicating instability when the pulser triggers were faster.

Normal Pulser Behaviour and Improved Detector Grounding

Following enhancements in detector grounding and confirmation of pulser stability under reduced speeds, the additional capacitance cable was removed, allowing the pulser to operate at nominal speed. Results demonstrated relatively stable signal behaviour even with the fast pulser (Figure 6.6 , middle), underscoring the importance of detector grounding for signal stability.

Gold Coated Detector Housing

Subsequent to improvements in detector grounding, the significant impact of grounding on signal stability became apparent. The initial detector housing, composed of polyether ether ketone (PEEK) and coated with titanium, exhibited electrical properties unsuitable for effective grounding due to the formation of a titanium-oxide layer akin to aluminium. Consequently, the detector housing was gold-coated (Figure 6.7). Following these modifications, it became evident that the instrument, including gas inlet and vacuum chamber pressure, required approximately 24 hours of stabilisation before safe operation. Post-stabilisation, voltage optimisations were conducted, resulting in signal stability with less than a 10% loss over 20 hours (Figure 6.6 , bottom).
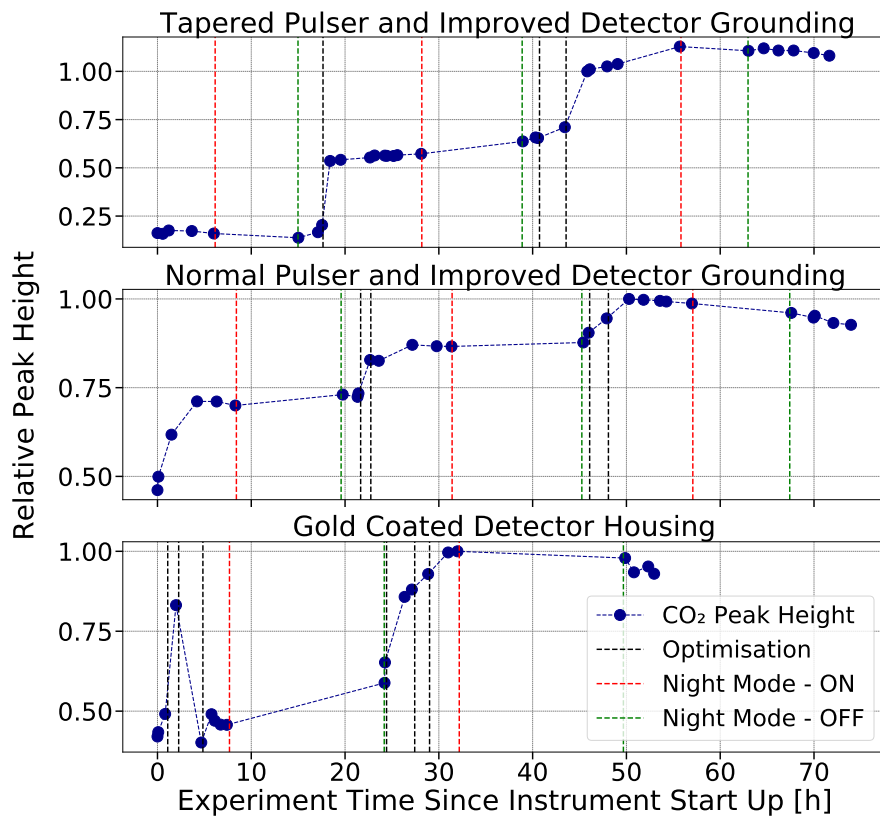
FIGURE 6.6: Maximum peak value of injected gas as function of time since the instrument was started for measurements with a tapered pulser (top), normal pulser behaviour (middle) and gold coated detector housing (bottom). The values are normalised to the first measurement after the last optimisation of each experiment. The black vertical lines show instrument voltage optimisations and the red and green vertical lines depict the start and the end of the night mode, respectively. During the night mode, the backplane voltage was adjusted that no ions pass through the reflectron to protect the detector from undesirable ageing.

6.3 Noise Analysis

Shielding and Filtering

Improvements in the shielding and filtering of LV and HV supply cables involved the addition of aluminium tape around the cables, cable enclosure grounded by ceramic capacitors, and implementation of RC filters where the cables pass through feedthroughs. Examination of the initial portion of the spectrum, where the first mass peaks (i.e., m/z 1 and 2) and most of the pulser noise are situated, revealed a significant reduction in noise amplitude due to shielding and filtering, particularly when combined (Figure 6.8). However, these measures inadvertently introduced high-frequency noise, possibly originating from standing waves trapped in the oversized vacuum chamber. To mitigate this, a cage was installed atop the instrument to attenuate standing waves in the chamber. While the cage reduced some high-frequency noise, it also introduced additional noise at lower frequencies, as evident from Figure 6.8.
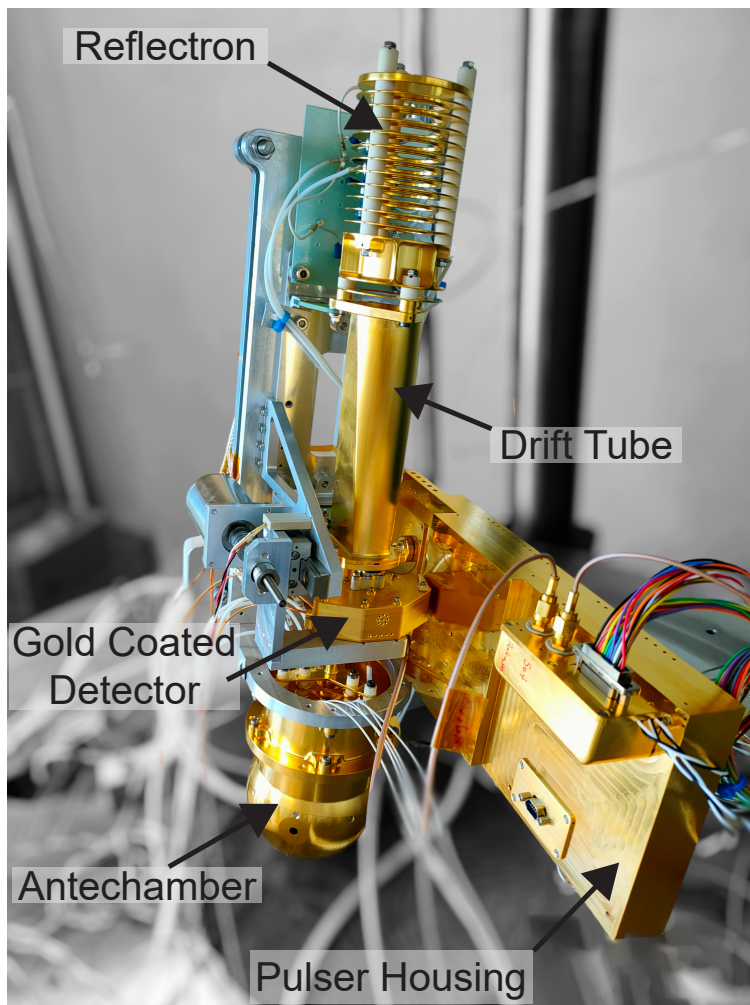
FIGURE 6.7: Full SHU prototype with prototype pulser and gold coated detector housing.

Moreover, only the measurement using the initial setup and the setup with the shield alone displayed peaks at m/z 1 and 2, where hydrogen is expected (see grey rectangles in Figure 6.8). However, this discrepancy may be attributed to the absence of a bake-out procedure following the installation of the shield, which has resulted in the retention of residual water and its fragments within the chamber. Nonetheless, traces of H and H_2 should still have been detectable in the subsequent configurations.

Comparison of noise levels across different filtering and shielding configurations, the shielding cage for the vacuum chamber, and various pulser fall times at a later spectrum stage (i.e., after the Ar and CO_2 peaks at 7.5 μs after the pulse trigger) revealed a consistent trend (Figure 6.9). Configurations incorporating shield and filter systems exhibited the lowest noise levels. Additionally, the introduction of the standing wave attenuation tent marginally decreased noise levels, contrasting findings from Figure 6.8 but likely attributable to diminishing pulser noise influence in later spectrum stages.

In conclusion, filtering and shielding of LV and HV cables are crucial, particularly in reducing pulser noise influence. Thus, it has been determined that a suitable filtering and shielding concept should be implemented for the flight model of the SHU. The temporary cage aimed to address issues related to the oversized vacuum chamber and will not be necessary with the implementation of a new, appropriately sized chamber and the foreseen conductive cover around the SHU flight model.
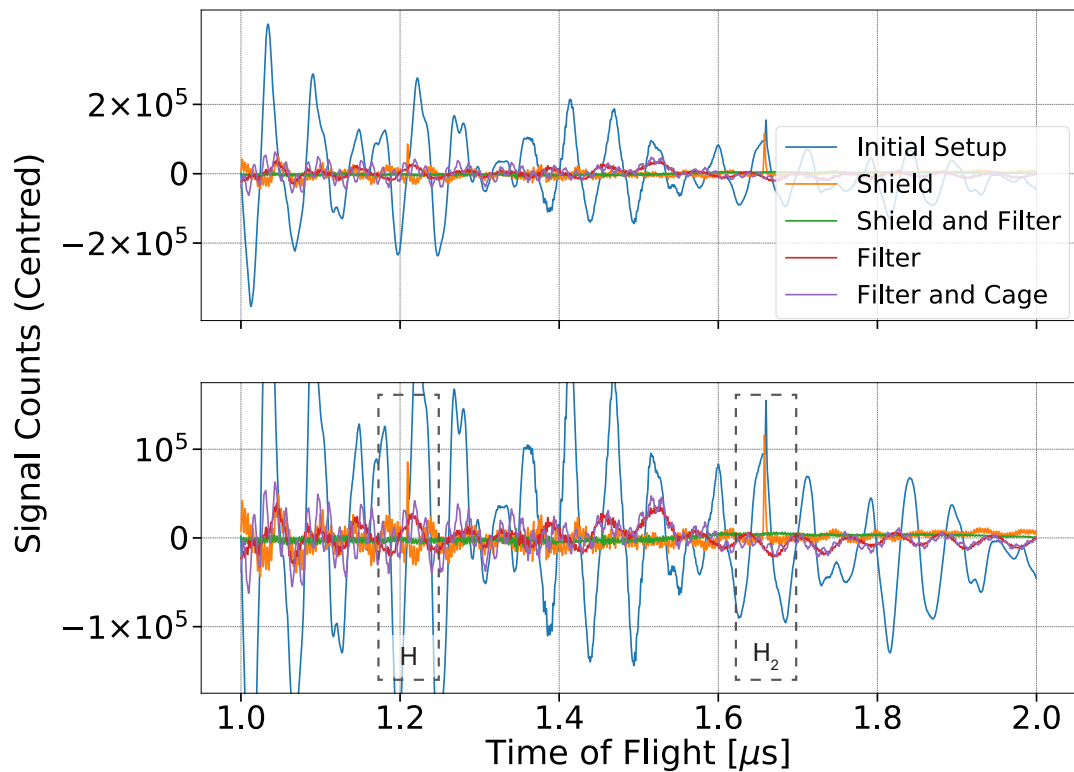
FIGURE 6.8: Signal count levels for different SHU measurement configurations for the spectrum time of flight between 1 and 2 μs. Top: Full data, centred for normalisation reasons. Bottom: Zoom to visualise smaller noise levels. The initial and the shielded and filtered setup show peaks at m/z 1 and 2 for H and H_2, not visible in the other configurations.
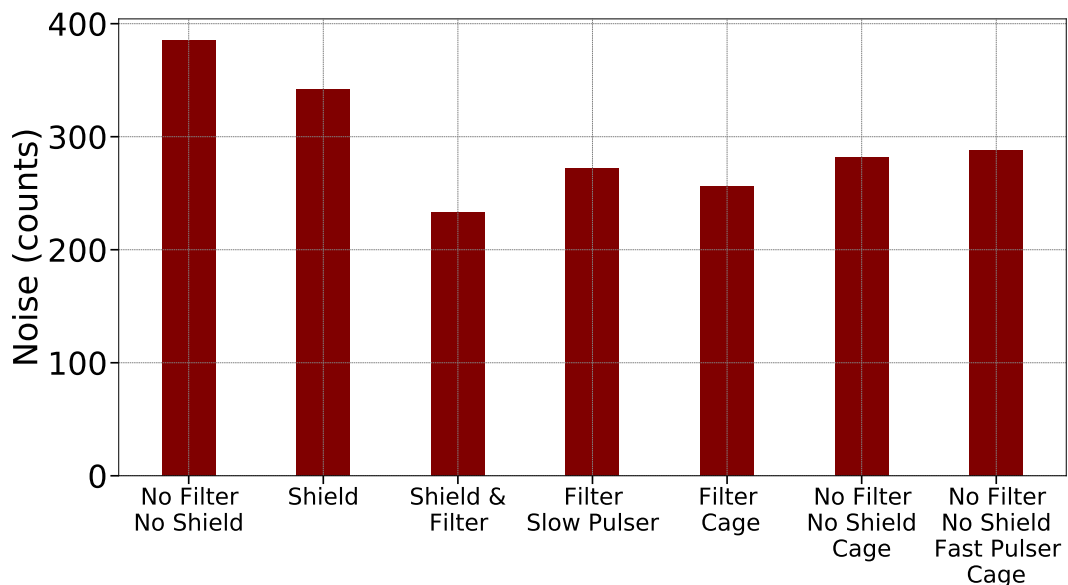

FIGURE 6.9: Root mean square noise levels for different instrument configurations, including filtering and shielding of LV and HV cables, a shielding cage for the vacuum chamber, and different pulser fall times. The noise has been acquired for 0.5 μs, 7.5 μs after the pulse trigger in the spectrum (i.e. after the Ar and CO_2 peaks).

6.4 Detector Behaviour

The MANiaC detector (WP211219A) underwent testing to assess its performance and gain. Galactic Cosmic Rays (GCR) measurements were conducted with the detector at various MCP voltages, each lasting 10 minutes. The number of analysed waveforms, indicative of incoming particle frequency, the Full Width at Half Maximum (FWHM) of pulses, and the MCP gain, were recorded for each MCP voltage (Table 6.2).

TABLE 6.2: Detector performance test results.

MCP Voltage [V]	FWHM Time of Pulses [ps]	Mean Signal [mV]	MCP Gain [-]
1620	184	1	$1.26 \cdot 10^4$
1670	170	1	$1.32 \cdot 10^4$
1720	220	1	$2.48 \cdot 10^4$
1770	459	15	$1.63 \cdot 10^6$
1820	786	23	$2.49 \cdot 10^6$
1870	810	33	$3.92 \cdot 10^6$
1920	984	51	$6.33 \cdot 10^6$
1950	1030	60	$7.95 \cdot 10^6$

The detector exhibited very low gain at MCP voltages below 1750 V, demonstrating proper functionality only at higher voltages. Beyond 1750 V, the detector gain approached levels comparable to those achieved with the NIM FS detector (Föhn, 2021). However, the FWHM time of pulses, approximately 1 ns at higher MCP voltages, suggests room for improvement through PCB design adjustments. Subsequent detector tests with GCR measurements were performed after the detector accumulated more than 1,000 hours of operation, revealing a tenfold decrease in detector gain over this period, highlighting the importance of detector ageing (Figure 6.10).
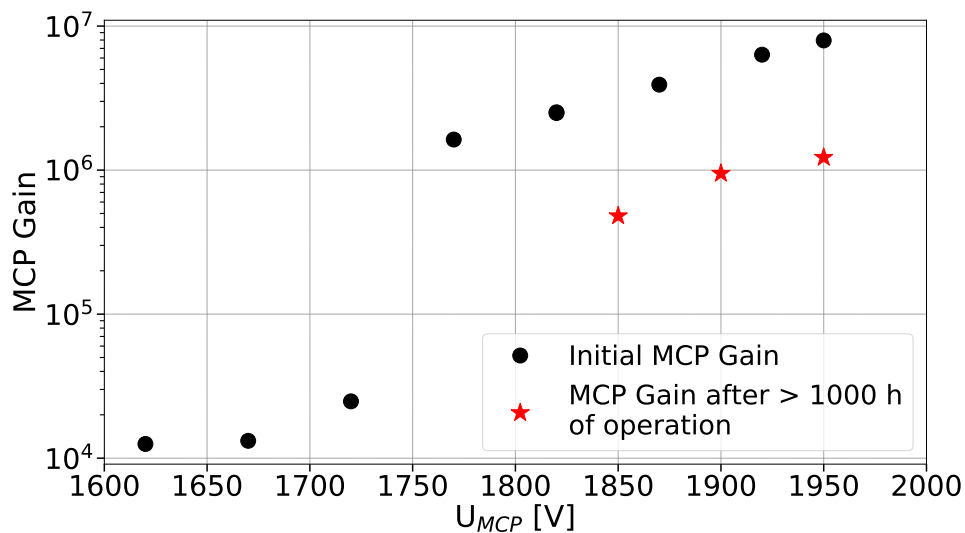

FIGURE 6.10: MCP gain as function of MCP voltage for detector WP211219A. Black circles represent the detector gain values for the pristine MCP's and the red stars show the gain after more than 1'000 hours of operation.

6.5 Mass Resolution Depending on Pulser Fall Time

The fall time of the pulser affects the speed at which ions are accelerated and directed into the mass separation segment of the instrument. To manipulate the pulser fall time, an additional measurement cable was introduced (Section 6.2). Two distinct pulser fall times were employed: the nominal pulse fall time was 5.2 ns, whereas the slower fall time was 10.9 ns. Figure 6.11 illustrates that mass resolution, expressed as R = m/Δm, notably improves with a faster pulser fall time due to remarkably narrower peak shapes (smaller Δm). This improvement is particularly pronounced for smaller masses and weaker signals. Hence, this demonstrates the importance of a fast pulser fall time.
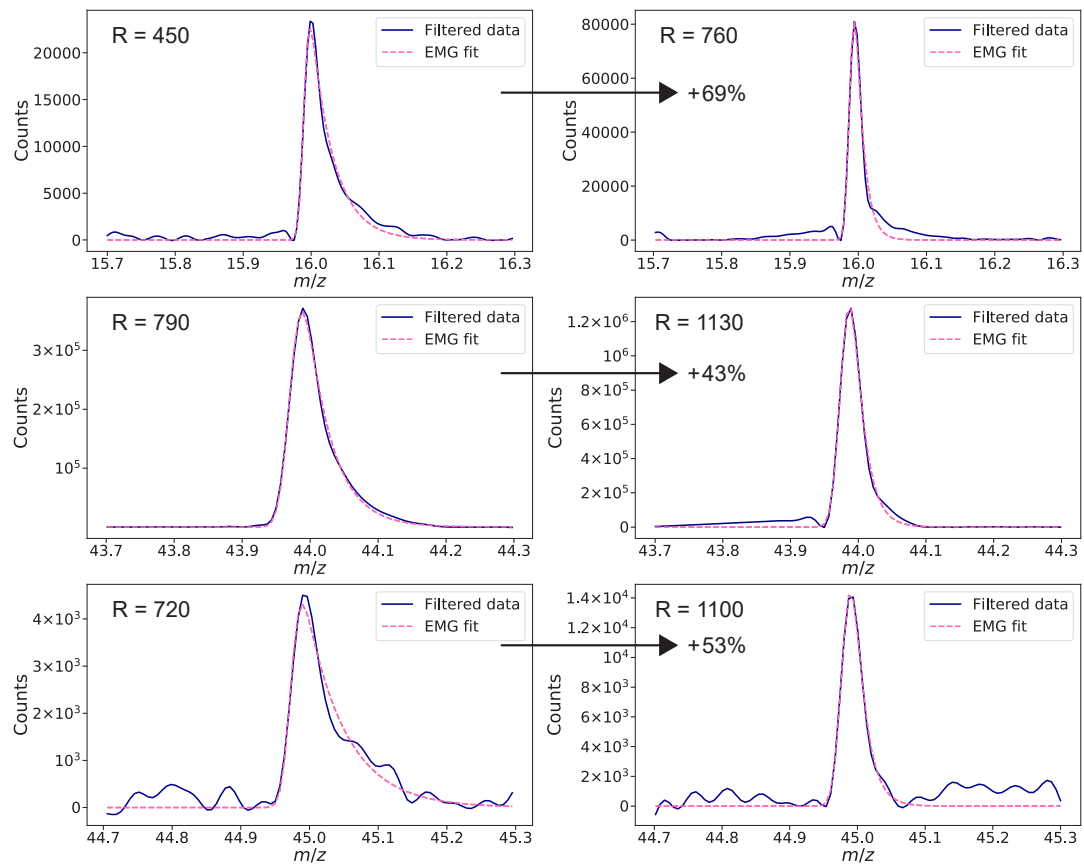
FIGURE 6.11: Mass peaks and respective mass resolution of *m/z* 16, 44, and 45 in spectra acquired with the slow pulser (left) and the nominal pulser (right). The data has been filtered with a Butterworth high-pass filter of third order and a cut-off frequency of 0.3 GHz. An exponentially modified Gaussian (EMG) fit has then been applied to the filtered data as this function showed the best performance for the peak shapes obtained with the SHU prototype. The EMG fit is further explained in Stanic (2024).

Evaluation of NDG and SHU Performance

7

Chapter 5 and Chapter 6 detailed the conducted experiments and presented their results. This section summarises these findings and compares them with the instrument requirements defined in Section 4.2.4 to evaluate the performance of both the NDG and SHU.

7.1   NDG Performance

IR1-PRF-4:   Temporal Resolution

> MANiaC (SHU and NDG) shall achieve a temporal resolution of 0.05 s.

Spatial resolution during the closest approach should be on the order of the nucleus diameter to study the spatial distribution of the volatiles in the coma. Assuming a 4 km diameter object at a 80 km/s flyby velocity requires a 0.05 s time resolution. Such a high measurement rate may also allow to distinguish the nominal coma from possible dust impacts near closest approach. The resolution is defined by the read-out electronics. The NDG continuously ionises the incoming molecules and the measurement can be done as fast as one chooses the read-out electronics to work. Thus, 50 ms is of no issue for the NDG and this requirement is fulfilled.

IR1-PRF-5:   Stability

> Relative abundances from MANiaC and total densities from NDG shall be stable (within 10%) for 1 hour of operation.

The NDG data shown in Figure 7.1 represent the measured ion current from starting the instrument and setting up the chamber pressure at time zero until 25 hours later. The first few hours are not stable due to instrument heat-up and chamber pressure instabilities during start up. By normalising to the chamber pressure and only looking at the data acquired after 3.5 hours of the start-up, the ion current is stable within $\pm 10\%$ for more than 20 hours (Figure 7.2). The total density is directly correlated to the measured ion current and thus this requirement is fulfilled. However, it also highlights that the NDG should be operated several hours before the actual encounter to allow thermal stabilisation.
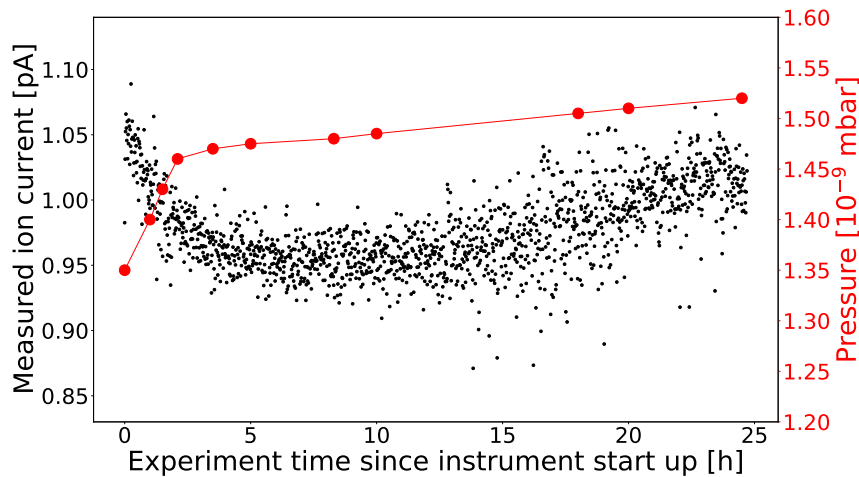
FIGURE 7.1: Measured ion current (left y-axis, black) and pressure (right y-axis, red) as function of experiment time with time zero when the instrument was started and the chamber pressure was set.
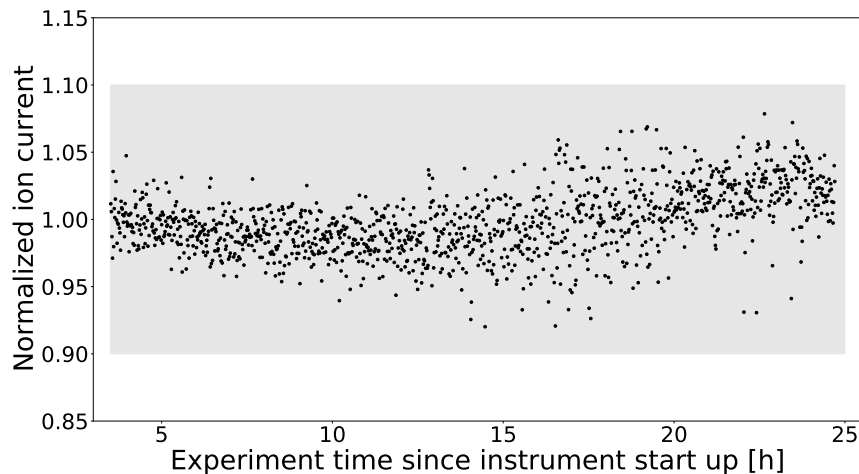

FIGURE 7.2: Ion current normalised to chamber pressure 3.5 hours after the start of the operation. The grey zone represents the $\pm10\%$ range of the measured ion current.

IR1-PRF-7: Detection Range NDG

> The NDG shall detect pressures in the range between $10^{-5} - 10^{-11}$ mbar.

The experiments have measured pressures between $10^{-6} - 10^{-9}$ mbar. The repeatability and linearity of the results is shown in Figure 5.2. Lower pressures were not possible due to pumping limitations of the vacuum chamber. However, lower signals could still be simulated and were accurately measured by reducing the emission current and detuning the instrument voltages. Hence, if the read-out electronics is sensitive enough, there should be no reason for the instrument not to work at the lower requirement limit of the pressure of 10^{-11} mbar.

IR1-PRF-8:   NDG Density Measurement Accuracy

> The NDG shall have an accuracy of 10% from $10^{-5} - 10^{-11}$ mbar within $1 - 10$ s integration time.

The NDG antechamber density shall be known to 10% to obtain the total outgassing rate of the comet. This corresponds to a collected ion current accuracy of at least 10%, e.g., 100 ± 10 fA to 100 ± 10 nA within $1 - 10$ s integration time. Measurements taken on different integration times show only a small variance less than 1% for measurements taken at 20 pA ion current. There is not more uncertainty expected for larger signals. However, for smaller signals down to 100 fA, the uncertainty largely increases due to the signal noise of the electronics. For the lower current range of the requirement, Figure 7.3 shows that the original data points measured with an integration time of 20 ms are largely scattered around the prescribed 100 fA and are not within the $\pm 10\%$ limits. However, when the data are integrated over 1 s or 10 s the measurements are within the $\pm 10\%$ limits and this thus satisfies the requirement on the density measurement accuracy.
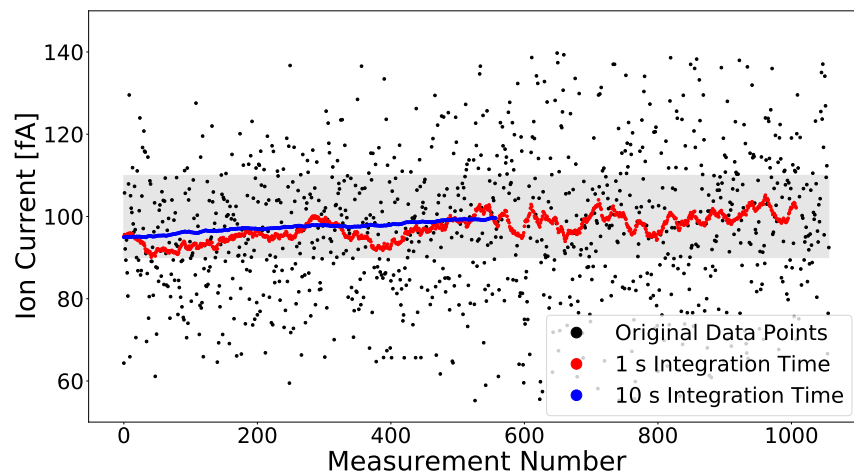

FIGURE 7.3: Ion current measurements for the 100 fA measurement level. Black points represent the original data points, the red points are integrated over 1 s and the blue points are integrated over 10 s. The grey zone represents the $\pm 10\%$ range of the measured ion current.

7.2 SHU Performance

IR1-PRF-1:   Dynamic Range

> MANiaC shall achieve $\geq 10^6$ dynamic range.
> Detection of all major and major minor species to the ‰-level w.r.t.
> the dominant water peak.

Figure 7.4, top shows a mass spectrum acquired with the SHU on March 2, 2023. The chamber pressure was $1.20 \cdot 10^{-6}$ mbar, and the chamber was not baked-out, resulting in the water signal (m/z 18) being the most prominent. In Figure 7.4, bottom, the y-axis is zoomed in, and baseline removal has been applied to reveal smaller peaks. The orange line indicates the ‰-level relative to the dominant water peak, while the green line represents the 10^6 dynamic range. The species expected in a mass spectrum of water are described in Table 7.1. Consequently, the major peak of H_2O at m/z 18 and the minor peaks at m/z 16, 17, 19, and 20 are all visible within the ‰-level (Figure 7.4, bottom).

Comparing the relative abundances from the NIST database with the SHU measurements (Table 7.1) reveals that the relative abundances are of the same order of magnitude for all m/z values, except for m/z 16. The significantly higher relative abundance at m/z 16 may be due to background gas. Since no additional gas was introduced into the chamber, only noise could be removed by background subtraction, and the remaining background gas was still measured and could not be discerned from the water signal. The excess of m/z 16 might thus be attributed to fragments of O_2 or CO_2, both visible in the spectrum.

The D/H ratio in water can be determined through this measurement. As indicated in Table 7.1, H_2O shows a fragmentation into OH of 0.2212. Additionally, the $^{16}O/^{18}O$ ratio is ascertained by the relative abundance values of m/z 18 and 20, given that the abundance of D_2O is negligible. Thus, $^{16}O/^{18}O$ equals 500, which aligns closely with the terrestrial literature value of 499 (Meija et al., 2016). However, the $^{16}O/^{17}O$ ratio cannot be determined because HDO, $H_2^{17}O$, and $H^{18}O$ cannot be distinguished by the SHU's resolution. For the laboratory measurements, we assume a terrestrial $^{16}O/^{17}O$ ratio of 2632 (Meija et al., 2016). It will also be necessary to assume the $^{16}O/^{17}O$ ratio for the Comet Interceptor data.

Previous studies, such as Müller et al. (2022) and Schroeder et al. (2019), have shown that the ratios of $^{16}O/^{17}O$ and $^{16}O/^{18}O$ have only been enriched by 11% in comet 67P. This enrichment falls within the range of measurement uncertainties of the SHU, justifying the assumption of the $^{16}O/^{17}O$ ratio. However, if the $^{16}O/^{18}O$ ratio from the intercepted pristine comet significantly deviates, a more thorough investigation will be necessary.

The relative abundance of m/z 19 compared to m/z 18 is calculated using the formula $2 \cdot (D/H) + {}^{17}O/{}^{16}O + OH/H_2O \cdot {}^{18}O/{}^{16}O$, where the factor of two in the D/H term accounts for the two possible placements of D in HDO. Employing a terrestrial D/H value of $1.558 \cdot 10^{-4}$ (Meija et al., 2016), a relative abundance of m/z 19 of 0.11 is obtained. Thus, the measured m/z 19 from Table 7.1 is slightly below the theoretical value but remains within the same order of magnitude. The NIST values for m/z 19 and 20 appear to be too high in light of these considerations, and this discrepancy remains unresolved due to the lack of detail in the NIST documentation regarding the methodology used to derive these values.

The dynamic range level of 10^6 corresponds to the current noise level. Therefore, the full dynamic range could not be resolved and the noise has to be reduced significantly for the flight model.

In conclusion, the requirement IR1-PRF-1 was met with respect to detecting all major and minor species to the ‰-level relative to the dominant water peak. However, the dynamic range of 10^6 could not yet be achieved.

TABLE 7.1: H_2O mass spectrum according to NIST (NIST Mass Spectrometry Data Center, 2023) compared to SHU measurement. The relative abundances are normalised to the main peak at *m/z* 18. The values in the VSMOW column are calculated using VSMOW ratios for the D/H, $^{16}O/^{17}O$, and $^{16}O/^{18}O$ from Meija et al. (2016) and account for the fragmentation of H_2O to OH based on SHU measurements.

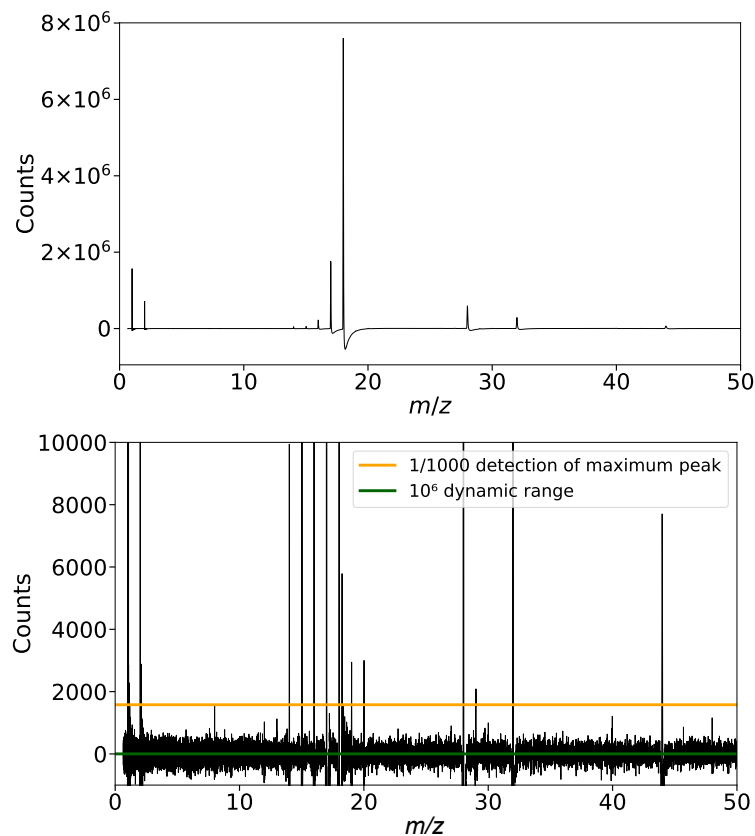| Mass [*m/z*]	Molecule	Relative Abundance		
		NIST	SHU	VSMOW
16	O	0.90	2.98	N/A
17	OH	21.22	22.12	N/A
18	H_2O	100.00	100.00	100.00
19	HDO, $H_2{}^{17}O$ & $H^{18}O$	0.50	0.09	0.11
20	D_2O & $H_2{}^{18}O$	0.30	0.20	0.20

FIGURE 7.4: Mass spectrum acquired with SHU. Panel a: Full mass spectrum acquired on March 2, 2023 at a pressure of $1.20 \cdot 10^{-6}$ mbar. The chamber was not baked-out for this test such that a relatively high water signal was present. Panel b: Zoom of the mass spectrum from panel a) after baseline removal, to remove undershoots after the large signals and to show the peaks with low counts. The orange line presents the ‰-level with respect to the dominant water peak. The green line represents the 10^6 dynamic range.

IR1-PRF-2:   Mass Resolution

> MANiaC shall achieve a mass resolution of m/Δm = 800.
> Target is a mass resolution of m/Δm = 1000.

From the mass spectrum of May 5, 2023 acquired at a pressure of $8.9 \cdot 10^{-7}$ mbar, the m/z 16, 44, and 45 have been analysed for their mass resolution (see Figure 6.11). For m/z 16, the resolution is slightly below 800, however, this can be overcome by using higher filament emission or MCP voltage. The changes needed would be marginal as the achieved resolution nearly meets the requirement. For m/z 44 and 45, the resolutions are clearly above target. The requirement IR1-PRF-2 is thus fulfilled.

IR1-PRF-3:   Mass Range

> MANiaC shall achieve a mass range 1 – 1000 m/z.

Xenon was the largest molecule measured until now. Thus the largest m/z measured was 136 (from ^{136}Xe). Nevertheless, larger masses should not present a problem, as the pulser timing for releasing and storing ions has been designed to accommodate for masses up to m/z 1000. Hence, the requirement IR1-PRF-3 is fulfilled.

IR1-PRF-4:   Temporal Resolution

> MANiaC (SHU and NDG) shall achieve a temporal resolution of 0.05 s.

As in Section 7.1, a time resolution of 0.05 s is required. This resolution is defined by the read-out electronics and the storage space. The SHU is pulsed by a 10 kHz pulse and thus has a storage phase of 100 μs. Hence, 50 ms accounting for 500 individual extractions is of no issue for the SHU and this requirement is fulfilled.

IR1-PRF-5:   Stability

> Relative abundances from MANiaC and total densities from NDG
> shall be stable (within 10%) for 1 hour of operation.

The flyby duration depends on the relative velocity and lasts from a few to several hours around closest approach. For this time, the measurement has to be stable. Several stability tests on the SHU showed that the instrument, the vacuum chamber and the auxiliary gas inlet need to stabilise over several hours (i.e. around ten hours).

After that the measured signal is relatively stable (Figure 7.5). A signal loss of less than 20% has been observed over a time span of 20 hours. During 1 hour of operation, as stated in the requirement, the signal is stable within less than 10%, considered that the instrument has been warmed-up for around 10 hours before taking the measurements. Therefore, this requirement is fulfilled.
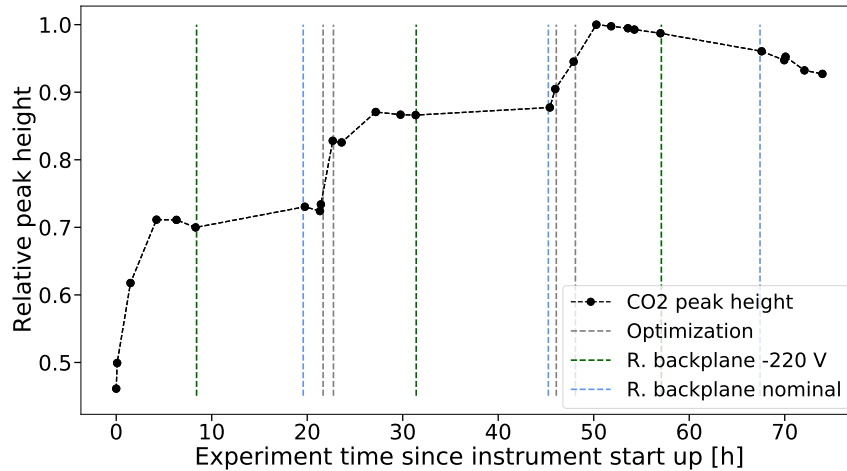

FIGURE 7.5: Relative peak height of the CO_2 peak from starting up the instrument at time zero for the measurement starting on May 1, 2023. The grey vertical lines represent voltage optimisations on the instrument. The green vertical lines show where the voltage on the reflectron backplane was changed to protect the detector during the night time and the blue line marks when the reflectron backplane was set back to its nominal value. The line between the data points is only for reader guidance, as there was no continuous data acquisition.

IR1-PRF-6:   Detection Limit SHU

> Species with an ambient density of 1000 cm^{-3} shall be detectable.

This requirement means that minor species with low abundances shall be detected. As per Jones et al. (2022), H_2O densities will have to be $> 10^7$ cm^{-3} to obtain the D/H ratio. Using D/H $\sim 10^{-4}$ the amount of heavy water will be $\sim 10^3$ cm^{-3} which drives the detection limit. Currently, the instrument achieves a Signal-to-Noise (S/N) ratio of $\sim 10'000$ at a pressure of $1 \cdot 10^{-6}$ mbar. The expected coma density is of the order of $1 \cdot 10^{-10}$ mbar. This means approximately $2.5 \cdot 10^6$ molecules cm^{-3}. Assuming linearity, the SHU would have a S/N of 1 at the expected coma density and thus the detection of $2.5 \cdot 10^6$ molecules cm^{-3} would just not be possible. There are a few possible improvements to overcome this issue:

- The detector voltage can be increased: Gain of a factor 10 possible (Figure 6.10).

- The filament emission can be increased: Gain of a factor 3 possible (Figure 7.6).

- The ram pressure in the antechamber during the fly-by will increase the number of molecules: Gain of a factor 18 possible at a fly-by velocity of 10 km/s (Figure 7.7).

In total, the sensitivity can thus be improved by a factor of $\sim$540. Hence, this would give a S/N of 1 for about 4'600 molecules cm^{-3}. To ensure detectability the lowering of the noise of a factor 5 is still required. This might be achieved by a more compact model, especially regarding electronics and cabling of the instrument and the associated grounding. To conclude, the requirement IR1-PRF-6 is not yet fulfilled, but possible improvements are to be integrated when testing the next instrument model.
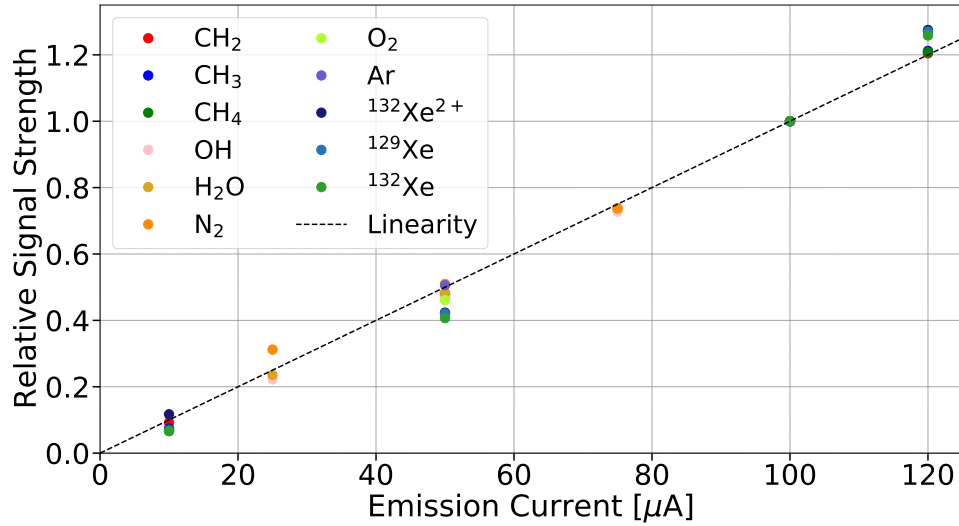
FIGURE 7.6: Relative change in peak signal as function of emission current for different molecules normalised to the signal value at 100 μA emission.
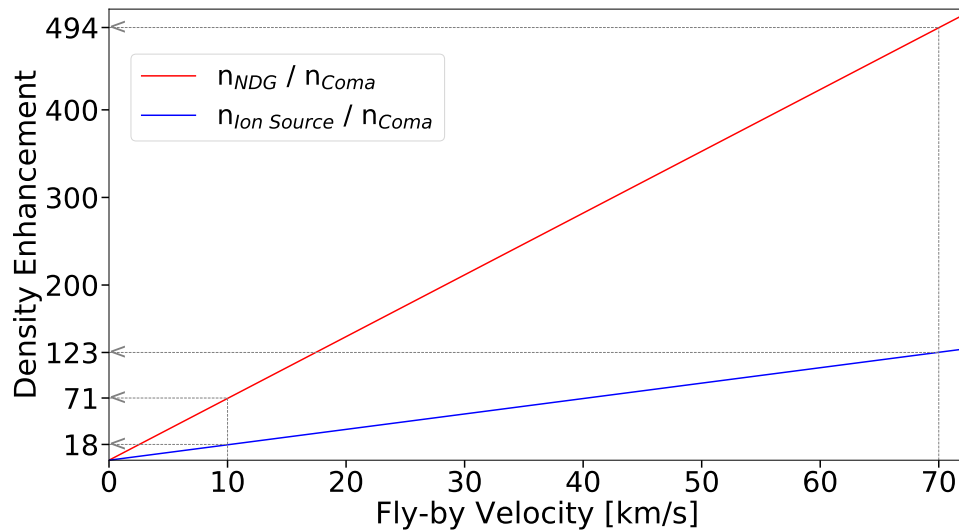
FIGURE 7.7: Density enhancement as function of fly-by velocity. The density inside the SHU's antechamber enhances by $\sim$18 for a fly-by velocity of 10 km/s which is the lower limit of the mission definition (Rubin, 2021).

7.3 Summary of Instrument Performance

The requirements discussed in Section 4 are mostly fulfilled by the MANiaC instruments SHU and NDG (Table 7.2). The largest drawback is the noise in the SHU measurements. The considerably large noise decreases the detection limit of the SHU as well as the dynamic range. The level of the dynamic range of 10^6 represents the current noise level. Thus, the full dynamic range could not be resolved and a further reduction of noise by a factor of 5 is still required for the detection limit. A more compact flight model, particularly in terms of the electronics and cabling of the instrument, might be able to achieve this.

Note, that these measurements and their subsequent conclusions have been taken with laboratory measurement devices which are highly reliable. Thus, the measurement accuracy and noise levels needs to be checked again when the supply and read-out electronics for the flight model are ready to be tested.

TABLE 7.2: Requirement and fulfilment overview.

Requirement	Fulfilled	
	SHU	NDG
IR1-PRF-1: Dynamic Range	✓/✗	N/A
IR1-PRF-2: Mass Resolution	✓	N/A
IR1-PRF-3: Mass Range	✓	N/A
IR1-PRF-4: Temporal Resolution	✓	✓
IR1-PRF-5: Stability	✓	✓
IR1-PRF-6: Detection Limit SHU	✗	N/A
IR1-PRF-7: Detection Range NDG	N/A	✓
IR1-PRF-8: NDG Density Measurement Accuracy	N/A	✓

Summary and Outlook

8

This thesis is divided into two parts: the data analysis of ROSINA data from the Rosetta mission, with two published papers, and the characterisation of the MANiaC instrument for ESA's future Comet Interceptor mission. Both missions focus on studying specific comets. The Rosetta mission orbited comet 67P for more than two years, providing unprecedented data about this comet. In contrast, the Comet Interceptor mission aims to fly past a dynamically new comet, offering insights into the composition and structure of a more pristine comet than the short-period comet 67P. This thesis integrates both the scientific aspects of comet research with the engineering challenges of developing an instrument for a comet mission. The following sections summarise the results from the ROSINA data analysis and the MANiaC calibration, along with ideas for future work in each area.

8.1 Rosetta/ROSINA Data Analysis

Two studies using Rosetta/ROSINA DFMS data were conducted as part of this thesis: a study on isotope ratios in water and alkanes in comet 67P, and another study on gas composition changes in the comet's coma, which discussed outburst trigger mechanisms. These studies are summarised in the following subsections and future research ideas are suggested.

8.1.1 Isotope Ratios on Comet 67P

The study on isotopic ratios in water and alkanes (Section 3.1), published in *Astronomy and Astrophysics* (Müller et al., 2022), demonstrates the independence of the D/H ratio in water from factors such as heliocentric distance, cometary activity level, or spacecraft location relative to the nucleus. This suggests a common origin for the two lobes of comet 67P and indicates that its water originates from a relatively uniform reservoir. Moreover, the elevated D/H ratios observed in alkanes, while being consistent with those of other organic molecules found on different comets, highlight the complexity of cometary organic chemistry. The relative stability of the $^{13}C/^{12}C$ ratio across various organic molecules on diverse comets further supports our understanding of cometary organic composition.

To further validate the invariability of the D/H ratio in comets, additional measurements from various comets and alternative approaches are necessary. Investigating the isotopic ratios of doubly deuterated alkanes or alkanes with two ^{13}C atoms presents an intriguing avenue, especially given the higher D/H ratio in doubly deuterated water (HDO) compared to its singly deuterated counterpart (Altwegg et al., 2017). Additionally, the consistent $^{13}C/^{12}C$ ratio across many organic molecules,

except for H_2CO (Altwegg et al., 2020), further warrants exploration. These investigations will deepen our understanding of cometary organic chemistry and the origins of water and organic compounds in the Solar System.

8.1.2 Outburst Mechanisms on Comets

The extensive coverage of 67P's outgassing by the Rosetta mission enabled a thorough analysis of over 40 outburst events, revealing distinct compositions associated with different triggering mechanisms (Section 3.2). Published in the *Monthly Notices of the Royal Astronomical Society* (Müller et al., 2024), the study identified two primary outburst mechanisms on comet 67P. Outbursts caused by landslides or cliff collapses are likely water-driven, due to the exposure of fresh water ice on the surface near the event source regions (e.g., Vincent et al., 2016, Pajola et al., 2017). In contrast, eruptions during perihelion are characterised by increased highly volatile species, particularly CO_2, believed to originate from deeper subsurface pockets (e.g., Belton et al., 2013, Agarwal et al., 2017, Bockelée-Morvan et al., 2022).

Unresolved questions remain, such as the correlation between dust and gas components and the dependence of outburst triggers on heliocentric distance. The emergence, size, and build-up time of subsurface pockets also require further study. Addressing these questions necessitates multidisciplinary investigations, encompassing laboratory experiments, simulations, observations, and space missions. Future research may involve modelling to estimate the size and behaviour of subsurface pockets, and laboratory techniques and experiments to create similar pockets in small, comet-like, porous bodies. Adapting techniques used in Martian ice analogue experiments (Portyankina et al., 2019) to comet analogues could provide further insights into the mechanisms driving cometary outbursts.

8.2 MANiaC Calibration

Both prototypes of the neutral density gauge (NDG) and the time-of-flight mass spectrometer (sensor head unit, SHU) of the MANiaC instrument suite were tested and calibrated in the laboratory for this work. The results are summarised below.

8.2.1 NDG

The NDG underwent comprehensive static and dynamic measurements and calibrations to assess its performance. Static measurements determined the instrument's sensitivity to pressure changes for several gases (Section 5.1.1), while dynamic measurements validated the theory of pressure enhancement at various velocity levels for both neutral (Section 5.1.3) and ionised (Section 5.1.4) species. The sensitivity of the NDG is comparable to ROSINA/COPS from the Rosetta mission and the gas dependence of sensitivity aligns with literature values. The dynamic measurements with a neutral gas beam covered velocities below the anticipated fly-by velocity of the Comet Interceptor mission, while the ion beam measurements covered the upper range of possible fly-by velocities, showing close agreement with theoretical density enhancements.

All instrument requirements for the NDG were met (Section 7.1). Furthermore, measurements with the NDG-e FE (Section 5.1.2) confirmed effective operation and data read-out at a femto-ampere level. These results suggest that the final implementation of the complete NDG in flight configuration should proceed smoothly.

However, a calibration of the flight model is necessary to ensure comparable sensitivity between the flight model and the prototype using the power supplies and read-out electronics from the flight model.

8.2.2 SHU

A parameter study on various instrument voltages (Section 6.1) identified correlation trends. Furthermore, the potential search space for the different voltages for signal strength optimisations could be significantly reduced.

Overcoming initial instabilities in the SHU signal required significant effort, but ultimately, stability requirements were met (Section 6.2). While all requirements except the SHU detection limit and dynamic range were satisfied (Section 7.2), recommendations to enhance detection sensitivity include increasing detector voltage and filament emission, reducing noise through shorter cable connections, and minimising external power supply and data acquisition system interference after assembly of the flight model.

Future efforts for the SHU involve assembling and calibrating the instrument flight model, using the data processing unit, read-out electronics, and associated voltage and filtering boards. Although only laboratory electronics and power supplies have been used thus far, the SHU prototype demonstrated satisfactory performance, providing confidence in its functionality. Further calibration measurements with the flight model and flight spare (twin instrument of the flight model that stays on Earth) are necessary to determine fragmentation patterns for various molecules, instrument sensitivity, signal-to-noise ratio, and establish optimal voltage settings. Additionally, dynamic tests similar to those conducted for the NDG will be needed to understand how fragmentation patterns and mass spectra change with different fly-by velocities. While fragmentation pattern analysis can largely be conducted on the flight spare post-flight model integration, significant work remains to ensure the SHU's readiness for space deployment.

Appendix: Instrument Drawings

A.1 Technical Drawing of the NDG

Antechamber

Ionization Zone

Ion Collector

Electron Repeller
Anode Base
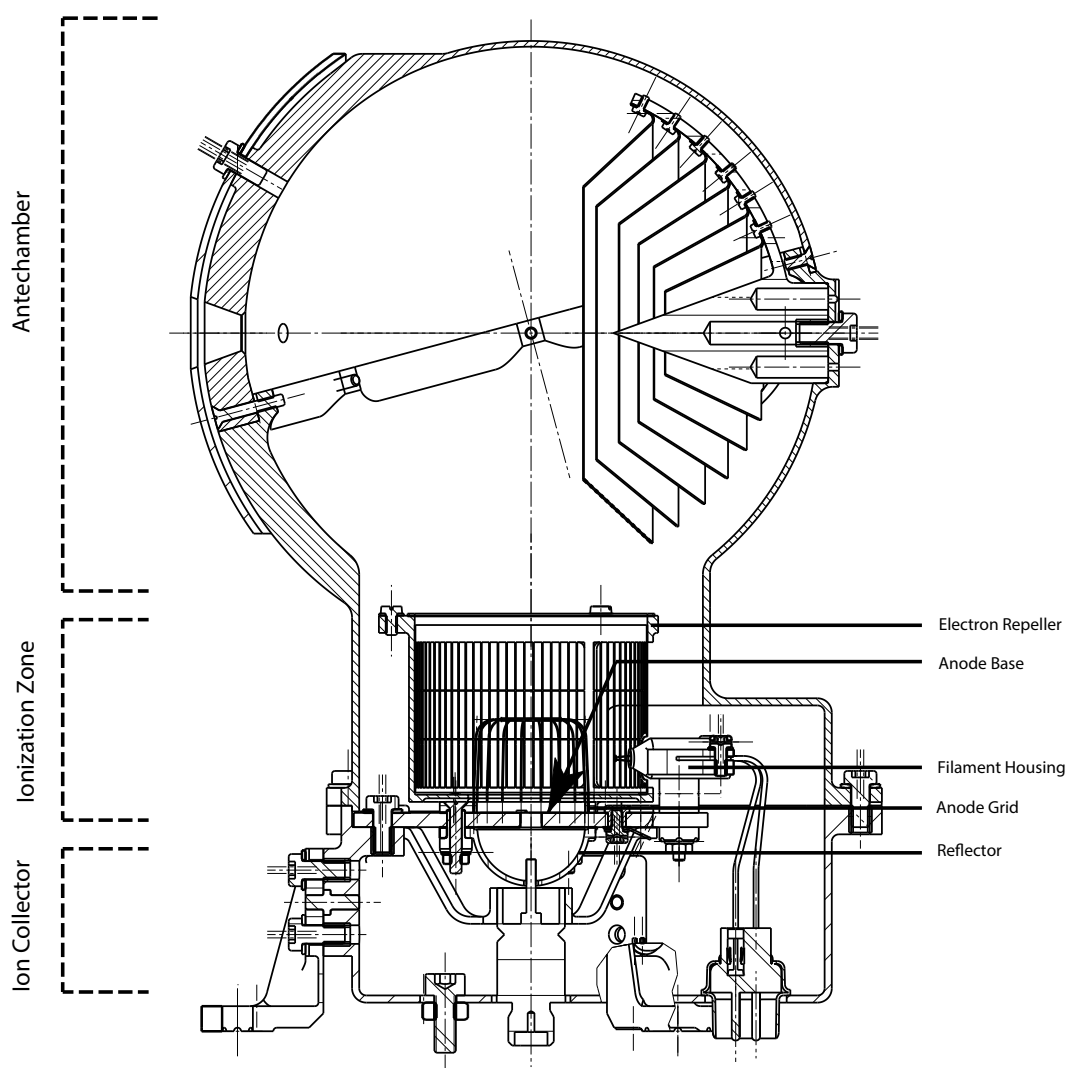Filament Housing
Anode Grid
Reflector

FIGURE A.1: Technical drawing of the NDG.
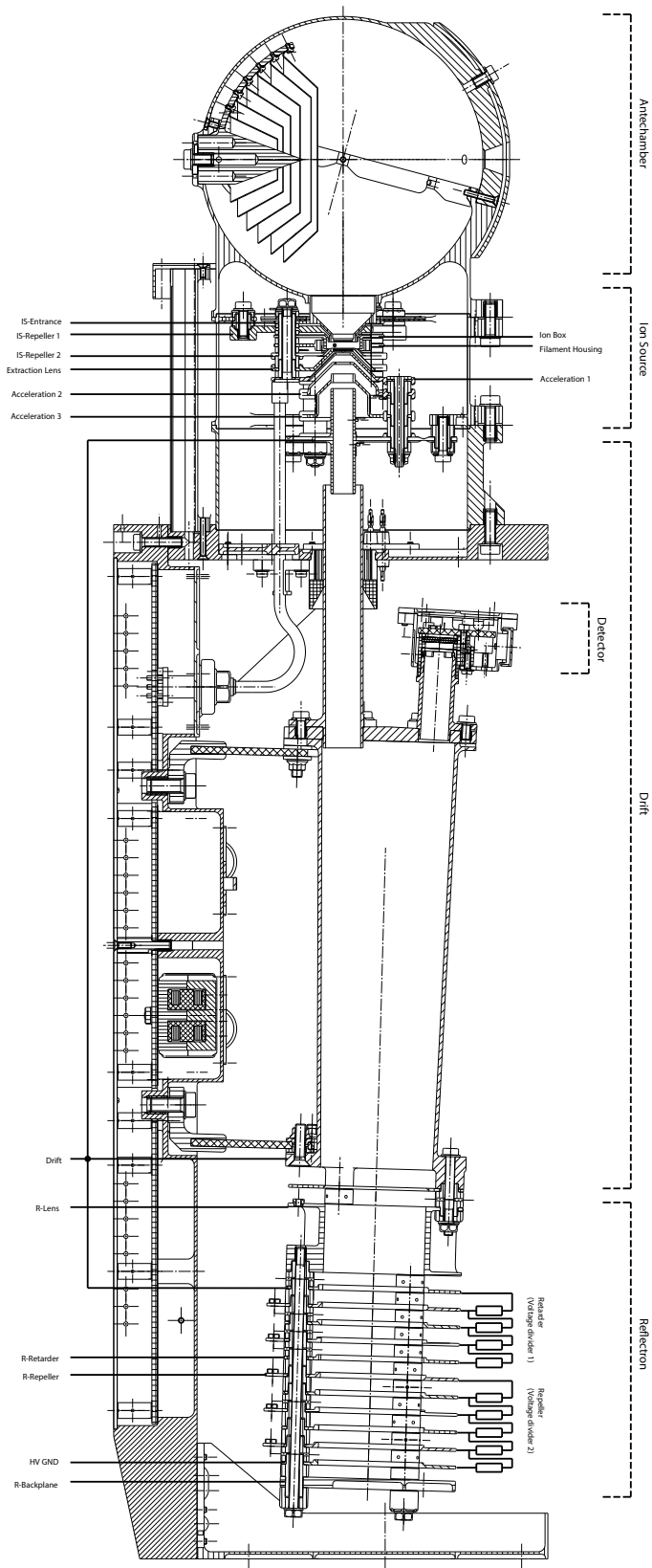
A.2 Technical Drawing of the SHU

FIGURE A.2: Technical drawing of the SHU.

Appendix: Pressure Gauge Scale Factors

B

Different gases have different ionisation probabilities. Hence, pressure gauge scale factors are needed. They are usually normalised to N_2. Table B.1 and Table B.2 present such scale factors for the most important calibration gases for the two different pressure gauges used in this work (MKS Instruments Inc., 2020; Pfeiffer Vacuum GmbH, 2005):

TABLE B.1: Scale factors to use with *MKS Instruments* ionisation pressure gauges.

Gas	Scale Factor	Gas	Scale Factor
He	5.56	CO	$9.52 \cdot 10^{-1}$
Ne	3.33	H_2O	$8.93 \cdot 10^{-1}$
H_2	2.17	Ar	$7.75 \cdot 10^{-1}$
N_2	1.00	CO_2	$7.04 \cdot 10^{-1}$
Air	1.00	Kr	$5.15 \cdot 10^{-1}$
O_2	$9.90 \cdot 10^{-1}$	Xe	$3.48 \cdot 10^{-1}$

TABLE B.2: Scale factors to use with *Pfeiffer Vacuum* ionisation pressure gauges.

Gas	Scale Factor	Gas	Scale Factor
He	5.9	Xe	0.4
Ne	4.1	Kr	0.5
H_2	2.4	Ar	0.8
Air (N_2, O_2, CO)	1.0		

Bibliography

Agarwal, J., V. Della Corte, P. D. Feldman, et al. (July 2017). "Evidence of sub-surface energy storage in comet 67P from the outburst of 2016 July 03". In: *Mon. Not. R. Astron. Soc.* 469, s606–s625. DOI: 10.1093/mnras/stx2386. arXiv: 1710.10235 [astro-ph.EP].

Altwegg, K., H. Balsiger, A. Bar-Nun, et al. (Jan. 2015). "67P/Churyumov-Gerasimenko, a Jupiter family comet with a high D/H ratio". In: *Science* 347.6220, 1261952, p. 1261952. DOI: 10.1126/science.1261952.

Altwegg, K., H. Balsiger, A. Bar-Nun, et al. (May 2016). "Prebiotic chemicals–amino acid and phosphorus–in the coma of comet 67P/Churyumov-Gerasimenko". In: *Science Advances* 2.5, e1600285–e1600285. DOI: 10.1126/sciadv.1600285.

Altwegg, K., H. Balsiger, J. J. Berthelier, et al. (May 2017). "D_2O and HDS in the coma of 67P/Churyumov-Gerasimenko". In: *Philosophical Transactions of the Royal Society of London Series A* 375.2097, 20160253, p. 20160253. DOI: 10.1098/rsta.2016.0253.

Altwegg, K., H. Balsiger, M. Combi, et al. (Nov. 2020). "Molecule-dependent oxygen isotopic ratios in the coma of comet 67P/Churyumov-Gerasimenko". In: *Mon. Not. R. Astron. Soc.* 498.4, pp. 5855–5862. DOI: 10.1093/mnras/staa2701. arXiv: 2012.05788 [astro-ph.EP].

Asphaug, E. and W. Benz (July 1994). "Density of comet Shoemaker-Levy 9 deduced by modelling breakup of the parent 'rubble pile'". In: *Nature* 370.6485, pp. 120–124. DOI: 10.1038/370120a0.

Bailey, M.E., S.V.M. Clube, W.M. Napier, et al. (1990). *The Origin of Comets*. Elsevier Science & Technology Books. ISBN: 978-0-080-34858-2.

Balsiger, H., K. Altwegg, P. Bochsler, et al. (Feb. 2007). "Rosina Rosetta Orbiter Spectrometer for Ion and Neutral Analysis". In: *Space Science Review* 128.1-4, pp. 745–801. DOI: 10.1007/s11214-006-8335-3.

Belton, Michael J. S., Peter Thomas, Brian Carcich, et al. (Feb. 2013). "The origin of pits on 9P/Tempel 1 and the geologic signature of outbursts in Stardust-NExT images". In: *Icarus* 222.2, pp. 477–486. DOI: 10.1016/j.icarus.2012.03.007.

Bieler, A., K. Altwegg, H. Balsiger, et al. (Oct. 2015). "Abundant molecular oxygen in the coma of comet 67P/Churyumov-Gerasimenko". In: *Nature* 526.7575, pp. 678–681. DOI: 10.1038/nature15707.

Bieler, A., K. Altwegg, L. Hofer, et al. (Nov. 2011). "Optimization of mass spectrometers using the adaptive particle swarm algorithm". In: *Journal of Mass Spectrometry* 46.11, pp. 1143–1151. DOI: 10.1002/jms.2001.

Biver, N., R. Moreno, D. Bockelée-Morvan, et al. (May 2016). "Isotopic ratios of H, C, N, O, and S in comets C/2012 F6 (Lemmon) and C/2014 Q2 (Lovejoy)". In: *Astron. Astrophys.* 589, A78, A78. DOI: 10.1051/0004-6361/201528041. arXiv: 1603.05006 [astro-ph.EP].

Bockelée-Morvan, D., N. Biver, C. A. Schambeau, et al. (Aug. 2022). "Water, hydrogen cyanide, carbon monoxide, and dust production from distant comet 29P/Schwassmann-Wachmann 1". In: *Astron. Astrophys.* 664, A95, A95. DOI: 10.1051/0004-6361/202243241. arXiv: 2205.11425 [astro-ph.EP].

Bodendorfer, Michael (2008). "SWISSCASE development and characterization of an electron cyclotron resonance ion source for the calibration of space flight

instruments". PhD thesis. Lausanne: EPFL, p. 185. DOI: https://doi.org/10.5075/epfl-thesis-4194.

Brandt, J.C. and R.D. Chapman (2004). *Introduction to Comets*. Cambridge Planetary Science. Cambridge University Press. ISBN: 9780521004664.

Brown, K. L. and G. W. Tautfest (Sept. 1956). "Faraday-Cup Monitors for High-Energy Electron Beams". In: *Review of Scientific Instruments* 27.9, pp. 696–702. DOI: 10.1063/1.1715674.

Capaccioni, F., A. Coradini, G. Filacchione, et al. (Jan. 2015). "The organic-rich surface of comet 67P/Churyumov-Gerasimenko as seen by VIRTIS/Rosetta". In: *Science* 347.6220, aaa0628, aaa0628. DOI: 10.1126/science.aaa0628.

Clark, Roger A., Philip M. Benson, Andrew J. Carter, et al. (Sept. 2009). "Anisotropic P-wave attenuation measured from a multi-azimuth surface seismic reflection survey". In: *Geophysical Prospecting* 57.5, pp. 835–845. DOI: 10.1111/j.1365-2478.2008.00772.x.

Dahl, David A. (Dec. 2000). "simion for the personal computer in reflection". In: *International Journal of Mass Spectrometry* 200.1-3, pp. 3–25. DOI: 10.1016/S1387-3806(00)00305-5.

de Hoffmann, E. and V. Stroobant (2007). *Mass Spectrometry: Principles and Applications*. 3rd ed. J. Wiley. ISBN: 978-0-470-03310-4.

Fausch, Rico (2020). "Mass Spectrometry for In Situ Planetary Research". PhD thesis. Bern. URL: https://boris.unibe.ch/id/eprint/144755.

Fletcher, Alex, Sigrid Close, and Donovan Mathias (Sept. 2015). "Simulating plasma production from hypervelocity impacts". In: *Physics of Plasmas* 22.9, 093504. DOI: 10.1063/1.4930281.

Föhn, Martina (2021). "NIM: The Neutral Gas and Ion Mass Spectrometer to Explore the Galilean Ice Worlds". PhD thesis. Bern. URL: http://boristheses.unibe.ch/3277/.

Fulle, Marco, N. Altobelli, B. Buratti, et al. (Nov. 2016). "Unexpected and significant findings in comet 67P/Churyumov-Gerasimenko: an interdisciplinary view". In: *Mon. Not. R. Astron. Soc.* 462, S2–S8. DOI: 10.1093/mnras/stw1663.

Gardner, Esko, Harry J. Lehto, Kirsi Lehto, et al. (Dec. 2020). "The detection of solid phosphorus and fluorine in the dust from the coma of comet 67P/Churyumov-Gerasimenko". In: *Mon. Not. R. Astron. Soc.* 499.2, pp. 1870–1873. DOI: 10.1093/mnras/staa2950. arXiv: 2010.13379 [astro-ph.EP].

Gargaud, Muriel, William M. Irvine, Ricardo Amils, et al. (2023). *Encyclopedia of Astrobiology*. DOI: 10.1007/978-3-662-65093-6.

Gasc, Sébastien, Kathrin Altwegg, Björn Fiethe, et al. (Jan. 2017). "Sensitivity and fragmentation calibration of the time-of-flight mass spectrometer RTOF on board ESA's Rosetta mission". In: *Planetary and Space Science* 135, pp. 64–73. DOI: 10.1016/j.pss.2016.11.011.

Gerber, T. and D. R. Müller (May 2021). *NDG FE Board Test Report*. Test Report COMET-UBE-MNC-TR-016. University of Bern.

Ghielmetti, A. G., H. Balsiger, R. Baenninger, et al. (Apr. 1983). "Calibration system for satellite and rocket-borne ion mass spectrometers in the energy range from 5 eV/charge to 100 keV/charge". In: *Review of Scientific Instruments* 54.4, pp. 425–436. DOI: 10.1063/1.1137411.

Graf, S., K. Altwegg, H. Balsiger, et al. (May 2004). "A cometary neutral gas simulator for gas dynamic sensor and mass spectrometer calibration". In: *Journal of Geophysical Research (Planets)* 109.E7, E07S08, E07S08. DOI: 10.1029/2003JE002188.

Gross, Jürgen H. (2017). *Mass Spectrometry - A Textbook*. 3rd ed. Springer. ISBN: 978-3-319-54397-0. DOI: 10.1007/978-3-319-54398-7.

Hänni, N., K. Altwegg, M. Combi, et al. (June 2022). "Identification and characterization of a new ensemble of cometary organic molecules". In: *Nature Communications* 13, 3639, p. 3639. DOI: 10.1038/s41467-022-31346-9.

Hässig, M., K. Altwegg, H. Balsiger, et al. (Jan. 2015). "Time variability and heterogeneity in the coma of 67P/Churyumov-Gerasimenko". In: *Science* 347.6220, aaa0276, aaa0276. DOI: 10.1126/science.aaa0276.

Hässig, Myrtha (2013). "Sensitivity and fragmentation calibration of the ROSINA double focusing mass spectrometer". PhD thesis. Bern. URL: https://boristheses.unibe.ch/id/eprint/1004.

Hofer, Lukas (2015). "Development of the gas chromatograph – mass spectrometer to investigate volatile species in the lunar soil for the Luna-Resurs mission". PhD thesis. Bern. URL: https://boris.unibe.ch/id/eprint/81671.

Hughes, D. W. (Dec. 1975). "Cometary Outbursts, A Brief Survey". In: *Q. J. R. Astron. Soc.* 16, p. 410.

Hughes, D. W. (Jan. 1991). "Possible Mechanisms for Cometary Outbursts". In: *IAU Colloq. 116: Comets in the post-Halley era*. Ed. by Jr. Newburn R. L., M. Neugebauer, and J. Rahe. Vol. 167. Astrophysics and Space Science Library, p. 825.

Jones, Geraint, Hideyo Kawakita, Luisa Lara, et al. (Apr. 2022). *Comet Interceptor - Visiting a pristine comet*. Tech. rep. ESA-SCI-DIR-RP-001. European Space Agency.

Jones, Geraint, Colin Snodgrass, Cecilia Tubiana, et al. (Jan. 2024). "The Comet Interceptor Mission". In: *Space Science Review* 220.1, 9, p. 9. DOI: 10.1007/s11214-023-01035-0.

Keller, H. U. (Dec. 1989). "Comets - dirty snowballs or icy dirtballs?" In: *Physics and Mechanics of Cometary Materials*. Ed. by James J. Hunt and T. Duc Guyenne. Vol. 302. ESA Special Publication, pp. 39–45.

Lagrange, Joseph-Louis (1892). "Oeuvres de Lagrange. T. 6". In: Gauthier-Villars. Chap. Chapitre II: Essai sur le problème des trois corps, pp. 229–334. URL: https://gallica.bnf.fr/ark:/12148/bpt6k229225j.

Laidler, Keith J. and John H. Meiser (1999). *Physical Chemistry*. 3rd ed. Houghton Mifflin Company. ISBN: 0-395-91848-0.

Le Roy, Léna, Kathrin Altwegg, Hans Balsiger, et al. (Nov. 2015). "Inventory of the volatiles on comet 67P/Churyumov-Gerasimenko from Rosetta/ROSINA". In: *Astron. Astrophys.* 583, A1, A1. DOI: 10.1051/0004-6361/201526450.

Lis, Dariusz C., Dominique Bockelée-Morvan, Rolf Güsten, et al. (May 2019). "Terrestrial deuterium-to-hydrogen ratio in water in hyperactive comets". In: *Astron. Astrophys.* 625, L5, p. L5. DOI: 10.1051/0004-6361/201935554. arXiv: 1904.09175 [astro-ph.EP].

Lunine, Jonathan I. and Sushil K. Atreya (Mar. 2008). "The methane cycle on Titan". In: *Nature Geoscience* 1.3, pp. 159–164. DOI: 10.1038/ngeo125.

Mehta, N. (Sept. 2023a). *Instrument Requirements Specification*. Requirement Specification COMET-UBE-MNC-RS-001. University of Bern.

Mehta, N. (Sept. 2023b). *MANiaC EICD*. Interface Control Document COMET-UBE-MNC-ICD-001. University of Bern.

Meija, Juris, Tyler Coplen, Michael Berglund, et al. (Feb. 2016). "Isotopic Compositions of the Elements 2013 (IUPAC Technical Report)". In: *Pure and Applied Chemistry* 88, pp. 293–306. DOI: 10.1515/pac-2015-0503.

Minor Planet Center, International Astronomical Union (2023). *67P/Churyumov-Gerasimenko*. http://www.minorplanetcenter.net/db_search/show_object?object_id=67P. Accessed: (20.02.2024).

MKS Instruments Inc. (Mar. 2020). *Series 370 - Stabil-Ion® Vacuum Measurement Controller*. Revision C. Available at `https://www.mksinst.com`. MKS Instruments Inc. Andover, MA.

Morton, David W. and Colin L. Young (Sept. 1995). "Analysis of Peak Profiles Using Statistical Moments". In: *Journal of Chromatographic Science* 33.9, pp. 514–524. ISSN: 0021-9665. DOI: `10.1093/chromsci/33.9.514`. URL: `https://doi.org/10.1093/chromsci/33.9.514`.

Mottola, S., S. Lowry, C. Snodgrass, et al. (Sept. 2014). "The rotation state of 67P/Churyumov-Gerasimenko from approach observations with the OSIRIS cameras on Rosetta". In: *Astron. Astrophys.* 569, L2, p. L2. DOI: `10.1051/0004-6361/201424590`.

Müller, D. R., K. Altwegg, J. J. Berthelier, et al. (June 2022). "High D/H ratios in water and alkanes in comet 67P/Churyumov-Gerasimenko measured with Rosetta/ROSINA DFMS". In: *Astron. Astrophys.* 662, A69, A69. DOI: `10.1051/0004-6361/202142922`. arXiv: `2202.03521 [astro-ph.EP]`.

Müller, D. R., K. Altwegg, J. J. Berthelier, et al. (Apr. 2024). "Deciphering cometary outbursts: linking gas composition changes to trigger mechanisms". In: *Mon. Not. R. Astron. Soc.* 529.3, pp. 2763–2776. DOI: `10.1093/mnras/stae622`.

Nave, Carl R (2017). *Mean Free Path*. URL: `http://hyperphysics.phy-astr.gsu.edu/hbase/Kinetic/menfre.html`.

NIST Mass Spectrometry Data Center, William E. Wallace (director) (2023). *NIST Chemistry WebBook, NIST Standard Reference Database Number 69*. Ed. by P.J. Linstrom and W.G. Mallard. National Institute of Standards and Technology (NIST). Chap. Mass Spectra. DOI: `10.18434/T4D303`.

Noll, Keith S., Harold A. Weaver, and Paul D. Feldman (July 1996). "The Collision of Comet Shoemaker-Levy 9 and Jupiter". In: *IAU Colloq. 156: The Collision of Comet Shoemaker-Levy 9 and Jupiter*.

Paganini, L., M. J. Mumma, E. L. Gibb, et al. (Feb. 2017). "Ground-based Detection of Deuterated Water in Comet C/2014 Q2 (Lovejoy) at IR Wavelengths". In: *Astrophys. J. Lett.* 836.2, L25, p. L25. DOI: `10.3847/2041-8213/aa5cb3`.

Pajola, M., S. Höfner, J. B. Vincent, et al. (Mar. 2017). "The pristine interior of comet 67P revealed by the combined Aswan outburst and cliff collapse". In: *Nature Astronomy* 1, 0092, p. 0092. DOI: `10.1038/s41550-017-0092`.

Pajola, Maurizio, Jean-Baptiste Vincent, Carsten Güttler, et al. (Nov. 2015). "Size-frequency distribution of boulders ≥7 m on comet 67P/Churyumov-Gerasimenko". In: *Astron. Astrophys.* 583, A37, A37. DOI: `10.1051/0004-6361/201525975`.

Pätzold, Martin, Thomas P. Andert, Matthias Hahn, et al. (Feb. 2019). "The Nucleus of comet 67P/Churyumov-Gerasimenko - Part I: The global view - nucleus mass, mass-loss, porosity, and implications". In: *Mon. Not. R. Astron. Soc.* 483.2, pp. 2337–2346. DOI: `10.1093/mnras/sty3171`.

Pestoni, B., K. Altwegg, H. Balsiger, et al. (Jan. 2021a). "Detection of volatiles undergoing sublimation from 67P/Churyumov-Gerasimenko coma particles using ROSINA/COPS. I. The ram gauge". In: *Astron. Astrophys.* 645, A38, A38. DOI: `10.1051/0004-6361/202039130`. arXiv: `2012.01495 [astro-ph.EP]`.

Pestoni, B., K. Altwegg, H. Balsiger, et al. (July 2021b). "Detection of volatiles undergoing sublimation from 67P/Churyumov-Gerasimenko coma particles using ROSINA/COPS. II. The nude gauge". In: *Astron. Astrophys.* 651, A26, A26. DOI: `10.1051/0004-6361/202140634`. arXiv: `2105.09965 [astro-ph.EP]`.

Pestoni, B., K. Altwegg, V. Della Corte, et al. (Mar. 2023). "Multi-instrument analysis of 67P/Churyumov-Gerasimenko coma particles: COPS-GIADA data fusion". In: *Astron. Astrophys.* 671, A168, A168. DOI: `10.1051/0004-6361/202245279`.

Pfeiffer Vacuum GmbH (Nov. 2005). *Compact FullRange Gauge - PBR 260*. Available at https://www.pfeiffer-vacuum.net. Pfeiffer Vacuum GmbH. Asslar, Germany.

Portyankina, G., J. Merrison, J. J. Iversen, et al. (Apr. 2019). "Laboratory investigations of the physical state of CO_2 ice in a simulated Martian environment". In: *Icarus* 322, pp. 210–220. DOI: 10.1016/j.icarus.2018.04.021.

Rubin, M. (May 2021). *Instrument Operations Plan*. Plan COMET-UBE-MNC-PL-003. University of Bern.

Rubin, Martin, Kathrin Altwegg, Hans Balsiger, et al. (Oct. 2019). "Elemental and molecular abundances in comet 67P/Churyumov-Gerasimenko". In: *Mon. Not. R. Astron. Soc.* 489.1, pp. 594–607. DOI: 10.1093/mnras/stz2086. arXiv: 1907.11044 [astro-ph.EP].

Scherer, S., K. Altwegg, H. Balsiger, et al. (Mar. 2006). "A novel principle for an ion mirror design in time-of-flight mass spectrometry". In: *International Journal of Mass Spectrometry* 251.1, pp. 73–81. DOI: 10.1016/j.ijms.2006.01.025.

Schlueter, M. (2019). *MIDACO Solver*. URL: http://www.midaco-solver.com.

Schroeder, Isaac R. H. G. (2020). "Isotopic Composition of Water in Comet 67P/Churyumov-Gerasimenko and Characterisation of the ROSINA DFMS FS". PhD thesis. Bern. URL: https://boris.unibe.ch/id/eprint/158960.

Schroeder, Isaac R. H. G., Kathrin Altwegg, Hans Balsiger, et al. (Oct. 2019). "$^{16}O/^{18}O$ ratio in water in the coma of comet 67P/Churyumov-Gerasimenko measured with the Rosetta/ROSINA double-focusing mass spectrometer". In: *Astron. Astrophys.* 630, A29, A29. DOI: 10.1051/0004-6361/201833806. arXiv: 1809.03798 [astro-ph.EP].

Schuhmann, Markus (2020). "An Investigation of CH- and CHO-bearing Molecules with the ROSINA-DFMS". PhD thesis. Bern. URL: https://boris.unibe.ch/id/eprint/158961.

Schulz, Rita (Jan. 2010). "The Rosetta Mission: Comet and Asteroid Exploration". In: *Icy Bodies of the Solar System*. Ed. by Julio A. Fernandez, Daniela Lazzaro, Dina Prialnik, et al. Vol. 263, pp. 312–316. DOI: 10.1017/S1743921310001997.

Schwehm, G. and R. Schulz (Oct. 1999). "Rosetta Goes to Comet Wirtanen". In: *Space Science Review* 90, pp. 313–319. DOI: 10.1023/A:1005231006010.

Shinnaka, Yoshiharu, Takafumi Ootsubo, Hideyo Kawakita, et al. (Nov. 2018). "Mid-infrared Spectroscopic Observations of Comet 17P/Holmes Immediately After Its Great Outburst in 2007 October". In: *The Astronomical Journal* 156.5, 242, p. 242. DOI: 10.3847/1538-3881/aadfea. arXiv: 1808.07606 [astro-ph.EP].

Snodgrass, Colin and Geraint H. Jones (Nov. 2019). "The European Space Agency's Comet Interceptor lies in wait". In: *Nature Communications* 10, 5418, p. 5418. DOI: 10.1038/s41467-019-13470-1.

Stanic, Lucijana (Jan. 2024). "Fragmentation and Sensitivity Measurements with the MANiaC Reflectron-type Time-Of-Flight Mass Spectrometer". MA thesis. Universität Bern.

Tarantino, P., A. Goel, A. Corso, et al. (Sept. 2018). "An electrostatic method to model the expansion of hypervelocity impact plasma on positively biased surfaces". In: *Physics of Plasmas* 25.9, 092103, p. 092103. DOI: 10.1063/1.5039656.

Thomas, N., S. Ulamec, E. Kührt, et al. (Nov. 2019). "Towards New Comet Missions". In: *Space Science Review* 215.8, 47, p. 47. DOI: 10.1007/s11214-019-0611-0.

Thomas, Nicolas (2020). *An Introduction to Comets; Post-Rosetta Perspectives*. DOI: 10.1007/978-3-030-50574-5.

Vincent, J. -B., M. F. A'Hearn, Z. -Y. Lin, et al. (Nov. 2016). "Summer fireworks on comet 67P". In: *Mon. Not. R. Astron. Soc.* 462, S184–S194. DOI: 10.1093/mnras/stw2409. arXiv: 1609.07743 [astro-ph.EP].

Westermann, Christian B. (Jan. 2000). "A Novel Calibration System for the Simulation of Cometary Atmospheres". PhD thesis. University of Bern, Switzerland.

Westermann, Christian B., Wolfram Luithardt, Ernest Kopp, et al. (Sept. 2001). "A high precision calibration system for the simulation of cometary gas environments". In: *Measurement Science and Technology* 12.9, pp. 1594–1603. DOI: 10.1088/0957-0233/12/9/327.

Whipple, F.L. (Mar. 1950). "A comet model. I. The acceleration of Comet Encke". In: *Astrophys. Journal* 111, pp. 375–394. DOI: 10.1086/145272.

Whipple, F.L. (May 1951). "A Comet Model. II. Physical Relations for Comets and Meteors." In: *Astrophys. Journal* 113, p. 464. DOI: 10.1086/145416.

Whipple, F.L. and D.W.E. Green (1985). *The Mystery of Comets*. Smithsonian library of the solar system. Smithsonian Institution Press. ISBN: 978-0-874-74968-7.

Wierzchos, K. and M. Womack (Apr. 2020). "CO Gas and Dust Outbursts from Centaur 29P/Schwassmann-Wachmann". In: *The Astronomical Journal* 159.4, p. 136. DOI: 10.3847/1538-3881/ab6e68. arXiv: 2001.09537 [astro-ph.EP].

Zhan, Zhi-Hui, Jun Zhang, Yun Li, et al. (2009). "Adaptive Particle Swarm Optimization". In: *IEEE Transactions on Systems, Man, and Cybernetics, Part B (Cybernetics)* 39.6, pp. 1362–1381. DOI: 10.1109/TSMCB.2009.2015956.

Curriculum Vitae

Personal Information

Full Name: Daniel Robert Müller

Address: Bernstrasse 47
                  3312 Fraubrunnen, Switzerland

Date of Birth: July 4, 1993

Place of Birth: Redwood City, CA, USA

Nationality: Swiss, American

Education

2020 – 2024   PhD in Physics, Division of Space Research and Planetary Sciences, Physics Institute, University of Bern, Switzerland

2017 – 2019   Master in Mechanical Engineering, Federal Institute of Technology Zurich (ETHZ), Switzerland

2013 – 2016   Bachelor in Mechanical Engineering, Federal Institute of Technology Lausanne (EPFL), Switzerland

---

Academic Record

2024   PhD Thesis in Physics, University of Bern, Division of Space Research and Planetary Sciences, entitled "In Situ Comet Research - From Rosetta To Comet Interceptor", Supervisor: PD Dr. Martin Rubin

2019   Master Thesis in Mechanical Engineering, Institute of Composite Structures and Adaptive Systems, German Aerospace Center (DLR), Germany, entitled "Development and characterisation of elastic hinges for large-area, ultra-light deployable space structures", Supervisor: Dr. Martin E. Zander (DLR), Prof. Dr. Paolo Ermanni (ETHZ)

2018   Semester Project, Laboratory of Composite Structures and Adaptive Materials, Federal Institute of Technology Zurich, ETHZ, entitled "Characterising folding and deployment behaviour of a foldable, ultrathin composite heart stent device", Supervisor: Dr. Arthur Schlothauer

2018   Student Assistant Project, Institute for Mechanical Systems, Federal Institute of Technology Zurich, ETHZ, entitled "Material parameter studies with FEM for human skin behaviour under gravity loads", Supervisor: Prof. Dr. Edoardo Mazza

2016   Bachelor Thesis in Mechanical Engineering, Laboratory of Applied Mechanics and Reliability Analysis, Federal Institute of Technology Lausanne (EPFL), entitled "Topology optimisation of a drone arm with Abaqus/Tosca", Supervisor: Prof. Dr. Joël Cugnoni

Professional Training

2020 – 2024   Teaching assistant of physics laboratory class and exercises for students of physics and other branches, Physics Institute, University of Bern, CH

2019 – 2020   Mechanical Engineer, Institute of Composite Structures and Adaptive Systems, German Aerospace Center (DLR), GER

2014 – 2016   Teaching assistant of solid mechanics exercises for mechanical engineering students, Federal Institute of Technology Lausanne (EPFL), CH

Declaration of Originality

Name, First Name: Müller, Daniel Robert

Matriculation Number: 13-811-039
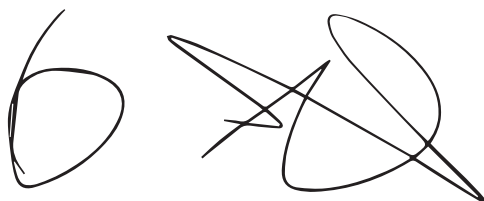
Study Program: PhD in Physics

Supervisor: PD Dr. Martin Rubin

Title of the Thesis: In Situ Comet Research – From Rosetta To Comet Interceptor

I declare herewith that this thesis is my own work and that I have not used any sources other than those stated. I have indicated the adoption of quotations as well as thoughts taken from other authors as such in the thesis. I am aware that the Senate pursuant to Article 36 paragraph 1 litera r of the University Act of September 5th, 1996 and Article 69 of the University Statute of June 7th, 2011 is authorized to revoke the doctoral degree awarded on the basis of this thesis. For the purposes of evaluation and verification of compliance with the declaration of originality and the regulations governing plagiarism, I hereby grant the University of Bern the right to process my personal data and to perform the acts of use this requires, in particular, to reproduce the written thesis and to store it permanently in a database, and to use said database, or to make said database available, to enable comparison with theses submitted by others.

Bern, July 4, 2024

Daniel Robert Müller